UNIVERSITY OF PADOVA

CENTER OF STUDIES AND ACTIVITIES FOR SPACE
"GIUSEPPE COLOMBO" - CISAS
Director Prof. Giampaolo Piotto

Ph.D. COURSE IN
SCIENZE, TECNOLOGIE E MISURE SPAZIALI
SPACE SCIENCES, TECHNOLOGIES AND MEASUREMENTS
CURRICULUM IN
SCIENCES AND TECHNOLOGIES FOR AERONAUTICS
AND SATELLITE APPLICATIONS

XXXIV Cycle

PLANETARY MAPPING AT DIFFERENT SCALES: INSIGHTS ON ATMOSPHERE-LESS TERRESTRIAL BODIES

Ph.D. Course Director: *Prof. Francesco Picano*
Supervisor: *Prof. Matteo Massironi*
Co-supervisor: *Prof. Giampiero Naletto*
Dr. Riccardo Pozzobon
Dr. Lorenza Giacomini

Ph.D. student: *GLORIA TOGNON*

To R. and V.,
for their unwavering love

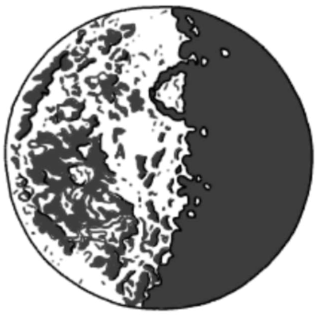

Convertitevi a me con tutto il vostro cuore

e non disprezzatemi perché sono nera e oscura.

Infatti il Sole mi privò del colore

e gli abissi coprirono il mio aspetto

e la terra è stata contaminata nelle mie opere,

è stata avvolta dalle tenebre.

(Tommaso d'Aquino)

Contents

Riassunto **13**

Abstract **15**

1 Introduction **17**
1.1 The PLANMAP project . . . 17
1.2 Research goal . . . 18
1.3 The art of mapping . . . 18
1.4 Innovative geologic maps: integration of spectral and color information . . . 20

2 Small-scale mapping on Mercury **23**
2.1 Introduction . . . 23
2.1.1 Mercury: planet of extremes . . . 23
2.1.2 Exploration history . . . 26
2.1.3 Geology of Mercury . . . 33
2.1.4 The H-9 Eminescu quadrangle . . . 41
2.2 Data and basemaps . . . 44
2.3 Methods . . . 46
2.4 Results . . . 49
2.4.1 Geologic map . . . 49
2.4.2 Color-based spectral map . . . 53
2.4.3 Target definition for the BepiColombo mission . . . 54
2.5 Discussion . . . 59

3 Large-scale mapping on the Moon **61**
3.1 Introduction . . . 61
3.1.1 The Moon: life companion . . . 61
3.1.2 A short history of lunar exploration . . . 65
3.1.3 Geology of the Moon . . . 71
3.1.4 The Tsiolkovskiy crater . . . 76
3.2 Data and basemaps . . . 79
3.3 Methods . . . 81
3.4 Results . . . 82
3.4.1 Morpho-stratigraphic map . . . 82
3.4.2 Color-based spectral map . . . 84
3.4.3 Age determinations . . . 86
3.4.4 Spectro-stratigraphic map . . . 90
3.4.5 Insight on landing site characterization . . . 94
3.5 Discussion . . . 97

4 Conclusions **103**

A PLANMAP and GMAP deliverables **107**

B Mercury data catalog **109**

C Geologic units, legend description **111**

D Moon data catalog **113**

Acknowledgements **137**

List of Figures

1.1 Topological rules defined for polylines' errors check. 20
1.2 Topological rules defined for polygons' errors check. 20
1.3 Examples of contextual interpretation (*top panel*, modified from Semenzato et al. (2020)) and in-series interpretation (*bottom panel*, modified from Giacomini et al. (2021)). 21

2.1 Photographs of the mathematician and engineer Giuseppe Colombo during a lesson in Padua (*left panel*, courtesy of ESA) and of the physician Albert Einstein in 1921 (*right panel*, coutesy of the Albert Einstein archives). 24
2.2 Interior structure of the terrestrial planets and the Moon. *Top panel:* comparison between the interior structure of Mercury and that of the Earth (modified from Stevenson (2012)). *Bottom panel:* comparison of the interior structure of Mercury, Venus, the Earth, the Moon and Mars (courtesy of NASA-JPL-Caltech). 25
2.3 Labeled diagram of the M10 spacecraft (courtesy of NASA-JPL). 27
2.4 *Left panel:* an artistic impression of the MESSENGER spacecraft along its journey to Mercury (courtesy of NASA-JPL). *Right panel:* Labeled diagram of the MESSENGER spacecraft (courtesy of NASA-JPL). 28
2.5 *Top panel:* Labeled diagram of the BepiColombo spacecraft, with all its modules (courtesy of ESA-JAXA). *Bottom left panel:* MPO module during its assembly (courtesy of ESA-B. Guillaume). *Bottom right panel:* MMO module during its assembly (courtesy of ESA-G. Murakami). 30
2.6 Labeled diagram of the SIMBIO-SYS imaging system onboard the MPO module of the BepiColombo spacecraft (from Cremonese et al. (2020). 31
2.7 The first black-and-white snapshots of Mercury provided by the Monitoring Cameras onboard the MTM module of the BepiColombo spacecraft (courtesy of ESA-JAXA). 31
2.8 Mercury's time-stratigraphic systems. 33
2.9 MESSENGER MDIS BDR view of intercrater (centered at 27.7°N, 71.0°W, *top panel*), intermediate (centered at 22.6°S, 58.4°W, *central panel*) and smooth (centered at 28.3°N, 157.9°W, *bottom panel*) plains. 35
2.10 MESSENGER MDIS BDR view of wrinkle ridges on Tir Planitia (centered at 13.2°S, 163.7°E, *left panel*), the Beagle Rupes (centered at 1.9°S, 101.1°E, *central panel*) and the Antoniadi Dorsum (centered at 30.0°N, 31.1°W, *right panel*). . . . 37
2.11 MESSENGER MDIS BDR view of radial and concentric graben structures in the Rachmaninoff basin (centered at 27.6°N, 57.6°E, *left panel*) and the Caloris basin (centered at 30.5°N, 163.2°E, *right panel*). 37
2.12 Schematic representations for the three models proposed for Mercury's tectonic evolution, from (Massironi et al., 2015b). (a) global contraction. (b) tidal despinning. (c) mantle convection. 38

2.13 MESSENGER MDIS Enhanced-color image and reflectance spectra. *Top panel*: the Caloris basin is in the upper right and it is filled with a light orange region of HRP and bordered to the west and south by light blue LBP; at the right margin is the Tolstoj basin surrounded by a ring of dark blue LRM; below right of center is a small crater with RM on its floor; above left of center is a particularly young crater with BCFD rays (courtesy of NASA-JHU Applied Physics Lab-Carnegie Inst. of Washington). *Bottom left panel*: reflectance spectra of the enhanced-color units, as from Ernst et al. (2010). *Bottom right panel*: Tyagaraja crater (centered at 3.9°N, 148.9°W) seen in enhanced-colors, where it is possible to distinguish the bright blue and intense orange colors of hollows and pyroclastic deposits respectively. 40

2.14 Water ice deposit in an unnamed permanently shadowed crater in the north polar region. *Top left panel*: the pink line delimits the crater rim, while the green box defines the edge of the 24 m/px, low-altitude broadband MDIS image. *Top right panel*: the yellow arrows individuate the boundary of a low-reflectance region. *Bottom panel*: detailed view of the shadowed interior of the crater. Temperature models predict for this area the presence of a >10 cm-thick surficial layer of volatile and organic-rich material overlying a thicker layer of water ice (courtesy of NASA-JHU Applied Physics Lab-Carnegie Inst. of Washington). 41

2.15 Subdivision of Mercury in 15 quadrangles in positive west equirectangular projection centered at 180°E on top of the MESSENGER Enhanced Color basemap (∼665 m/px). The letter H, prefix for Mercury, precedes each region's number. Names are given based on outstanding geologic features, while names in parentheses are based on albedo features. Equatorial, mid-latitude and polar quadrangles cover 7.7%, 6.5% and 4.7% of hermean surface respectively. 42

2.16 Mihail Eminescu (*left panel*) and its namesake crater viewed in grayscale (*central panel*) and enhanced colors (*right panel*). 43

2.17 Serie of 1:5 regional geologic maps produced on Mariner 10 data, from Prockter (2015). 43

2.18 MESSENGER MDIS BDR basemap (∼166 m/px) in equirectangular projection. The monochrome basemap is assembled using MDIS NAC or WAC 750 nm images with moderate incidence angles and low emission angles. The basemap was produced by mosaicking the BDR tiles of the Eminescu quadrangle in the ISIS3 software. 45

2.19 MESSENGER MDIS HIE basemap (∼166 m/px) in equirectangular projection. The monochrome basemap is assembled using MDIS NAC or WAC 750 nm images with high incidence angles and illumination from the East. The basemap was produced by mosaicking the HIE tiles of the Eminescu quadrangle in the ISIS3 software. 45

2.20 MESSENGER MDIS HIW basemap (∼166 m/px) in equirectangular projection. The monochrome basemap is assembled using MDIS NAC or WAC 750 nm images with high incidence angles and illumination from the West. The basemap was produced by mosaicking the HIW tiles of the Eminescu quadrangle in the ISIS3 software. 45

2.21 MESSENGER MDIS LOI basemap (∼166 m/px) in equirectangular projection. The monochrome basemap is assembled using MDIS NAC or WAC 750 nm images with low incidence angles and low emission angles. The basemap was produced by mosaicking the LOI tiles of the Eminescu quadrangle in the ISIS3 software. . 45

2.22 MESSENGER USGS global DEM v2 (∼665 m/px) in equirectangular projection. The basemap was trimmed from the Mercury_Messenger_USGS_DEM_Global_665m_v2 and it is visualized on top of the BDR basemap with 50% of transparency. 45

2.23 MESSENGER MDIS Enhanced Color global mosaic (∼665 m/px) in equirectangular projection. The basemap emphasizes color variations on Mercury's surface by using a mosaic with the 430 nm, 750 nm and 1000 nm bands and placing the second principal component, the first principal component and the 430/1000 nm ratio in the red, green and blue channels respectively. The basemap was trimmed from the Mercury_MESSENGER_MDIS_Basemap_EnhancedColor_Mosaic_Global_665m. 45
2.24 MESSENGER MDIS MD3 Color global mosaic (∼665 m/px) in equirectangular projection. The basemap emphasizes color variations on Mercury's surface by placing the 1000 nm, 750 nm and 430 nm narrow-band filters in the red, green and blue channels respectively. The basemap was trimmed from the Mercury_MESSENGER_MDIS_Basemap_MD3Color_Mosaic_Global_665m. 45
2.25 Geologic contacts linework. MESSENGER MDIS BDR basemap (*left panel*) with digitized certain (black line) and approximate (dashed black line) contacts (*right panel*). 47
2.26 Linear features linework for craters. MESSENGER MDIS BDR basemap (*left panel*) with digitized craters with 5<D<20 km (black lines), craters with D>20 km (black lines with double inner ticks), buried/degraded craters (black dashed and dot lines) and a putative volcanic vent (black line with single inner tick) (*right panel*). 47
2.27 Linear features linework for structures. MESSENGER MDIS BDR basemap (*left panel*) with digitized certain thrusts (continuous black lines with triangles), uncertain thrusts (dashed black lines with triangles) and wrinkle ridges (purple lines) (*right panel*). 47
2.28 MESSENGER MDIS BRD basemap with craters classified as *c1*, *c2* or *c3*. 48
2.29 Examples of surface features mapping as seen on top of the MESSENGER MDIS BDR basemap. *Top panel*: view of the Eminescu crater presenting a cluster of hollows and isolated hollows (cyan features) above dark materials (maroon feature) on its crater floor, a rough ejecta blanket (noisette feature) on its W-SW portion and catenae of secondary craters (black features) radiating S-SW. *Bottom panel:* a catenae (pointed out by the red arrow) not clearly related to a primary impact. 50
2.30 Examples for the *sp*, *CSP*, *OF*, *VEF*, *CRE*, *c3*, *c2*, *c1*, *cfs* and *cfh* geologic units that have been mapped in the study area. 52
2.31 The present state of the geologic linework (geologic contacts, linear features, surface features and point features) for the eastern portion of the H-9 Eminescu quadrangle. 52
2.32 Linear features linework for craters. 52
2.33 Linear features linework for structures. 52
2.34 The present state of the geologic map of the eastern portion of the H-9 Eminescu quadrangle. Refer to the text for unit descriptions. 52
2.35 The present state of the geologic map of the eastern portion of the H-9 Eminescu quadrangle visualized on top of the MESSENGER MDIS BDR basemap (∼166 m/px) with a 50% of transparency. Refer to the text for unit descriptions. 52
2.36 Color-based spectral linework mapping produced on an area located to the south of the Eminescu crater. 53
2.37 Location of targets classified by category visualized on top of the MESSENGER MDIS BDR basemap (∼166 m/px) with a 50% of transparency. 56
2.38 Examples of targets as from the MESSENGER MDIS BDR and Enhanced color mosaic basemaps. 58

3.1 Interior structure of the Moon. 62

3.2 Hypothetic cross-section of the upper crust showing the megaregolith layer and the effects of large-scale cratering, as from Hiesinger and Head (2006). 63
3.3 *Left panel*: computer simulation of a giant impact for the formation of the Moon, modified from (Canup, 2004). *Right panel*: illustration of the Moon's formation within a terrestrial synestia, modified from (Lock et al., 2018). 64
3.4 Lunar swirls associated with magnetic anomalies. *Left panel*: LROC-WAC view of the swirls inside Mare Ingenii (centered at 35.0°S, 163.3°E). *Right panel*: LROC-WAC view of the magnetic anomaly of Reiner Gamma Formation (centered at 7.4°N, 300.9°E). 65
3.5 Artistic impression of the Clementine spacecraft (courtesy of NASA). 66
3.6 *Left panel*: an artistic impression of the Kaguya spacecraft with Okina and Ouna in orbit around the Moon (courtesy of JAXA). *Right panel*: labelled diagram of the Kaguya spacecraft, as from Kato et al. (2008). 67
3.7 *Left panel*: an artistic impression of the Chandrayaan-1 spacecraft in orbit around the Moon (courtesy of ISRO). *Right panel*: labelled diagram of the Chandrayaan-1 spacecraft, as from Bhandari and Srivastava (2014). 68
3.8 *Left panel*: an artistic impression of the LRO spacecraft in orbit around the Moon (courtesy of NASA). *Right panel*: labelled diagram of the LRO spacecraft (courtesy of NASA) 70
3.9 The Moon's time-stratigraphic periods. 71
3.10 Volcanic landforms on the Moon. *Top left panel*: LROC-WAC view of a lava flow on Mare Imbrium (centered at 31.2°N, 23.6°W). *Top right panel*: LROC-WAC view of sinuous rilles at Rimae Prinz (centered at 41.2°N, 43.5°W). *Central left panel*: LROC-NAC view of a lunar pit in Mare Tranquillitatis (centered at 8.3°N, 33.2°E). *Central right panel*: LROC-WAC view of 13 vents on the floor of the Alphonsus crater (centered at 13.4°S, 2.8°W). *Bottom left panel*: LROC-NAC view of a cinder cone on the floor of the Copernicus crater (centered at 10.3°N, 19.9°W). *Bottom right panel*: LROC-WAC view of the non-mare Gruithuisen Domes (centered at 36.4°N, 40.2°W). 74
3.11 Structure of Tsiolkovskiy crater (on the right) superposing on the ∼230 km diameter Fermi crater (on the left). The white dashed circle identifies the approximate rim of Fermi; the black dashed and dotted line delimits Tsiolkovskiy's landslide, modified from (Boyce et al., 2020); the blue arrow indicates the impact direction for Tsiolkovskiy crater. 77
3.12 Profile graph (*bottom panel*) derived from the line of interpolation (green line) drawn on the southern portion of Tsiolkovskiy's central peak (*top panel*) evidencing the height reached by the peak itself with respect to the surrounding mare. 78
3.13 LROC-WAC basemap (∼100 m/px) in equirectangular projection. The monochrome basemap is assembled using WAC 643 nm images with incidence angles between 55°-75°. The basemap was trimmed from the Lunar_LRO_LROC-WAC_Mosaic_global_100m_June2013. 80
3.14 Kaguya TC mosaicked images (∼10 m/px) in equirectangular projection. 80
3.15 LRO-LOLA and Kaguya Tc DEM merge (∼59 m/pixel and 3-4 m respectively) in equirectangular projection. The basemap was trimmed from the Lunar_LRO_LrocKaguya_DEMmerge_60N and it is visualized on top of the DEM-derived hillshade basemap with a 50% of transparency. 80
3.16 Surface slope map for slopes <15°visualized on top of the DEM-derived hillshade basemap. 80
3.17 Slope map for slopes >40°visualized on top of the DEM-derived hillshade basemap. 80

3.18 Clementine UVVIS Warped Color Ratio mosaic (∼200 m/px) in equirectangular projection. The basemaps enphatizes color variations on the Moon's surface by using a mosaic with the 750/415 nm, 750/1000 nm and 415/750 nm band ratios in the red, green and blue channels respectively. The baseamap was trimmed from the Lunar_Clementine_UVVIS_Warp_ClrRatio_Global_200m. 80
3.19 Spectral Units map in equirectangular projection. The basemap summarizes all the information held in several spectral indices mosaics allowing for a quick and straightforward understanding of the compositional properties of the area. 80
3.20 LROC-NAC images (∼0.92 m/px) of the southern portion of Tsiolkovskiy's central peak. 80
3.21 Examples for the *sm*, *hm*, *cp*, *sp*, *ss* and *is* geologic units mapped in the study area. 83
3.22 Morpho-stratigraphic map of the Tsiolkovskiy crater visualized on top of the DEM-derived hillshade with a 50% of transparency. Refer to the text for unit descriptions. 83
3.23 Detailed view of the SE portion of the Tsiolkovskiy crater. Spectral contacts linework (*left panel*) and color-based spectral map (*right panel*) discriminate the presence of characteristic combinations of color shades, highlighted by double black arrows, as from the Clementine UVVIS Warped Color Ratio mosaic. 84
3.24 Color-based spectral map of Tsiolkovskiy crater visualized on top of the Clementine UVVIS Warped Color Ratio mosaic with a 50% of transparency. Refer to the text for unit descriptions. 85
3.25 CSFD measurements areas defined on the basis of the Color-based spectral linework and visualized on top of the LROC-WAC basemap. 86
3.26 CSFD measurements performed on the (a) *hm* geologic unit for determining the formation age of Tsiolkovskiy crater and on the (b) orange (i.e. *bp1* spectral unit) (c), purple-blue (i.e. *bp2* spectral unit) and (d) yellow (i.e. *bp3* spectral unit) color units discriminated on the crater floor. The randomness analysis results are shown in the panel above the CSFDs. 87
3.27 Detailed view on LROC-WAC and Clementine color basemaps of Tsiolkovskiy's crater floor highlighting the presence of brighter yellow hues due to the excavation of fresher underlying materials. 89
3.28 Updated color-based spectral map of Tsiolkovskiy crater visualized on top of the Clementine UVVIS Warped Color Ratio mosaic with a 50% of transparency. Refer to the text for unit descriptions. 89
3.29 Spectro-stratigraphic map of Tsiolkovskiy crater visualized on top of the Spectral Units map with a 50% of transparency. Refer to the text for unit descriptions. . 91
3.30 *Top panel*: plot of the average reflectance spectra of the SUs. *Bottom panel*: same as the top panel with continuum removal. 92
3.31 *Top panel*: average derived band centers for Ca-free (plus), low-Ca (diamonds) and high-Ca (triangles) synthetic pyroxenes (Klima et al., 2011a,b) and for the SUs (full circles, refer to the legend for color interpretation) plotted within the range of 1000 nm (BCI) and 2000 nm (BCII). *Bottom panel*: abundances of wollastonite (Wo), enstatite (En) and ferrosilite (Fs) for Ca-free, low-Ca and high-Ca synthetic pyroxenes; the different colors reflect the ones used in the *top panel*. 93
3.32 Distribution of boulders gathered along the southern portion of Tsiolkovskiy's central peak on top of a black background, for enhancing the visibility of point features. The zoom in show the rolling trails visible on the southeastern wall of the central peak, and partly visible also on the southwestern one, and a rockslide-like deposit at the base of the southwestern wall. 95

3.33 High-resolution geologic map of the southern portion of Tsiolkovskiy's central peak visualized on top of LROC-NAC images with a 50% of transparency. Refer to the text for unit descriptions. 95
3.34 Identification of target (*tx*) areas worthy to be better analyzed in a landing site characterization. 96
3.35 LROC-WAC-derived TiO_2 abundance estimation basemap of Tsiolkovskiy's mare infilling, modified from (Sato et al., 2017). The color bar indicates 2 wt% bins in TiO_2 content. 99

C.1 Geologic units presented in the main chapters are descripted using the following scheme: stratigraphic order, letter sign, group and description, for both Mercury and the Moon. 111

List of Tables

2.1 Scientific instruments onboard the M10 spacecraft (Davies et al., 1978). 28
2.2 Scientific instruments onboard the MESSENGER spacecraft (Leary et al., 2007). 29
2.3 Scientific instruments onboard the BepiColombo dual spacecraft (Benkhoff et al., 2010). 32
2.4 List of scientific targets of interest defined for future investigation by the BepiColombo SIMBIO-SYS instrument. For each target is defined its location (coordinates). Targets are classified by category (craters, hollows, structures, volcanic and other features), type (general description based on the category), rank (ranging from 1-low priority to 5-high priority) and rank description (description of the scientific relevance of the target). 55

3.1 Scientific instruments onboard the Clementine spacecraft (Nozette et al., 1994). . 66
3.2 Scientific instruments onboard the Kaguya spacecraft (Kato et al., 2008). 68
3.3 Scientific instruments onboard the Chandrayaan-1 spacecraft (Goswami and Annadurai, 2008). 69
3.4 Scientific instruments onboard the LRO spacecraft (Tooley et al., 2010). 70
3.5 The first column resume the names of the areas considered for the CSFD measurements. The areas location is visible on Figure 3.25. The second, third and fourth columns contain the surface extent of each area, the number of crater selected as standard and as marked (e.g. irregular craters, possible secondary craters or possible clusters of craters). The fifth, sixth and seventh columns contain the diameter range of the selected craters and the relative age with correlated errors as from Craterstats2 (Michael and Neukum, 2010). 88

A.1 List of cited deliverables with related links from PLANMAP and GMAP. 107

B.1 List of basemaps used for the geologic mapping of the H-9 Eminescu quadrangle with original filenames, spatial resolutions and sources. 109

D.1 List of basemaps used for the geologic study of the Tsiolkovskiy crater with original filenames, spacial resolutions and sources. 113

Riassunto

L'obiettivo di questa tesi, sviluppata all'interno del progetto Europeo Horizon 2020 PLANMAP, è la produzione di carte geologiche sia standard che innovative su differente scala focalizzate su due corpi terrestri privi di atmosfera di primario interesse per la futura esplorazione Europea, ovvero Mercurio e la Luna. Questi prodotti cartografici realizzati per studiare la geologia e l'evoluzione geologica dell'area d'interesse mirano non solo a caratterizzare la morfologia superficiale ma anche ad integrare informazioni spettrali e composizionali, non individuabili solamente su base morfologica, e sono destinati a supportare la futura esplorazione planetaria.

Per Mercurio, un progetto in corso per la produzione di una serie di carte geologiche regionali a scala 1:3,000,000 per i suoi 15 quadrangoli è iniziato con la produzione di carte geologiche individuali per evolvere successivamente in un piano coordinato di mappatura globale. Con lo scopo di produrre la prima carta regionale a piccola scala del quadrante H-9 Eminescu (22.5°N-22.5°S, 72°E-144°E), ho prodotto i) una carta geologica a scala 1:3M, derivata dall'interpretazione morfologica della superficie, di una vasta parte della porzione orientale del quadrangolo Eminescu e ii) una carta spettrale basata su basemaps a colori, derivata da variazioni di colore all'interno delle unità geologiche identificate, su un'area più circoscritta . Tali carte hanno permesso di concentrare gli sforzi nella iii) definizione di targets di interesse scientifico per lo strumento SIMBIO-SYS a bordo della missione spaziale BepiColombo di ESA-JAXA. Dal confronto dei risultati ottenuti si distingue una buona correlazione fra morfologia e variazioni di colore della superficie. La mappatura basata sul colore permette di desumere molte più informazioni riguardo alla superficie di Mercurio rispetto all'uso di sole immagini monocromatiche, discriminando fra differenti materiali. Tra i principali targets per la missione BepiColombo sono stati considerati peculiari variazioni di colore associate all'esumazione di materiali sottostanti, che presentano verosimilmente una distinta composizione, così come vents vulcanici che non presentano particolari variazioni di colore e crateri fagliati che permettono di derivare la cinematica delle strutture

tettoniche.

Per quanto riguarda la Luna, invece, diversi tipi di prodotti cartografici sono stati prodotti sulla base di differenti dati, da immagini monocromatiche e a colori a diverse risoluzioni spaziali fino a informazioni multispettrali e all'integrazione di determinazioni di età relative e assolute. L'obiettivo finale di queste carte è quello di fornire uno studio geologico su larga scala del cratere Tsiolkovskiy (20.4°S, 129.1°E), situato sul lato nascosto della Luna, in modo da gettare le basi per una futura caratterizzazione dell'area come sito di atterraggio. Ho pertanto prodotto i) una carta morfo-stratigrafica, derivata dall'interpretazione foto-geologica, ii) una carta spettrale basata su variazioni di colore, derivata dall'associazione di variazioni compositive con le unità geologiche identificate, iii) determinazioni di età, per discriminare possibili differenze di età correlate con variazioni di colore, iv) una carta spettro-stratigrafica, derivata dall'integrazione di informazioni multispettrali, e v) una carta geologica ad alta risoluzione, per la definizione di una possibile area target. I risultati mostrano una chiara correlazione tra morfologie, variazioni di colore ed informazioni spettrali e permettono di dedurre più informazioni riguardo alla composizione di ogni unità geologica. Le determinazioni dell'età, in aggiunta, hanno permesso di ricostruire l'evoluzione vulcanica del fondo del cratere di Tsiolkovskiy e di associare variazioni compositive ai suoi eventi di riempimento. La mappatura geologica ad alta risoluzione, infine, mira a richiamare l'attenzione sul picco centrale del cratere e sui massi crollati che lo circondano, che potrebbero rappresentare un interessante target scientifico per studiare la composizione della crosta lunare e del mantello.

Abstract

The objective of this thesis, developed within the European Horizon 2020 PLANMAP project, is the production of both standard and innovative geologic maps at different scales focused on two atmosphere-less terrestrial bodies of primary interest for future European exploration, namely Mercury and the Moon. These cartographic products produced for studying the geology and geologic evolution of the area of interest aim not only at representing the surface morphology but also at integrating spectral and compositional information, not detectable from morphology alone, and they are intended for supporting future planetary exploration.

For Mercury, an ongoing project for the production of a series of 1:3,000,000 regional geologic maps for its 15 quadrangles started with the production of individual geologic maps to later evolve into a coordinated global mapping plan. Aiming at producing the first small-scale regional map of the H-9 Eminescu quadrangle (22.5°N-22.5°S, 72°E-144°E), I have been producing i) a 1:3M geologic map, derived from morphologic interpretation of the surface, of a wide part of the eastern portion of the Eminescu quadrangle and ii) a color-based spectral map, derived from color variations within the identified geologic units, for a limited area. These maps permitted to better focus on iii) the definition of scientific targets of interest for the SIMBIO-SYS instrument onboard the ESA-JAXA BepiColombo mission. By comparing the obtained results a good correlation stands out between morphology and surface color variations. The color-based mapping allows inferring much more information about the hermean surface than from monochrome imagery alone, discriminating between different materials. Peculiar color variations associated with the exhumation of underlying materials, possibly presenting a distinct composition, have been considered among the main targets for the BepiColombo mission together with volcanic vents presenting no particular color variations and faulted craters allowing to derive the kinematics of tectonic structures.

As concerns the Moon, instead, several types of cartographic products have been produced based on different data, from monochrome and color imagery at different spatial resolutions up to multispectral information and the integration of relative and absolute age determinations. The final aim of these maps is to provide a large-scale geological study of the lunar far side mare-flooded Tsiolkovskiy crater (20.4°S, 129.1°E) in order to lay the groundwork for a future landing site characterization. I have thus been producing i) a morpho-stratigraphic map, derived from photogeological interpretation, ii) a color-based spectral map, derived by associating compositional variations with the identified morphological units, iii) age determinations, for discriminating possible age differences based on color variations, iv) a spectro-stratigraphic map, derived by integrating multispectral information, and v) a high-resolution geologic map, for the definition of a possible target area. The results show a clear correlation between morphologies, color variations and spectral information and allow to infer more information about the composition of each unit. Age determinations, then, allowed reconstruction of the volcanic evolution of Tsiolkovskiy's crater floor associating compositional variations to its infilling events. The high-resolution geologic mapping, finally, aims at drawing attention to the central peak of the crater and to the collapsed boulders surrounding it, which could represent an interesting scientific target to study, among others, the composition of the lunar crust and mantle.

Chapter 1

Introduction

In the next sections, I am going to introduce the context in which my research project was developed and its final goal and I will conclude with a couple of sections dedicated to the mapping technique, which is the basis of the small- and large-scale mappings presented in the next chapters, and the development of innovative maps.

1.1 The PLANMAP project

The 2020s will be remembered for their renewed commitment to space exploration. Between the world's major space agencies, indeed, a new space race, dedicated in particular to the human colonization of the Moon, has started.

In this scenario, geologic maps provide the context for the planning of a successful explorative mission on a planetary surface. However, the great majority of geological maps available and in progress are produced by the United States Geological Survey (USGS). This situation must change if the European space community wants to pursue its ambitions and be an active competitor in space exploration.

The European Horizon 2020 PLANMAP (PLANetary MAPping) project was precisely born aiming at providing highly informative geological maps of the three main bodies of interest for the European space exploration in the next decade, namely Mars, Mercury and the Moon.

The approach of PLANMAP consisted in the integration of highly differentiated datasets, such as imagery, topographic data, spectral cubes and compositional information, radar sounding data, absolute ages and ground truth observations, to produce regional to high-resolution multi-

layered geologic maps dedicated to the planetary exploration. Moreover, the combination of different levels of information allowed the reconstruction of 3D geologic models to interpret the subsurface and the realization of virtual reality environments useful in the training of astronauts. The PLANMAP project started in March 2018 and ended in February 2021. Its results are now exploited by the GMAP (Geological MAPping) infrastructure of the European Horizon 2020-EPN2024 project aiming at fostering planetary geological mapping in Europe.

1.2 Research goal

The research goal of this PhD project was the production of standard and innovative geologic maps aimed not only at characterizing the surface morphology but also at integrating spectral and compositional information undetectable from morphology alone.

During the research project, I focused on the production of geologic maps for two different atmosphere-less terrestrial bodies: Mercury and the Moon.

Probably presenting more differences than similarities, both bodies, by lacking an atmosphere, have in common intensely cratered surfaces, on which tectonism and volcanism played a major role.

The mappings were based on different types of remotely sensed data, from the monochrome imagery to the topographic data up to the spectral-color data enclosing compositional information.

Based on the resolution of the available images and the final aim of the mapping product, I produced regional small-scale mappings for Mercury, focused on one of the 15 quadrangles, and high-resolution large-scale mappings for the Moon, focused on a mare flooded crater.

The final products aim at characterizing the geology and geologic evolution of the areas, helping in the selection of targets of high interest for future orbital exploration and in identifying scientifically interesting and safe places for rover and/or human exploration.

1.3 The art of mapping

Behind a cartographic product is a meticulous technical and conceptual organization of the workflow, which includes the definition of the scales for mapping and printing the product, the

creation of vector layers accordingly to the elements to be mapped, up to finalization of the product.

Whereas the organization of a geodatabase is strictly dependent on the area and type of mapping, the definition of the mapping and output scales and the finalization of the map follow similar rules (see D2.1 from PLANMAP and D8.3, D9.1 from GMAP for more details, Appendix A.1).

Based on the basemap resolution, the recommended scale for drawing lines and features changes. The mapping scale is set following the rule defined by Tobler (1987), according to the equation:

$S_m = R_r \times 2000$

where S_m is the mapping scale and R_r is the raster resolution. However, the resolution of a basemap may be not even, especially if we consider a mosaicked basemap. The defined mapping scale has thus to be considered as a lower limit that can be increased based on the resolution of the datum.

The final "printable" output scale, instead, is defined according to the USGS recommendations (Tanaka et al., 2011), which suggest using a scale n times larger than the mapping scale following the equation:

$So_n = S_m \times n$

where So_n is the recommended output scale and n ranges between 2 and 5. To achieve the best and clearest result, for the following mapping products I chose an n of 5.

The mapping was performed on the novel technique based on the digitization of polylines, instead of polygons, that, once the mapping process is finished and all polylines are closed, can be used to construct polygon units. Before constructing polygons, however, a series of topological rules have to be defined in order to check for errors in the digitized polylines. The following rules were applied: must not have dangles, must not intersect, must not self-intersect and must be single part.

According to these rules, each line must touch other lines at both endpoints, must not intersect itself nor intersect or overlap other lines and must not have more than one part. A schematic representation of the rules is shown in Figure 1.1.

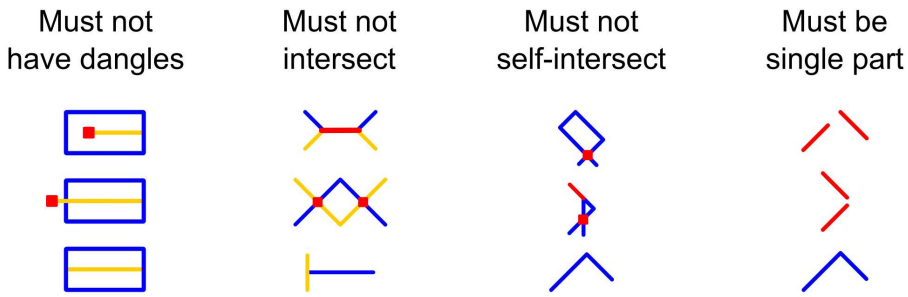

Figure 1.1: Topological rules defined for polylines' errors check.

Once the polylines are corrected, it is possible to construct the polygon units, initially with an empty attribute, and assign a geologic unit to each one.

As a final check, a couple more topological rules are defined for the polygon feature classes: must not overlap, meaning that there must not be overlapping polygons, and must not have gaps, so that no voids can exist between different polygons. A schematic representation of these rules is shown in Figure 1.2.

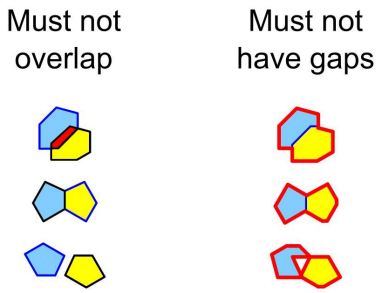

Figure 1.2: Topological rules defined for polygons' errors check.

1.4 Innovative geologic maps: integration of spectral and color information

In an era where planetary exploration represents a primary goal, it is even more evident that planetary morpho-stratigraphic maps do not provide the same level of information as the Earth's geologic maps.

On Earth, indeed, the possibility to perform in situ observations of the bedrock and to collect samples for laboratory analyses allow the production of comprehensive geologic maps coupling

remotely sensed data with ground-truth observations.

Aiming at filling in this information gap for the planetary surfaces, morpho-stratigraphic maps need to be integrated with additional data such as color-derived basemaps (i.e. color ratios, principal components, spectral indices) returning spectral information.

This integration can be achieved following two different interpretative approaches: the contextual and in-series ones.

The contextual approach includes the production of two different maps based on monochrome and color-derived imagery respectively. As a result, the spectral contacts defined on color variations may significantly diverge from contacts defined on morphology.

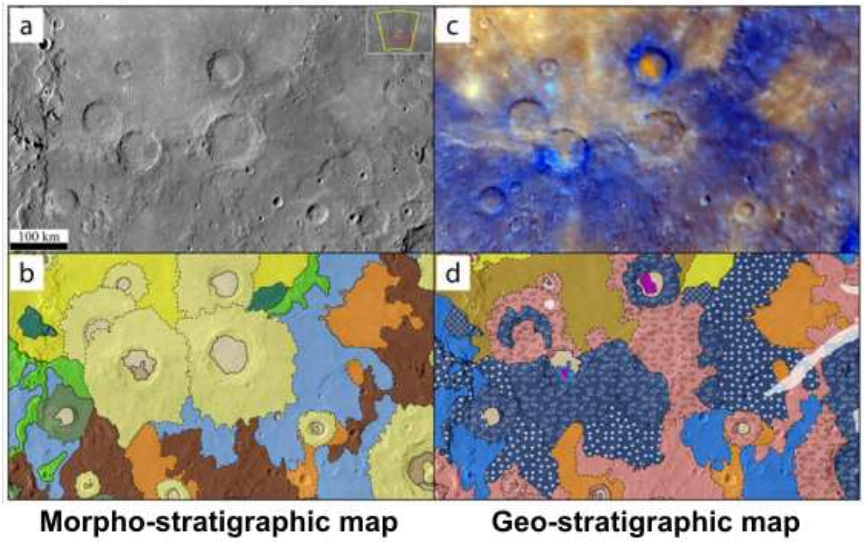

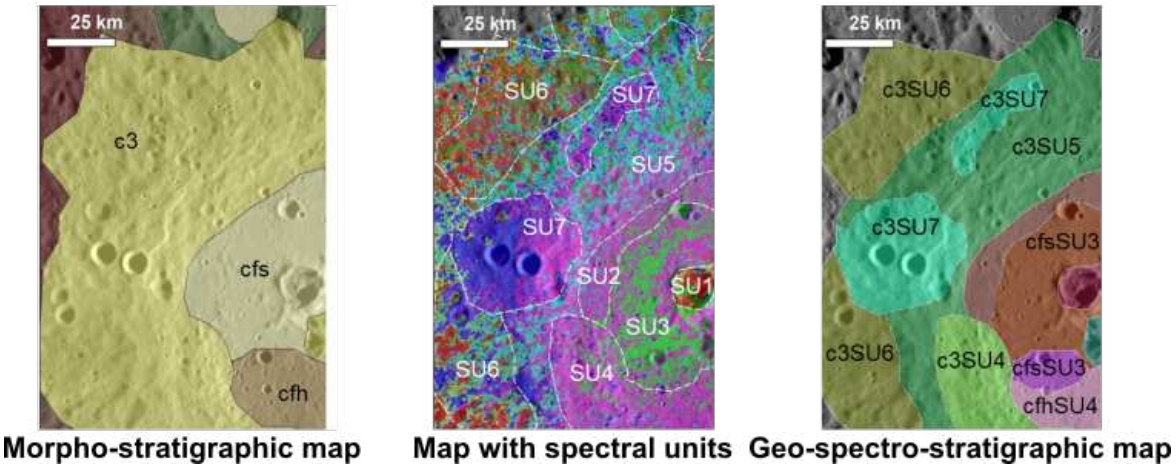

Figure 1.3: Examples of contextual interpretation (*top panel*, modified from Semenzato et al. (2020)) and in-series interpretation (*bottom panel*, modified from Giacomini et al. (2021)).

The in-series approach, instead, includes the improvement of a morpho-stratigraphic map through the integration of spectral and color information. The final result is a map in which geologic boundaries may be slightly modified and morpho-stratigraphic units are subdivided into sub-units according to color variations.

Figure 1.3 shows an example of contextual and in-series interpretation respectively.

The final product is, in both cases, a geo-spectro-stratigraphic map integrating the spectral information.

Chapter 2

Small-scale mapping on Mercury

In the next sections, I am going to give an overview on Mercury, about its physical and geological properties, and the space missions dedicated to its exploration. Sections dedicated to data and methods provide the basis for the geologic map, color-based spectral map and definition of scientific targets of interest for future exploration presented in the results section and further analyzed in the discussions.

2.1 Introduction

2.1.1 Mercury: planet of extremes

Among the terrestrial inner planets, Mercury stands out for being the smallest, the fastest and the closest to our star, the Sun.

The planet is named after the Roman god Mercury, the snappy messenger of the gods with winged sandals, also known in Greek mythology as Hermes, from which derives the adjective "hermean" often used when referring to this planet.

In its journey around the Sun, from which is only 0.4 au (vs 1 au of the Earth), Mercury follows a highly elliptical orbit that forces the planet to move ±0.1 au closer or farther from the star. Traveling at about 47 km/s (vs 30 km/s of the Earth), Mercury takes 88 Earth days to complete one orbit (vs 365 days of the Earth). In spite of that, the planet spins very slowly on its axis so much so that it takes 59 Earth days to complete one rotation (vs 24 h of the Earth), namely 2/3 of its orbital period. Hence, every two orbits around the Sun, Mercury completes 3 spins around its axis. The discovery of this 2:3 spin-orbit resonance was inferred by Giuseppe "Bepi" Colombo

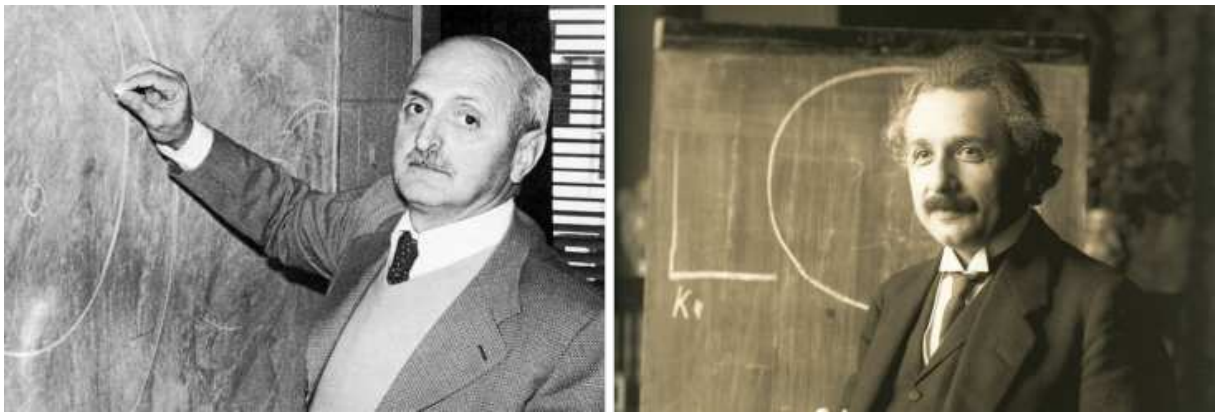

Figure 2.1: Photographs of the mathematician and engineer Giuseppe Colombo during a lesson in Padua (*left panel*, courtesy of ESA) and of the physician Albert Einstein in 1921 (*right panel*, coutesy of the Albert Einstein archives).

(1920-1984), Professor of Applied Mechanics at the University of Padova (Figure 2.1 *left panel*), that in response to the observations by Peale and Gold (1965) affirmed that a rotational period corresponding to the 2/3 of the orbital period would have been a more stable solution than the 1:1 resonance previously supposed (Colombo, 1965).

Furthermore, Mercury's orbit gradually rotates over time: after each revolution, indeed, the perihelion of the planet occurs in a slightly shifted position. The strange behavior of Mercury remained unclear until the beginning of the 20th century when the physicist Albert Einstein (1879-1955) (Figure 2.1 *right panel*) developed the Theory of General Relativity. According to his theory, space and time were not independent of each other and gravity was the cause of the warping of the four-dimensional continuum of spacetime. Being the closest body to the Sun, thus, Mercury orbits in a region where spacetime is bent by the mass of the Sun itself causing the perihelion precession of the planet.

Despite its small radius of 2439.7 km (vs 6378.1 km of the Earth), which is slightly larger than the Moon's one, Mercury is denser than Venus or Mars, presenting a density of 5.4 g/cm^3 similar to that of the Earth (i.e. 5.5 g/cm^3). This high bulk density is caused by the presence of a large and partially liquid iron-rich core (Margot et al., 2007) that, with a radius of about 2030 km, occupies about 83% of Mercury's radius. A solid outer shell, instead, constitutes the remaining radius. An upper silicate crust, ranging from 20 to 40 km and 50 to 80 km in thickness in the polar and equatorial regions respectively, overlies a very thin mantle and, further down, perhaps a solid FeS layer of iron sulphide (Smith et al., 2012; Stevenson, 2012) (Figure 2.2).

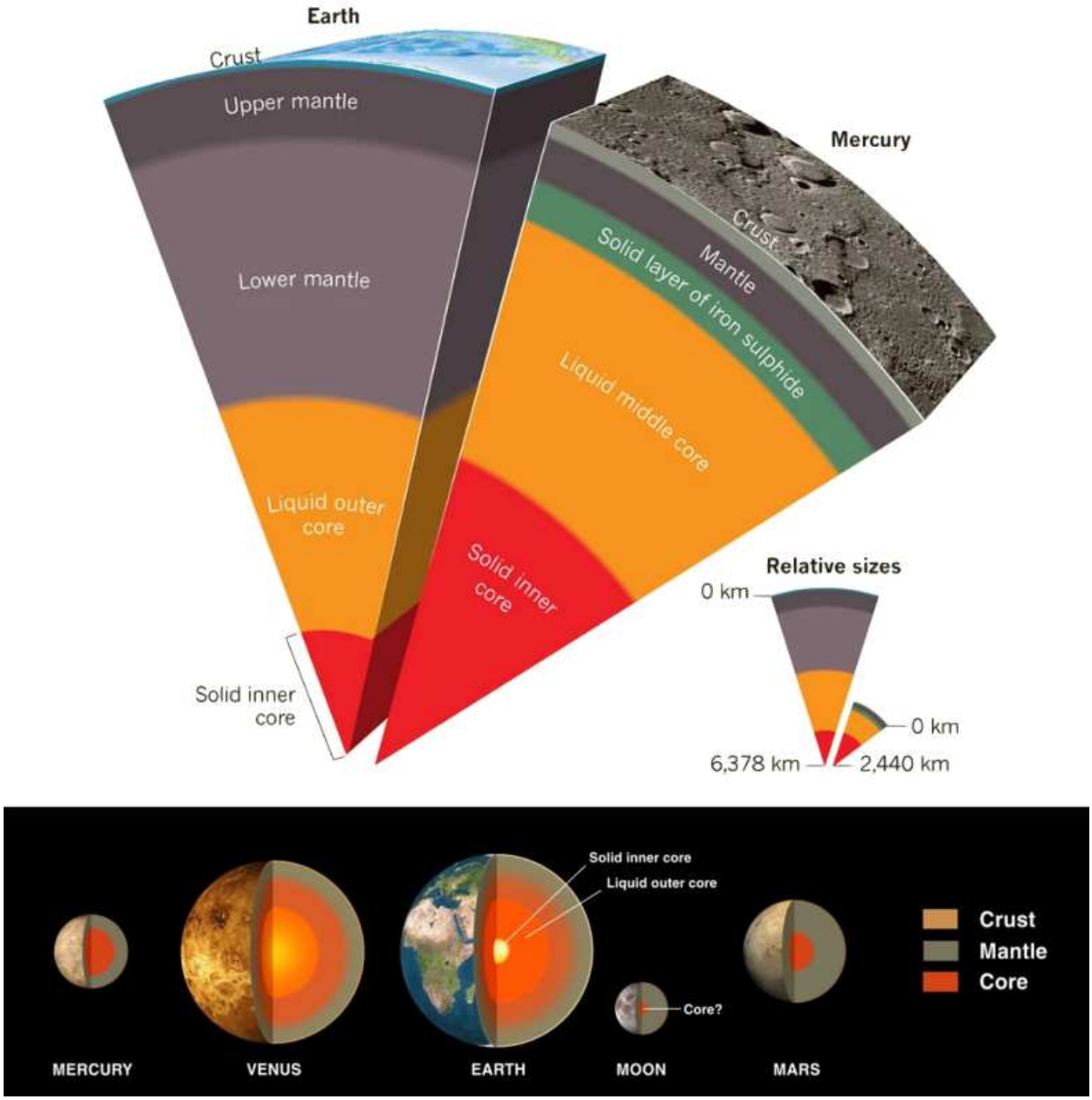

Figure 2.2: Interior structure of the terrestrial planets and the Moon. *Top panel:* comparison between the interior structure of Mercury and that of the Earth (modified from Stevenson (2012)). *Bottom panel:* comparison of the interior structure of Mercury, Venus, the Earth, the Moon and Mars (courtesy of NASA-JPL-Caltech).

The 3 most debated hypotheses proposed for explaining the unusually large and iron-rich core of Mercury are the selective accretion, the post-accretion vaporization and the giant impact, each of which involves the loss of volatiles and lighter elements (e.g. Na, S, Cl, K) and the enrichment in refractory elements (e.g. Al, Ca, Ti, Cr).

The selective accretion hypothesis (Weidenschilling, 1978) provides for the enrichment in heavier materials due to the depletion of volatiles and lighter materials caused by the solar irradiation and drag of nebular gas during the condensation of the Solar Nebula.

The post-accretion vaporization hypothesis (Cameron, 1985), instead, implies the intense radiation of the primordial Sun that caused the vaporization and loss of volatiles and lighter materials from the outer layers of the proto-Mercury.
The giant impact hypothesis (Benz et al., 1988), finally, provides for a giant collision on the proto-Mercury surface leading to the vaporization and spallation of volatiles and lighter materials.
Nevertheless, remote-sensed observations reveal a significant abundance of volatiles (Kerber et al., 2009; Blewett et al., 2011). This is quite astonishing considering that Mercury lacks a terrestrial-like atmosphere mitigating most of the impacts and the surface temperatures variation, which range between the diurnal 430°C and the -180°C of the hermean night. However, Mercury possesses a tenuous exosphere composed mostly of O, H, He, Na, K and Ca, whose distributions vary with latitude, time of day and Mercury's orbital position (Hunten and Morgan, 1988; Rothery, 2015).

Contrary to expectations, finally, even the small Mercury presents a well-developed bow shock wave and a magnetosphere-like region enclosed by terrestrial magnetopause-like boundaries (Ness et al., 1974; Milillo et al., 2010). The presence of this magnetic field seems to be intrinsic to the planet itself, unlike the Moon, Mars and Venus, and its dipolar structure is similar to the Earth's one, even if with a strength of 1% that of the Earth.

2.1.2 Exploration history

The exploration of Mercury began during the so-called "golden age" of space exploration (1960-1989) with NASA's Mariner 10 mission.
Providential to the great success of the mission was Giuseppe Colombo. Participating in a meeting on the mission to Venus and Mercury held at Caltech in 1970, Colombo suggested a trajectory correction to place the spacecraft in an orbit around the Sun with a period twice that of Mercury allowing thus to perform 3 flybys of the planet, giving the chance to collect much more data than previously planned.

The Mariner 10 (M10) spacecraft (Figure 2.3) was launched on 3 November 1973 from Cape Canaveral (Florida, USA). After a gravity assist from Venus, it performed the first flyby of Mercury on 29 March 1974 at a range of about 703 km. Two other flybys followed on 21 September

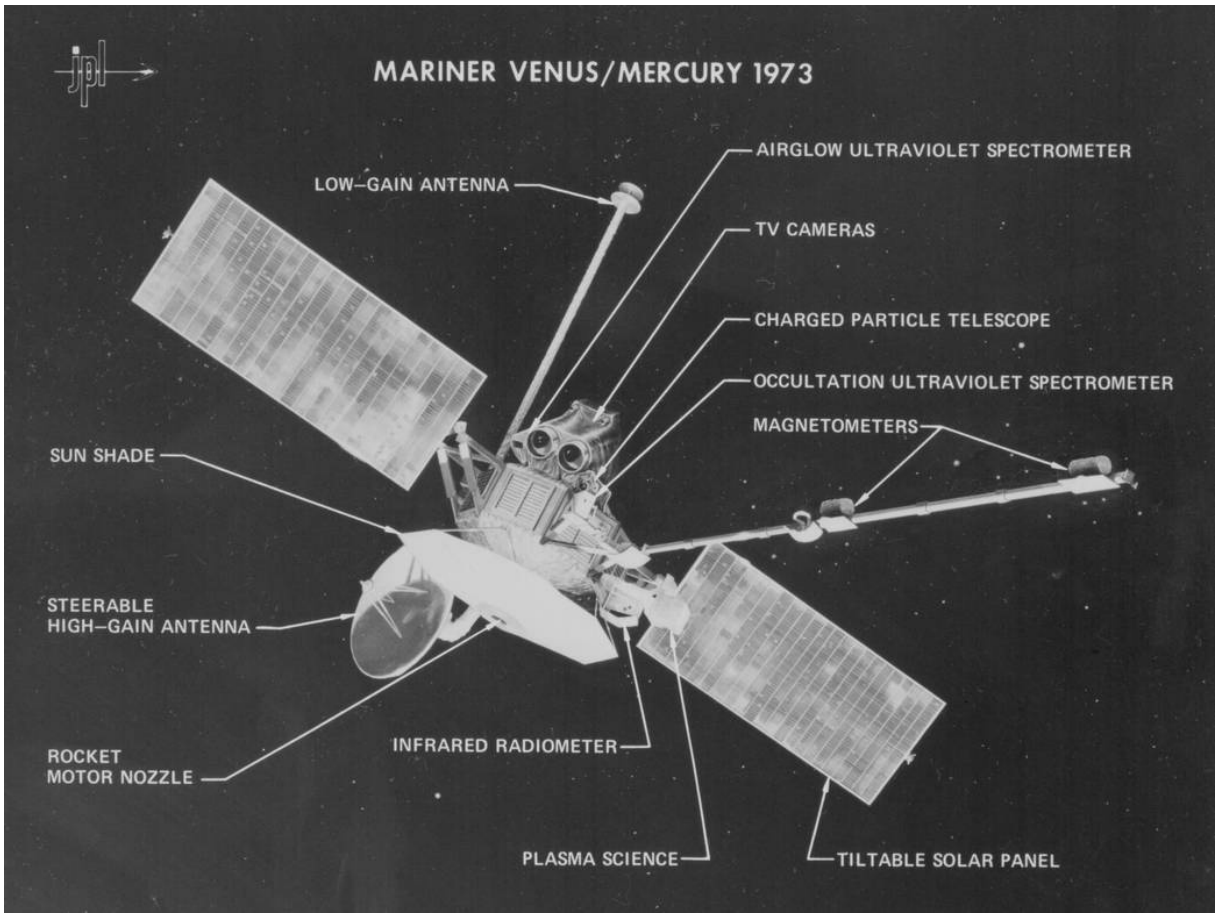

Figure 2.3: Labeled diagram of the M10 spacecraft (courtesy of NASA-JPL).

1974, with almost the same lightened surface, at a range of about 48,069 km and on 16 March 1975, the closest encounter at a range of about 327 km.

The M10 Television Experiment (Murray et al., 1975; Davies et al., 1978) transmitted about 3000 scientifically suitable images allowing more than 40% of Mercury's surface (about 75% of Mercury's sunlit portion during the cruise) to be photographed with a resolution of better than 2 km up to 100 m (Murray et al., 1975; Danielson et al., 1975).

Overall, the instruments on-board the M10 mission (Table 2.1) were able to depict a cratered surface similar to the Moon's landscape and to infer a great amount of information about the physical properties of Mercury, such as the absence of a real atmosphere and the presence of a thin exosphere, the presence of a magnetic dipole field, an iron-rich core relatively large for the size of the planet and a wide range of temperatures.

The M10 spacecraft shut down on 24 March 1975 after running out of fuel and, presumably, it is still orbiting around the Sun.

Table 2.1: Scientific instruments onboard the M10 spacecraft (Davies et al., 1978).

Instrument	Investigation
Celestial Mechanics and Radio Science	Measurement of Mercury's mass distribution and gravitational properties
Charged Particles	Measurement of the solar and galactic cosmic rays and detection of high-energy charged particles
Extreme Ultraviolet	Detection of Mercury's atmosphere and its composition
Infrared Radiometer	Measurement of the infrared thermal emissions and Mercury's superficial temperatures
Magnetic Field Experiment	Measurement of Mercury's magnetic field
Plasma Science	Measurement of the velocity and distribution of the solar wind components
Television Experiment	Providing monochrome imaging of the surface with different fields of view

More than 30 years later, NASA planned a new mission to Mercury, aimed at orbiting around the planet for the first time and performing an in-depth investigation.
The MErcury Surface, Space ENvironment, GEochemistry, and Ranging (MESSENGER) spacecraft (Figure 2.4) was launched on 3 August 2004 from Cape Canaveral (Florida, USA). After nearly seven years of cruise and several gravity assists from the Earth, Venus and Mercury itself, the spacecraft entered the orbit of the hermean planet on 18 March 2011.

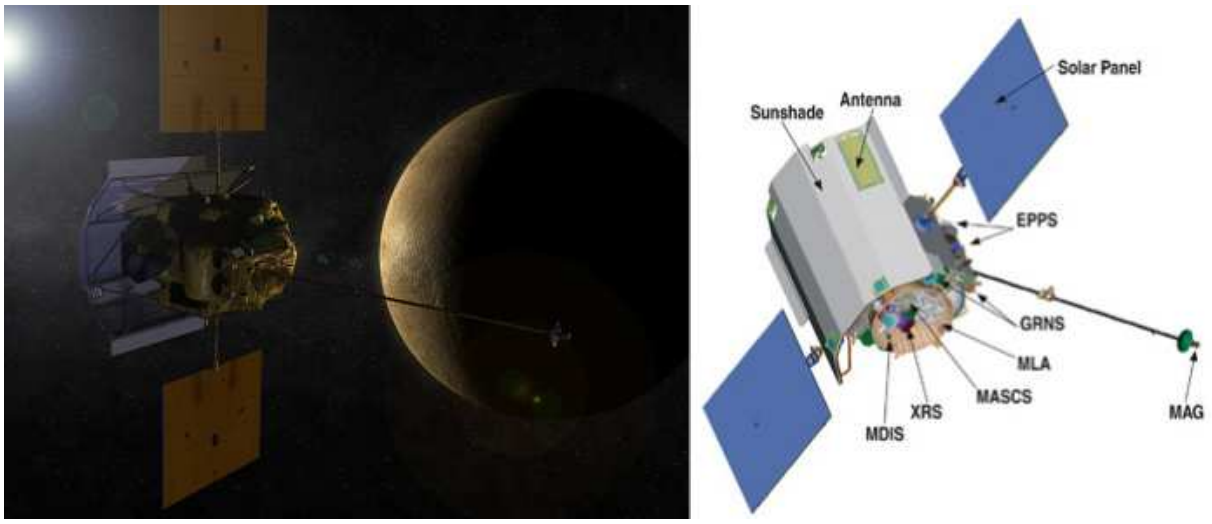

Figure 2.4: *Left panel:* an artistic impression of the MESSENGER spacecraft along its journey to Mercury (courtesy of NASA-JPL). *Right panel:* Labeled diagram of the MESSENGER spacecraft (courtesy of NASA-JPL).

Table 2.2: Scientific instruments onboard the MESSENGER spacecraft (Leary et al., 2007).

Instrument	Investigation
Energetic Particle and Plasma Spectrometer (EPPS)	Measurement of the distribution, energy and composition of charged particles in Mercury's magnetosphere
Gamma-Ray and Neutron Spectrometer (GRNS)	Detection of γ-rays and neutrons emissions to measure the relative abundances of various elements
Magnetometer (MAG)	Detection of magnetized rocks and measurement of Mercury's magnetic field
Mercury Atmospheric and Surface Composition Spectrometer (MASCS)	Detection of minerals and atmospheric gases on Mercury's surface and atmosphere respectively
Mercury Dual Imaging System (MDIS)	Providing monochrome and color imagery of the surface with different fields of view
Mercury Laser Altimeter (MLA)	Characterization of the topography of Mercury's surface
Radio Science Experiment (RS)	Measurement of Mercury's mass distribution
X-Ray Spectrometer (XRS)	Detection of X-rays emissions to measure the relative abundances of various elements

On-board the MESSENGER spacecraft (Table 2.2) (Leary et al., 2007), in particular, was the Mercury Dual Imaging System (MDIS) (Hawkins et al., 2007), consisting of an 11-filters VIS-NIR (395-1040 nm) multispectral and monochrome Wide-Angle Camera (WAC) and a monochrome Narrow-Angle Camera (NAC) capable of taking images with a resolution up to 24 m/px.
As a result of two mission extensions, MDIS was able to provide more than 250,000 images, thus enabling the global coverage of Mercury both in colors and high-resolution monochrome data. After accomplishing its mission and running out of propellant, finally, the MESSENGER spacecraft crashed near the Janáček crater (55.7°N, 155.1°W) in Suisei Planitia.

The last planned mission to Mercury was launched on 20 October 2018 from Kourou (French Guiana). It is the ESA-JAXA BepiColombo mission (Benkhoff et al., 2010), named in honor of the mathematician and engineer Giuseppe Colombo, which is expected to enter Mercury's orbit in December 2025 after a seven-year journey and nine flybys of the Earth, Venus and Mercury. BepiColombo is designed as a dual spacecraft mission (Figure 2.5) composed by the ESA's Mercury Planetary Orbiter (MPO) and the JAXA's Mercury Magnetospheric Orbiter (MMO, also referred to as MIO). The Mercury Transfer Module (MTM), finally, acts as a carrier spacecraft during the cruise phase. In proximity to Mercury, the 3 modules will separate and the MPO and MMO will insert in their respective orbits.

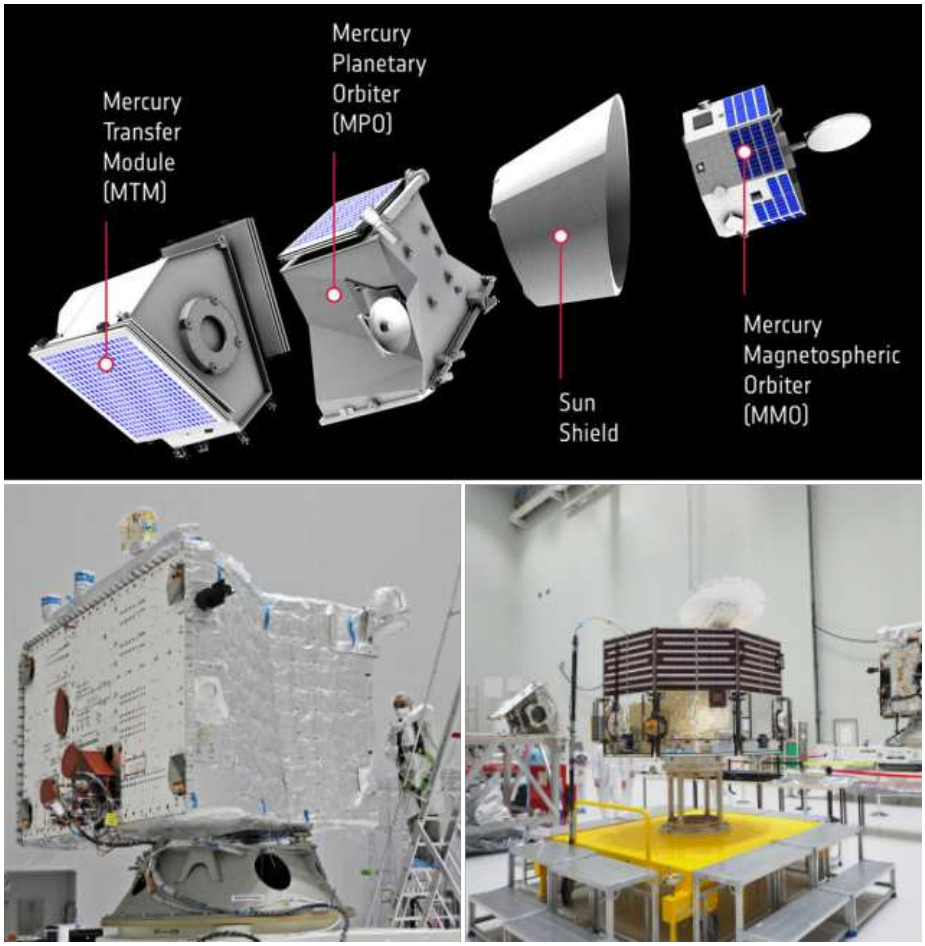

Figure 2.5: *Top panel:* Labeled diagram of the BepiColombo spacecraft, with all its modules (courtesy of ESA-JAXA). *Bottom left panel:* MPO module during its assembly (courtesy of ESA-B. Guillaume). *Bottom right panel:* MMO module during its assembly (courtesy of ESA-G. Murakami).

The MMO, the JAXA's module, will follow a 590 km × 11,639 km polar orbit and its 5 instruments on-board (Table 2.3) will investigate Mercury's magnetic field and its interactions with the solar wind.

The MPO, the ESA's module, instead, will follow a 480 km × 1500 km polar orbit and the 11 instruments on-board (Table 2.3) will be performing investigations on Mercury's surface, internal composition and exosphere.

In particular, the SIMBIO-SYS imaging system (Cremonese et al., 2020) consists of a High-Resolution Imaging Channel (HRIC), a STereo imaging Channel (STC) and a Visible and near-Infrared Hyperspectral Imaging channel (VIHI) (Figure 2.6). The channels will be providing high-resolution images (up to 6 m/px) with color capabilities for about 20% of Mercury, better than 80 m of accuracy Digital Terrain Models for the entire surface and high spatial (up to 120

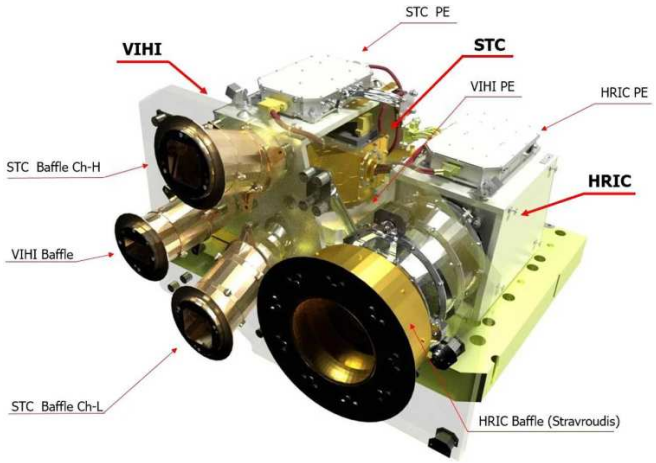

Figure 2.6: Labeled diagram of the SIMBIO-SYS imaging system onboard the MPO module of the BepiColombo spacecraft (from Cremonese et al. (2020).

m/px) and spectral (up to 6 nm) resolution images for global mineralogical mapping, respectively.

On 1 October 2021, BepiColombo performed the first flyby of Mercury at a range of about 199 km and the Monitoring Cameras positioned on the MTM collected the first snapshots of the planet (Figure 2.7).

The overall objectives of the mission are the study of Mercury's origin and evolution in its orbit so close to the Sun, the study of its geology, composition and interior structure, the investigation of the interior dynamics and origin of Mercury's magnetic field, the investigation of its exosphere and magnetosphere and the confirmation of the Theory of Relativity of Einstein.

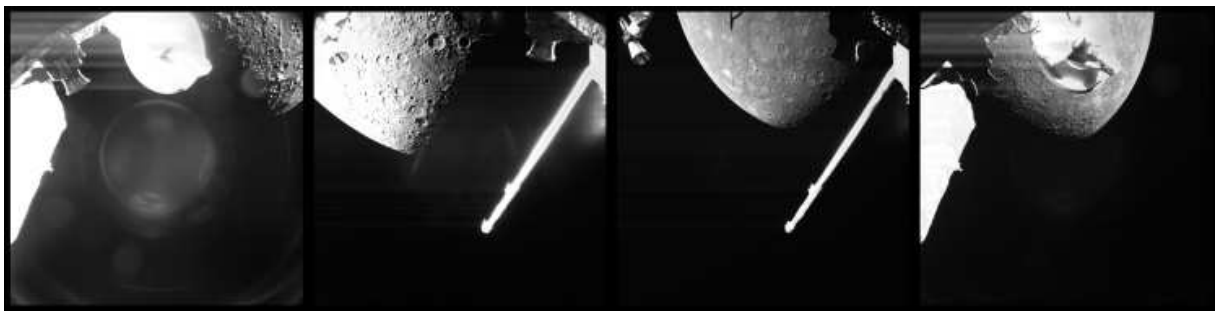

Figure 2.7: The first black-and-white snapshots of Mercury provided by the Monitoring Cameras onboard the MTM module of the BepiColombo spacecraft (courtesy of ESA-JAXA).

Table 2.3: Scientific instruments onboard the BepiColombo dual spacecraft (Benkhoff et al., 2010).

Instrument	Investigation
Mercury Planetary Orbiter	
BEpiColombo Laser Altimeter (BELA)	Characterization of the topography of Mercury's surface
Italian Spring Accelerometer (ISA)	Characterization of Mercury's interior structure and test Einstein's Theory of Relativity
Magnetic Field Investigation (MPO-MAG)	Description of Mercury's magnetic field and its source
MErcury Radiometer and Thermal Imaging Spectrometer (MERTIS)	Characterization of Mercury's mineralogical composition and global temperature range
Mercury Gamma-ray and Neutron Spectrometer (MGNS)	Detection of γ-rays and neutrons emissions to determine the elemental composition of Mercury's surface and the presence of volatiles in the polar areas
Mercury Imaging X-ray Spectrometer (MIXS)	Detection of X-rays emissions to determine the atomic composition of Mercury's surface
Mercury Orbiter Radio science Experiment (MORE)	Measurement of the size and physical state of Mercury's core and magnetic field
Probing of Hermean Exosphere by Ultraviolet Spectroscopy (PHEBUS)	Characterization of the composition and dynamic of Mercury's exosphere
Search for Exosphere Refilling and Emitted Neutral Abundances (SERENA)	Determination of the interactions between Mercury's surface, exosphere and magnetosphere and the solar wind
Spectrometer and Imaging for MPO BepiColombo Integrated Observatory SYStem (SIMBIO-SYS)	Providing high-resolution, stereo and infrared imaging of Mercury's surface
Solar Intensity X-ray and particle Spectrometer (SIXS)	Measurement of solar X-rays and particles
Mercury Magnetospheric Orbiter	
Mercury Dust Monitor (MDM)	Determine the distribution of interplanetary dust in Mercury's orbit
Mercury Magnetometer (MMO-MGF)	Description of Mercury's magnetosphere and its interactions with the solar wind and the planetary magnetic field
Mercury Sodium Atmospheric Spectral Imager (MSASI)	Measurement of the distribution, abundance and dynamics of sodium in Mercury's magnetosphere
Mercury Plasma Particle Experiment (MPPE)	Detection of low- and high-energetic particles in Mercury's magnetosphere
Mercury Plasma Wave Instrument (PWI)	Characterization of the structure and dynamics of Mercury's magnetosphere

2.1.3 Geology of Mercury

The surfaces of the Moon and Mercury are similar, both carrying the burden of many impacts resulting from meteoritic and cometary collisions.
Given the almost total absence of an atmosphere and hydrosphere, impact craters thus constitute the primary morphology on Mercury.
Nonetheless, if Mercury's crater density is similar to the Moon's for craters from 128 km to 512 km the same is not true for craters ranging from 20 to 128 km (Fassett et al., 2011). In its most densely cratered regions, indeed, Mercury presents a crater density 50% that of the Moon. Furthermore, the differences in terms of mean impact speed (42.5 km/s vs 19.4 km/s of the Moon) and surface gravity (3.7 m/s^2 vs 1.6 m/s^2 of the Moon) lead to the formation of larger amounts of impact melt and ejecta, the latter deposited with a scattering degree 0.65 times lower than on the Moon (Gault et al., 1975). Exceptionally, craters on Mercury possibly derived by cometary impacts can be characterized by bright rays extending even further than those generated on the Moon itself.

Precisely on the basis of distinct basins and related deposits, Mercury's chrono-stratigraphy has been divided into 5 time-stratigraphic systems: pre-Tolstojan (oldest), Tolstojan, Calorian, Mansurian and Kuiperian (youngest) (Figure 2.8).
The pre-Tolstojan system encompasses basins and terrains older than 4.00 Ga (Spudis and Guest, 1988; Strom and Neukum, 1988). The Tolstojan system is defined by the formation of the Tolstoj basin and it ends at ∼4.00-3.85 Ga (Spudis and Guest, 1988; Strom and Neukum, 1988), which is the base for the Calorian system, defined by the formation of the largest basin on Mercury, the Caloris basin. Finally, accordingly to recent absolute model ages, the Mansurian and Kuiperian systems, defined by the formation of the Mansur and Kuiper craters, begin at ∼1.70 Ga and ∼280 Ma respectively (Banks et al., 2016).

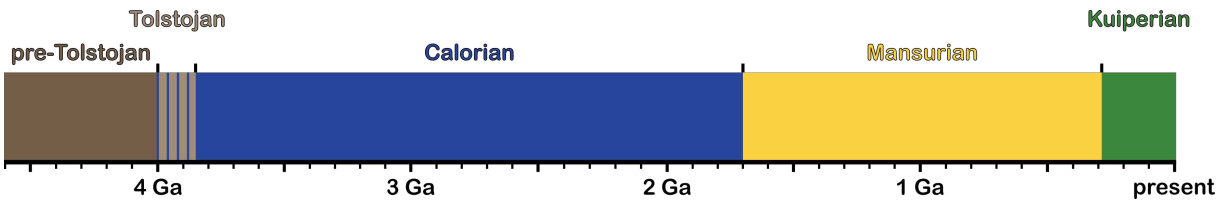

Figure 2.8: Mercury's time-stratigraphic systems.

Given the absence of hermean rocky samples to be analyzed and dated and the quality of M10 data, planetary geologists decided to combine different surface morphologies, reflecting lithology, composition and age of the underlying bedrock, in "terrain units" (Trask and Guest, 1975; Spudis and Guest, 1988). In particular, 3 different plains units have been identified: intercrater plains (heavily cratered), intermediate plains and smooth plains (sparsely cratered).
The intercrater plains (ICP), identified by rough to gently rolling surfaces marked by abundant secondary craters (Figure 2.9 *top panel*), present a very high crater density and thus probably represent the oldest and most widespread terrains on Mercury (Spudis and Guest, 1988). The ICP are thought to be volcanic in origin and their materials constitute Tolstojan to pre-Tolstojan (>3.90 Ga) remnants of flood volcanism (Trask and Guest, 1975; Spudis and Guest, 1988; Whitten et al., 2014; Denevi et al., 2016).
The intermediate plains (IMP), instead, are identified by undulating to planar surfaces characterized by a medium crater density (Spudis and Prosser, 1984) (Figure 2.9 *central panel*). However, the IMP show no clear contrast with the adjacent terrains and their distribution in patches makes it somewhat difficult to recognize and classify them (Denevi et al., 2013; Whitten et al., 2014).
The smooth plains (SP), finally, are identified by smooth and sparsely cratered surfaces mostly confined within basins or showing sharp boundaries with the adjacent plains (Trask and Guest, 1975; Denevi et al., 2013) (Figure 2.9 *bottom panel*). The evidence of lava flows and embayment relationships ascribe to the SP a volcanic nature (Byrne et al., 2013; Denevi et al., 2013). Age estimations based on crater density distribution imply that the SP are Calorian in age, formed earlier than 3.80 Ga (Strom et al., 2008), and thus they represent Mercury's youngest large-scale geologic unit.

Along with the 3 main geologic units, Guest and Greeley (1983) distinguished several units associated with the impact region of the Caloris basin: the Caloris Montes Formation and the Nervo Formation, characterizing the rim region, and the Van Eyck Formation and the Odin formation, considered as ejecta units.
The Caloris Montes Formation forms the rim crest of the Caloris basin and is composed of individual massifs interpreted as uplifted bedrock (Trask and Guest, 1975), while the Nervo Formation identifies slightly rugged smooth areas occurring in depressions formed by the arrangement of these massifs.

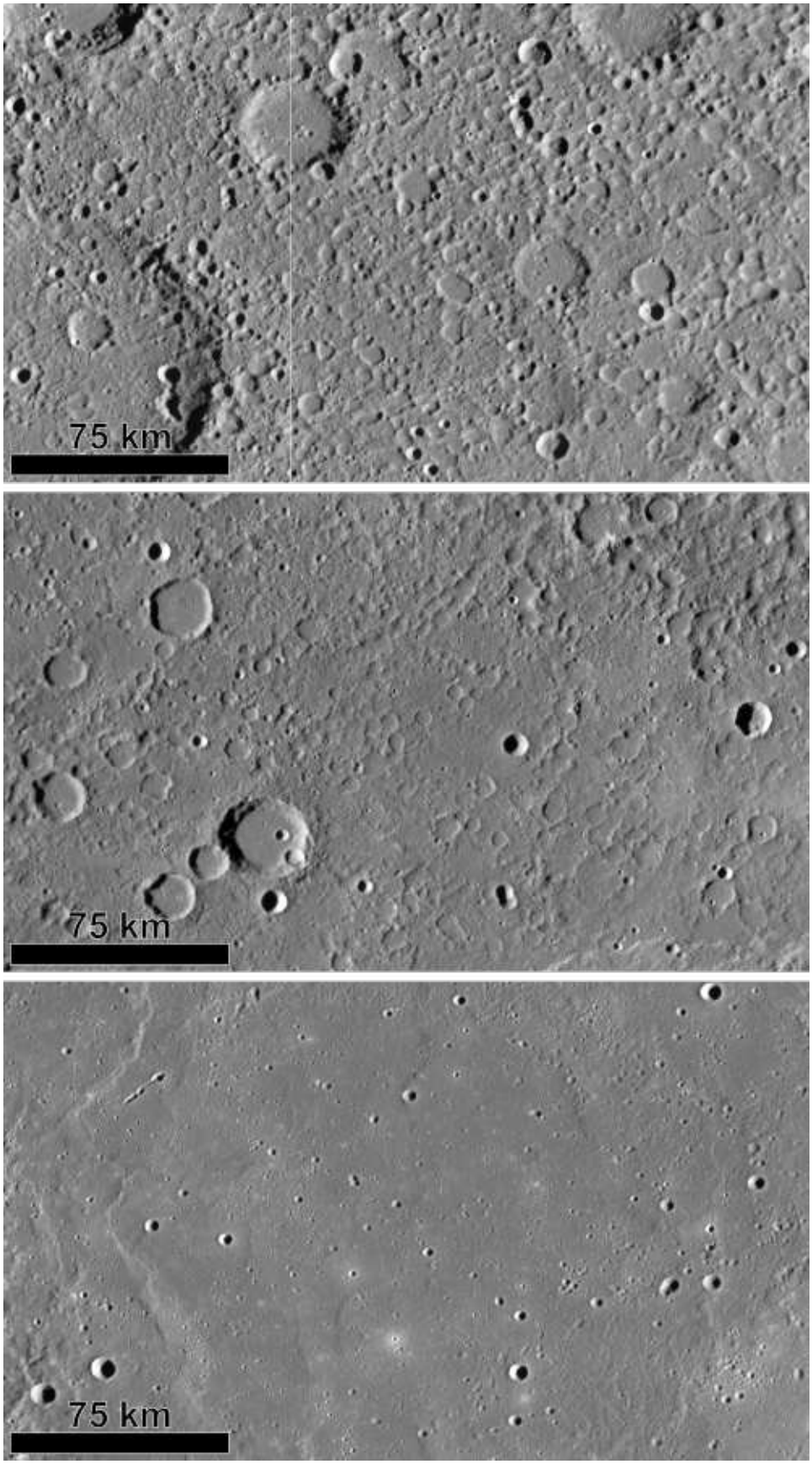

Figure 2.9: MESSENGER MDIS BDR view of intercrater (centered at 27.7°N, 71.0°W, *top panel*), intermediate (centered at 22.6°S, 58.4°W, *central panel*) and smooth (centered at 28.3°N, 157.9°W, *bottom panel*) plains.

The Van Eyck Formation consists of both sub-radial lineated ridges and grooves (Trask and Guest, 1975) and secondary craters (Schaber and McCauley, 1980), whereas the Odin Formation identifies hummocky deposits characterized by spaced hills and knobs (Trask and Guest, 1975).

The surface of Mercury is marked by widespread and mostly compressional tectonic landforms, such as wrinkle ridges, lobate scarps and high-relief ridges.
Wrinkle ridges are broad low-relief arches superimposed by narrow ridges (Figure 2.10 *left panel*) mainly occurring on smooth plains (Watters, 1988; Byrne et al., 2014b; Korteniemi et al., 2015). They can reach hundreds of meters in height and hundreds of kilometers in length (Walsh et al., 2013) and they are originated by a combination of thrust faulting and folding (Schultz, 2000; Watters et al., 2009).
Lobate scarps, also called "rupes" or "rupēs" in the IAU nomenclature, are widespread sinuous steep escarpments characterized by an asymmetrical profile, with rounded scarp faces and gently dipping slopes in the back limb (Strom et al., 1975; Watters and Nimmo, 2010; Byrne et al., 2014b) (Figure 2.10 *central panel*). Interpreted as thrust faults (Watters et al., 2004; Massironi et al., 2015a; Crane and Klimczak, 2019), they can reach hundreds of kilometers in length and a couple of kilometers in height and their kilometer-scale vertical offset allows to accommodate more crustal shortening than wrinkle ridges (Zuber et al., 2010).
High-relief ridges, also called "dorsum" or "dorsa" in the IAU nomenclature, finally, are not very common linear to arcuate symmetric features that can reach hundreds of kilometers in length and a couple of kilometers in height (Watters et al., 2009) (Figure 2.10 *right panel*). They represent compressional to transpressional landforms formed by reverse faulting (Watters and Nimmo, 2010; Massironi and Byrne, 2015) and are considered variant, probably pop-up structures with an antithetical conjugate, of the lobate scarps, with which they often show a transition.

Tectonic landforms associated with extensional deformation, on the other hand, are confined within large basins (e.g. Caloris, Raditladi, see (Mancinelli et al., 2016), Rachmaninoff, see (Wright et al., 2019)) and are characterized by a network of linear to sinuous grabens striking radially or concentrically from the basin center (Strom et al., 1975; Murchie et al., 2008; Watters et al., 2009; Blair et al., 2013) (Figure 2.11).

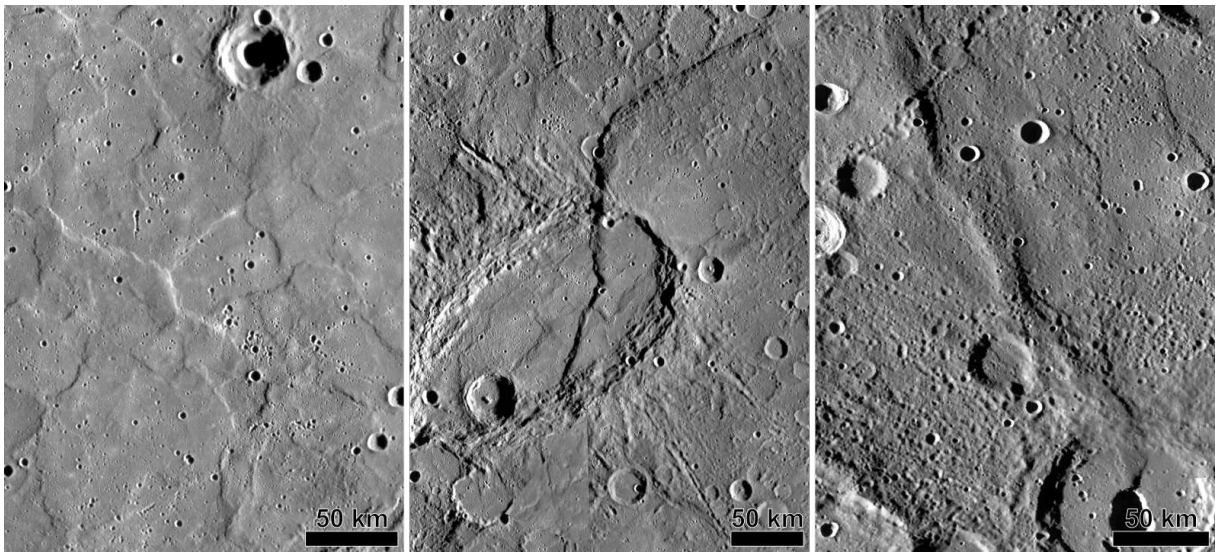

Figure 2.10: MESSENGER MDIS BDR view of wrinkle ridges on Tir Planitia (centered at 13.2°S, 163.7°E, *left panel*), the Beagle Rupes (centered at 1.9°S, 101.1°E, *central panel*) and the Antoniadi Dorsum (centered at 30.0°N, 31.1°W, *right panel*).

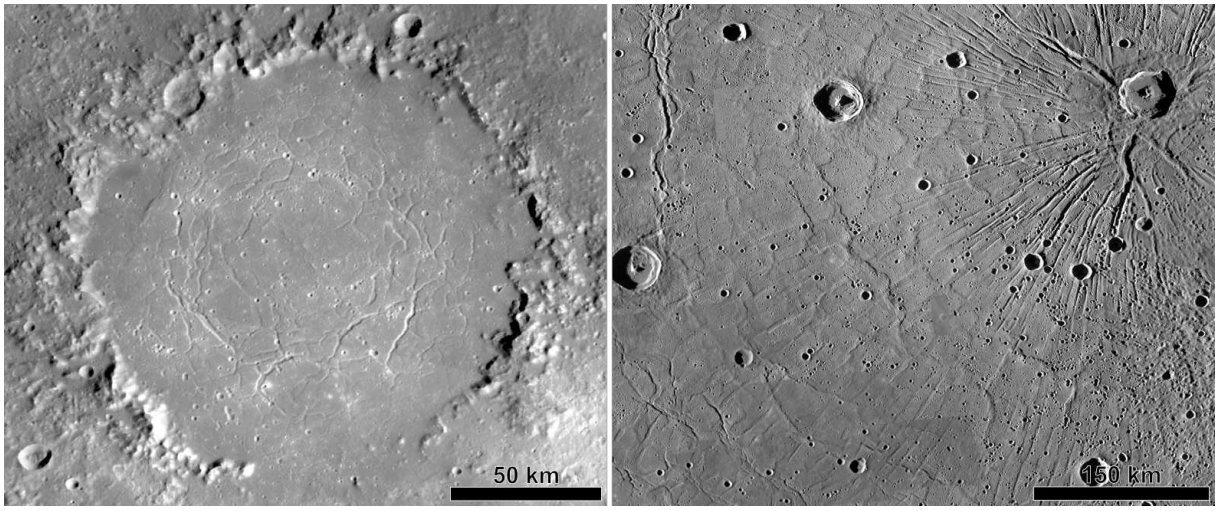

Figure 2.11: MESSENGER MDIS BDR view of radial and concentric graben structures in the Rachmaninoff basin (centered at 27.6°N, 57.6°E, *left panel*) and the Caloris basin (centered at 30.5°N, 163.2°E, *right panel*).

The 3 main models proposed for explaining the tectonic evolution of Mercury are the global contraction, the tidal despinning and the mantle convection (Figure 2.12).

The global contraction hypothesis is thought to reflect the cooling of the planet's interior, with the consequent shrinkage of the surface, supposedly started around 3.00 Ga (Strom et al., 1975; Watters et al., 2004). The measurement of the displacement-length ratio of thrusts estimated a total radius decrease of about 7 km (Di Achille et al., 2012; Byrne et al., 2014a).

The tidal despinning hypothesis, instead, relies on the decrease of Mercury's oblateness toward

a more spherical shape resulting in N-S compressional faults in the equatorial region, NW-SE strike-slip faults at mid-latitudes and E-W extensional systems at high latitudes (Melosh and Dzurisin, 1978).

The mantle convection hypothesis, finally, considers the convection of Mercury's mantle for the formation of patterns of sheet-like upwelling regions coherent with the lobate scarp's distribution (King, 2008).

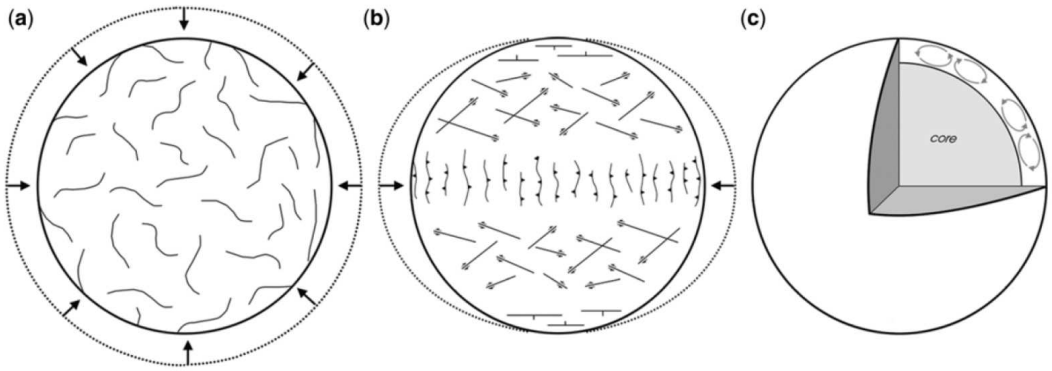

Figure 2.12: Schematic representations for the three models proposed for Mercury's tectonic evolution, from (Massironi et al., 2015b). (a) global contraction. (b) tidal despinning. (c) mantle convection.

However, the kinematic analysis of Mercury shows that strike-slip faults are widespread all over the planet (Massironi et al., 2015b) and that compressional features are visible even at high latitudes. Tidal despinning and global contraction, therefore, could have been coeval processes (Klimczak et al., 2015). As concerns the mantle convection, instead, the presence of frontal thrusts with lateral shearing indicating stable directions of tectonic transport, not consistent with the global contraction, suggests that mantle convection played an important role in the tectonic evolution of Mercury (Massironi et al., 2015b).

For what concerns Mercury's surface composition, the MESSENGER's MASCS and MDIS instruments confirmed the previous ground-based telescopic observations in the UV-VIS-NIR. The reflectance spectra, indeed, show an increase in reflectance at the NIR wavelengths, characteristic referred to as red spectral slope, and an almost absent ferrous iron absorption band between 900 and 1000 nm (Vilas, 1988; McClintock et al., 2008). These results indicate for the hermean crust a prevalent anorthositic composition, with a FeO content of silicates <2-3 wt% (Blewett et al., 1997; McClintock et al., 2008).

Nonetheless, enhanced-color images derived by a principal components transformation of the 9 narrow-band MDIS-WAC channels enabled to discern the relevant color variegation of Mercury's surface (Figure 2.13 *top panel*). The color images, in particular, allowed to discriminate different spectral units, possibly associated with different events and ages, suggesting a convoluted surface stratigraphy modified by impact cratering and volcanism (Denevi et al., 2009; Ernst et al., 2010).

In general, all surface materials show a red spectral slope with no clear absorption bands. However, different types of terrains have been identified based on spectral reflectance (Figure 2.13 *bottom left panel*): bright crater floor deposits (BCFD, bright whitish-blue), red material (RM, dark orange), high-reflectance red plains (HRP, light orange), intermediate plains and intercrater terrain (IP/IT, brownish), low-reflectance blue plains (LBP, light blue), low-reflectance material (LRM, dark blue) (Ernst et al., 2010).

A couple more very bright colors, finally, can be distinguished at the margins or inside large basins and craters and associated with exceptionally interesting materials: the intense orange pyroclastic deposits, related to volatile-induced explosive volcanism, and the bright blue hollows, irregular depressions produced by loss of volatiles (Figure 2.13 *bottom right panel*).

Pyroclastic deposits are widespread across Mercury, except for thicker crustal regions, and are strongly related to thrust faults and impact-generated fractures that allow the ascent and outpouring of magma and control the magma/volatile release (Kerber et al., 2009; Thomas et al., 2014b).

Hollows, which appear morphologically similar to the martian "swiss-cheese" and the comet 67/P's "honey comb" features, are high-reflectance rimless depressions reaching tens of meters to a few kilometers in width and a few tens of meters in depth (Blewett et al., 2011). They are associated mostly with impact structures (found in crater central peaks, floors, walls and ejecta) but can also be related with terrain units, in particular with the LRM color unit, and are generated by the loss of a volatile component due to sublimation, space weathering, solar wind interactions with the hermean surface and/or impacts (Blewett et al., 2011; Vaughan et al., 2012; Blewett et al., 2013; Thomas et al., 2014a; Lucchetti et al., 2021). Hollows, therefore, indicate that Mercury presents higher concentrations of volatile elements than previously supposed for a planet so close to the Sun and, since their younger origin than their host landforms, that their formation may be an ongoing process (Blewett et al., 2011).

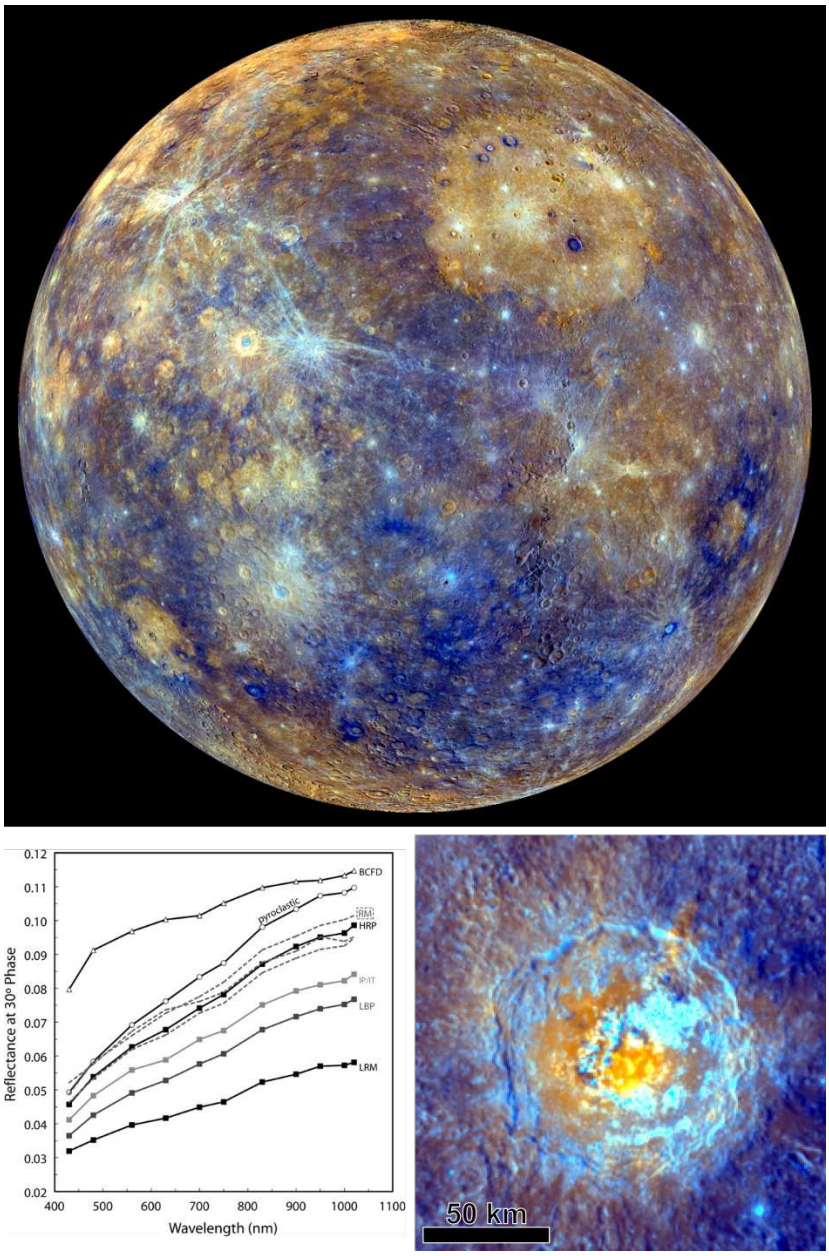

Figure 2.13: MESSENGER MDIS Enhanced-color image and reflectance spectra. *Top panel*: the Caloris basin is in the upper right and it is filled with a light orange region of HRP and bordered to the west and south by light blue LBP; at the right margin is the Tolstoj basin surrounded by a ring of dark blue LRM; below right of center is a small crater with RM on its floor; above left of center is a particularly young crater with BCFD rays (courtesy of NASA-JHU Applied Physics Lab-Carnegie Inst. of Washington). *Bottom left panel*: reflectance spectra of the enhanced-color units, as from Ernst et al. (2010). *Bottom right panel*: Tyagaraja crater (centered at 3.9°N, 148.9°W) seen in enhanced-colors, where it is possible to distinguish the bright blue and intense orange colors of hollows and pyroclastic deposits respectively.

To conclude, in 2012 MESSENGER discovered the presence of ice in the permanently shadowed craters in the north polar region (Chabot et al., 2013) (Figure 2.14), which was previously inferred from Earth-based radar observations (Slade et al., 1992; Butler et al., 1993). The occurrence of ice in the polar regions of Mercury is made possible by the near-zero obliquity of

the planet. The perpetual darkness and the very low temperatures granted by the absence of an atmosphere, indeed, allow the preservation of material possibly deposited by cometary impacts.

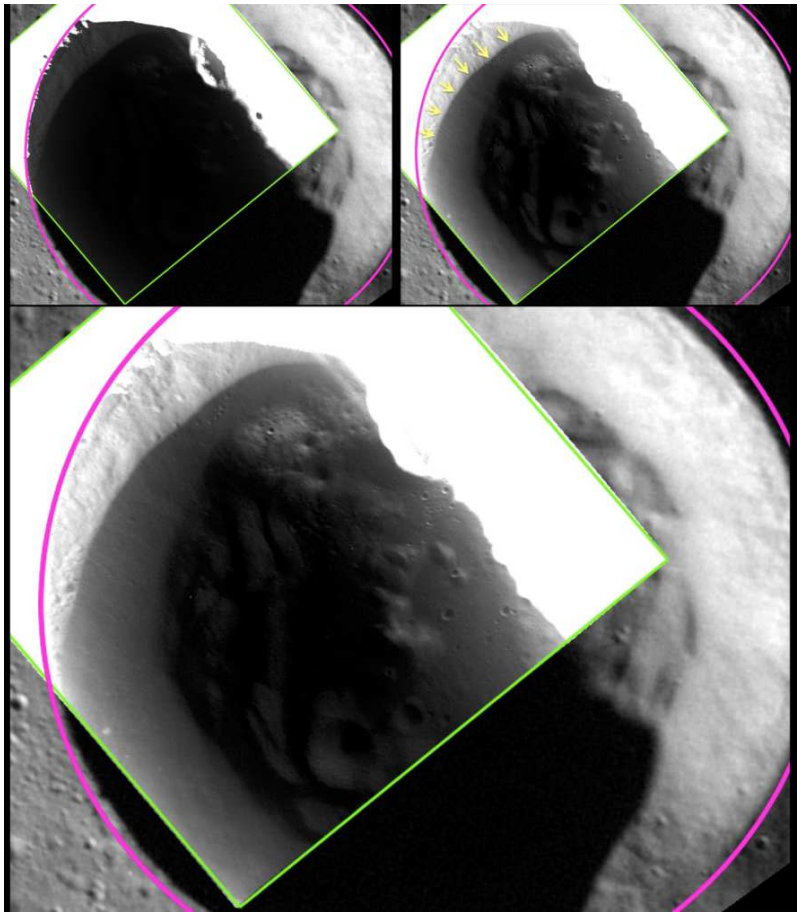

Figure 2.14: Water ice deposit in an unnamed permanently shadowed crater in the north polar region. *Top left panel*: the pink line delimits the crater rim, while the green box defines the edge of the 24 m/px, low-altitude broadband MDIS image. *Top right panel*: the yellow arrows individuate the boundary of a low-reflectance region. *Bottom panel*: detailed view of the shadowed interior of the crater. Temperature models predict for this area the presence of a >10 cm-thick surficial layer of volatile and organic-rich material overlying a thicker layer of water ice (courtesy of NASA-JHU Applied Physics Lab-Carnegie Inst. of Washington).

2.1.4 The H-9 Eminescu quadrangle

During the M10 mission, Mercury was divided into 15 geographical regions (Davies et al., 1978) to allow the subdivision of the spheroid in equivalent areas to be mapped using different types of projections, depending on the latitude, in order to minimize the geometric distortions. Of these quadrangles, 9 were named after outstanding morphologic and topographic features, where the M10 data collection was available, while the remaining 6 regions were named after albedo features as from telescopic observations (Figure 2.15).

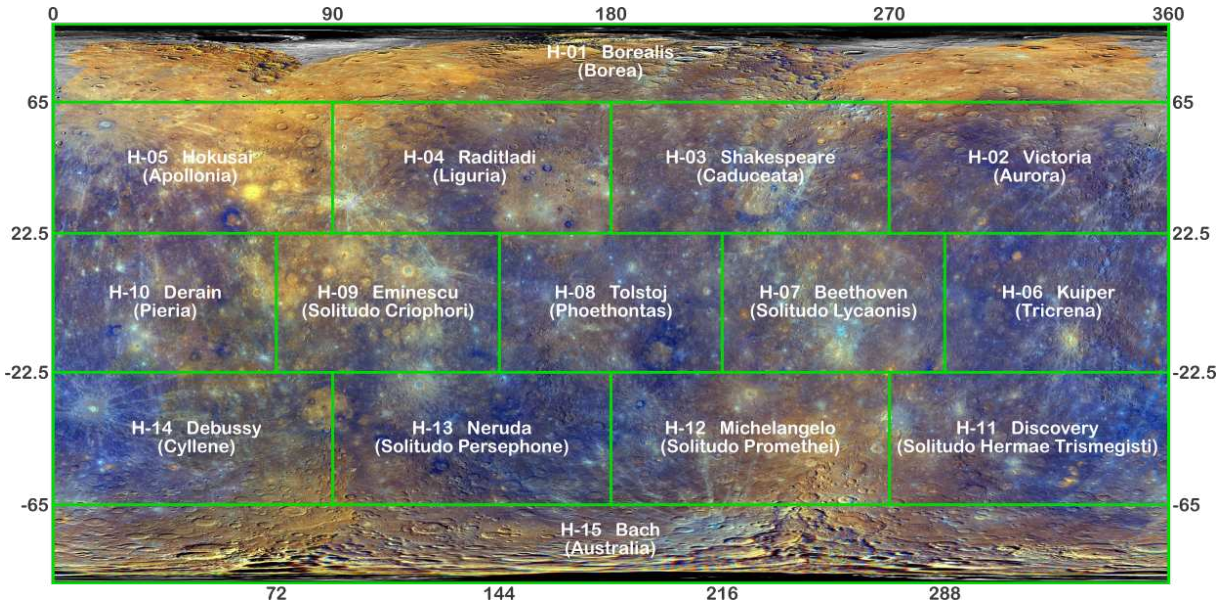

Figure 2.15: Subdivision of Mercury in 15 quadrangles in positive west equirectangular projection centered at 180°E on top of the MESSENGER Enhanced Color basemap (∼665 m/px). The letter H, prefix for Mercury, precedes each region's number. Names are given based on outstanding geologic features, while names in parentheses are based on albedo features. Equatorial, mid-latitude and polar quadrangles cover 7.7%, 6.5% and 4.7% of hermean surface respectively.

The equatorial H-9 Eminescu quadrangle is located between latitudes 22.5°N and 22.5°S and longitudes 72°E and 144°E. It was formerly named Solitudo Criophori (i.e. "desert of Criophorus", where Criophorus is an epithet associated with Hermes depicted with a ram) after a dark albedo feature characterizing the eastern portion of the quadrangle. With the data coverage provided by the MESSENGER mission, it was finally renamed Eminescu (i.e. Mihail Eminescu (1850-1889), a Romanian poet) (Figure 2.16 *left panel*) as the Kuiperian peak-ring basin centered at 10.8°N and 114.1°E (Schon et al., 2011) presenting bright clusters of hollows in stark contrast with the low reflectance material surrounding its central peak complex (Figure 2.16 *central* and *right panel*).

The M10 data coverage allowed the production of 1:5M regional geologic maps for 9 quadrangles out of 15, and in particular for the H-1 Borealis (Grolier and Boyce, 1984), H-2 Victoria (McGill and King, 1983), H-3 Shakespeare (Guest and Greeley, 1983), H-6 Kuiper (DeHon et al., 1981), H-7 Beethoven (King and Scott, 1990), H-8 Tolstoj (Schaber and McCauley, 1980), H-11 Discovery (Trask and Dzurisin, 1984), H-12 Michelangelo (Spudis and Prosser, 1984), and H-15 Bach (Strom et al., 1990) quadrangles (Figure 2.17).

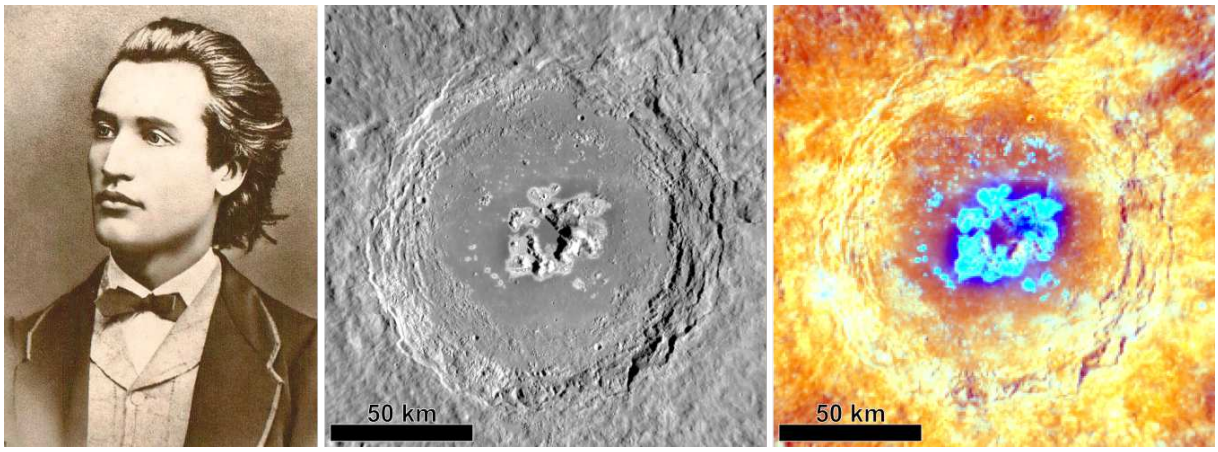

Figure 2.16: Mihail Eminescu (*left panel*) and its namesake crater viewed in grayscale (*central panel*) and enhanced colors (*right panel*).

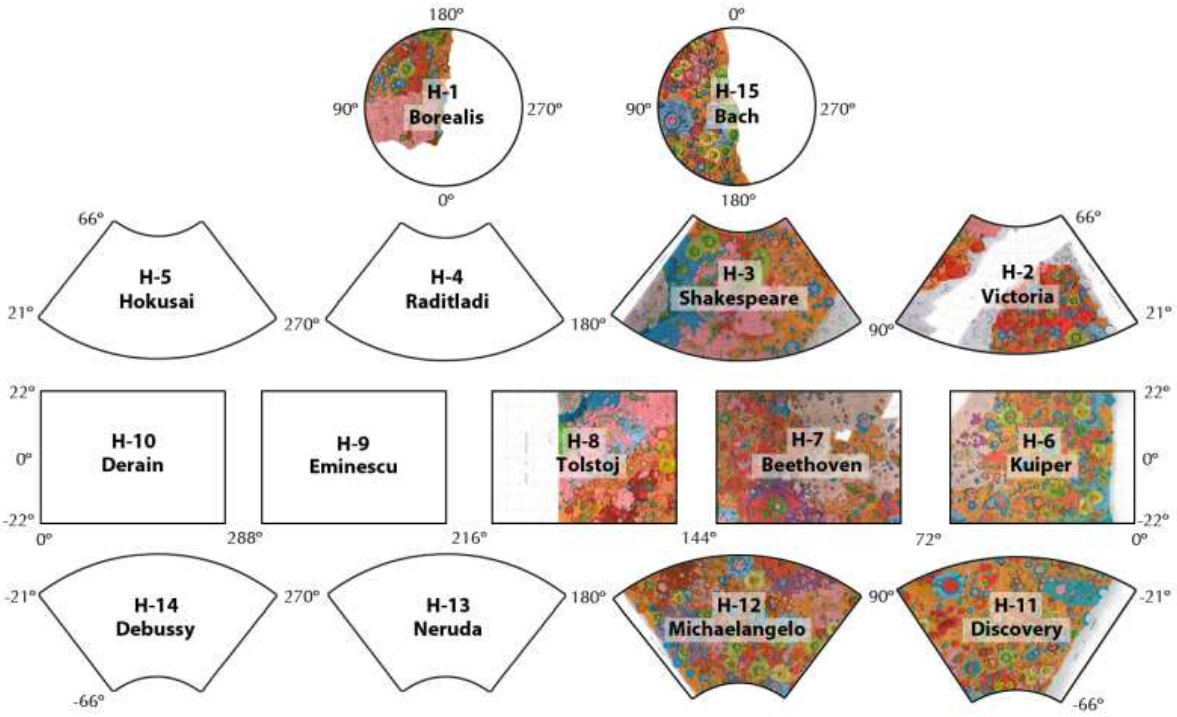

Figure 2.17: Serie of 1:5 regional geologic maps produced on Mariner 10 data, from Prockter (2015).

The draft of the first 1:15M global geologic map of Mercury produced on MESSENGER data recently presented (Kinczyk et al., 2019) provides the first geological mapping for the Eminescu quadrangle. However, this small-scale map discriminates only 2 unit terrains (i.e. ICPs and SPs) and uses 5 classes of craters, with the *c1* class indicating the youngest and freshest craters and the *c5* class indicating the oldest and most degraded ones, thus reversing the USGS

classification system (Mccauley et al., 1981).
The ongoing project for the production of a series of 1:3,000,000 (1:3M) regional geologic maps for Mercury started with the production of individual geologic maps for the H-2 (Galluzzi et al., 2016a), H-4 (Mancinelli et al., 2016) and H-3 (Guzzetta et al., 2017) quadrangles and it evolved in a coordinated global mapping plan (Galluzzi et al., 2016b, 2017). Aiming at delivering all the regional maps in time for the ESA-JAXA BepiColombo mission, I have been producing the first 1:3M geologic map for the eastern portion of the H-9 Eminescu quadrangle, between latitudes 22.5°N and 22.5°S and longitudes 108°E and 144°E.

2.2 Data and basemaps

The geologic analysis of a planetary surface is based on remotely sensed datasets, such as imagery and topographic data.
For Mercury, I produced i) a 1:3M geologic map, derived from photo-geological interpretation of the surface, for a wide part of the eastern portion of the Eminescu quadrangle, ii) a color-based spectral map, derived by associating compositional variations with the different morphologies and terrains, for a limited area and iii) a selection of scientific targets of interest for the Bepi-Colombo mission.

For the production of the geologic map of the H-9 Eminescu quadrangle, I used the most recent data acquired during the MESSENGER nominal mission (2011-2015).

MDIS WAC and NAC (Hawkins et al., 2007) imagery data were gradually released for public use in different levels of processing, namely as the raw uncalibrated Experiment Data Record (EDR), the calibrated and photometrically corrected Calibrated Data Record (CDR), the geometrically corrected Derived Data Record (DDR) and final Reduced Data Record (RDR) products. The latter are distinguished in map projected Basemap RDR (BDR) and map projected Multispectral RDR (MDR).
The geologic mapping was produced based on the BDR monochrome basemap (∼166 m/px), assembled using MDIS NAC or WAC 750 nm images with moderate incidence angles and low emission angles (Figure 2.18). Auxiliary ∼166 m/px monochrome basemaps with High Incidence

angles from East (HIE) (Figure 2.19) and West (HIW) (Figure 2.20) and with Low Incidence angles (LOI) (Figure 2.21) were useful to accentuate subtle morphologic and topographic features and reflectance variations. All the 4 monochrome basemaps were produced by mosaicking the 4 tiles (i.e. NE, NW, SE and SW) of the Eminescu quadrangle using the Integrated Software for Imagers and Spectrometers (ISIS3).

The panchromatic imagery was coupled with topographic information gathered through the MESSENGER USGS global Digital Elevation Model (DEM) version 2 (∼665 m/px). This DEM was produced using the ISIS3 software with data derived from MDIS WAC and NAC images (Becker et al., 2016) and it represents the only topographic data available for the entire surface (Figure 2.22). The topographic basemap for Eminescu quadrangle was trimmed from the global DEM.

The color-based spectral mapping, instead, was carried out on the Enhanced Color global mosaic (∼665 m/px) and the MD3 Color global mosaic (∼665 m/px), namely an MDR basemap assembled using 3 of the 11 WAC filters. The Enhanced Color basemap uses a mosaic with the 430 nm, 750 nm and 1000 nm bands and places the second principal component, the first principal component and the 430/1000 nm ratio in the red, green and blue channels respectively (Figure 2.23). The MD3 Color mosaic, instead, places the 1000 nm, 750 nm and 430 nm narrowband filters in the red, green and blue channels respectively (Figure 2.24). Both basemaps for the Eminescu quadrangle were trimmed from the global color mosaics.

The NE, NW, SE and SW tiles of the Eminescu quadrangle used for obtaining the BDR, HIE, HIW and LOI basemaps were downloaded from NASA's Planetary Data System (PDS) Cartography and Imaging Sciences Node. The USGS DEM, Enhanced Color mosaic and the MD3 Color mosaic were downloaded as global basemaps from the USGS Astrogeology Science Center website. Appendix B lists the basemaps used for this work.

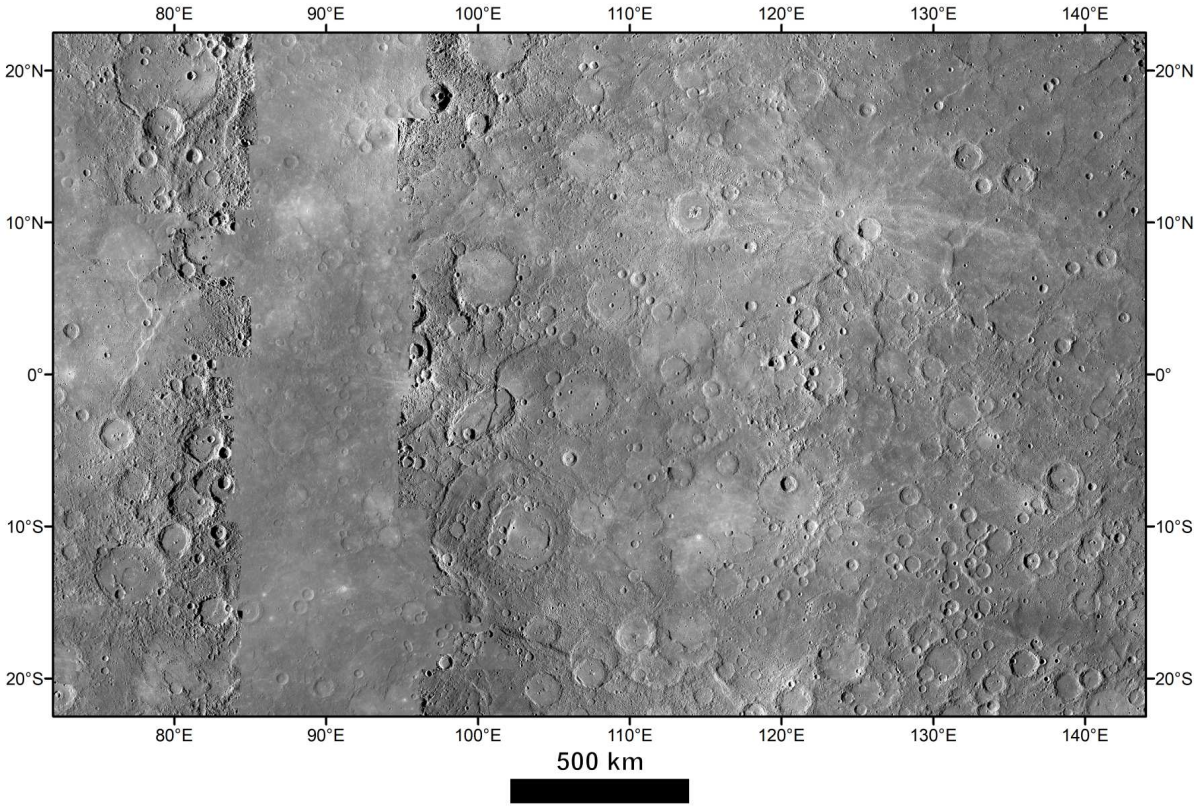

Figure 2.18: MESSENGER MDIS BDR basemap (∼166 m/px) in equirectangular projection. The monochrome basemap is assembled using MDIS NAC or WAC 750 nm images with moderate incidence angles and low emission angles. The basemap was produced by mosaicking the BDR tiles of the Eminescu quadrangle in the ISIS3 software.

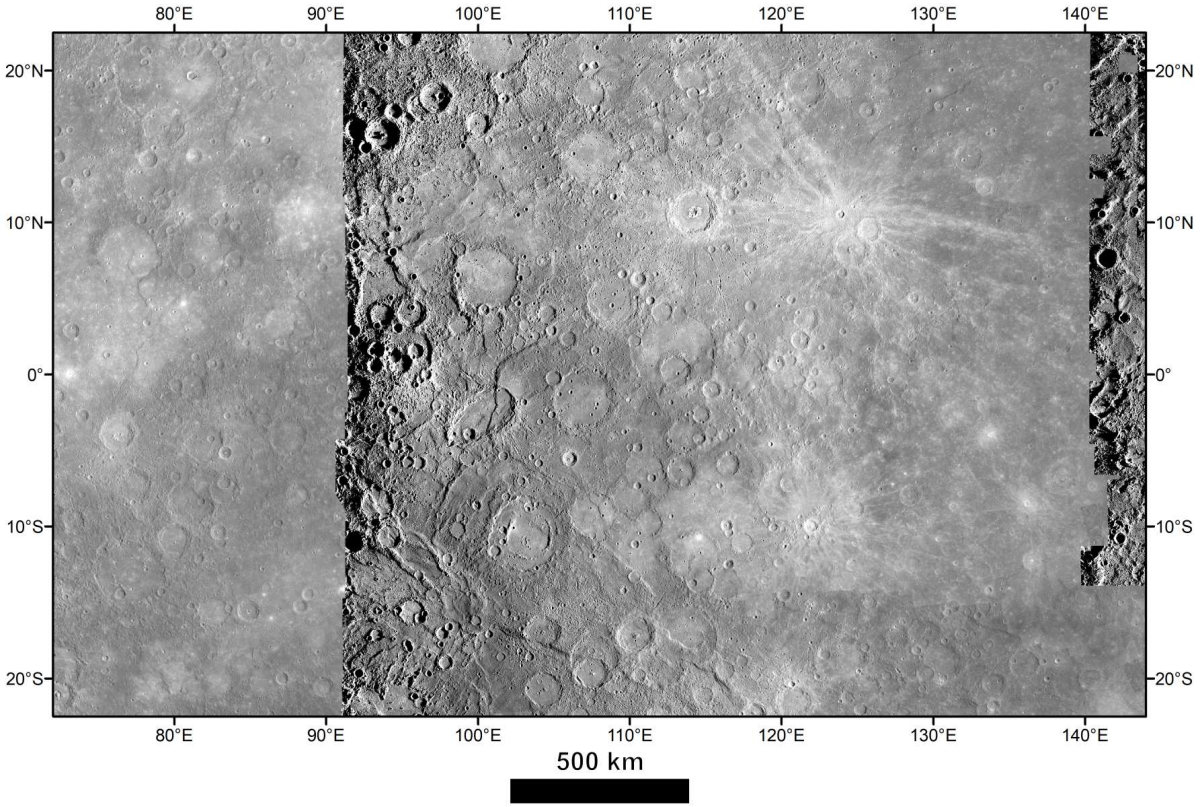

Figure 2.19: MESSENGER MDIS HIE basemap (∼166 m/px) in equirectangular projection. The monochrome basemap is assembled using MDIS NAC or WAC 750 nm images with high incidence angles and illumination from the East. The basemap was produced by mosaicking the HIE tiles of the Eminescu quadrangle in the ISIS3 software.

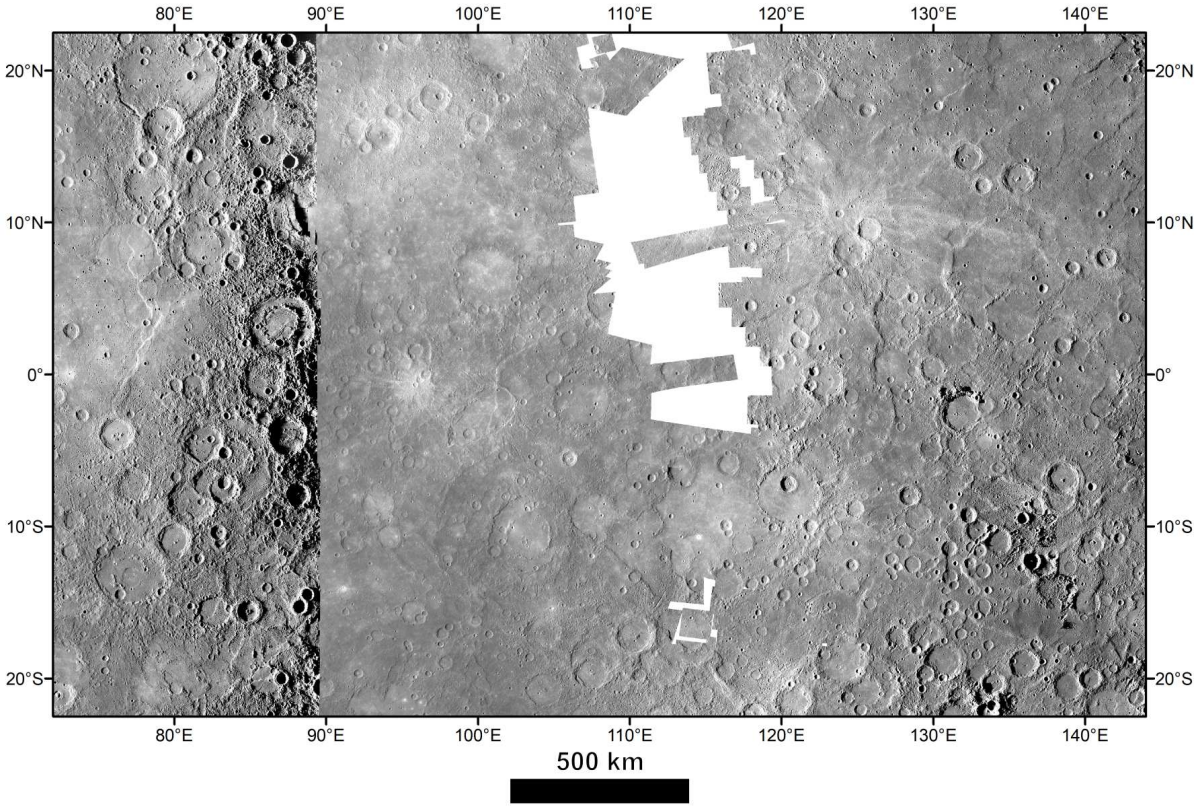

Figure 2.20: MESSENGER MDIS HIW basemap (∼166 m/px) in equirectangular projection. The monochrome basemap is assembled using MDIS NAC or WAC 750 nm images with high incidence angles and illumination from the West. The basemap was produced by mosaicking the HIW tiles of the Eminescu quadrangle in the ISIS3 software.

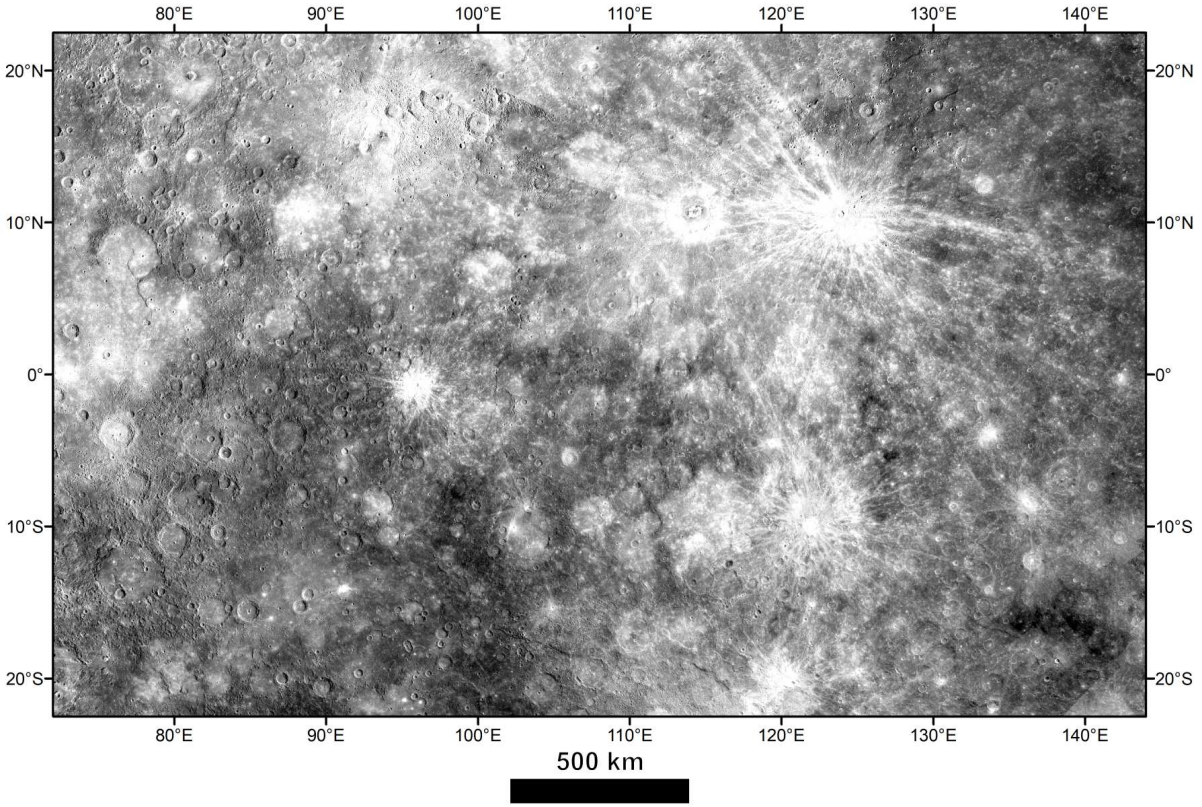

Figure 2.21: MESSENGER MDIS LOI basemap (∼166 m/px) in equirectangular projection. The monochrome basemap is assembled using MDIS NAC or WAC 750 nm images with low incidence angles and low emission angles. The basemap was produced by mosaicking the LOI tiles of the Eminescu quadrangle in the ISIS3 software.

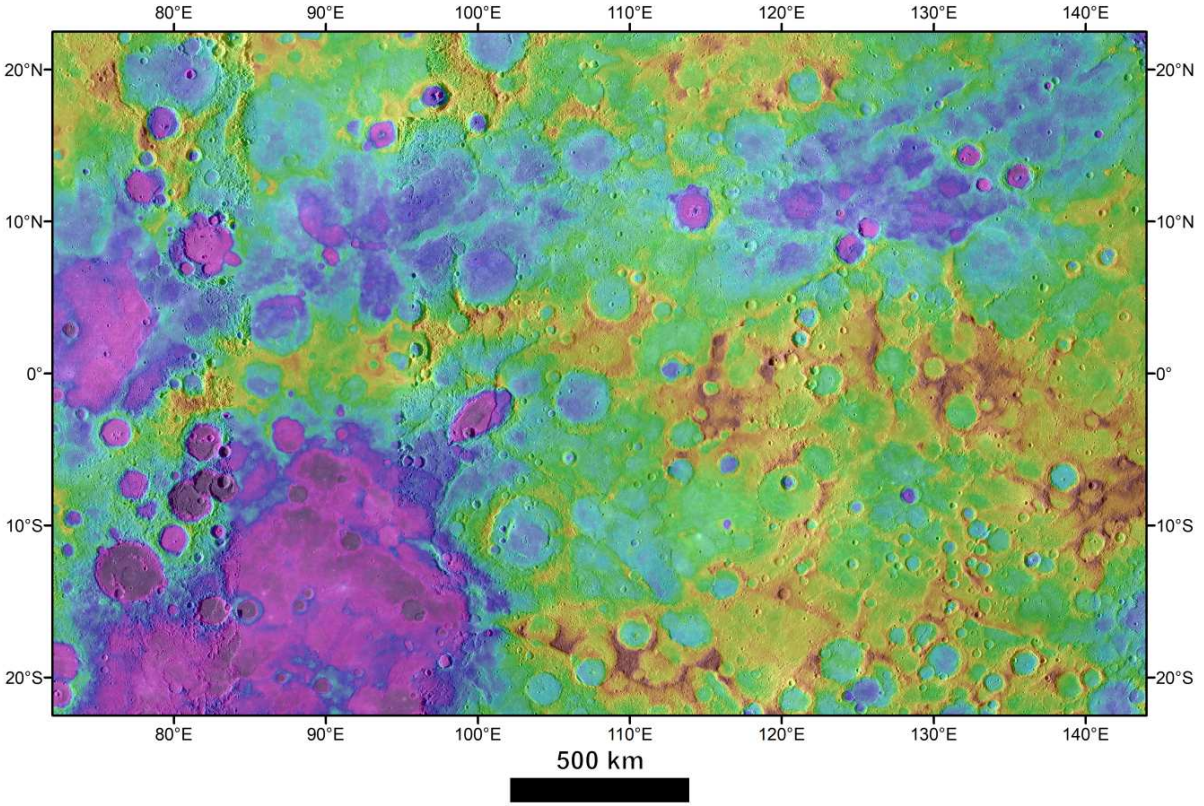

Figure 2.22: MESSENGER USGS global DEM v2 (∼665 m/px) in equirectangular projection. The basemap was trimmed from the Mercury_Messenger_USGS_DEM_Global_665m_v2 and it is visualized on top of the BDR basemap with 50% of transparency.

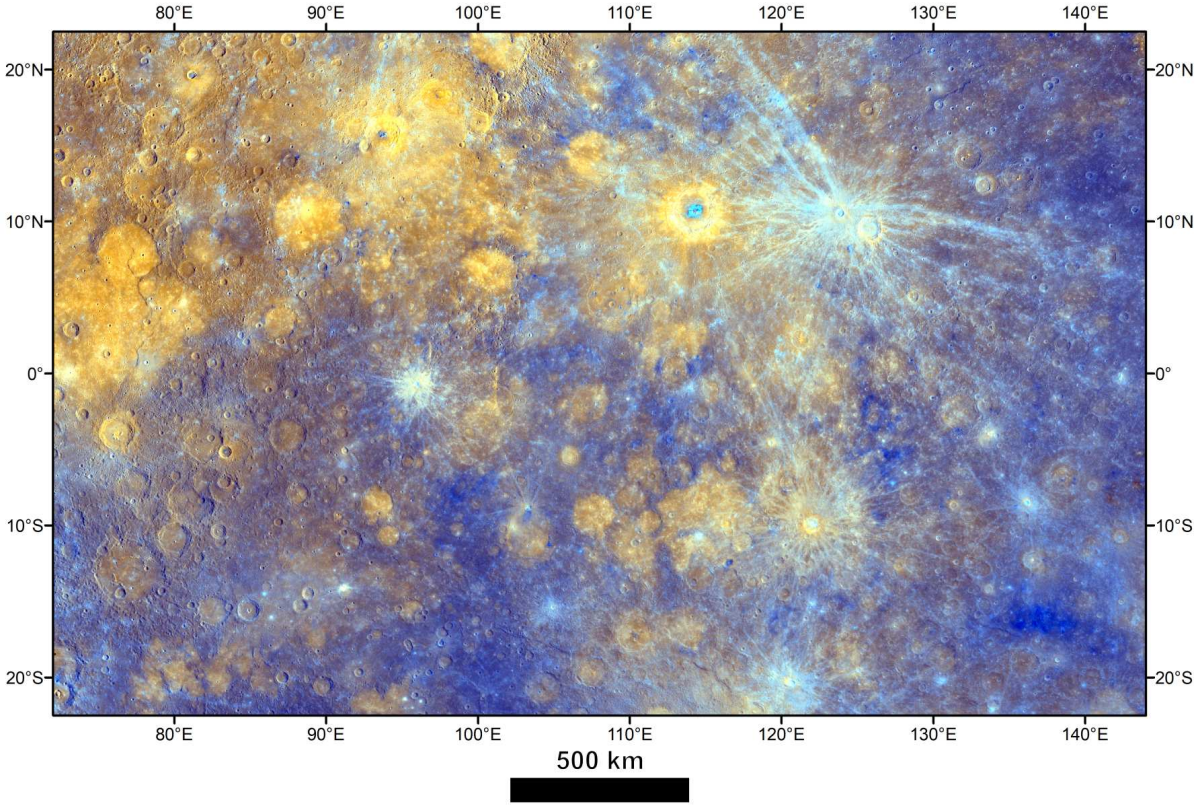

Figure 2.23: MESSENGER MDIS Enhanced Color global mosaic (∼665 m/px) in equirectangular projection. The basemap emphasizes color variations on Mercury's surface by using a mosaic with the 430 nm, 750 nm and 1000 nm bands and placing the second principal component, the first principal component and the 430/1000 nm ratio in the red, green and blue channels respectively. The basemap was trimmed from the Mercury_MESSENGER_MDIS_Basemap_EnhancedColor_Mosaic_Global_665m.

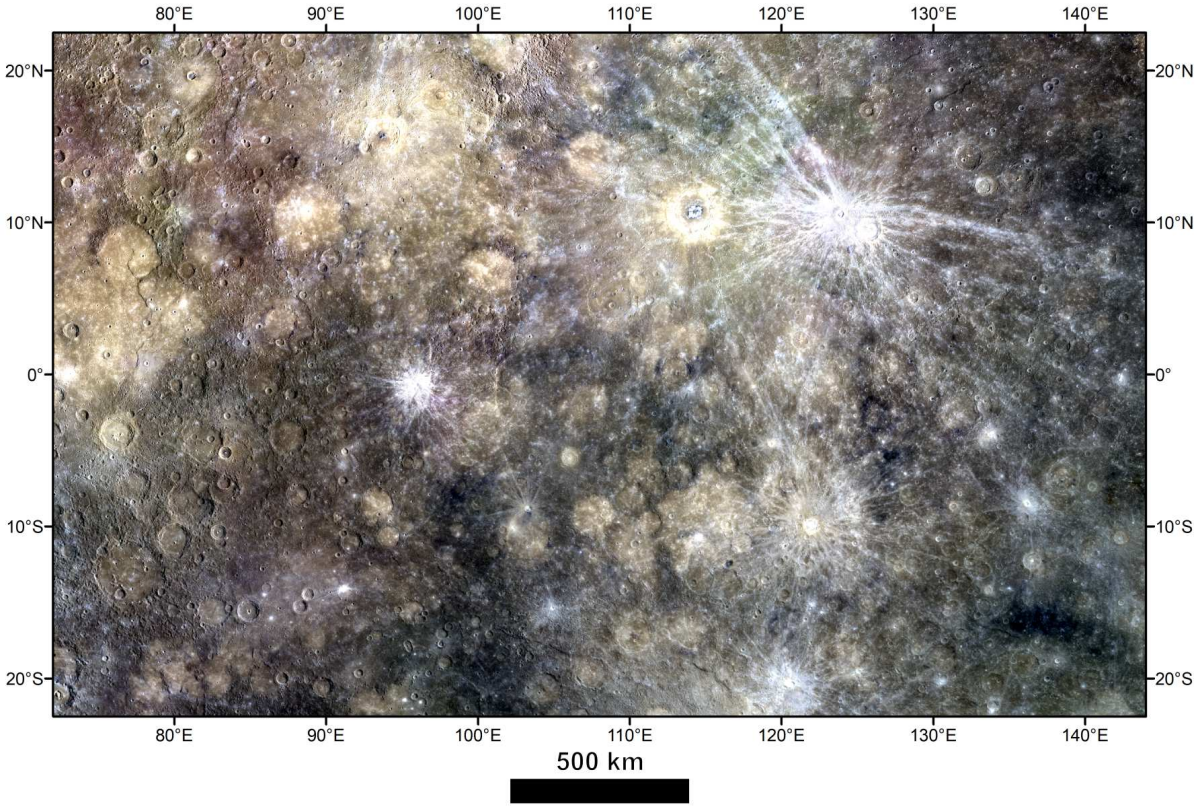

Figure 2.24: MESSENGER MDIS MD3 Color global mosaic (∼665 m/px) in equirectangular projection. The basemap emphasizes color variations on Mercury's surface by placing the 1000 nm, 750 nm and 430 nm narrow-band filters in the red, green and blue channels respectively. The basemap was trimmed from the Mercury_MESSENGER_MDIS_Basemap_MD3Color_Mosaic_Global_665m.

2.3 Methods

The geologic and color-based spectral mapping of the Eminescu quadrangle were performed in the ESRI ArcGIS 10.4.1 software.
Since the H-9 quadrangle is located in the equatorial region of Mercury, the two mappings were carried out in equirectangular projection using the D_Mercury_2015 datum.
According to their different basemaps resolutions, the mapping and output scales (see chapter 1.3) were set to 1:332,000 and 1:1,660,000 respectively for the geologic mapping and to 1:1,330,000 and 1:6,650,000 respectively for the color-based spectral mapping.
A geodatabase for enabling the distinction of linear and polygonal features by means of dedicated symbologies was assembled following most of the Federal Geographic Data Committee (FGDC) Digital Cartographic Standard for Geologic Map Symbolization prepared by the USGS (for more details see Galluzzi (2019)). The geodatabase provides for the distinction of geologic/spectral contacts (polyline layer), linear features (polyline layer) for morphologies and structures, surface features (polygon layer) and geologic units (polygon layer).

Geologic/spectral contacts, which represent the main digitizing layers, delimit the different geologic provinces and crater materials or spectrally different terrains. Unlike the USGS standards, which usually consider certain, approximate, concealed and inferred contacts, in this work were used only certain and approximate contacts. The firsts are used when unambiguous and sharp contrasts between different textures/colors/morphologies are visible, while approximate contacts are used when the transition between different terrains/colors/morphologies is ambiguous or gradational (Figure 2.25). These contacts are then used for generating the polygonal geologic units during the map finalization stage.

The linear features vector layer, instead, includes lineaments such as crests of crater rims, volcanic vents and tectonic structures. Craters are distinguished based on their size, distinguishing craters with diameters between 5-20 km and larger than 20 km, and degradation stage, namely buried/heavily degraded craters (Figure 2.26). Structures, like faults, thrusts and grabens are distinguished in certain and uncertain, similarly to the certain and approximate distinction made for contacts. Thrusts include lobate scarps and high relief ridges (see chapter 2.1.3), while wrinkle ridges (see chapter 2.1.3) are considered separately.

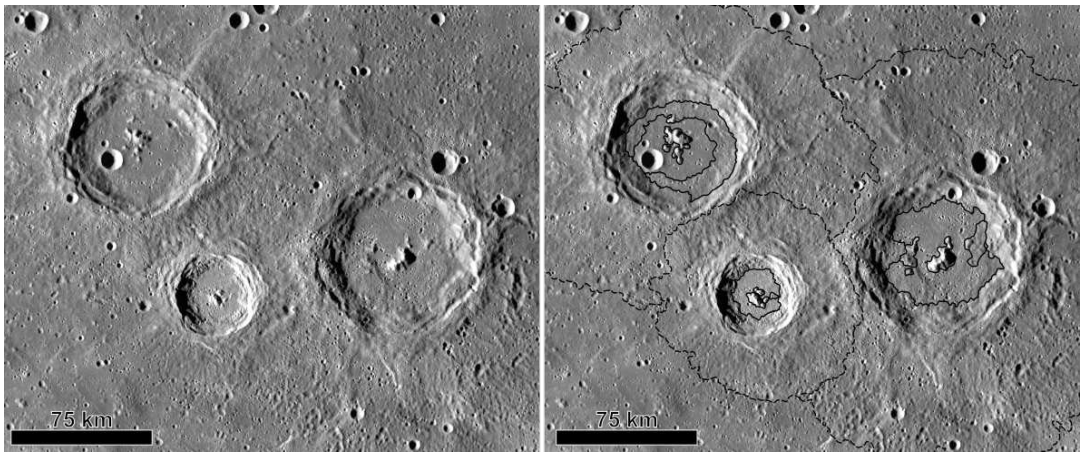

Figure 2.25: Geologic contacts linework. MESSENGER MDIS BDR basemap (*left panel*) with digitized certain (black line) and approximate (dashed black line) contacts (*right panel*).

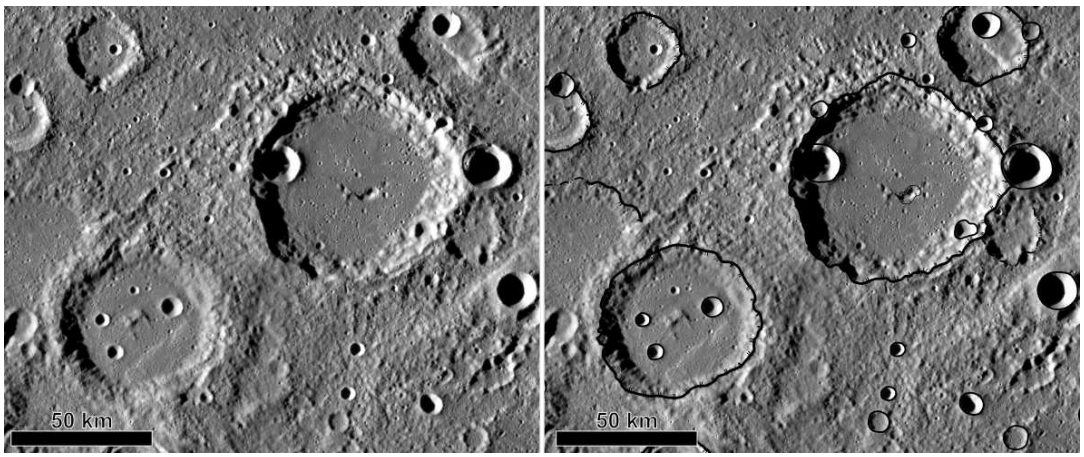

Figure 2.26: Linear features linework for craters. MESSENGER MDIS BDR basemap (*left panel*) with digitized craters with 5<D<20 km (black lines), craters with D>20 km (black lines with double inner ticks), buried/degraded craters (black dashed and dot lines) and a putative volcanic vent (black line with single inner tick) (*right panel*).

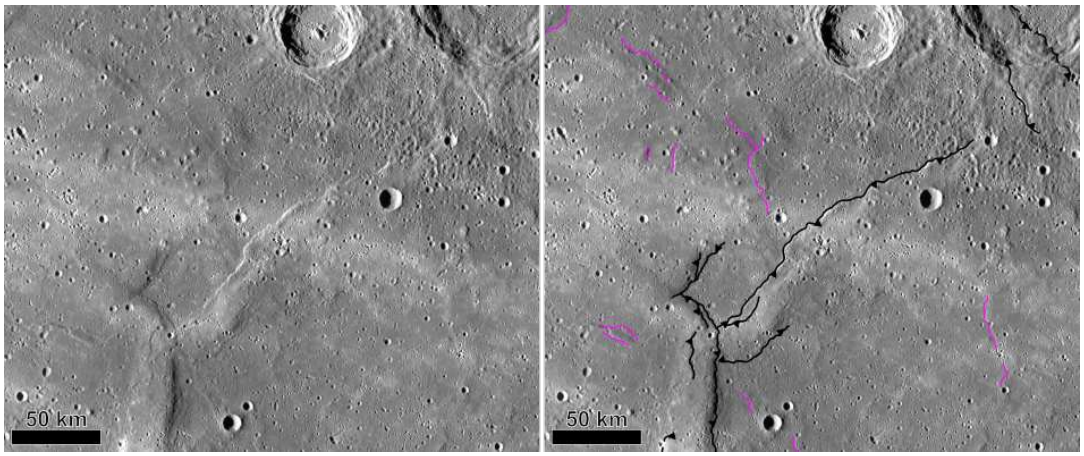

Figure 2.27: Linear features linework for structures. MESSENGER MDIS BDR basemap (*left panel*) with digitized certain thrusts (continuous black lines with triangles), uncertain thrusts (dashed black lines with triangles) and wrinkle ridges (purple lines) (*right panel*).

Surface features are represented as polygonal textures overlaying the main geologic units. They include bright and dark materials, namely bright crater rays and low-reflectance materials (see chapter 2.1.3) respectively, along with clusters of hollows (see chapter 2.1.3), clusters of craters or secondary crater chains and rough ejecta deposits. Point features, finally, represent isolated surface features <6 km^2, such as isolated bright or dark spots and isolated hollows.

Once the digitizing process and the topological analysis for errors check were finished, polygons were built and assigned to a geologic unit (see chapter 1.3). In particular, the following geologic units have been defined: SP, IMP, ICP, Caloris Rough Ejecta and Caloris Smooth Plain, Odin and Van Eyck Formations, smooth and hummocky crater floors, and, finally, 3 crater material classes dependent on the crater's morphological appearance.
In accordance with the 1:3M series of maps for Mercury published up to date (Galluzzi et al., 2016a; Mancinelli et al., 2016; Guzzetta et al., 2017; Wright et al., 2019; Pegg et al., 2021), 3 different crater classes have been distinguished for classifying crater deposits instead of the 5 classes previously discriminated (Mccauley et al., 1981), even if the geologic maps for the H-5 Hokusai and H-14 Debussy quadrangles were produced using both classifications. The 3-classes classification, specifically, identifies heavily degraded craters with discontinuous rims (*c1*), degraded craters with recognizable rims (*c2*) and fresh and well-preserved craters with sharp rims (*c3*) (Figure 2.28).

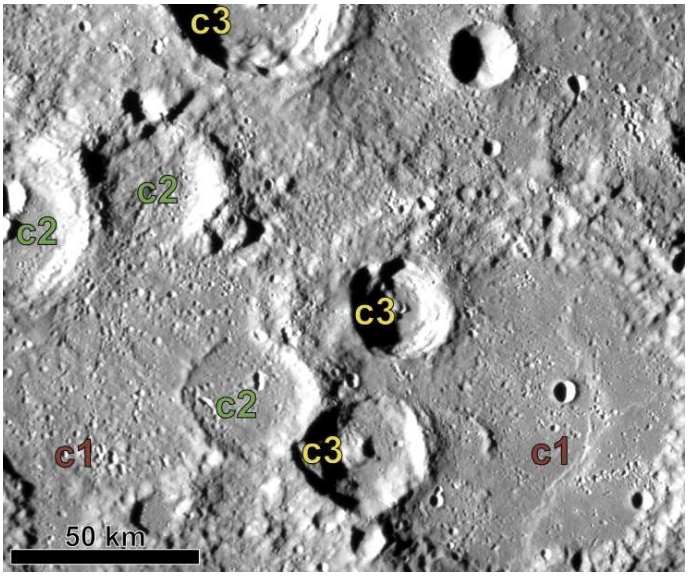

Figure 2.28: MESSENGER MDIS BRD basemap with craters classified as *c1*, *c2* or *c3*.

2.4 Results

2.4.1 Geologic map

The geologic mapping was performed on 85.45% (more than 4/5) of the eastern portion of the H-9 Eminescu quadrangle (Figure 2.31).

Morphologies constitute the most represented linear features (Figure 2.32). Crests of crater rims with diameters between 5-20 km are the most widespread features, followed by crests of crater rims with diameters larger than 20 km, whose ejecta are mapped respecting the superposing relationships. Crests of heavily degraded/buried rims are represented by discontinuous rims characterized by a high degree of degradation and, in most cases, are buried by the ejecta of other craters. The least represented morphologies are volcanic vents all of which are located near the center of craters and present no evident surrounding pyroclastic deposits.

As concerns tectonics, the area is marked by several thrusts cutting through craters, being cut by younger craters or creating elevation differences on terrains and presenting a preferential NE-SW and N-S orientation. Wrinkle ridges, instead, are present particularly on basin floors following a preferentially NE-SE trend (Figure 2.33).

Secondary craters derived by primary impacts are very common and widespread surface features on the Eminescu quadrangle. They are distinguished in clusters and chains. Chains of craters, also called "catenae" in the IAU nomenclature, are typically radial troughs a hundred kilometers long and about ten kilometers wide radiating outside the crater rim and beyond the ejecta blanket (Figure 2.29 *top panel*). However, some catenae, reaching hundreds of kilometers in length and tens of kilometers in width, have a much less unequivocal origin being not clearly relatable to the Caloris basin impact or other major impacts (Figure 2.29 *bottom panel*), e.g. (Rothery and Fegan, 2015).
By looking at the Eminescu crater, a new surface feature was defined. Beyond the ejecta deposits of Eminescu, indeed, the surface is marked by a discontinuous and concentric blanket of craters with a mean diameter of 3 km, also superposing larger and older craters, whose origin is related to the formation of Eminescu itself (Figure 2.29 *top panel*). This particular feature was named rough ejecta.

Hollows, both in clusters or isolated, are localized, in particular, on the crater floor of Eminescu (Figure 2.29 *top panel*), near the Abeeso Facula located in the H-8 Tolstoj quadrangle and in small craters. They can be associated with LRMs, mapped depending on their extent as surface or point features of dark materials, and/or pyroclastic deposits.

Bright materials, finally, defining the presence of bright rays generated by young impact craters, are not so widespread but they can cover large distances. Also bright spots, generated by very small and fresh impact, are mapped as point features.

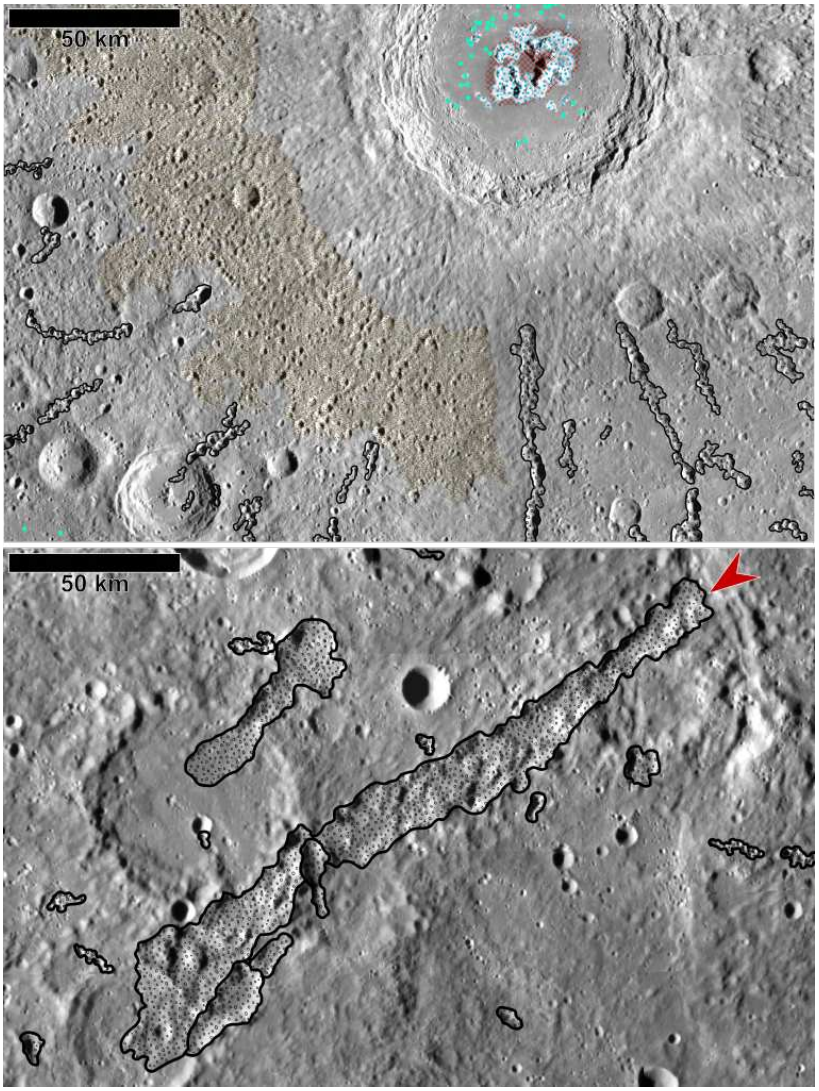

Figure 2.29: Examples of surface features mapping as seen on top of the MESSENGER MDIS BDR basemap. *Top panel*: view of the Eminescu crater presenting a cluster of hollows and isolated hollows (cyan features) above dark materials (maroon feature) on its crater floor, a rough ejecta blanket (noisette feature) on its W-SW portion and catenae of secondary craters (black features) radiating S-SW. *Bottom panel:* a catenae (pointed out by the red arrow) not clearly related to a primary impact.

The mapping for the Eminescu quadrangle is still in progress, but preliminary polygonal units have been created for providing a general context. The following units (Figure 2.30) have therefore been discriminated (see Appendix C for reading information).

1. *sp* – [plain materials] smooth plains material: flat to gently rolling sparsely cratered plains.
2. *CSP* – [basin materials – Caloris group] Caloris smooth plain: smooth materials filling the Caloris basin floor.
3. *OF* – [basin materials – Caloris group] Odin Formation: hummocky deposits characterized by spaced hills and knobs within smoothed materials.
4. *VEF* – [basin materials – Caloris group] Van Eyck Formation: lineated ridges and grooves sub-radial to the Caloris basin.
5. *CRE* – [basin materials – Caloris group] Caloris rough ejecta: rough and hummocky materials surrounding the Caloris impact basin.
6. *c3* – [crater materials] well preserved: young and fresh craters presenting continuous and sharp rims and well-recognizable ejecta deposits; their crater floors are sparsely cratered; they can display bright crater rays and chains of secondary craters.
7. *c2* – [crater materials] degraded: slightly degraded and subdued craters with still recognizable and continuous rims; distal ejecta are not as clearly recognizable as proximal ejecta.
8. *c1* – [crater materials] heavily degraded: heavily degraded craters with discontinuous and subdued rims and densely cratered floors; proximal ejecta may be recognizable just for very large craters.
9. *cfs* – [crater materials] smooth floor material: very planar and sparsely cratered crater floor material.
10. *cfh* – [crater materials] hummocky floor material: rough and moderately cratered crater floor material.

The geologic map is shown in Figure 2.34 and in Figure 2.35 on top of the MESSENGER MDIS BDR basemap.

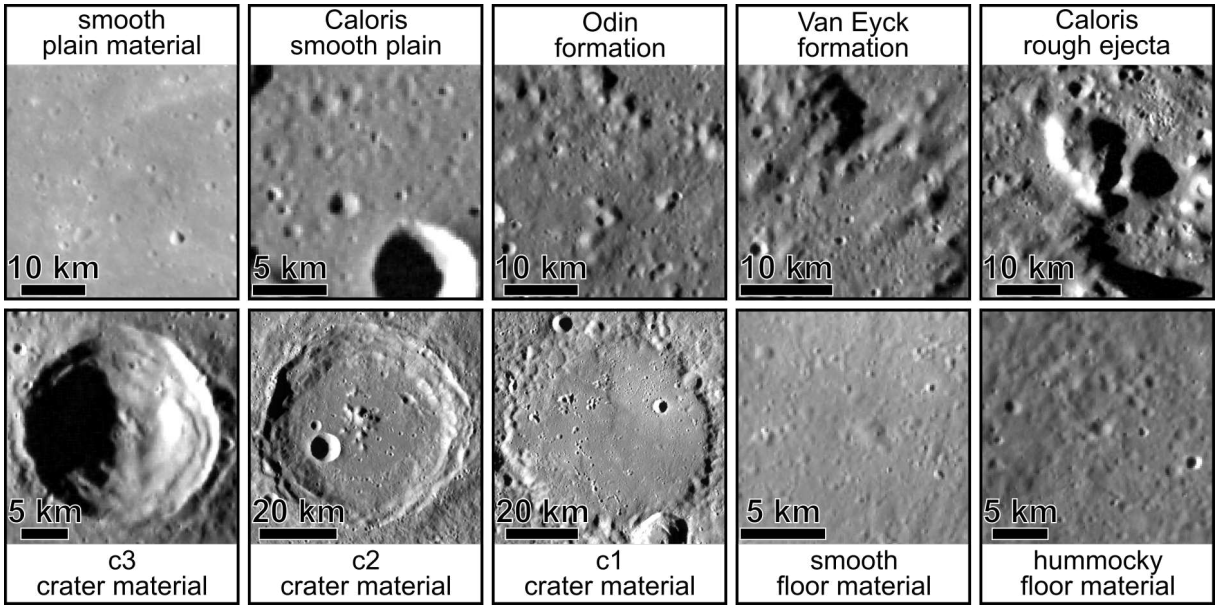

Figure 2.30: Examples for the *sp*, *CSP*, *OF*, *VEF*, *CRE*, *c3*, *c2*, *c1*, *cfs* and *cfh* geologic units that have been mapped in the study area.

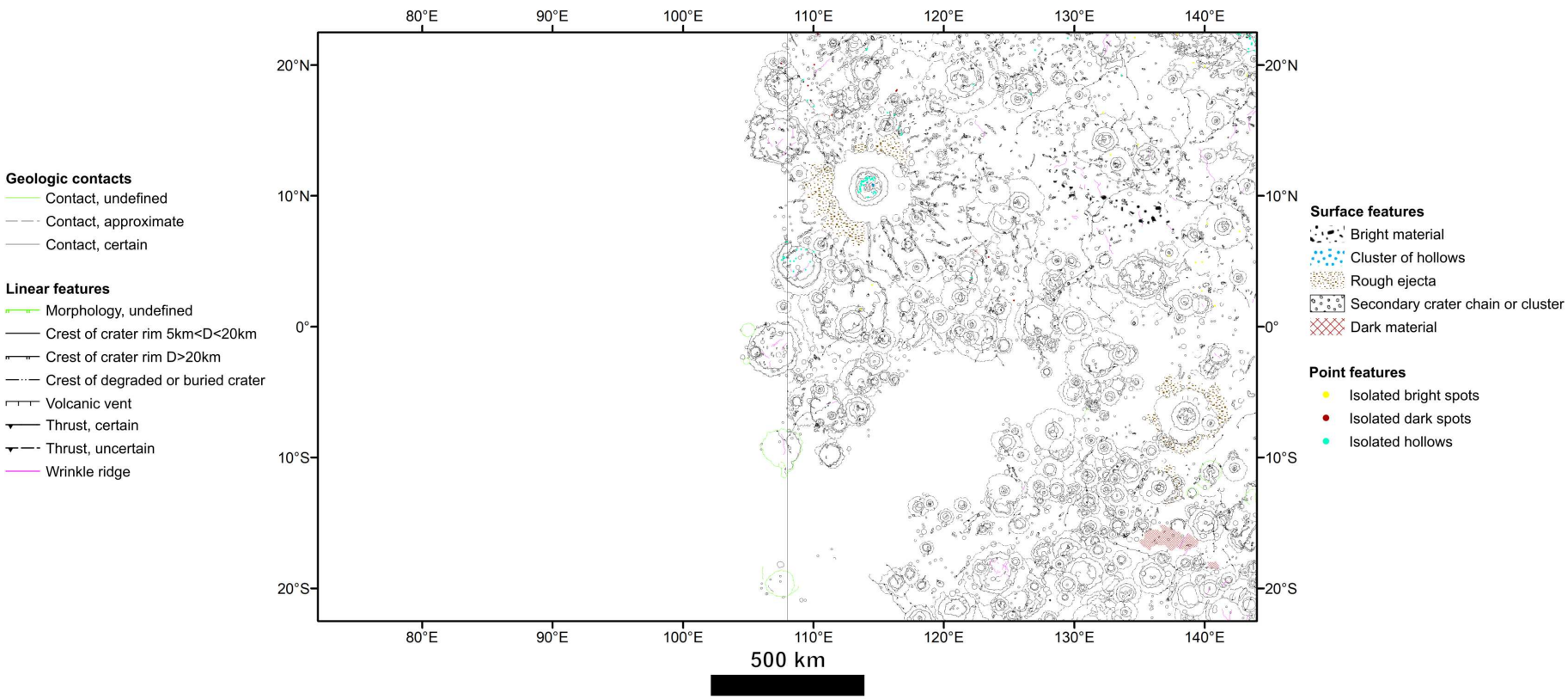

Figure 2.31: The present state of the geologic linework (geologic contacts, linear features, surface features and point features) for the eastern portion of the H-9 Eminescu quadrangle.

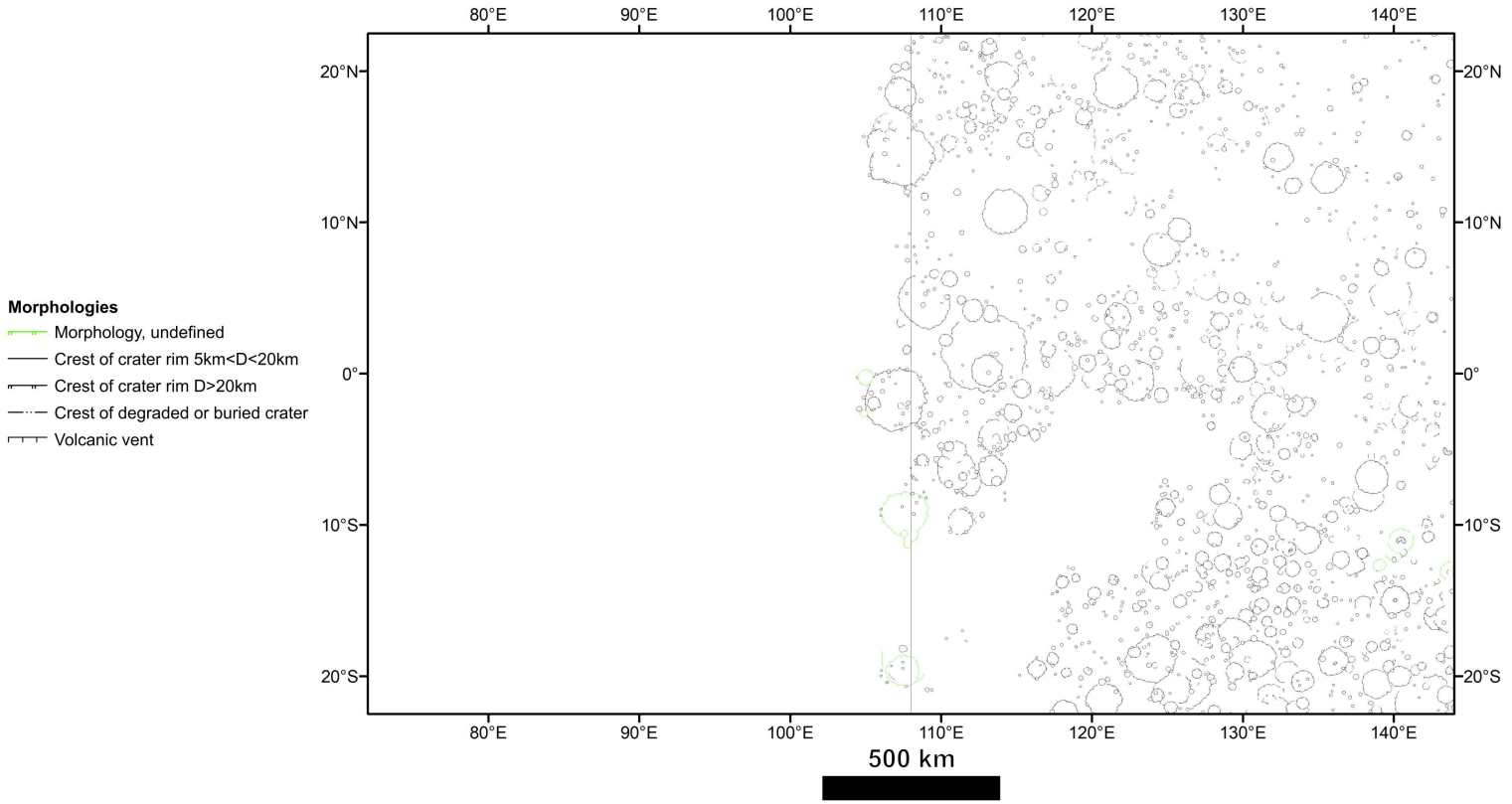

Figure 2.32: Linear features linework for craters.

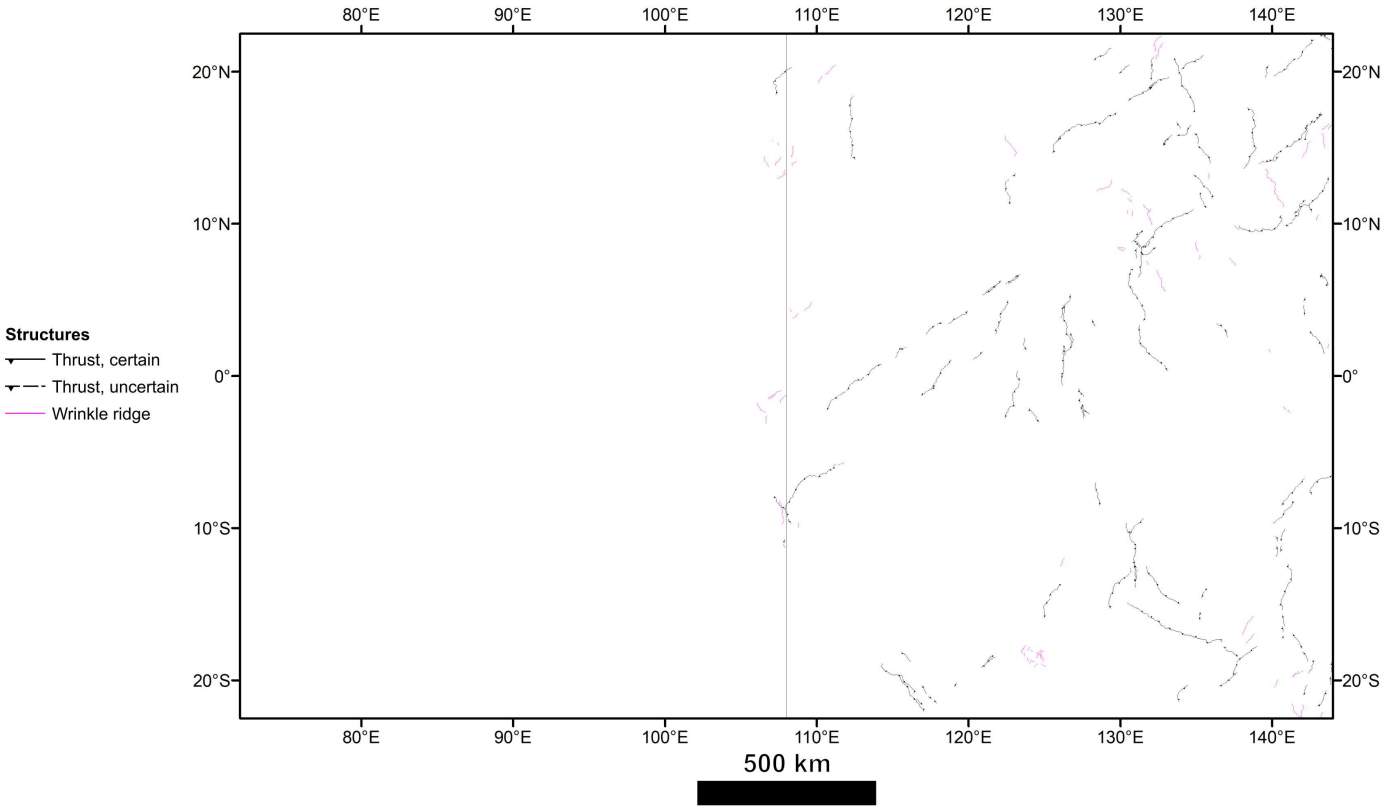

Figure 2.33: Linear features linework for structures.

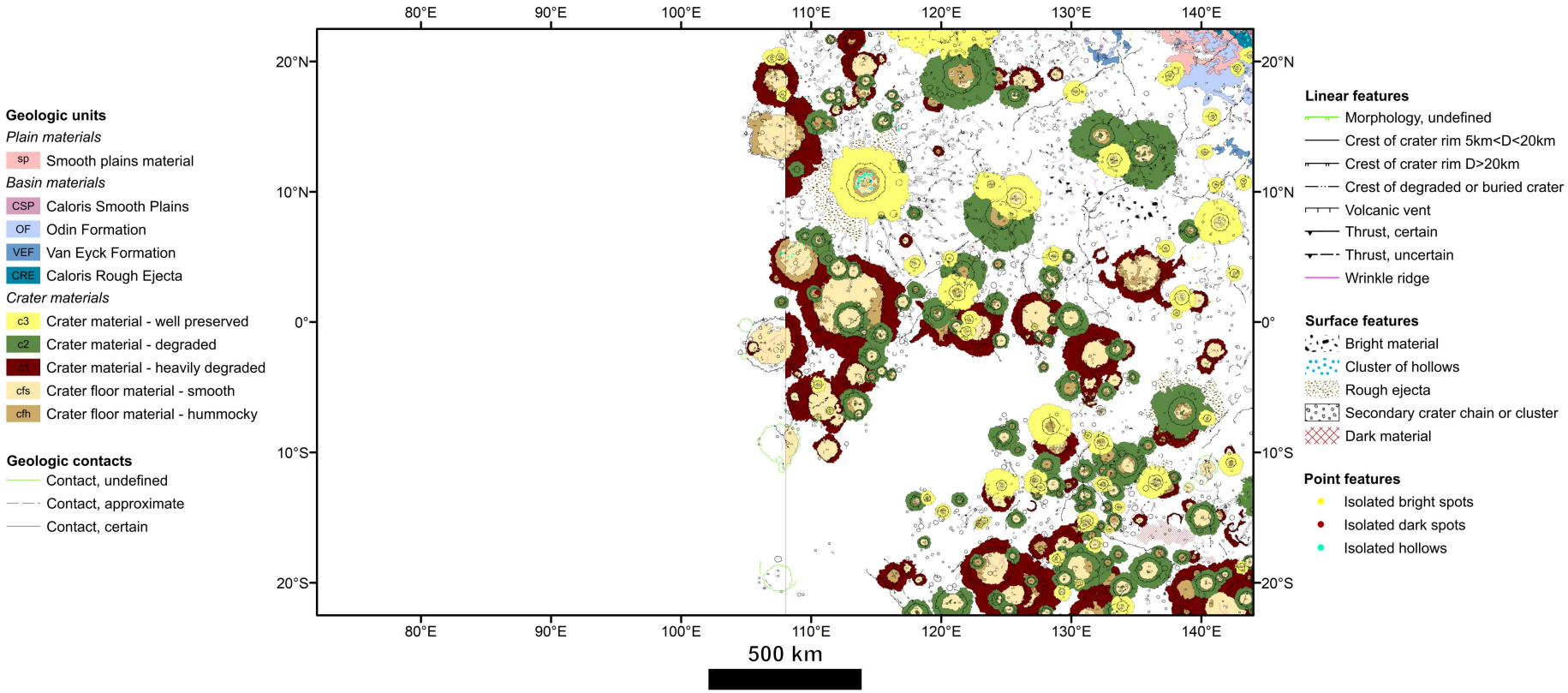

Figure 2.34: The present state of the geologic map of the eastern portion of the H-9 Eminescu quadrangle. Refer to the text for unit descriptions.

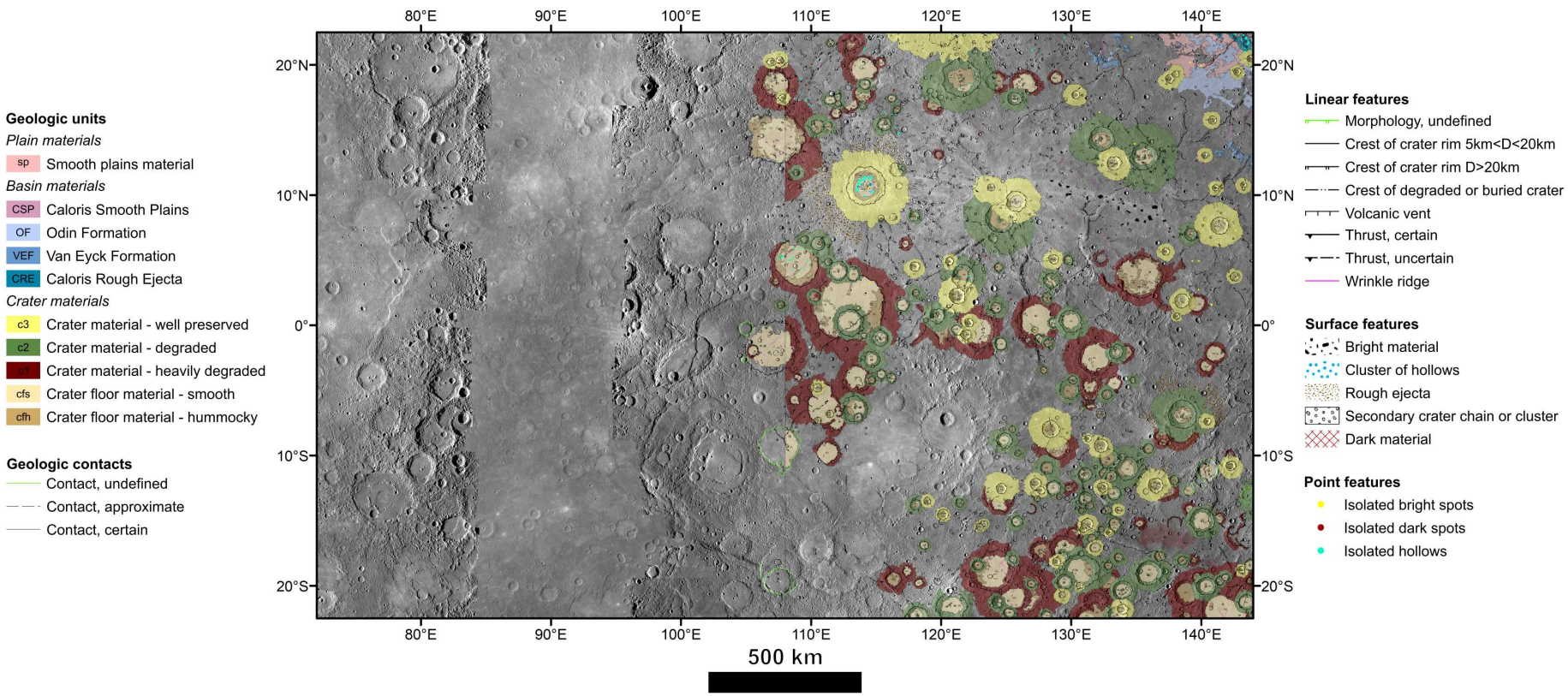

Figure 2.35: The present state of the geologic map of the eastern portion of the H-9 Eminescu quadrangle visualized on top of the MESSENGER MDIS BDR basemap (∼166 m/px) with a 50% of transparency. Refer to the text for unit descriptions.

2.4.2 Color-based spectral map

A color-based spectral map was produced over an area of about 250,000 km^2 located to the south of the Eminescu crater.

The mapping was performed based on the color variations as from the MESSENGER Enhanced Color mosaic and following the contextual approach (see chapter 1.4).

The spectral linework shows the incredible color variation of the hermean surface (Figure 2.36) and, in particular, it is possible to observe:

1. Hues variations of light orange color most probably related to different flooding events inside large impact basins.

2. Exposure from the shallow subsurface of hollow deposits due to secondary impacts $\leq$8 km in diameter impacted on the flooded floor of a basin located to the NW.

3. Excavation of LRMs localized on the western and eastern portions of the ejecta blanket of an 85 km-diameter crater (centered at 0.3°N, 113.0°E) located on the southern margin of a large flooded basin.

4. A central peak morphology located at the right margin characterized by a bright yellow color contrasting with the surrounding crater material indicating the excavation of a subsurface material with distinct composition.

5. Overlaying the great majority of the area is a thin blanket of bright materials radiating from a small young crater located outside of the NE margin of the mapped area.

6. Color differences between distinct terrain units characterized by different degrees of craterization; heavily cratered terrains, in general, present a bluer color with respect to the smoother and yellower ones.

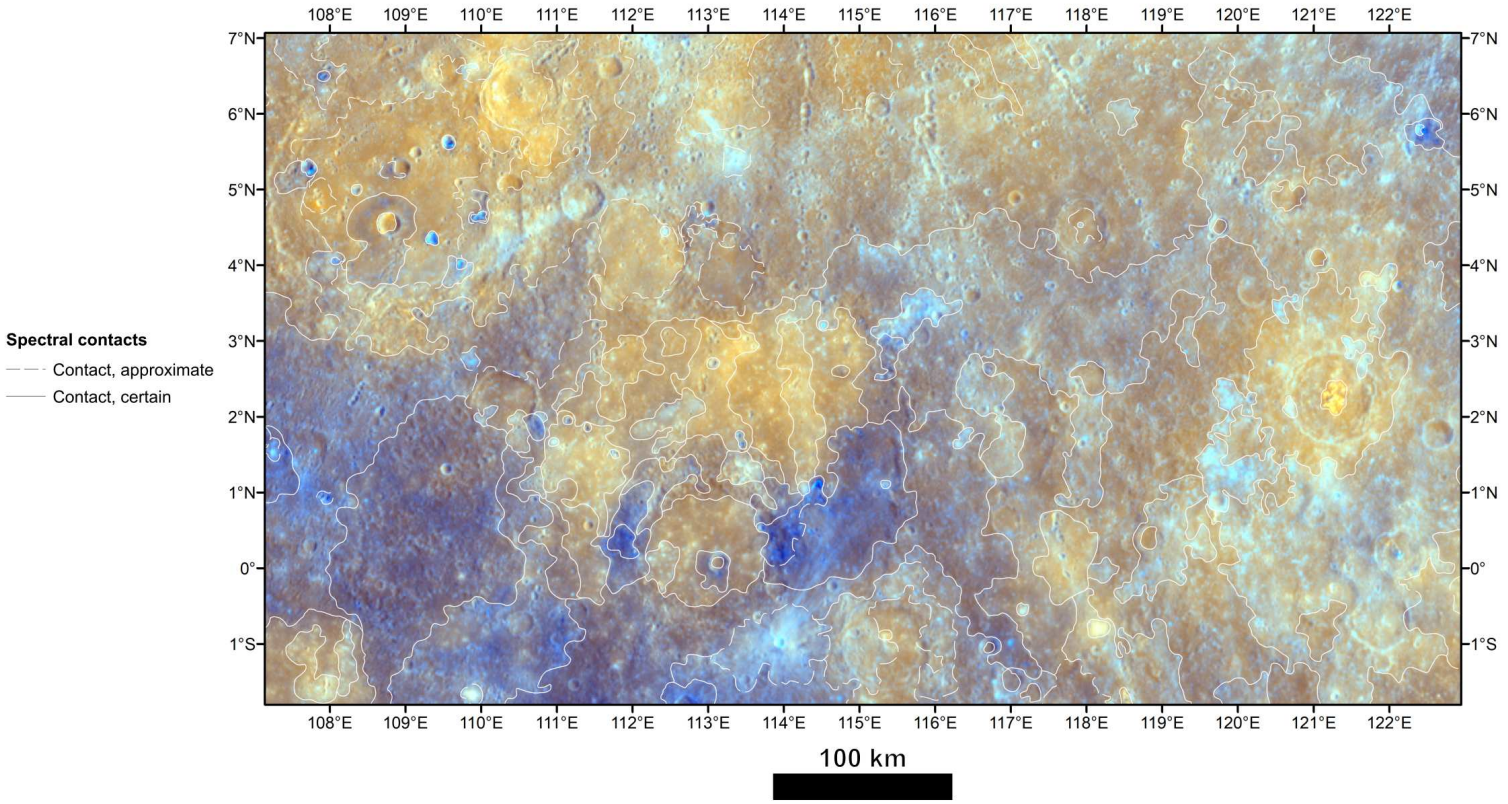

Figure 2.36: Color-based spectral linework mapping produced on an area located to the south of the Eminescu crater.

2.4.3 Target definition for the BepiColombo mission

The production of a geologic map for the Eminescu quadrangle led to a thorough knowledge of the working area that allowed the detection of several possible scientific targets of interest to be investigated by the SIMBIO-SYS cameras (Cremonese et al., 2020) onboard the ESA-JAXA BepiColombo mission to Mercury.

Targets have been classified by category and rank and for each target has been defined the working group of interest (i.e. WG5-interior and tectonics, WG6-composition and surface, WG7-volcanism, WG8-geological mapping and stratigraphy, WG9-surface-exosphere interactions), its coordinates (i.e. center latitude/longitude, minimum/maximum latitude/longitude), the type of target, its rank description, the scientific motivation, the TMX code, the incidence angle, resolution, coverage and necessity of repeated observations respectively for the HRIC, STC and VIHI cameras, and the necessity of observations coupled with other instruments.

In particular, I identified 31 targets of interest, ranging from hollows to volcanic features, from craters to deformational structures and specific terrains.

Table 2.4 provides a simplified list of submitted targets, classified by category, type, rank and rank description, whereas Figure 2.37 shows the location of targets.

Table 2.4: List of scientific targets of interest defined for future investigation by the BepiColombo SIMBIO-SYS instrument. For each target is defined its location (coordinates). Targets are classified by category (craters, hollows, structures, volcanic and other features), type (general description based on the category), rank (ranging from 1-low priority to 5-high priority) and rank description (description of the scientific relevance of the target).

Target	Coordinates	Category	Type	Rank	Rank description
1	10.7°N, 114.2°E	hollows	hollow field	5	hollow field on LRM and isolated hollows in the Eminescu crater
2	8.5°S, 136.1°E	craters	ejecta unit	5	partial orange ejecta on a young crater
3	12.3°S, 136.5°E	craters	central peak	4	crater with DSP (depth sampling peak)
4	9.2°S, 103.3°E	craters	crater units	5	different compositional units on a young crater presenting also an internal landslide
5	16.6°S, 137.9°E	terrains	plain unit	4	LRM area partially delimited by tectonic contacts
6	21.8°N, 143.6°E	volcanic	volcanic vent	5	pyroclastic deposits associated with vent activity and isolated hollows continuing on H-8
7	22.3°N, 137.8°E	other features	dark spot	3	LRM spot on a topographic high
8	14.7°N, 112.0°E	structures	fault	2	LRM exhumed by a fault?
9	11.0°S, 140.5°E	volcanic	irregular depression	5	putative volcanic vent
10	18.4°S, 124.3°E	craters	floor activity	3	putative different flooding events presenting different composition
11	7.8°S, 142.6°E	volcanic	dark deposits	5	putative volcanic vents with dark brown deposits and isolated hollows inside an ancient crater floor
12	9.8°N, 133.1°E	structures	fault	4	lobate scarp interrupted by another lobate scarp system
13	11.6°S, 133.0°E	craters	conic peak	5	putative explosive volcanism on the central peak
14	13.6°N, 133.8°E	craters	central peaks	4	3 craters with DSPs
15	21.4°N, 138.3°E	other features	aligned knobs	2	aligned knobs with peculiar composition related to the formation of the Caloris basin
16	18.9°N, 137.6°E	craters	central peak	3	crater with DSP and collapsing rim
17	2.3°N, 121.2°E	craters	central peak	3	crater with DSP

18	5.2°S, 143.5°E	volcanic	irregular depression	5	putative volcanic vent with dark brown contour and cyan color
19	14.2°S, 133.6°E	craters	landslide	4	young crater with internal collapses and different composition
20	18.2°S, 109.0°E	craters	central peak	3	2 craters with DSPs
21	9.9°S, 116.4°E	craters	central peak	3	crater with DSP
22	5.0°N, 108.7°E	hollows	craters hollow	5	multiple craters presenting hollows inside an ancient crater
23	0.6°N, 113.0°E	craters	ejecta unit	4	LRM ejecta on faulted crater
24	7.2°N, 138.7°E	craters	crater units	3	crater with DSP and LRM spots on the crater rim
25	8.0°N, 131.0°E	structures	fault	4	converging lobate scarp systems
26	3.7°N, 121.9°E	structures	fault	2	faulted crater
27	15.2°N, 133.4°E	structures	fault systems	4	extended faults system with several faulted craters
28	17.7°S, 103.9°E	structures	fault systems	3	parallel faults forming terraces on a crater
29	21.3°S, 124.1°E	craters	impact landslide	2	impact generated landslide
30	12.3°S, 132.2°E	craters	impact landslide	2	impact generated landslide
31	18.9°N, 116.1°E	other features	secondary event	2	ejecta groove related to the Caloris basin

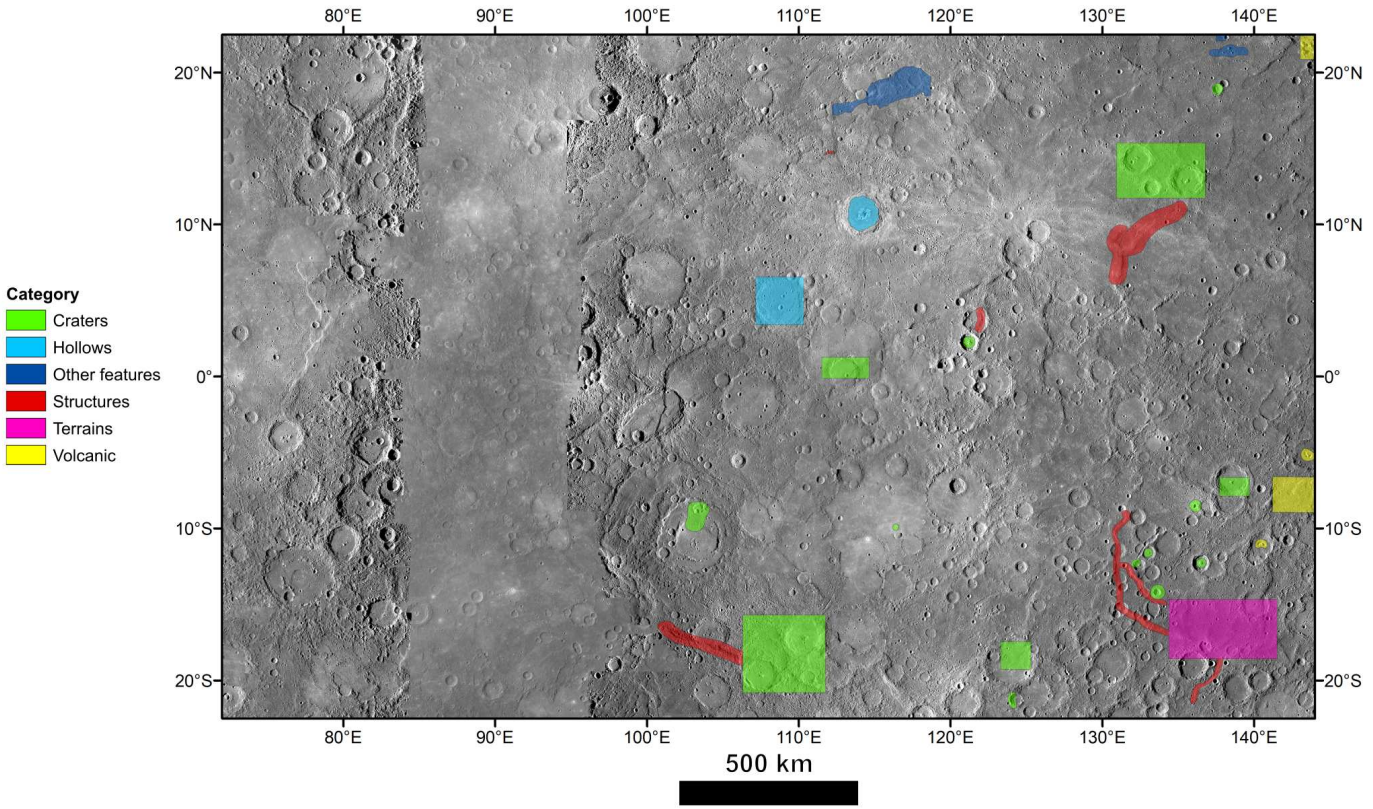

Figure 2.37: Location of targets classified by category visualized on top of the MESSENGER MDIS BDR basemap (∼166 m/px) with a 50% of transparency.

In particular, several targets (i.e. 2, 3, 4, 14, 16, 17, 20, 21, 23 and 24) aim at investigating the compositional variations of the hermean surface through the exposure of underlying materials thanks to impact events. These targets, indeed, present color variations, as from the MESSENGER MDIS Enhanced Color mosaic, on their ejecta deposits and/or central peaks. In the latter case, the term "Depth Sampling Peak" (DSP) was here coined to indicate crater central peaks presenting color variations on the peak itself. The peculiar color variations of the surface, ascribable to compositional variations of the materials, allow inferring more about the inner stratigraphy and mineralogy of Mercury. The complete (e.g. targets 20 and 21, Figure 2.38) or partial (e.g. targets 3, Figure2.38, and 4) exposure of underlying materials presenting a distinct composition suggest the presence of lateral and vertical compositional boundaries between different materials in the subsurface. In target 14 (Figure 2.38), for instance, 3 complex craters present DSPs: of the 3, the smaller and fresher crater in the center presents only a partial exposure of material with a distinct composition on its peak. The investigation of this target by means of the high resolution, VIS-NIR and stereo imaging capabilities of SIMBIO-SYS, coupled with MERTIS, thus, would allow determining the upper boundary and lateral variation of the underlying material and determine its mineralogy with respect to the surrounding materials (Rothery et al., 2020).

Several more, interesting targets are the ones of putative volcanic vents (i.e. targets 9, 11, 18), pyroclastic deposits associated with hollows (i.e. target 6) and the evidence of explosive volcanism (i.e. target 13). Targets 9 (Figure 2.38) and 18, in particular, represent compound vents, located on the floor of craters, presenting a C-shaped form and a faint cyan bordered of brown color, as from the MESSENGER MDIS Enhanced Color mosaic; target 11 (Figure 2.38), instead, includes two smaller putative vents, located inside a heavily degraded basin cut by the Paramour Rupes thrust system, surrounded by brown deposits, as from the MESSENGER MDIS Enhanced Color mosaic, and possibly associated with isolated hollows. Target 6 (Figure 2.38) includes pyroclastic deposits located at the southwest margin of the Caloris basin, near the Abeeso and Agwo faculae, characterized by intense orange color and isolated bright blue spots, as from the MESSENGER MDIS Enhanced Color mosaic, representing isolated hollows. Target 13 (Figure 2.38), finally, represent a steep-sided conic peak possibly associated with explosive volcanism (Thomas et al., 2014b) located in proximity to a putative C-shaped vent presenting no particular color variations. The investigation of these targets by BepiColombo will improve our understanding of the morphology and nature of these landforms and the quantities of volatile

species associated with explosive processes but also their relative age and longevity (Rothery et al., 2020).

One last target to be analyzed in detail is target 1 (Figure 2.38), located on the floor of the Eminescu crater, which includes a hollow field on LRMs surrounding the central peak complex and isolated hollows scattered on the floor. The investigation of this target, for instance, would allow determining the elemental and mineralogical composition, the texture and grainsize of hollows and surrounding materials, identifying the volatile species and the mechanisms leading to the formation of hollows and understanding the close relationship of hollows with LRMs (Rothery et al., 2020). Finally, it would be of interest to look for any detectable surface changes that occurred on hollow deposits since the MESSENGER observations.

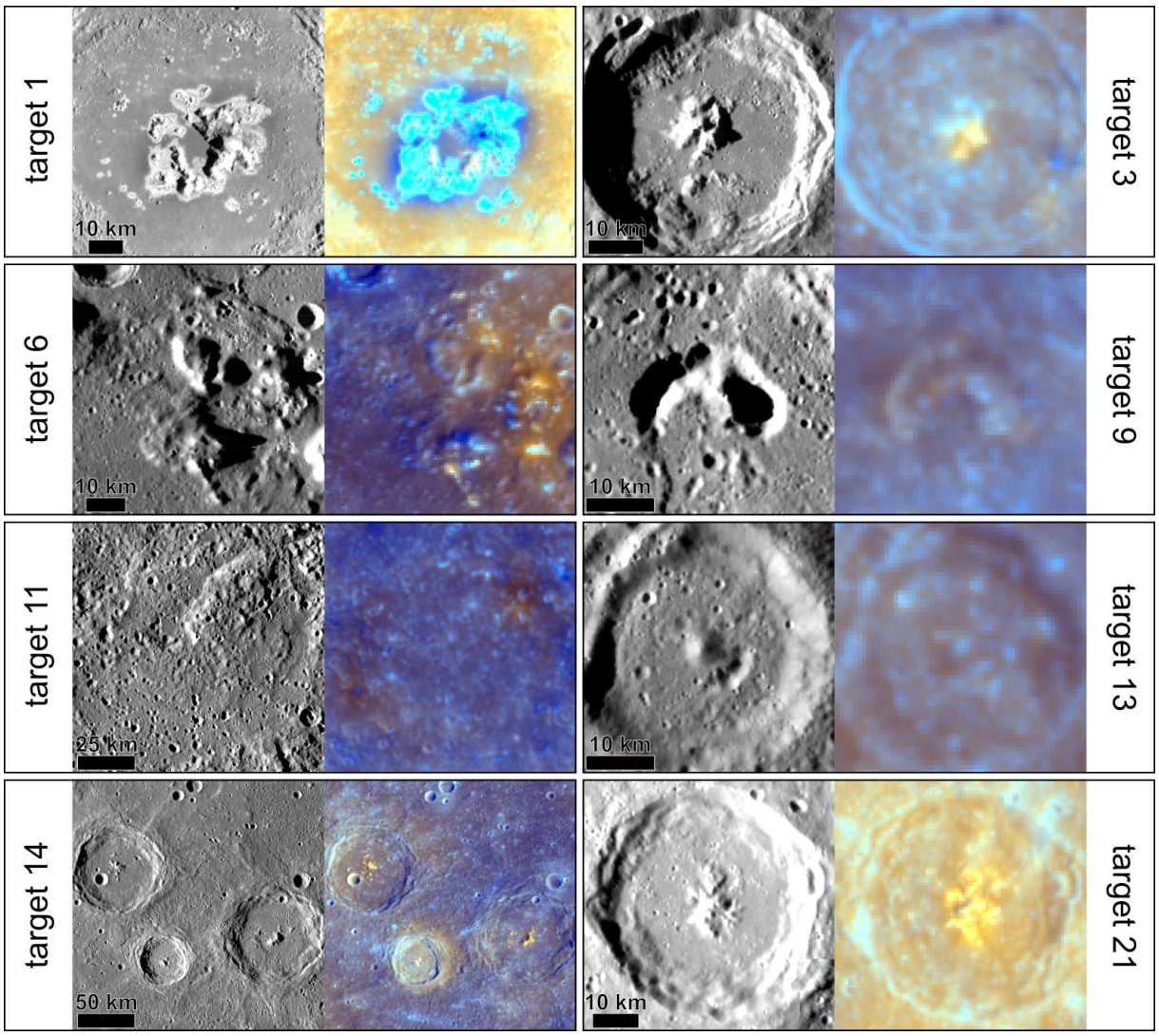

Figure 2.38: Examples of targets as from the MESSENGER MDIS BDR and Enhanced color mosaic basemaps.

2.5 Discussion

The 1:3M geologic map of the H-9 Eminescu quadrangle presented here constitutes the first of its genre for this area, achieving a higher detail of information than the recently produced 1:15M global geologic map (Kinczyk et al., 2019). The current geologic map produced for the eastern portion of the quadrangle (hereafter the reference area) (Figure 2.35) depicts a northeastern margin largely affected by the impact of the Caloris basin. The largest impact on Mercury, indeed, led to a general flattening of the surface characterized by smooth materials, interpreted as exterior volcanic plains, on which are exposed the ridges constituting the *VEF* interspersed by the knobby hummocky deposits of the *OF*. The *CRE* and *CSP* units near the border with the H-8 Tolstoj and the H-4 Raditladi quadrangles, finally, delimit the margin of the Caloris impact basin.

Conversely, the remaining surface, and in particular the southern portion of the quadrangle, is more densely cratered and presents a larger number of *c1* craters, lacking in the proximity of the Caloris basin.

This dichotomy is also highlighted by the crater ejecta distribution. In the northern area, indeed, the ejecta blankets of craters are usually larger than the ones in the southern area which are often superposed and/or superposing to other craters and whose density makes it difficult to trace the ejecta coverage up to long distances.

To the north, moreover, the area is marked by several thrusts aligned radially or concentrically to the Caloris basin and formed by its impact, whereas to the south the deformational structures are mainly aligned in the N-S and NW-SE direction. Wrinkle ridges, which are spread all over the quadrangle and in particular inside basins, finally, show a preferential trend in the NE-SW direction.

By comparing the geologic map with the color-based spectral map (Figure 2.36) it is possible to appreciate the great spectral and compositional variation of the surface which is not noticeable from morphology alone. The light orange color of flooding events, in particular, can be clearly associated with the geologic smooth crater floor units, hollows deposits are definitely identified by bright blue colors, whereas the bright whitish-blue identifies bright material deposits. On the other hand, peculiar color variations such as the dark blue of LRMs on ejecta blankets and the outstanding color of central peaks, connected to the exhumation of underlying materials pre-

senting compositional differences, are not always correlated to distinct morphologies and remain detectable exclusively from color basemaps. This interesting spectral variation should need to be better investigated.

As concerns the definition of scientific targets of interest for the BepiColombo mission, the proposed targets (Table 2.4) aim at shedding light on scientific questions concerning Mercury's origin, evolution and shape (Rothery et al., 2020). The integration of SIMBIO-SYS data with information coming from the MERTIS, BELA, MGNS and MIXS instruments, in particular, will allow to i) determine the abundance and distribution of key elements, minerals and rocks on the hermean crust, ii) determine the presence of distinct geochemical terranes and their correlation with morphology and tectonics, iii) characterize and correlate geomorphological features with compositional variations, iv) investigate on the nature, history, composition and mechanisms of effusive and explosive events, and determine their relative and absolute ages, v) determine the nature of processes related with volatile loss, the mineralogical and elemental composition of volatiles and, in particular, the formation of hollows, their texture and grainsize, their growth rates and association with other materials and/or volcanic deposits, vi) determine the displacement and kinematics of tectonic deformations, the mechanisms responsible for their formation and their age and to vii) verify the occurrence of any detectable change in and around hollows and pyroclastic deposits since MESSENGER observations.
The achievement of these results is made possible by an improved suite of instruments, in relation to the M10 and MESSENGER missions, capable of determining the physical, chemical, mineralogical and topographic properties of Mercury. These instruments will allow the collection of higher spatial and spectral resolution data with a more uniform coverage and the mapping of a larger number of elements, providing thus a more complete and detailed imaging and topographic mapping and elemental and mineralogical mappings. The choice of the proposed targets, to conclude, is thought to be helpful in unraveling some of the abovementioned key questions about the origin and evolution of Mercury.

Chapter 3

Large-scale mapping on the Moon

In the next sections, I am going to give an overview on the Moon, about its physical and geological properties, and on the missions dedicated to its exploration, in particular of the space missions whose data have been used during this work. Sections dedicated to data and methods provide the basics for the morpho-stratigraphic map, color-based spectral map, age determinations, spectro-stratigraphic map and high-resolution map presented in the results section and further analyzed in the discussions. Parts of the analyses presented in this chapter have been published in a peer-reviewed, open access scientific journal (Tognon et al., 2021).

3.1 Introduction

3.1.1 The Moon: life companion

The closest and brightest object in the night sky is the sole natural satellite of the Earth and the only other place where man ever set foot: the Moon.
Orbiting at a distance of ∼384,400 km from the Earth, the Moon moderates and influences the oscillations of the terrestrial axis, granting a rather stable climate, and the formation of tides. Moreover, by rotating on its own axis at about the same rate that it revolves around the Earth, the Moon is in synchronous rotation with the Earth and thus it shows it always the same hemisphere, the so-called "near side" distinguished by the never visible so-called "far side". Due to the Moon's libration, however, up to 60% of the lunar surface is visible from Earth.
In its 27 Earth days journey around the Earth, finally, different parts of the Moon phase from darkness to sunlight depending on the position of the natural satellite with respect to the Sun.

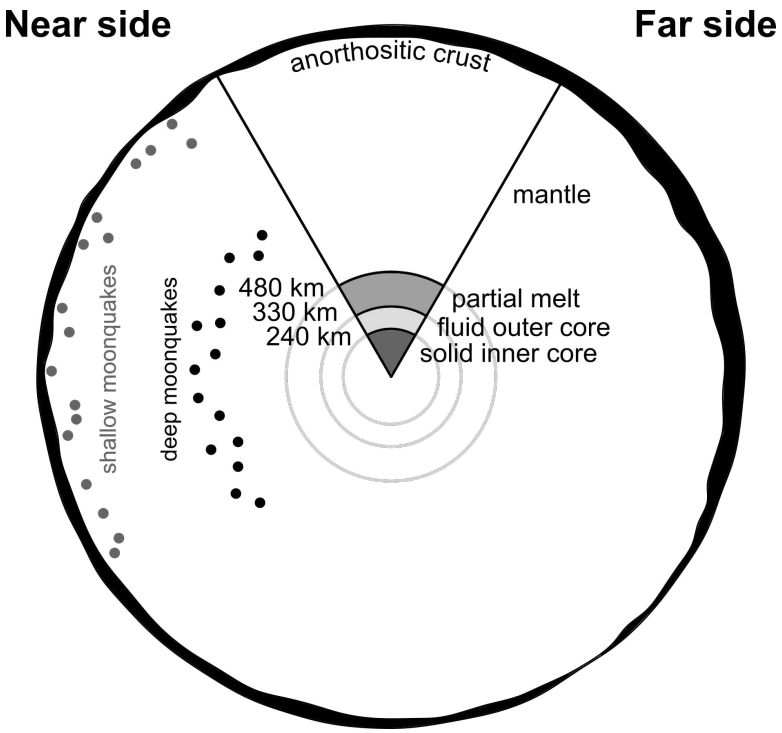

Figure 3.1: Interior structure of the Moon.

With a radius of 1738.0 km (vs 6378.1 km of the Earth), the Moon is a little more than a quarter of the Earth's size and it has a density of 3.3 g/cm^3 (vs 5.5 g/cm^3 of the Earth) that, among the terrestrial bodies, is greater only than that of the asteroid-moons of Mars.
This very low bulk density is due to a lunar iron-rich core relatively small of 330±20 km composed of both a liquid outer core and a solid inner one, the latter of about 220 km of radius (Weber et al., 2011). A 150 km partially molten layer surrounds the core and constitutes the base of the mantle which extends up to the bottom of the crust. The uppermost layer of the Moon is an anorthositic crust with large differences in thickness between the near and far sides. The average crustal thickness is ∼60 km, and it reaches a maximum thickness of 90-100 km on the far side and a minimum of 15-20 km inside the main basins (Wieczorek et al., 2006) (Figure 3.1).

A so-called "megaregolith" layer, generated by the numerous impacts, in particular, characterizes the shallower part of the crust, up to >10 km in-depth (Figure 3.2). From top to bottom, it is possible to recognize a layer of very fine-grained (up to 200 nm) and poorly sorted material constituting the lunar surface regolith, coarse-grained deposits of breccias, glasses and impact melts representing ejecta deposits and a progressively less disturbed and fractured bedrock (Hiesinger and Head, 2006).

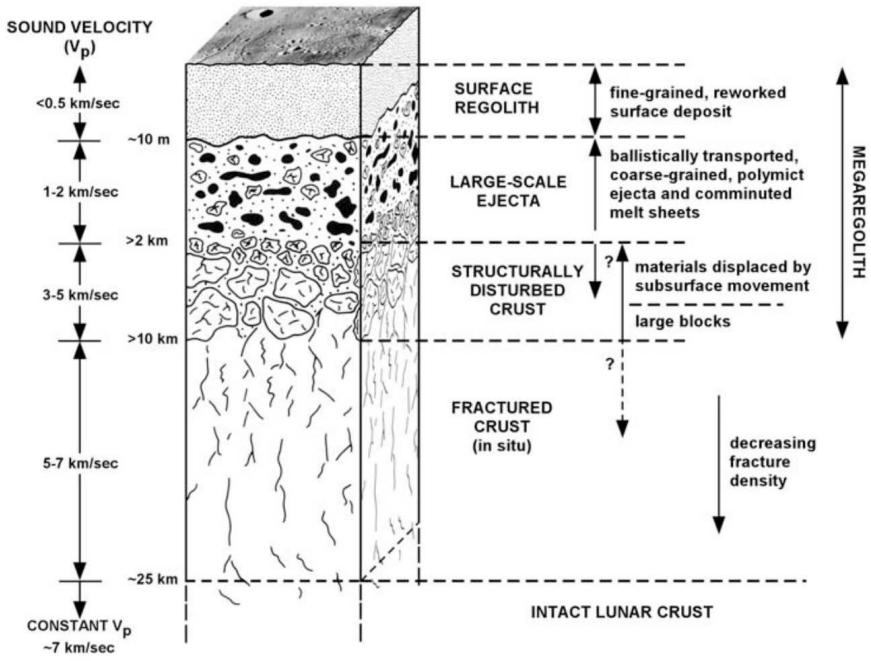

Figure 3.2: Hypothetic cross-section of the upper crust showing the megaregolith layer and the effects of large-scale cratering, as from Hiesinger and Head (2006).

Several hypotheses have been proposed for the formation of the Moon, from the capture by the Earth's gravity of a supposedly primitive and undifferentiated body wandering in the Solar System to the tidal forces-induced fission of the Moon from a rapidly rotating Earth. However, the current leading theory, which can best explain the lunar bulk composition, the paucity of volatiles, the small size of its core and the Earth-Moon high angular momentum is that of a giant impact due to the collision of a differentiated Mars-sized body, named Theia, with the proto-Earth around 4.50 Ga (Hartmann and Davis, 1975; Kipp and Melosh, 1986; Canup, 2004). During the impact, most of Theia's denser material would have been incorporated into the mantle and core of the Earth while part of the Earth's crust and shallower mantle would have been ejected into the terrestrial orbit along with the remaining material from Theia. The ejected material progressively would have re-accreted to form the proto-Moon (Figure 3.3 *left panel*).

Trying to explain the lunar composition and isotopic similarity with the Earth, however, a recently developed model suggests a new origin theory involving the formation of the Moon within a terrestrial synestia (i.e. a continuous mantle-atmosphere-disk structure) provoked by a high-energy and high-angular momentum giant impact (Lock et al., 2018). The Moon would have formed by accretion of moonlets generated by condensates of silicate vapor within the Earth's synestia, inheriting thus its composition. As the synestia cools and contracts, the Moon

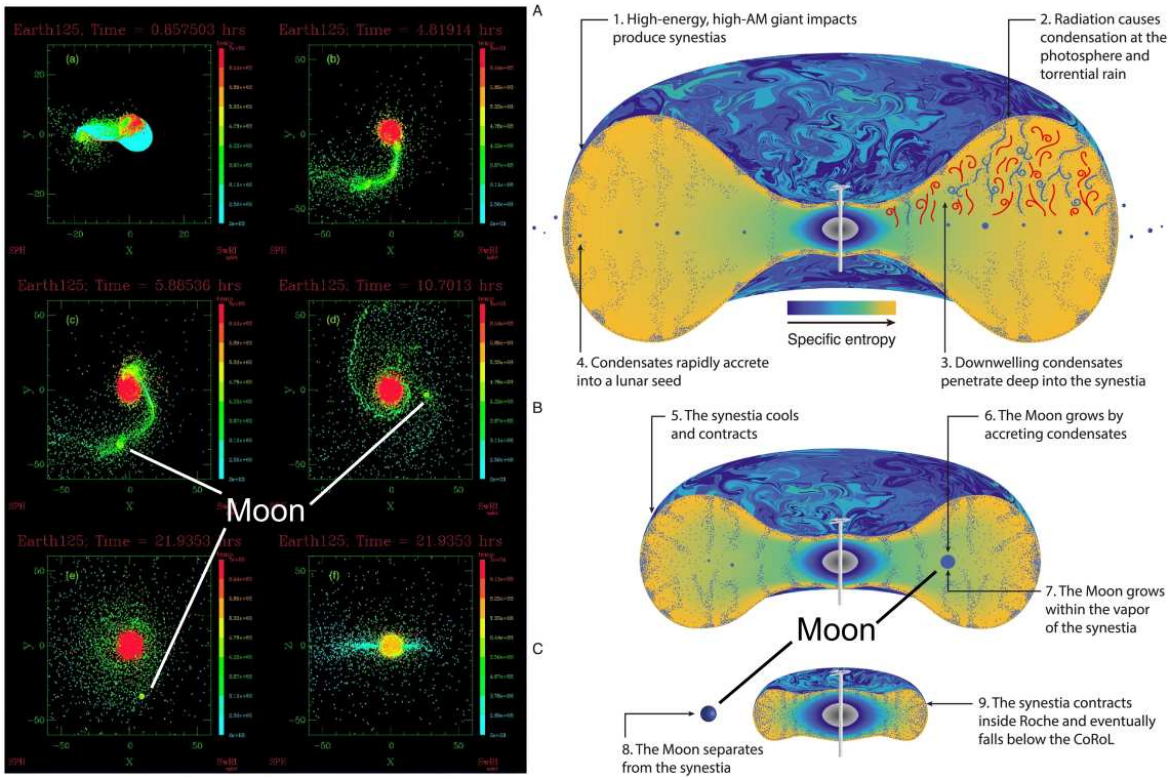

Figure 3.3: *Left panel*: computer simulation of a giant impact for the formation of the Moon, modified from (Canup, 2004). *Right panel*: illustration of the Moon's formation within a terrestrial synestia, modified from (Lock et al., 2018).

would have separated from the system and started to solidify. The synestia would have then contracted inside the Roche limit and cooled down (Figure 3.3 *right panel*).

Similarly to Mercury, the Moon possesses a very thin and tenuous exosphere that has no mitigating effect from meteoritic impacts and surface temperatures range, which reach a maximum of 127°C in the sunlit hemisphere and up to -272°C in the shadowed one.
The Moon, moreover, lacks a substantial magnetic field and thus the lunar surface remains exposed to solar radiations and space weathering. Nevertheless, some regions both on the near (i.e. Rima Sirsalis, Reiner Gamma Formation) and far (i.e. Gerasimovic crater, Mare Ingenii) sides (Hood et al., 2001) and some Apollo rock samples present a residual paleomagnetization indicating that the early Moon was able to generate and maintain a magnetic dynamo that likely ceased between 1.92-0.80 Ga (Mighani et al., 2020).
The crustal magnetic anomalies are usually correlated with high albedo twisting morphologies called "swirls" (Figure 3.4). They are thought to be possibly originated from local magnetic anomalies shielding the surface from space weathering (Hood et al., 2001), or recent surface

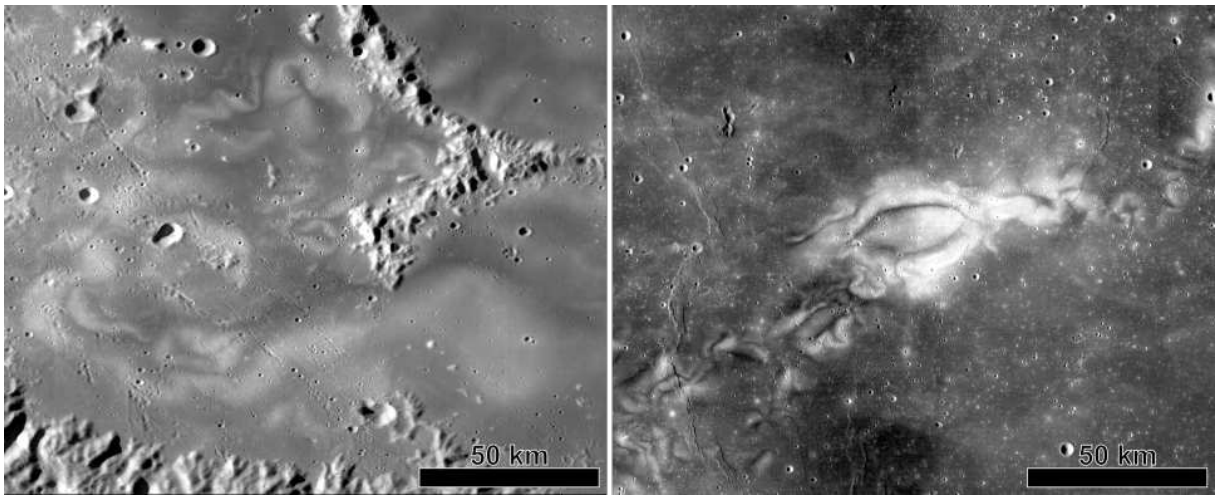

Figure 3.4: Lunar swirls associated with magnetic anomalies. *Left panel*: LROC-WAC view of the swirls inside Mare Ingenii (centered at 35.0°S, 163.3°E). *Right panel*: LROC-WAC view of the magnetic anomaly of Reiner Gamma Formation (centered at 7.4°N, 300.9°E).

disturbances caused by the fall of cometary fragments (Pinet et al., 2000) or, finally, from electromagnetic fields leading to the selective accumulation of high-reflectance regolith (Garrick-Bethell et al., 2011).

3.1.2 A short history of lunar exploration

At the end of the 1950s, the United States and the Soviet Union were struggling for being the first to orbit the Earth and, more importantly, the Moon.
The Soviets were the first to orbit the Moon, taking the first images of the lunar far side, and to land on its surface but the most striking success was achieved by the Americans with the landing of the first manned mission.
From those first achievements many more orbiters and landers, both robotic and manned, explored the Moon, making it the most explored planetary body.

The American Clementine spacecraft (Figure 3.5) was launched on 25 January 1994 from the Vandeberg Air Force Base (California, USA). After two flybys of the Earth, it entered orbit around the Moon on 19 February 1994.

The 5 different imaging systems onboard the Clementine mission (Table 3.1) were able to provide global coverage of the Moon in a range of wavelengths from ultraviolet to infrared by

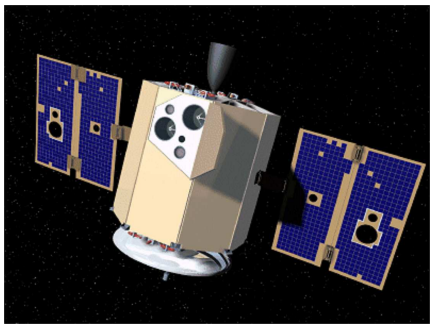

Figure 3.5: Artistic impression of the Clementine spacecraft (courtesy of NASA).

collecting about 1,800,000 images at a resolution of 80-330 m/px (McEwen and Robinson, 1997). The wide-angle UVVIS camera, in particular, had a filter wheel equipped with 6 different filters from 415 nm to 1000 nm, including a 400-950 nm broad-band filter.

Before running out of propellant and ending its mission, remarkably, the spacecraft was able to detect the presence of ice in a permanently shadowed crater at the lunar south pole and a rocky region on the rim of the north polar Peary crater (88.5°N, 30.0°E) possibly perpetually illuminated, renamed "peaks of eternal light".

Table 3.1: Scientific instruments onboard the Clementine spacecraft (Nozette et al., 1994).

Instrument	Investigation
Bistatic Radar Experiment	Characterization of the lunar polar regions and detection of ice deposits in permanently shadowed craters
Charged Particle Telescope (CPT)	Characterization of the solar and magnetospheric energetic-particles environment
S-band Transponder Doppler Gravity Experiment	Measurement of the lunar gravity field
HIgh-RESolution camera (HIRES)	Providing monochrome and color high-resolution images
Laser Image Detection And Ranging (LIDAR)	Characterization of the surface morphology and topography
Long-Wave InfraRed camera (LWIR)	Providing spectral images for determining the thermal properties of materials
Near-InfraRed camera (NIR)	Providing spectral images for characterizing the petrologic properties of the surface material
Star Tracker Cameras	Providing images of the background stars for attitude determination and control
UltraViolet-VISible camera (UVVIS)	Providing spectral images for characterizing the petrologic properties of the surface materials

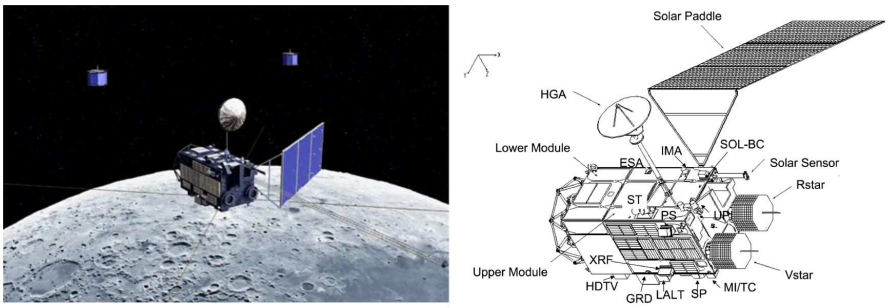

Figure 3.6: *Left panel*: an artistic impression of the Kaguya spacecraft with Okina and Ouna in orbit around the Moon (courtesy of JAXA). *Right panel*: labelled diagram of the Kaguya spacecraft, as from Kato et al. (2008).

The Kaguya dual spacecraft (Figure 3.6), also known as SELenological and ENgineering Explorer (SELENE), was the second mission launched by JAXA (Kato et al., 2008). One month after its launch on 14 September 2007 from the Tanegashima Space Center (Japan), the spacecraft entered the Moon's orbit and released its 2 small orbiters, Okina and Ouna. Onboard the Kaguya, in total, there were as many as 15 instruments dedicated to scientific investigations (Table 3.2).

In particular, the Lunar Imager-SpectroMeter (LISM), consisting of 3 sub-instruments, namely the Terrain Camera (TC), Multi-band Imager (MI) and Spectral Profiler (SP), provided the first global high-resolution imagery and spectroscopic data for the Moon.

Of the 3 instruments, the TC (Haruyama et al., 2008) provided stereo images of the lunar surface with a resolution up to 10 m/px that allowed the reconstruction of accurate Digital Terrain Models (DTMs) for studying the lunar geology and topography.

The mission ended on 10 June 2009 with the programmed impact of Kaguya to the southeast of the Gill crater (63.9°S, 75.9°E).

India started its exploration of the Moon with the Chandrayaan-1 mission (Goswami and Annadurai, 2008). The spacecraft (Figure 3.7) was launched on 22 October 2008 from the Satish Dhawan Space Centre (India). Together with the Chandrayaan-1 orbiter was the Chandrayaan's Moon Impact Probe (MIP), a module designed to impact the lunar surface near the lunar south pole.

Among its 13 instruments (3 of which mounted on the MIP) (Table 3.3), was NASA's Moon Mineralogy Mapper (M3).

The M3 provided both global and targeted high spectral resolution data for the lunar surface allowing a detailed mineralogical characterization (Pieters et al., 2009a). Global data, specif-

Table 3.2: Scientific instruments onboard the Kaguya spacecraft (Kato et al., 2008).

Instrument	Investigation
Charged Particle Spectrometer (CPS)	Measurement of the solar and galactic cosmic rays
Differential VLBI Radio source experiment (VRAD)	Measurement of the lunar gravity field
Four-way Doppler measurements by Relay Satellite And main orbiter Transponder (RSAT)	Measurement of the lunar gravity field in the lunar far side
Gamma-Ray Spectrometer (GRS)	Detection of γ-rays emissions to measure the global distribution of the major elements
High-Definition TeleVision (HDTV)	Providing monochrome and color images from slant view
Laser ALTimeter (LALT)	Characterization of the lunar topography
Lunar MAGnetometer (LMAG)	Detection of magnetic anomalies and measurement of the lunar magnetic field
Lunar Radar Sounder (LRS)	Detection of the surface and subsurface structures using active sounding
Multi-band Imager (MI)	Characterization of the lunar surface mineralogical composition
Plasma energy Angle and Composition Experiment (PACE)	Measurement of the energy and composition of charged particles in the lunar plasma environment
Radio Science experiment (RS)	Detection of the lunar ionosphere
Spectral Profiler (SP)	Determination of the spectral properties of the lunar surface
Terrain Camera (TC)	Providing high-resolution monochrome images and topographic information of the lunar surface
Upper-atmosphere and Plasma Imager (UPI)	Measurement of the Earth's plasmasphere and observation of ionospheric disturbances
X-Ray Spectrometer (XRS)	Detection of X-ray emissions to measure the global distribution of elements

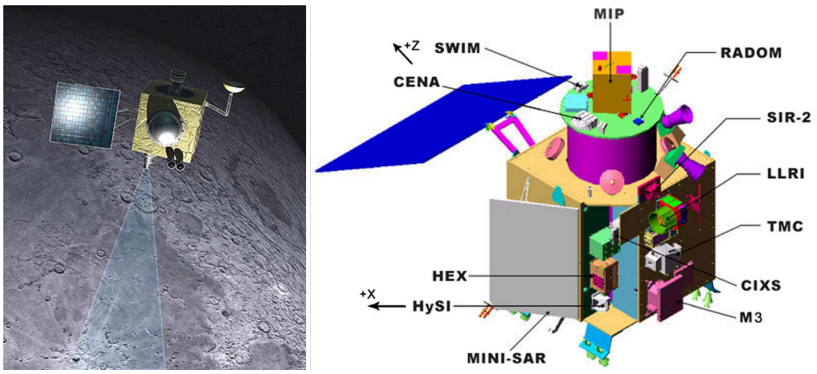

Figure 3.7: *Left panel*: an artistic impression of the Chandrayaan-1 spacecraft in orbit around the Moon (courtesy of ISRO). *Right panel*: labelled diagram of the Chandrayaan-1 spacecraft, as from Bhandari and Srivastava (2014).

ically, were acquired at a spatial resolution of about 140 m/px using 86 of the available 260 spectral channels (from 420 to 3000 nm). The global mineralogical characterization of the lunar surface, overall, evidenced absorption features associated with OH/H_2O-bearing molecules on the Moon's polar regions (Pieters et al., 2009b).

The last contact with the Chandrayaan-1 spacecraft was on 29 August 2009 probably due to the failure of the power supply caused by the overheating of the satellite.

Table 3.3: Scientific instruments onboard the Chandrayaan-1 spacecraft (Goswami and Annadurai, 2008).

Instrument	Investigation
Chandrayaan-1	
Chandrayaan-1 X-ray Spectrometer (CIXS)	Detection of X-ray emissions to measure the relative abundances of various elements
High Energy X-ray spectrometer (HEX)	Measurement of the transportation of volatiles
Hyper Spectral Imager (HySI)	Characterization of the lunar surface's mineralogy
Lunar Laser Ranging Instrument (LLRI)	Characterization of the lunar topography
Miniature Synthetic Aperture Radar (Mini SAR)	Detection through radar-scanning of water ice in permanently shadowed craters
Moon Mineralogy Mapper (M3)	Determination of the spectral properties of the lunar surface
Near InfraRed Spectrometer (SIR-2)	Determination of the spectral properties of the lunar surface
RAdiation DOse Monitor (RADOM)	Measurement of the particle flux and radiation hazards
Sub kev Atom Reflecting Analyzer (SARA)	Detection of low energy neutral atoms to measure the lunar surface composition
Terrain Mapping Camera (TMC)	Providing monochrome images and topographic information of the lunar surface
Moon Impact Probe	
CHandra's Altitudinal Composition Explorer (CHASE)	Detection of trace gases in the lunar exosphere
Radar Altimeter	Characterization of the lunar topography
Video Imaging System	Providing monochrome images for attitude determination and control

In the new millennium, the first NASA's mission to the Moon was the Lunar Reconnaissance Orbiter (LRO) (Figure 3.8) launched on 18 June 2009 from Cape Canaveral (Florida, USA). LRO's main goal, lately successfully achieved, was obtaining a high-resolution near-topographical map of the lunar surface.

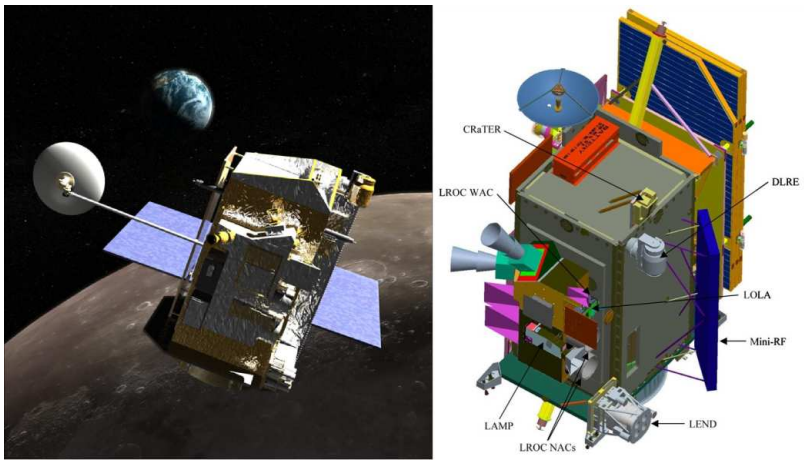

Figure 3.8: *Left panel*: an artistic impression of the LRO spacecraft in orbit around the Moon (courtesy of NASA). *Right panel*: labelled diagram of the LRO spacecraft (courtesy of NASA)

Onboard the spacecraft (Table 3.4), indeed, were the Lunar Reconnaissance Orbiter Camera (LROC) (Robinson et al., 2010), consisting of a 7-filters UV-VIS (320-690 nm) multispectral and monochrome WAC and 2 monochrome NACs, capable of taking images with a resolution up to 100 m/px and 0.5 m/px for the WAC and NACs, respectively. The Lunar Orbiter Laser Altimeter (LOLA) (Smith et al., 2010), instead, provided accurate measurements of the Moon's surface providing information on the surface's roughness, slopes and elevation variations. Nowadays, the LRO spacecraft, even if not fully functional, is still orbiting the Moon.

Table 3.4: Scientific instruments onboard the LRO spacecraft (Tooley et al., 2010).

Instrument	Investigation
Cosmic Ray Telescope for the Effects of Radiation (CRaTER)	Characterization of the lunar radiation environment
Diviner Lunar Radiometer Experiment (DLRE)	Measurement of surface and subsurface temperatures for detecting potential ice deposits
Lunar Exploration Neutron Detector (LEND)	Detection of neutrons in the lunar radiation environment and characterization of the hydrogen distribution
Lunar Orbiter Laser Altimeter (LOLA)	Characterization of the lunar topography
Lunar Reconnaissance Orbiter Camera (LROC)	Providing monochrome imagery of the surface with different fields of view
Lyman-Alpha Mapping Project (LAMP)	Providing images of permanently shadowed craters showing the Lyman-Alpha line and detection of surface ice
Miniature Radio Frequency radar (Mini-RF)	Detection of water ice in the polar regions and communication with an Earth-based ground station

3.1.3 Geology of the Moon

As previously described, the surface of the Moon is completely exposed to cratering and space weathering due to the absence of an atmosphere and magnetosphere. Impact cratering, volcanism and tectonics represent one again, thus, the main geological processes on this planetary surface.

As for Mercury, large basins and ejecta blankets have been used to define a relative stratigraphy for the lunar surface, successively integrated by radiometric dating of returned lunar samples that allowed to ascribe absolute ages. The Moon's chrono-stratigraphy has been divided into 5 time periods: pre-Nectarian (oldest), Nectarian, Imbrian, Eratosthenian and Copernican (youngest) (Figure 3.9).

The pre-Nectarian period encompasses basins and crustal rocks older than ∼4.10-3.92 Ga (Wilhelms, 1987; Neukum and Ivanov, 1994; Stoffler and Ryder, 2001). The Nectarian period is defined by the formation of the Nectaris basin and it ends at ∼3.92-3.85 Ga (Wilhelms, 1987; Neukum and Ivanov, 1994; Stoffler and Ryder, 2001), which is the base for the Imbrian period, defined by the formation of the Imbrium basin. The Imbrian is further divided into the Early (older) and Late (younger) Imbrian by the formation of the Orientale basin around 3.75 Ga (Stoffler and Ryder, 2001). Finally, the Eratosthenian and Copernican periods, constrained by the formation of the Eratosthenes and Copernicus craters, begin at ∼3.20 Ga and ∼1.00-0.80 Ga respectively (Wilhelms, 1987; Neukum and Ivanov, 1994; Stoffler and Ryder, 2001).

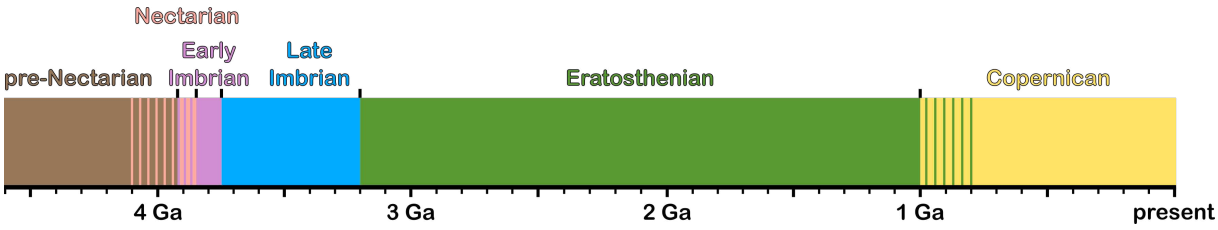

Figure 3.9: The Moon's time-stratigraphic periods.

On the lunar surface, it is possible to identify 2 main terrains: the feldspathic highlands (or terrae) and the basaltic lowlands (or maria).

The highlands constitute ∼83% of the lunar surface and thus represent the predominant terrain on the Moon (Abbud-Madrid, 2018). They present a high albedo and a high density of craters that led to a very rough topography. The highland material consists of the original primordial

crust and it is mainly composed of anorthosites, containing over 90% of plagioclase feldspar with a minor amount of mafic components. The highland rocks, overall, can be subdivided into 3 geochemical suites (e.g. Wieczorek et al. (2006)): Fe-anorthosites, Mg-suite and alkali-suite. Fe-anorthosites, representing the oldest rocks, are mainly composed of Ca-plagioclase (anorthites) with an iron mafic component. The Mg-suite consists of rocks with high Mg/Fe values of mafic minerals (norites, troctolites and ultra-mafic rocks). The alkali-suite, finally, represents rocks enriched in Na and K contents (gabbronorite, monzodiorite, monzogabbro). Additionally, some basalts presenting high concentrations of potassium (K), rare earth elements (REE) and phosphorus (P), named KREEP, seem to be originated by late fractional crystallization of the Mg-suite. KREEP basalts are concentrated in the Oceanus Procellarum and Mare Imbrium forming the Procellarum KREEP Terrane (Jolliff et al., 2000).
The lowlands, instead, constitute the remaining lunar surface (∼17%) and are almost entirely localized on the near side. Maria represent extensive lava flows, originated by partial melting of the mantle, filling large impact basins (Abbud-Madrid, 2018). Contrary to the highlands, they present very smooth surfaces and are characterized by a low albedo due to the presence of basaltic rocks, mainly composed of olivine and pyroxenes with minor amounts of ilmenite and spinel oxides. Lunar basalts are usually distinguished based on their amount of TiO_2 in very low-Ti basalts (<1.5 wt% TiO_2), low-Ti basalts (1.5-6.0 wt% TiO_2) and high-Ti basalts (>9 wt% TiO_2).

The Moon presents a high density of craters which can range from micrometers up to the ∼2500 km in diameter of the South Pole Aitken basin, the largest impact structure on the Moon and in the Solar System (Hiesinger and Head, 2006). Craters and their related ejecta deposits, thus, constitute the main morphology of the lunar surface, more so in the far side highlands.

The near side maria, instead, present the highest concentration of volcanic landforms. Volcanic features include basaltic lava flows, sinuous rilles, pits, pyroclastic deposits and volcanic cones and domes.
The high temperatures and the low viscosities of basaltic lavas as well as the higher effusion rates typical of low gravity bodies (e.g. Wilson and Head (2017)) and the potential inflation processes allow lavas to flow for very long distances across the lunar surface (Figure 3.10 *top left panel*), reaching up hundreds to thousands of kilometers in length and tens of meters in thickness (e.g.

Hiesinger and Head (2006)). Lava flows, caused by the outpouring of basaltic magmas through dykes, are generated by the partial melting of the lunar mantle and the upwelling of magmas due to the removal of crustal materials both caused by basin-forming impacts.

Sinuous rilles, in particular, are generated by the channeling of lava flows caused by thermal and mechanical erosion of the substrate (e.g Bussey et al. (1997); Hurwitz et al. (2012)). They are meandering channels characterized by an irregular rounded depression at their starting point and a fading downslope ending (Greeley, 1971; Hiesinger and Head, 2006) (Figure 3.10 *top right panel*). They range from a few kilometers to ∼300 km in length and from tens of meters to ∼3 km in width (e.g. Schubert et al. (1970); Hurwitz et al. (2012)).

Over 250 pits across the Moon allow to shed light on what lies below the surface. Lunar pits range from 5 to 900 m in diameter and expose up to 100 m of terrain in depth (Figure 3.10 *central left panel*). Their origin is still unclear but the most accreditable hypotheses suggest that they could originate from collapses of lava tubes' roofs caused by impacts, gravity, moonquakes, the withdrawal of lavas from the tube itself, tidal forces or the additional weight of yourger lava emplacements (Haruyama et al., 2009; Martellato et al., 2013), or from the fracturing of cooling impact melt ponds due to the rebound of the crust (Wagner and Robinson, 2021).

Explosive volcanism caused by the buildup of volatiles (e.g. CO_2) in the upper portion of the magmatic chamber can result in pyroclastic eruptions, mainly occurring at the margins of impact basins and usually associated with vents and sinuous rilles. These eruptions lead to the deposition of a halo of dark-mantle deposits which can spread up to >1000 km depending on the magma's volatile content, viscosity and composition and on the geometric shape of the vent, the lunar gravity and lithostatic pressure gradient (Wilson and Head, 1981; Hiesinger and Head, 2006) (Figure 3.10 *central right panel*).

Cones, or cinder cones, represent explosive volcanism usually associated with sinuous rilles, fractures and vents (Platz et al., 2014). They are low-albedo landforms measuring less than 100 m in height and 2-3 km in diameter and presenting craters of less than 1 km in diameter on their summit (Guest and Murray, 1976) (Figure 3.10 *bottom left panel*).

Lunar domes, finally, can be distinguished, based on their flank slopes, in mare domes and non-mare domes (Hawke et al., 2003; Hiesinger and Head, 2006). The first are similar to small terrestrial shield volcanoes up to tens of kilometers in diameter and a hundreds of meters in height and thus presenting very flat slopes (<10°). Non-mare domes, instead, can reach up to tens of kilometers in diameter and more than a thousand meters in height and are characterized

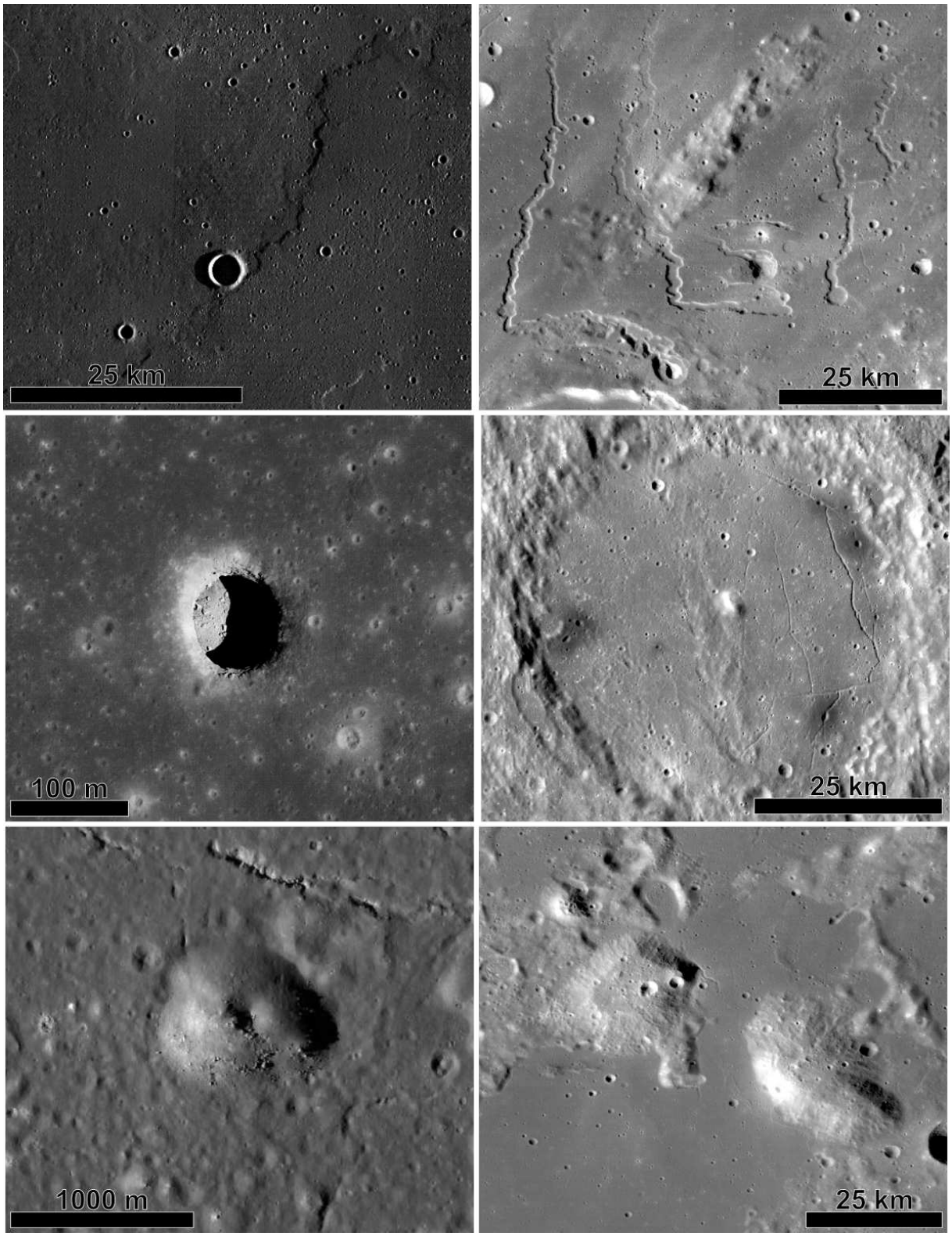

Figure 3.10: Volcanic landforms on the Moon. *Top left panel*: LROC-WAC view of a lava flow on Mare Imbrium (centered at 31.2°N, 23.6°W). *Top right panel*: LROC-WAC view of sinuous rilles at Rimae Prinz (centered at 41.2°N, 43.5°W). *Central left panel*: LROC-NAC view of a lunar pit in Mare Tranquillitatis (centered at 8.3°N, 33.2°E). *Central right panel*: LROC-WAC view of 13 vents on the floor of the Alphonsus crater (centered at 13.4°S, 2.8°W). *Bottom left panel*: LROC-NAC view of a cinder cone on the floor of the Copernicus crater (centered at 10.3°N, 19.9°W). *Bottom right panel*: LROC-WAC view of the non-mare Gruithuisen Domes (centered at 36.4°N, 40.2°W).

by steeper slopes (>20°) and strong absorption in the UV. The difference in slope is due to the viscosity of lavas so that low-viscosity basaltic lavas lead to the formation of the almost flat morphologies of mare domes, while eruptions and extrusions of more viscous silica-rich lavas lead to the formation of non-mare domes (Figure 3.10 *bottom right panel*).

Similarly to Mercury, the lunar tectonic landforms consist of both extensional and compressional tectonic features, such as grabens, wrinkle ridges and lobate scarps, caused by impact-induced stresses and stresses induced by thermal effects (i.e. expansion and contraction), the load of basaltic flows within impact basins and tidal forces (e.g. Melosh (1975); Solomon and Chaiken (1976); Schultz and Zuber (1994); Hiesinger and Head (2006)).
Impacts and the loading of the crust with basaltic infillings can induce the formation of concentric and/or radial extensional grabens propagating outward from the basin (Wilhelms, 1987; Ahrens and Rubin, 1993). Grabens can reach hundreds of kilometers in length.
Lunar wrinkle ridges are very common in mare regions. They can reach up to 10 km in width and hundreds of kilometers in length and have a vertical offset up to a hundred meters (Wilhelms, 1987). Wrinkle ridges are interpreted as thrust faults formed by compressional stresses inside flooded basins and imply localized crustal shortening cause by interior cooling (Watters and Johnson, 2010; Byrne et al., 2014b).

Conversely, the lunar highlands are commonly characterized by lobate scarps, compressive asymmetric landforms with rounded fault surfaces consisting of a series of structures connected to form complexes reaching up to 10 km in length and a hundred meters in height (Watters et al., 2009; Banks et al., 2012; Platz et al., 2014).

As concerns the seismic activity, the deployment of seismic stations on the Moon during the Apollo missions allowed to detect in an 8-year time period more than 12,000 events, named moonquakes. Moonquakes are divided based on their source region in shallow (at depth of 50-200 km) and deep (at depths of 700-1100 km) moonquakes, with the latters occurring in monthly intervals suggesting a correlation between moonquakes and tidal effects exerted by the Earth and the Sun (Nakamura, 2003, 2005). Compared to earthquakes, however, moonquakes release an infinitesimal fraction of the energy released by terrestrial seismic activity (Goins et al., 1981). Additionally, the seismic data recorded ∼2700 events originated by impacts of meteoroids on

the Moon's surface.

The Moon, finally, is a still intact reservoir of valuable resources, such as H, ^{3}He, O_2, C, N, regolith and water ice stored in polar permanently shadowed craters (Paige et al., 2010; Li et al., 2018) and as interstitial water or within impact glasses (Honniball et al., 2021). These pristine resources are necessary to achieve final products in terms of propellant, consumables and building materials (Anand et al., 2012; Baasch et al., 2021; Osio-Norgaard et al., 2021; Pouwels et al., 2020) and are the main target for the In-Situ Resource Utilization (ISRU).

3.1.4 The Tsiolkovskiy crater

The Tsiolkovskiy crater is a ∼200 km diameter complex crater located at 20.4°S, 129.1°E. With its approximately 12,000 km^2 basaltic floor, it stands out in being one of the few mare exposures of the lunar far side. The crater presents an irregular shape, as do its ejecta deposits. The uneven ejecta distribution reflects the origin of Tsiolkovskiy through an oblique impact in the NW-SE direction (Whitford-Stark, 1982). In particular, evidence of this asymmetry lies in an ejecta forbidden zone extending outside the NW outer rim, indicating an impact angle of <45°with an azimuth of ∼315°, and a shortened ejecta blanket marked by lobate margins in the SE direction (Morse et al., 2021).
Moreover, the formation of Tsiolkovskiy crater is responsible for the generation of an apparently unique long runout landslide on the Moon, formed soon after the crater impact on its western rim (Boyce et al., 2020). The collapse of the crater rim led to an encroachment into the adjacent Pre-Nectarian, un-flooded, Fermi crater by the ∼72 km long runout landslide, marked by lobes and parallel flow lines, which covered most of the Fermi crater floor (Figure 3.11).

In contrast to the fate of Fermi, Tsiolkovskiy crater was not affected by impacts of younger Eratosthenian nor Copernican craters and related ejecta rays, thus it still preserves a clear and pristine morphology. From the remarkable flat smooth floor, a ∼6.5 km high well-preserved central peak (Figure 3.12) formed by the rebound of the crust during the impact clearly stands out with respect to the dark color of the surrounding mare. A slightly uprange offset of the central peak itself is yet more evidence for the oblique origin of the crater (Schultz, 1992). The large size of Tsiolkovskiy and the height of its central peak, moreover, would suggest that the

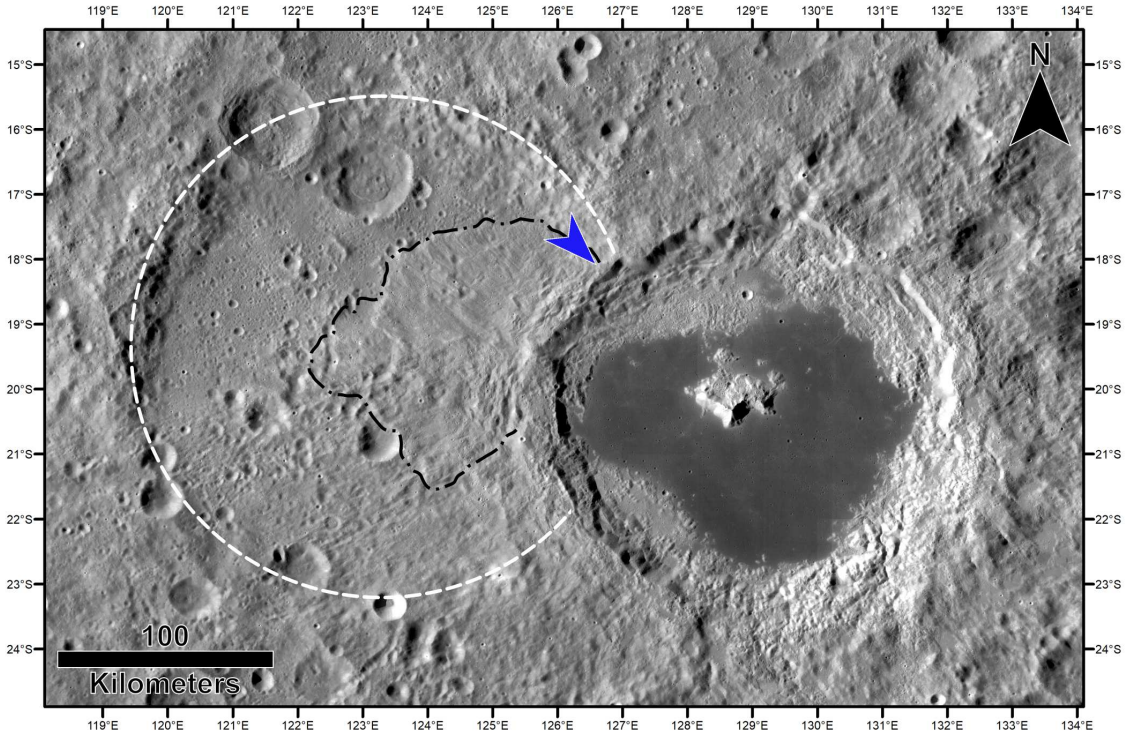

Figure 3.11: Structure of Tsiolkovskiy crater (on the right) superposing on the ∼230 km diameter Fermi crater (on the left). The white dashed circle identifies the approximate rim of Fermi; the black dashed and dotted line delimits Tsiolkovskiy's landslide, modified from (Boyce et al., 2020); the blue arrow indicates the impact direction for Tsiolkovskiy crater.

impact leading to the formation of this crater could have exhumed materials from the lower crust (Pieters and Tompkins, 1999) or even from the upper mantle.

The mare deposit, of which the average thickness is calculated to be about 116 m (Craddock and Greeley, 1988), is thought to be the result of several small eruptive events (Wilbur, 1978) that has produced a difference in the present crater floor elevation of more than 450 m, higher in the NW sector and lower in the SE one (Whitford-Stark, 1982; Mouginis-Mark and Boyce, 2017). Furthermore, the low-reflectance mare is characterized by slightly different reflectance values possibly indicating distinct lava flows with different chemical compositions and/or ages. In terms of composition, more detailed information is discernible from the Clementine UVVIS Color Ratio mosaic (Lucey et al., 2000). Even at first glance, it is possible to appreciate the high color variegation of Tsiolkovskiy crater with respect to the surrounding highland crust. As observed from the multispectral analysis made by (Pieters and Tompkins, 1999), the impact of Tsiolkovskiy crater led to the excavation of large amounts of anorthosites and norites mixed with highland soil along the crater rim. A more varied composition, additionally including the presence of troctolites (Heather and Dunkin, 2002), characterizes the central peak of the crater

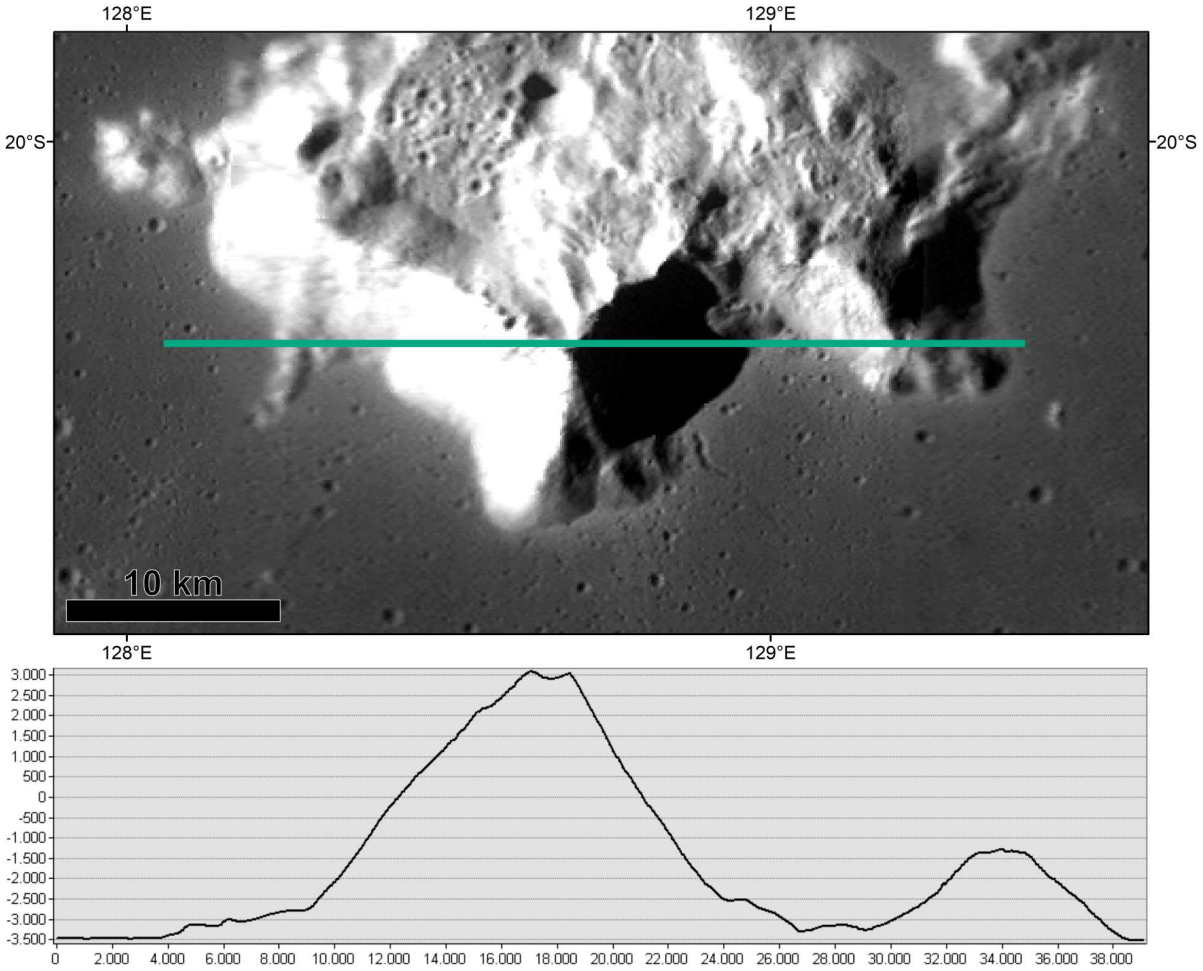

Figure 3.12: Profile graph (*bottom panel*) derived from the line of interpolation (green line) drawn on the southern portion of Tsiolkovskiy's central peak (*top panel*) evidencing the height reached by the peak itself with respect to the surrounding mare.

on which purest anorthosite (PAN) (Ohtake et al., 2009; Lemelin et al., 2015), composed of nearly 100% anorthite, and olivine (Pieters et al., 1996; Corley et al., 2018) have been detected. The peculiarity of this crater, however, is the basaltic mare material covering the crater floor which, despite its particularly dark color, is not as rich in TiO_2 as the mare exposures on the nearside (Pieters et al., 1995).

Recent crater counts performed on the ejecta and landslide deposits of Tsiolkovskiy crater have determined a formation age of 3.55±0.1 Ga (Boyce et al., 2020), similarly to the Upper or Late Imbrian ages inferred by (Wilhelms and El-Baz, 1977; Wilhelms, 1987; Tyrie, 1988). A lower limit age of 3.2-3.3 Ga (Williams et al., 2013; Pasckert et al., 2015; Greenhagen et al., 2016) was in contrast derived from crater counting areas defined on the mare deposit.

3.2 Data and basemaps

Depending on the final aim of the product, different types of data can be used.
For the Moon, I produced i) a morpho-stratigraphic map, derived from photo-geological interpretation, ii) a color-based spectral map, derived by associating compositional variations with the identified geologic units, iii) age determinations, for discriminating possible age differences based on color variations, iv) a spectro-stratigraphic map, derived by integrating multispectral information, and v) a high-resolution map, for defining scientific targets of interest.

The morpho-stratigraphic mapping was produced based on the LROC-WAC (Robinson et al., 2010) monochrome global mosaic version 3 (∼100 m/px), assembled using WAC 643 nm images with incidence angles between 55°-75°(Figure 3.13). In order to discriminate small morphological features, in particular on the flat, dark and shadow-less crater floor, a higher resolution mosaic produced using ∼10 m/px images from the Kaguya TC (Haruyama et al., 2008) (Figure 3.14) was used in support of the LROC-WAC mosaic. An even higher resolution mosaic produced using LROC-NAC (Robinson et al., 2010) images covering the entire crater would have been too large to be easily managed.

The panchromatic imagery was coupled with the topographic data derived from the merging of data from the LOLA (Smith et al., 2010) and Kaguya TC DEM (Barker et al., 2016) with a horizontal and vertical resolution of ∼59 m/px and 3-4 m respectively (Figure 3.15). From the elevation data we derived a topographic hillshade, with default azimuth of 315°and altitude of 45°, and we generated a surface slope map to discriminate surfaces within defined steepness thresholds, ranging from high (>40°) to low (<15°) (Figures 3.16 and 3.17).

The color-based spectral mapping was produced following the contextual approach (see chapter 1.4) on the Clementine UVVIS Warped Color Ratio mosaic (∼200 m/px), assembled using the 415 nm, 750 nm and 1000 nm spectral filters (Red: 750/415 nm; Green: 750/1000 nm; Blue: 415/750 nm) (Figure 3.18). According to (Lucey et al., 2000), red colors are ascribable to low titanium or high glass contents, and thus also to pyroclastic deposits. High iron contents and mafic minerals, in contrast, are represented by green colors. The combination of the presence of mafic minerals and agglutinitic glass-like coatings due to maturation processes is shown by

yellow-green colors. Finally, blue colors represent high titanium contents and bright albedos.

A different spectral mapping was additionally produced on M3-derived data following the contextual approach (see chapter 1.4).
The M3 (Pieters et al., 2009a) multispectral data were progressively released for public use in different levels of processing, namely as raw uncalibrated data (level 0), recalibrated radiance data (level 1B) and calibrated and photometrically corrected reflectance data (level 2). After selecting the reflectance data covering the whole Tsiolkovskiy, a set of spectral indices, helpful in enhancing compositional variations, were derived to create spectral parameter mosaics. These parameters correspond to the reflectance at 540 nm (R540), band depth at 1000 nm (BDI), band depth at 2000 nm (BDII) and the spectral slope between 540 nm and the maximum of the first and second shoulder of the BDI (SSBI). Spectral Units (SUs) were then derived by thresholding the value of each spectral index into 6 intervals (from low to very high values) and retrieving all possible combinations of these intervals for all parameters. Units with similar spectral characteristics were merged while the sparsely populated and less significant ones were automatically excluded (Zambon et al., 2022). Finally, a Spectral Units map with 10 SUs, conveying the spectral information fulfilled by all the spectral parameters, was produced (Figure 3.19) (see D4.1, D4.2, D4.3 and D4.4 from PLANMAP for more details, Appendix A.1).

Age determinations and the production of the high-resolution mapping, finally, were both performed on LROC-NAC (Robinson et al., 2010) images. The images were selected based on the area of interest and their mean ground resolution and illumination conditions (i.e. maximum incidence angle ranging between 56.8°-87.3°). Overall, the downloaded LROC-NAC images have resolutions ranging between 0.6 and 1.5 m/px. Areas selected for performing age determinations are directly shown in chapter 3.4.3, whereas Figure 3.20 shows the area surrounding the southern portion of Tsiolkovskiy's central peak selected for producing a high-resolution mapping.

The LROC-WAC and Clementine mosaics and the DEM merge basemap were downloaded from the USGS Astrogeology Science Center website, whereas the TC images were downloaded from the Kaguya Data Archive. The LROC-NAC images, instead, were downloaded from the USGS Planetary Image Locator Tool (PILOT) data portal. Finally, the M3 data were downloaded from NASA's Planetary Data System (PDS) Cartography and Imaging Sciences Node. Appendix D lists the basemaps used for this work.

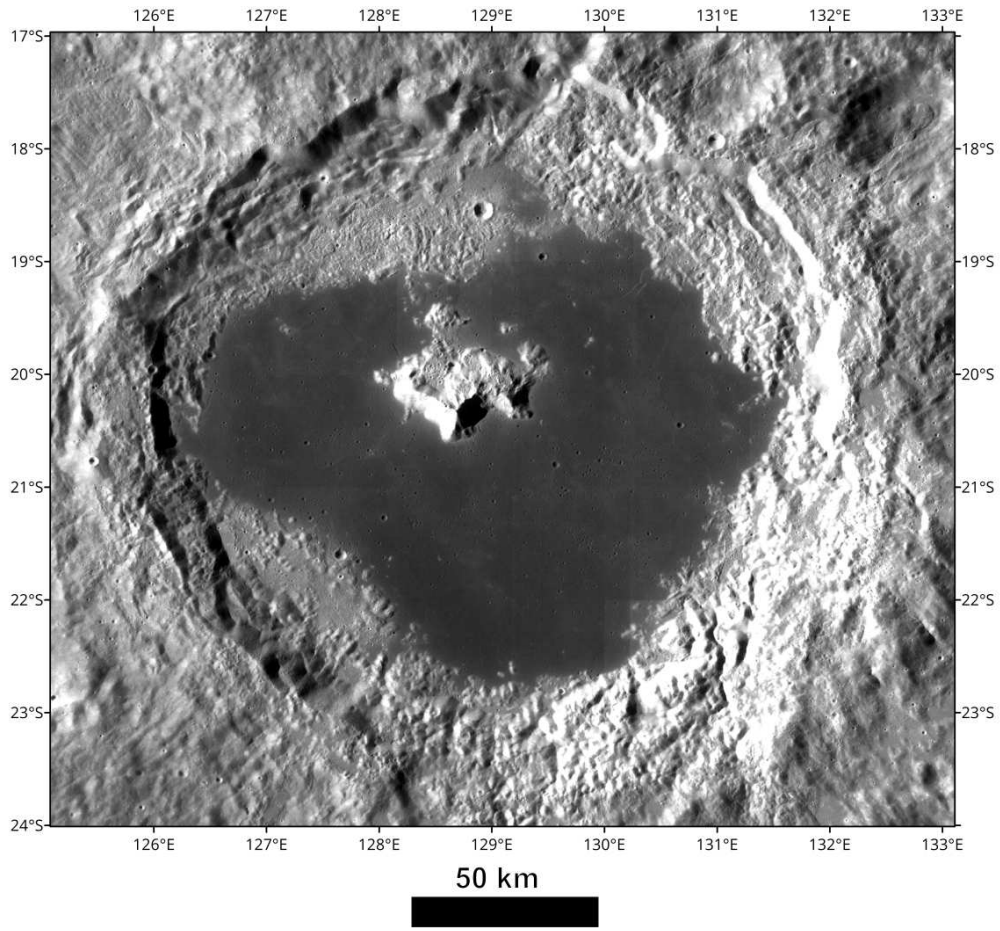

Figure 3.13: LROC-WAC basemap (∼100 m/px) in equirectangular projection. The monochrome basemap is assembled using WAC 643 nm images with incidence angles between 55°-75°. The basemap was trimmed from the Lunar_LRO_LROC-WAC_Mosaic_global_100m_June2013.

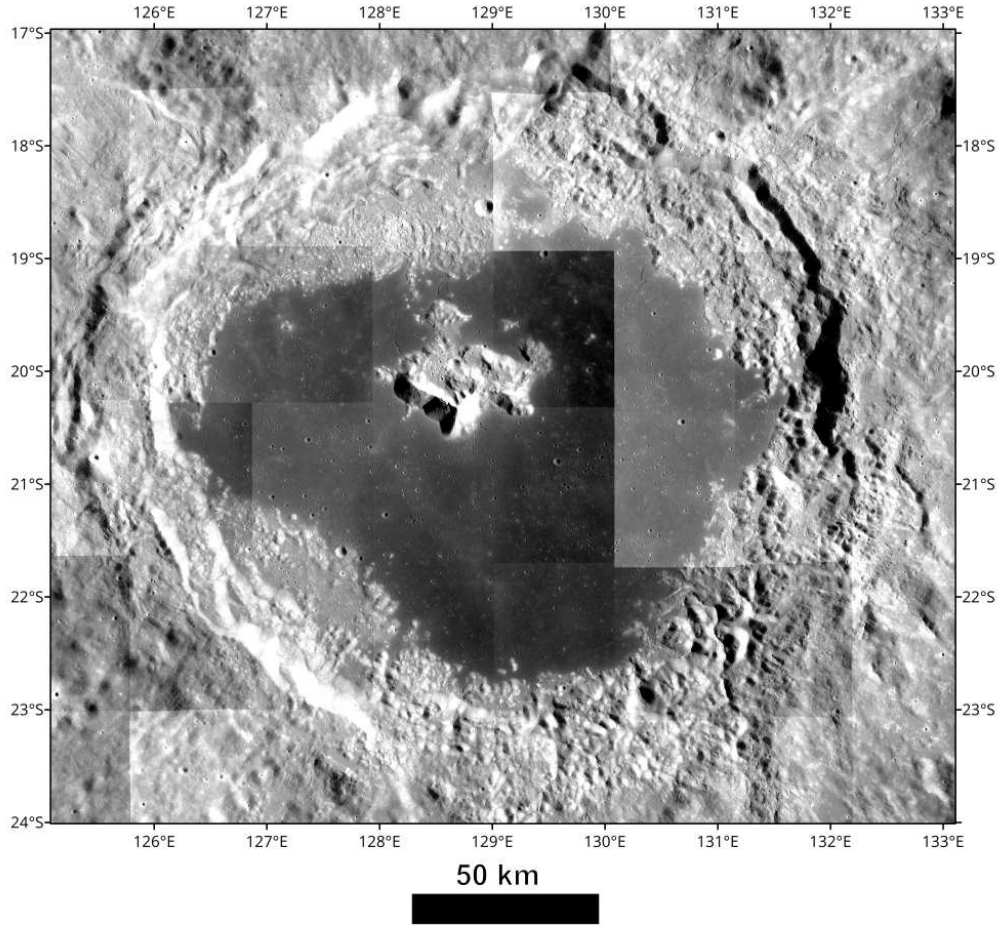

Figure 3.14: Kaguya TC mosaicked images (∼10 m/px) in equirectangular projection.

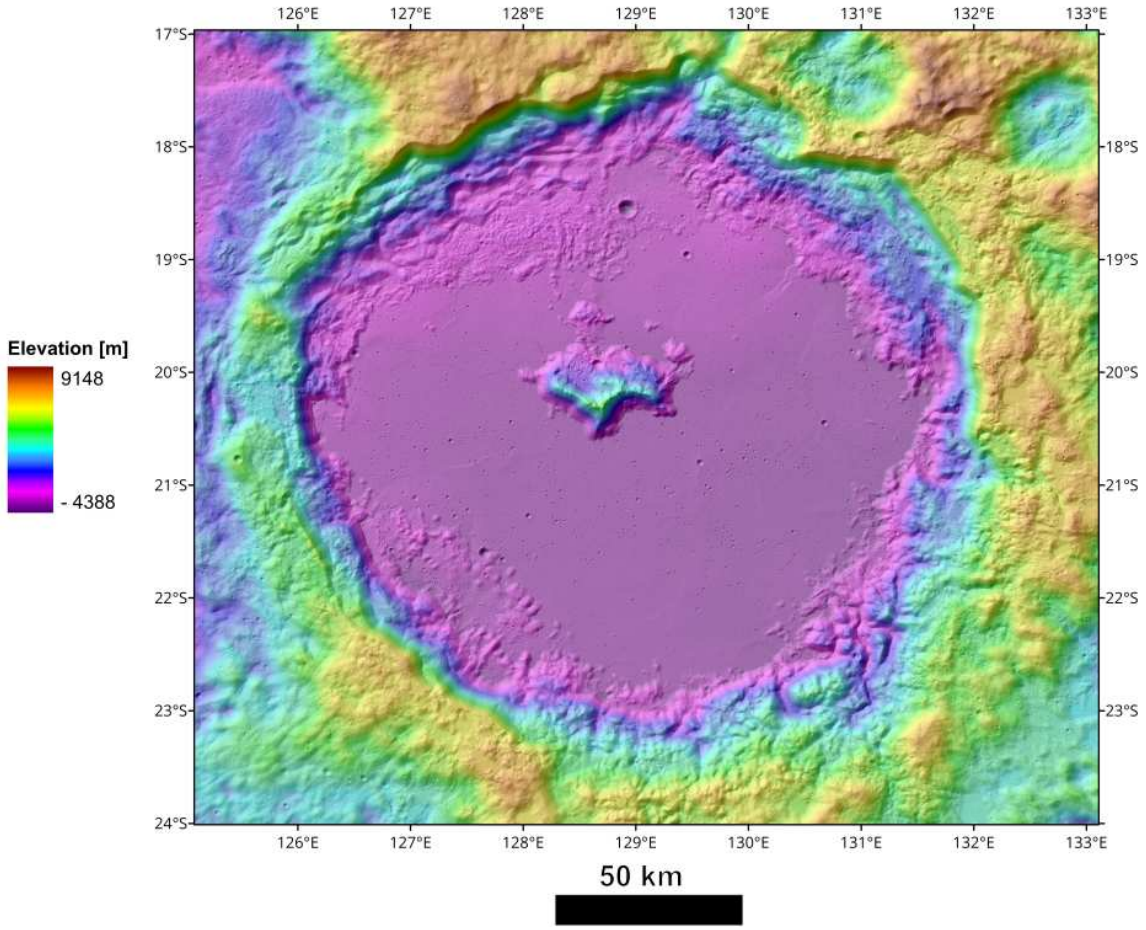

Figure 3.15: LRO-LOLA and Kaguya Tc DEM merge (∼59 m/pixel and 3-4 m respectively) in equirectangular projection. The basemap was trimmed from the Lunar_LRO_LrocKaguya_DEMmerge_60N60S_512ppd and it is visualized on top of the DEM-derived hillshade basemap with a 50% of transparency.

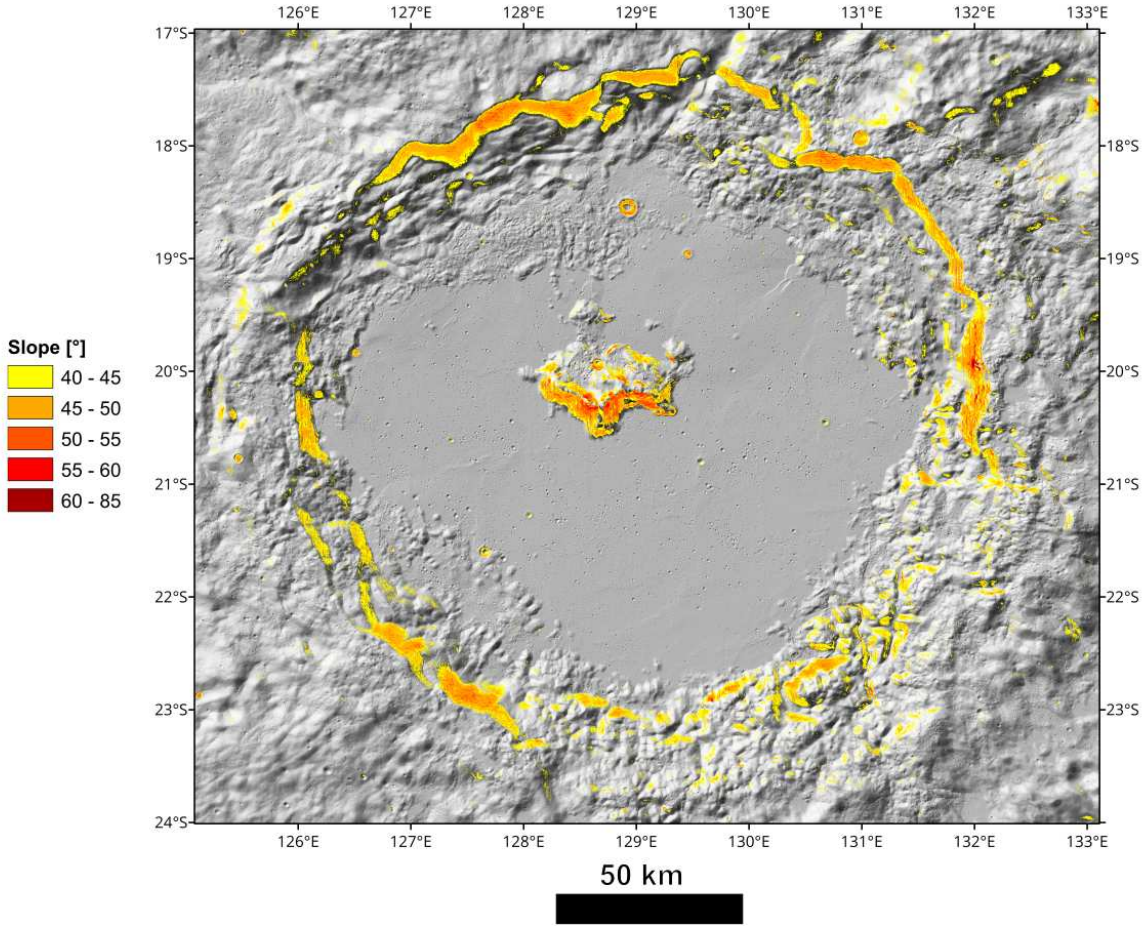

Figure 3.16: Surface slope map for slopes <15°visualized on top of the DEM-derived hillshade basemap.

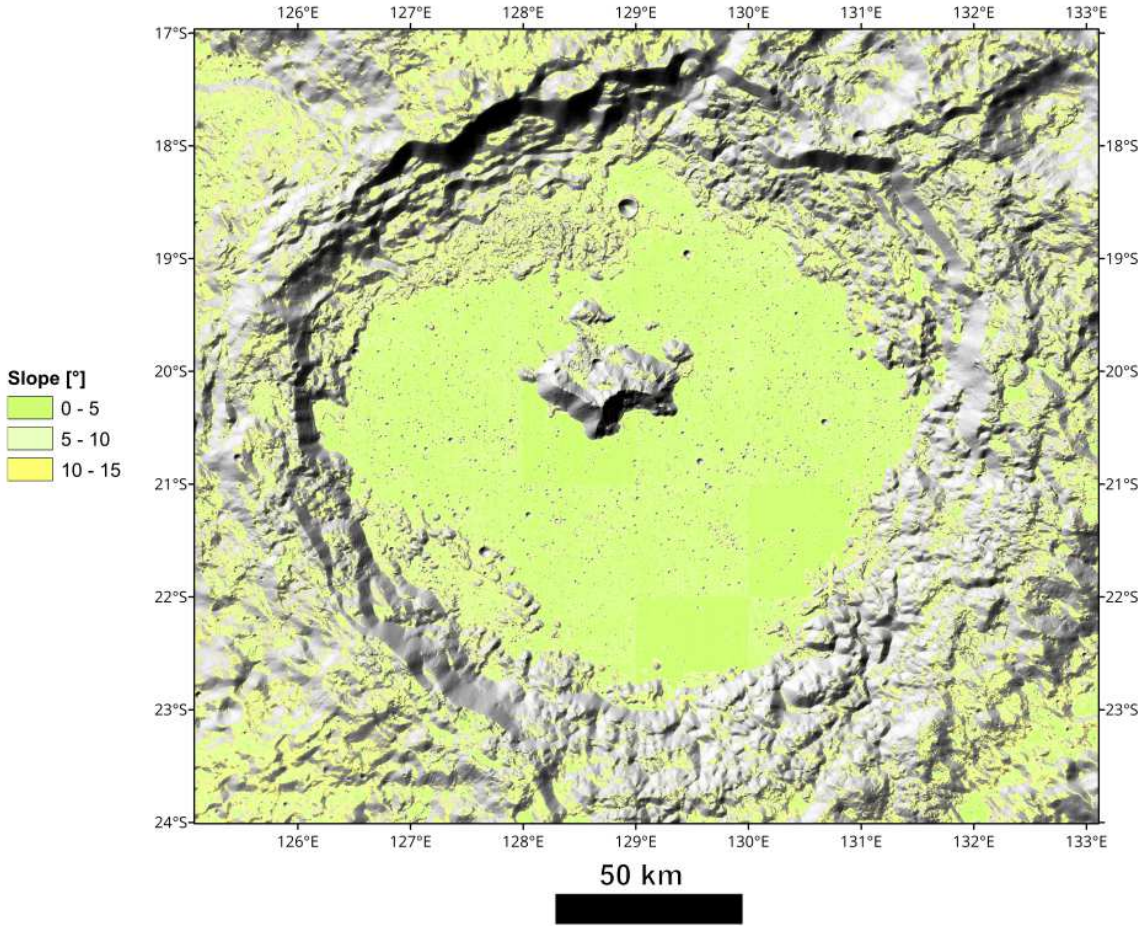

Figure 3.17: Slope map for slopes >40°visualized on top of the DEM-derived hillshade basemap.

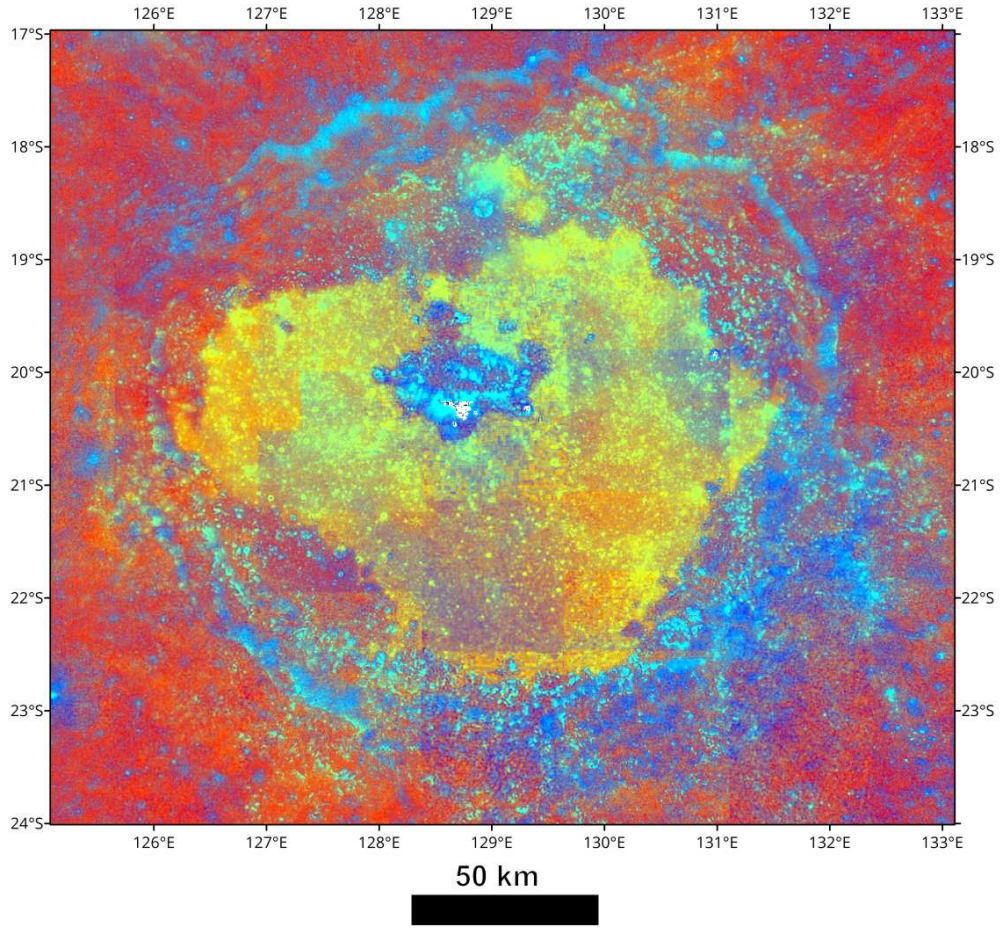

Figure 3.18: Clementine UVVIS Warped Color Ratio mosaic (∼200 m/px) in equirectangular projection. The basemaps enphatizes color variations on the Moon's surface by using a mosaic with the 750/415 nm, 750/1000 nm and 415/750 nm band ratios in the red, green and blue channels respectively. The baseamap was trimmed from the Lunar_Clementine_UVVIS_Warp_ClrRatio_Global_200m.

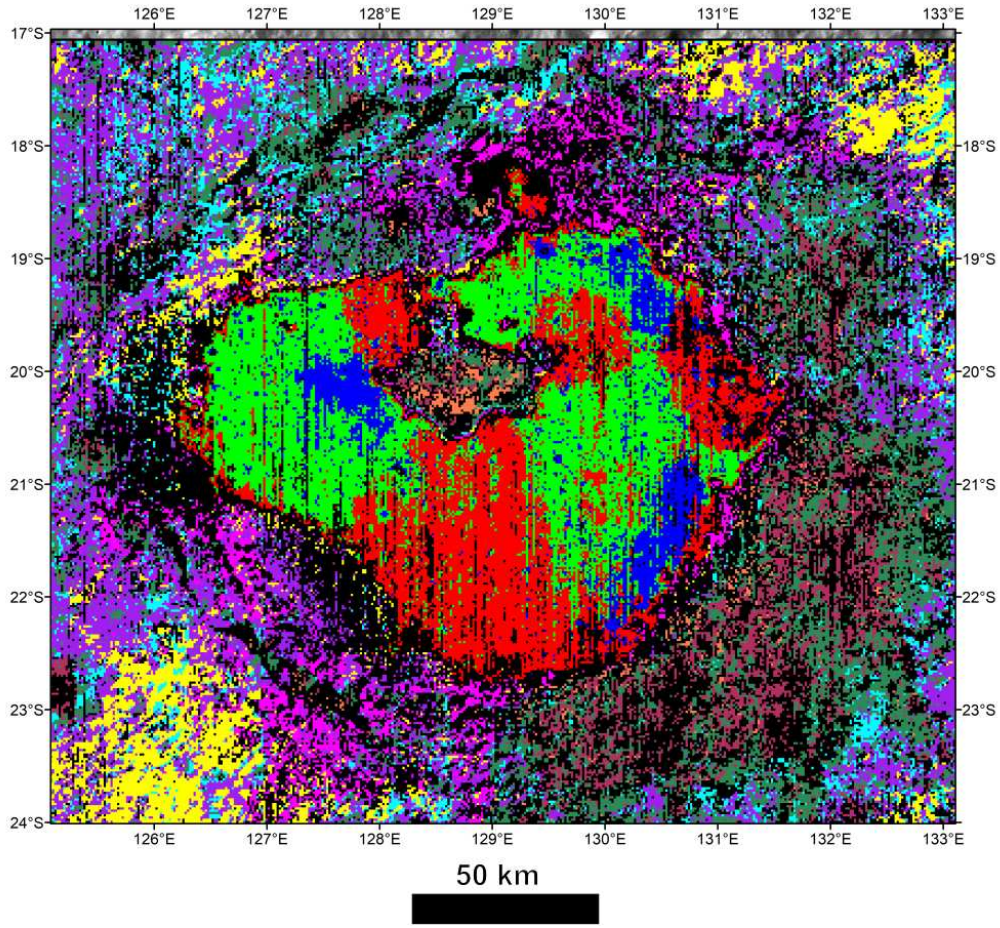

Figure 3.19: Spectral Units map in equirectangular projection. The basemap summarizes all the information held in several spectral indices mosaics allowing for a quick and straightforward understanding of the compositional properties of the area.

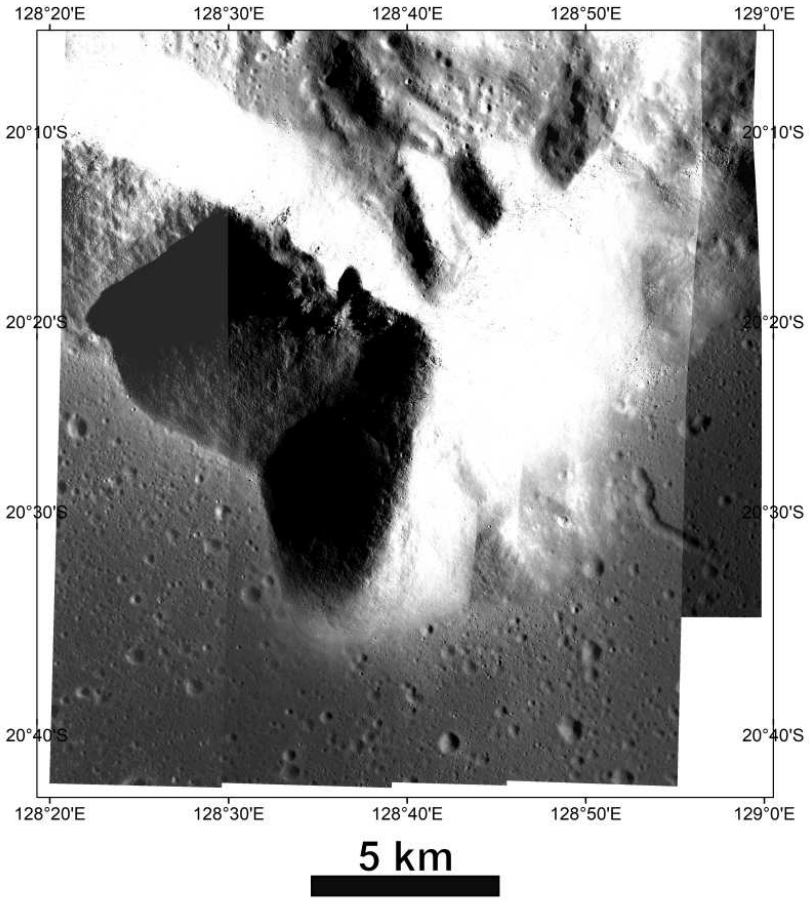

Figure 3.20: LROC-NAC images (∼0.92 m/px) of the southern portion of Tsiolkovskiy's central peak.

3.3 Methods

The different mappings for Tsiolkovskiy crater were performed in the Esri ArcGIS 10.4.1 software.
Since Tsiolkovskiy is located at 20.4°S, the mappings were carried out in equirectangular projection using the D_MOON datum.

The mapping and output scales (see chapter 1.3) were set to 1:200,000 and 1:1,000,000 respectively for the morpho-stratigraphic mapping and to 1:400,000 and 1:2,000,000 respectively for the color-based spectral mapping and spectro-stratigraphic mapping. For the high-resolution mapping, instead, I considered a resolution of 1 m/px and thus the mapping and output scales were set to 1:2000 and 1:10,000 respectively.

Similarly to Mercury, a dedicated geodatabase was assembled to enable the distinction of linear and polygonal features.
The geodatabase provides for the distinction of geologic/spectral contacts (polyline layer), linear features (polyline layer) for morphologies and structures, point features (point features), and geologic/spectral units (polygon layer).

Geologic/spectral contacts, once again, represent the main digitizing layers, delimiting the different crater materials or spectrally different terrains by means of certain and approximate contacts (see chapter 2.3). The linear features vector layer, instead, includes morphostructures such as the crest of Tsiolkovskiy's rim, the crest of crater rims up to 1000 m (for the morpho-stratigraphic mapping) or 200 m (for the high-resolution mapping) in diameter and mare rilles. Faults are distinguished in certain and uncertain, similarly to the certain and approximate distinction made for contacts, while wrinkle ridges are considered separately. Point features, finally, were used during the production of the high-resolution mapping for determine the position of boulders, both isolated, in small clusters of 2 to 5 boulders and in large clusters of more than 5 boulders.

Once the digitizing process and the topological analysis for errors check were accomplished, the polygons of the geologic/spectral units were built. The morpho-stratigraphic mapping, in particular, distinguished geologic units within the crater floor and at the crater walls. The

crater floor units encompass the smooth and hummocky materials and Tsiolkovskiy's central peak, whereas the crater wall units include steep scarps, smooth ponds and the inner slope materials. For the spectral mappings, instead, units were constructed based on the color of the terrain they are representing. The high-resolution mapping, finally, introduced the unit for the secondary craters materials.

To determine the formation age of the Tsiolkovskiy crater and the absolute stratigraphy of the different crater floor units identified by the color-based spectral mapping, I performed crater size-frequency distribution (CSFD) measurements.
The CSFDs were performed on several areas of about 100 km^2 using the CraterTools add-on (Kneissl et al., 2011) for the Esri ArcGIS software and exported as a Spatial Crater Count (.scc) summary file. The exported data were then plotted in the Craterstats2 software (Michael and Neukum, 2010) using pseudo-log binning (Michael et al., 2016) on cumulative plots and fitted with the (Neukum et al., 2001) production and chronology functions. A randomness analysis (Michael et al., 2012) performed by means of the Mean 2nd-Closest Neighbour Distance (M2CND) measurement was used to verify the homogeneity of the crater population and, eventually, to exclude spatially non-random craters.

3.4 Results

3.4.1 Morpho-stratigraphic map

The crater rim morphology of Tsiolkovskiy crater delimits the mapping area.
The morphology of this complex crater allowed me to distinguish three main units for the crater floor and three more units for the crater walls. The stratigraphic correlations between the different geologic units were inferred by determining their relative age by observing morphological evidence.
Here follows a brief description of the geologic units (Figure 3.21) associated with unit labels enlisted in stratigraphic order (see Appendix C for reading information).

1. *sm* – [floor unit] smooth material: particularly horizontal (mostly <10°) and dark mare deposit punctured by minor impacts rarely reaching 5 km in diameter; this smooth material presents sharp boundaries with adjacent materials and scattered wrinkle ridges and mare rilles.

2. *hm* – [floor unit] hummocky material: pre-mare material presenting rolling areas and high-standing bulges characterized by rough material reworked during the impact and debris collapsed from the crater walls.

3. *cp* – [floor unit] central peak: exclusively well-preserved and bright central peak morphology rising about 6.5 km over the crater floor.

4. *sp* – [wall unit] ponds: smooth areas interpreted as melt ponds texturally contrasting with the surrounding steep and rough areas.

5. *ss* – [wall unit] steep scarps: exposed steep scarps (collapsed deposits were not included) with slopes >40°.

6. *is* – [wall unit] inner slope: terraces and scarps <40°generated by the inward collapse of the crater inner slope during the modification stage.

The northern side of the crater floor is marked by several mare rilles, reaching up to 16.14 km of length and mostly trending in the NNW-SSE direction. In terms of deformations and faulting, the crater inner walls exhibit many concentric normal faults whereas the crater floor is characterized by several wrinkle ridges, mostly arranged radially to the central peak.
The morpho-stratigraphic map is shown in Figure 3.22 on top of the DEM-derived hillshade basemap.

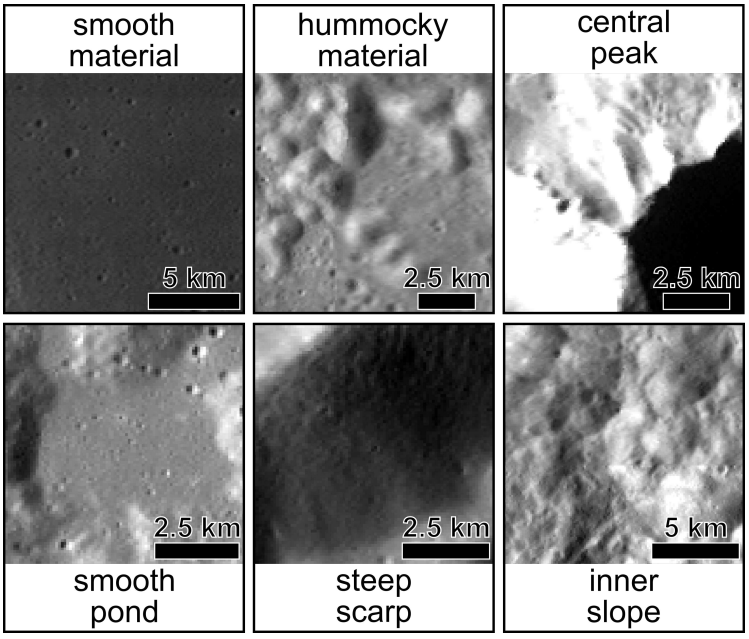

Figure 3.21: Examples for the *sm*, *hm*, *cp*, *sp*, *ss* and *is* geologic units mapped in the study area.

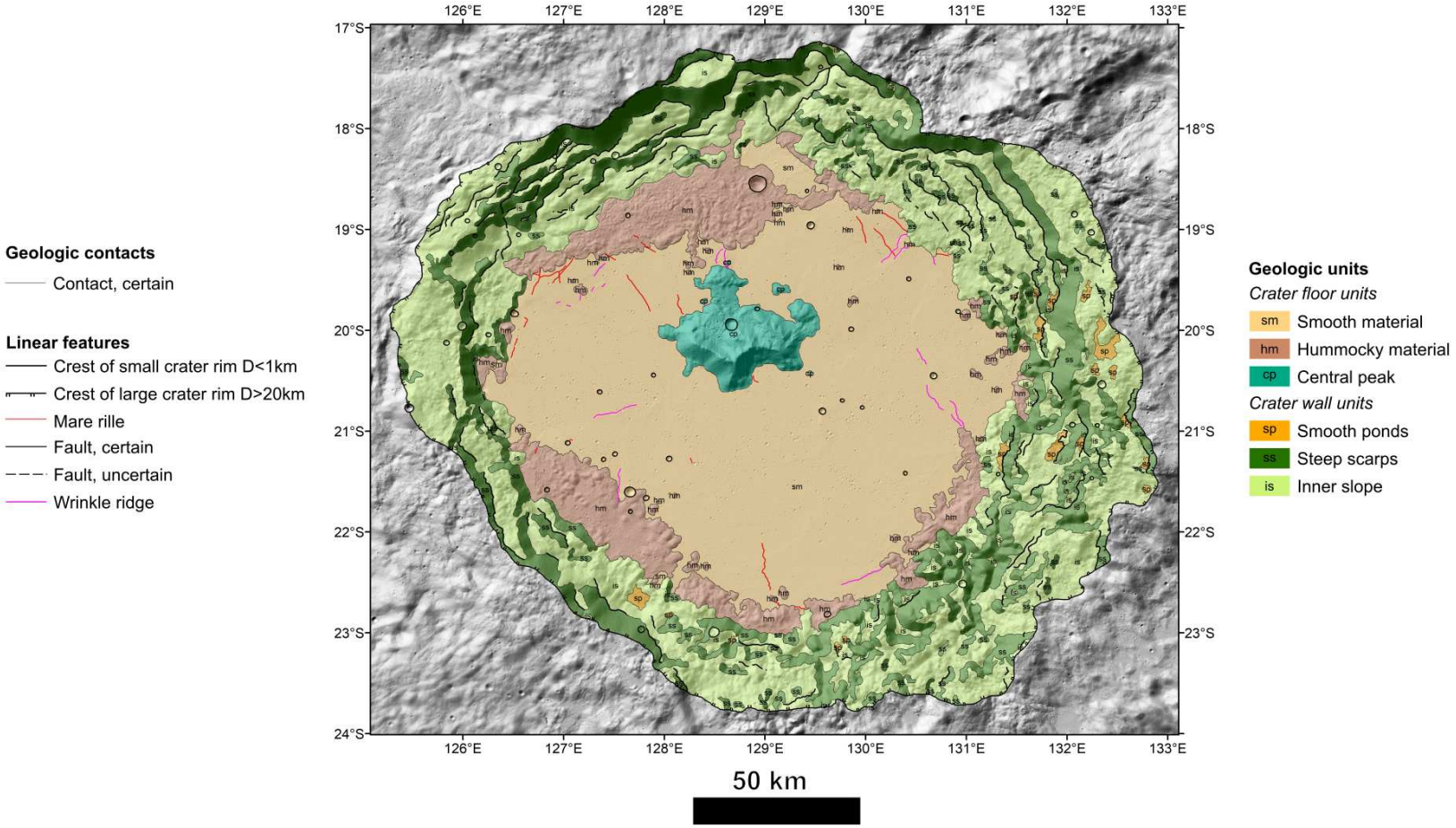

Figure 3.22: Morpho-stratigraphic map of the Tsiolkovskiy crater visualized on top of the DEM-derived hillshade with a 50% of transparency. Refer to the text for unit descriptions.

3.4.2 Color-based spectral map

The color-based spectral mapping was performed on the basis of the color variation as from the Clementine UVVIS Color Ratio mosaic. The different color of the units can be linked to different degrees of maturity and/or composition of the materials (Lucey et al., 2000).
In this case, color variation led me to identify and delimit different units showing different hues of the same color. However, due to the low resolution of the basemap there was insufficient confidence for constructing fully independent units and, thus, each color unit groups within it different shades of the same color (Figure 3.23).

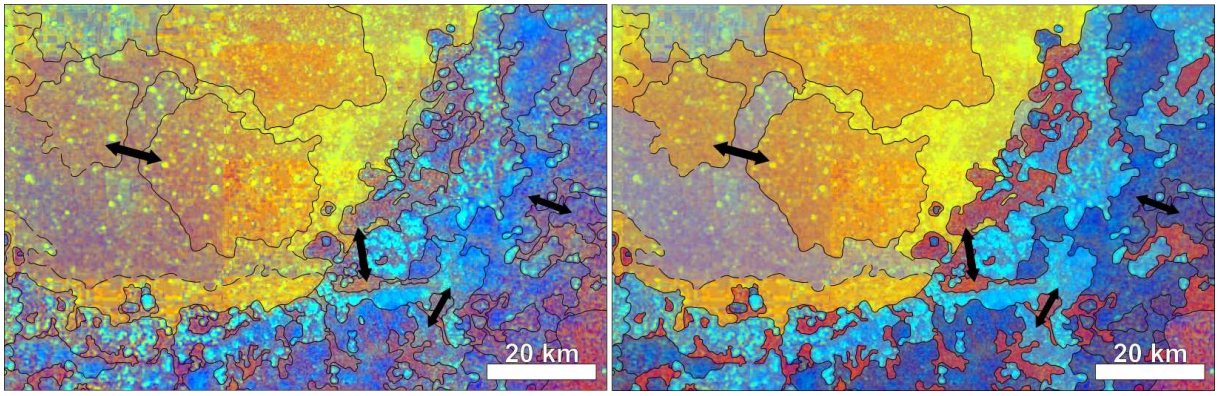

Figure 3.23: Detailed view of the SE portion of the Tsiolkovskiy crater. Spectral contacts linework (*left panel*) and color-based spectral map (*right panel*) discriminate the presence of characteristic combinations of color shades, highlighted by double black arrows, as from the Clementine UVVIS Warped Color Ratio mosaic.

Here follows the spectral units that have been distinguished associated with unit labels and enlisted in stratigraphic order.

1. *bp* – basaltic plain: a collection of units presenting respectively higher 415/750 nm (purple-blue) ratio, higher 750/415 nm (orange) ratio and average values of 750/415 nm and 750/1000 nm ratios (yellow) representative of distinct events of lava emplacement characterized by a different composition and/or age.

2. *nt* – noritic-anorthosite/troctolite: average values of 750/1000 nm and 415/750 nm ratios (cyan) indicating lithologies with minor amounts of Fe-bearing minerals such as noritic anorthosite and troctolite (Pieters and Tompkins, 1999).

3. *an* – anorthosite: high 415/750 nm ratio (blue) indicating surfaces with a bright albedo related to a possibly mainly anorthositic composition (Pieters and Tompkins, 1999).

4. *hs* – mature and reworked highland soil: high 750/415 nm ratio (red) indicating highland soil with a high glass content due to the reworking of pre-mare materials and to the maturation of the surface materials associated with prolonged exposure to space weathering.

The color-based spectral map is shown in Figure 3.24 on top of the Clementine UVVIS Warped Color Ratio basemap.

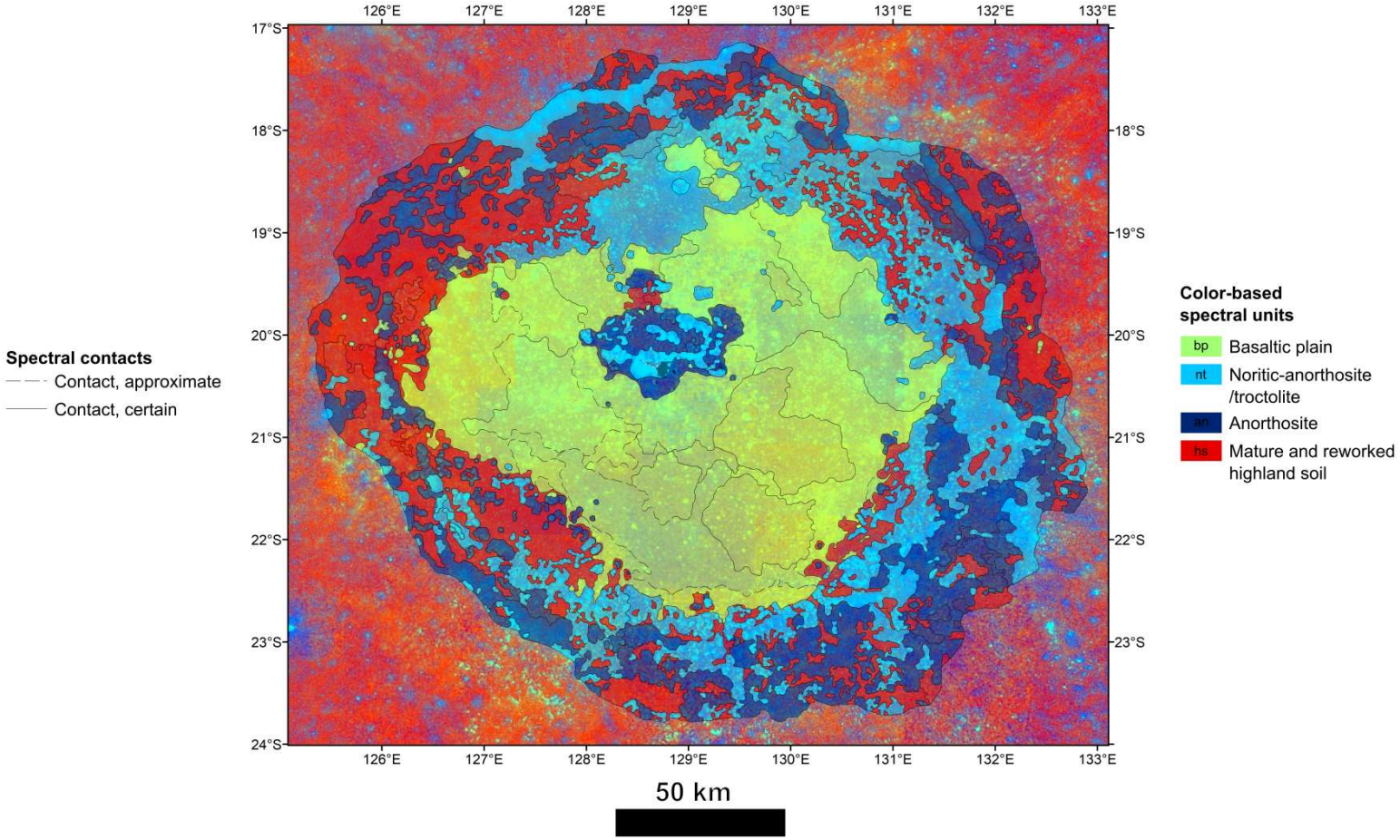

Figure 3.24: Color-based spectral map of Tsiolkovskiy crater visualized on top of the Clementine UVVIS Warped Color Ratio mosaic with a 50% of transparency. Refer to the text for unit descriptions.

3.4.3 Age determinations

The CSFD measurements for determining the formation age of the Tsiolkovskiy crater were performed on hummocky areas located to the NW and SW of the mare infilling (white polygons on Figure 3.25) over an area of ∼615 km^2 (Table 3.5). The results indicate a Late Imbrian age of ∼3.6 Ga for the Tsiolkovskiy crater (Figure 3.26 and Table 3.5).

In addition, with the aim of discriminating possible age differences related to distinct eruptive events, and eventually determine their absolute stratigraphic relationships, I defined several areas on the crater floor units identified by the color-based spectral linework mapping for measuring the CSFDs (i.e. *bp* units).

In particular, I selected 3 areas inside the purple-blue color units (purple polygons on Figure 3.25), 3 areas on the orange color units (orange polygons on Figure 3.25) and 2 areas inside the yellow color units (yellow polygons on Figure 3.25) covering an area of about 100 km^2 each (Table 3.5).

Figure 3.26 and Table 3.5 show the obtained age results.

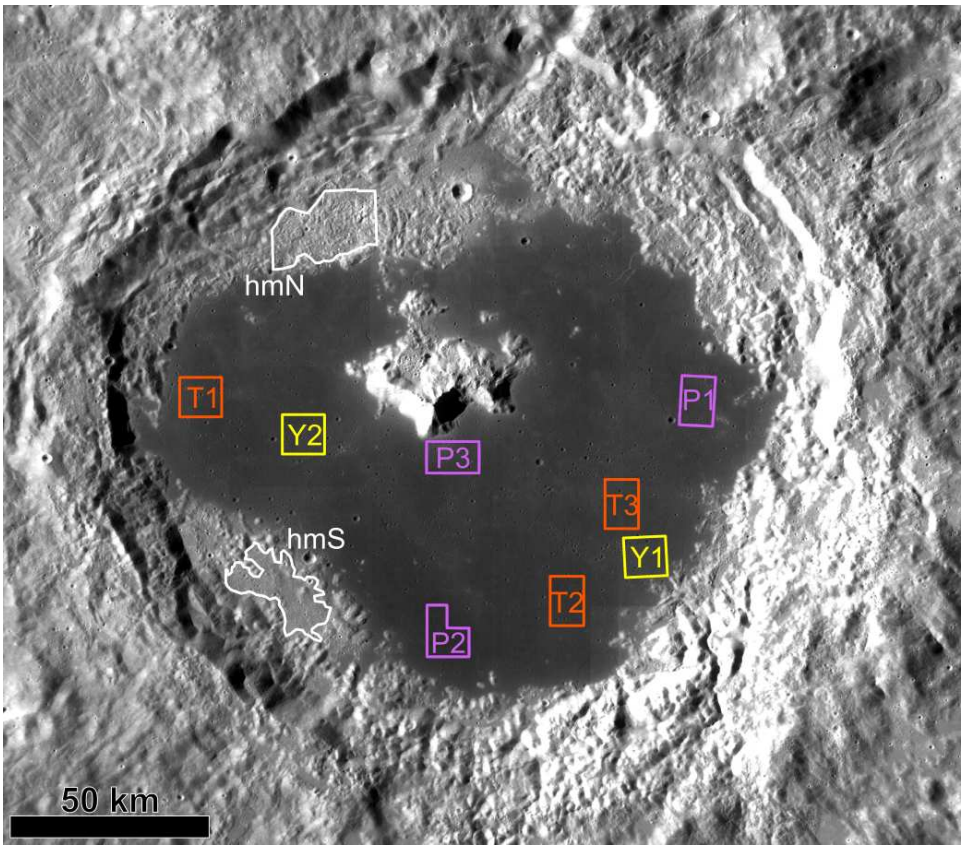

Figure 3.25: CSFD measurements areas defined on the basis of the Color-based spectral linework and visualized on top of the LROC-WAC basemap.

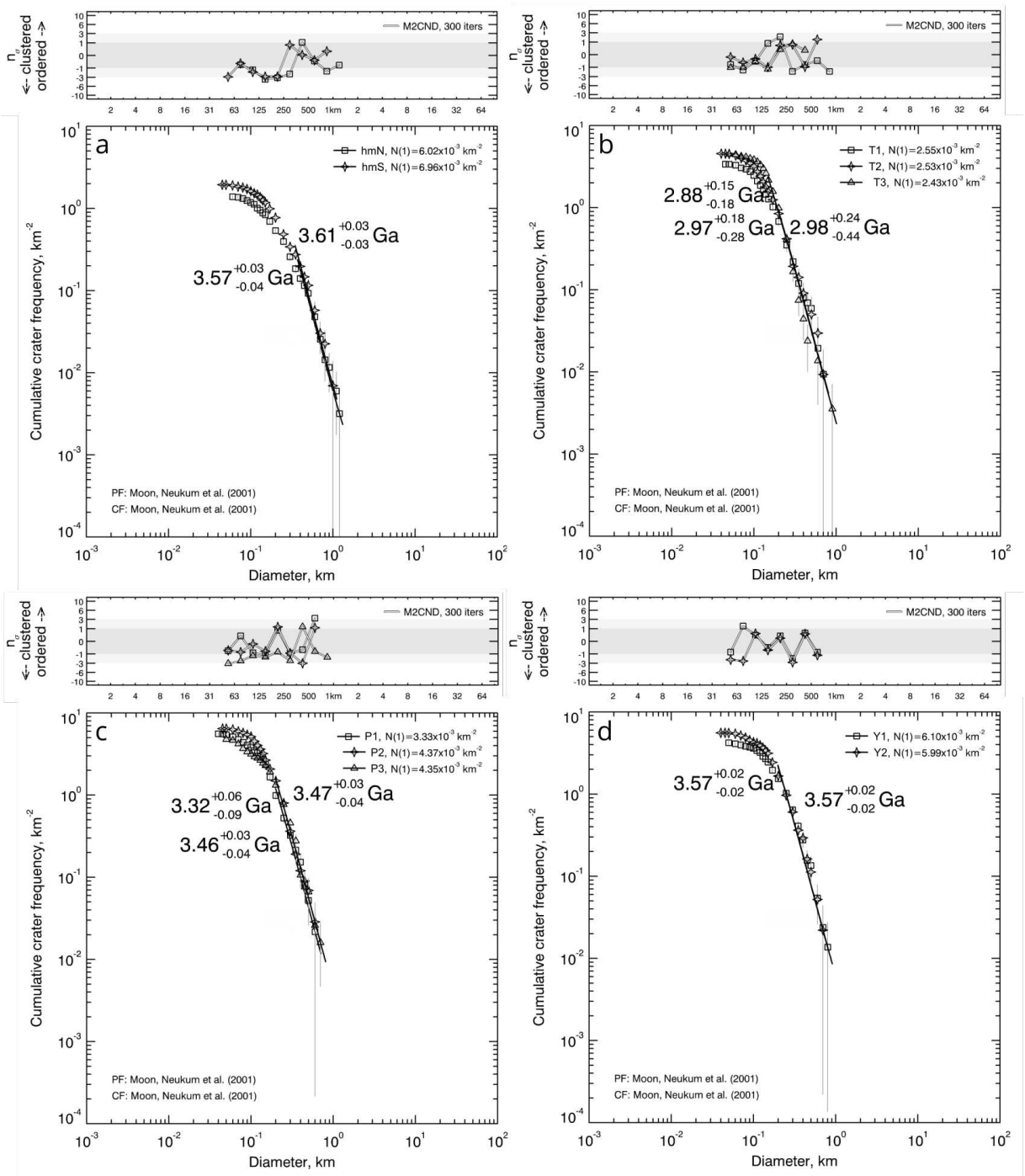

Figure 3.26: CSFD measurements performed on the (a) *hm* geologic unit for determining the formation age of Tsiolkovskiy crater and on the (b) orange (i.e. *bp1* spectral unit) (c), purple-blue (i.e. *bp2* spectral unit) and (d) yellow (i.e. *bp3* spectral unit) color units discriminated on the crater floor. The randomness analysis results are shown in the panel above the CSFDs.

In particular, the orange color unit stands out as the youngest basaltic unit with an average age of 2.94 Ga, followed by the 3.42 Ga intermediate purple-blue color unit. Conversely, the yellow color unit shows similar age results to the formation age of Tsiolkovskiy crater itself, and thus emerges as the oldest crater floor unit with an age of 3.57 Ga.

Table 3.5: The first column resume the names of the areas considered for the CSFD measurements. The areas location is visible on Figure 3.25. The second, third and fourth columns contain the surface extent of each area, the number of crater selected as standard and as marked (e.g. irregular craters, possible secondary craters or possible clusters of craters). The fifth, sixth and seventh columns contain the diameter range of the selected craters and the relative age with correlated errors as from Craterstats2 (Michael and Neukum, 2010).

Area name	Area (km^2)	No. of *standard* craters	No. of *marked* craters	Fit diameter range (m)	Relative age (Ga)	Relative age errors (Ga)
hmN	354.44	406	90	60-1300	3.57	+0.03 -0.04
hmS	260.55	392	107	45-1100	3.61	+0.03 -0.03
T1	100.00	325	14	45-800	2.98	+0.24 -0.44
T2	99.30	413	32	40-800	2.97	+0.18 -0.28
T3	99.30	361	81	50-1000	2.88	+0.15 -0.18
P1	99.30	447	104	40-700	3.32	+0.06 -0.09
P2	99.99	460	175	45-700	3.47	+0.03 -0.04
P3	100.00	437	38	50-800	3.46	+0.03 -0.04
Y1	100.00	299	118	50-900	3.57	+0.02 -0.02
Y2	100.00	431	122	40-800	3.57	+0.02 -0.02

These results allowed, therefore, to redefine the stratigraphic relationships of the spectral units as suggested by the age determinations.
Here follows the upgraded distinction of the spectral units that have been distinguished for the crater floor associated with unit labels and enlisted in stratigraphic order.

1. *bp1* – basaltic plain 1: localized units with higher 750/415 nm (orange) ratio representative of younger events of lava emplacement not necessarily indicating a change in composition; even if a slight difference in composition should not be excluded, it is indeed more probable a lower degree of maturity due to a shorter exposition to space weathering.

2. *bp2* – basaltic plain 2: localized units with higher 415/750 nm (purple-blue) ratio representative of intermediate events of lava emplacement, older than the *bp1* unit and younger than the *bp3* unit.

3. *bp3* – basaltic plain 3: average values of 750/415 nm and 750/1000 nm ratios (yellow) indicating a high concentration of weathered mafic minerals indicative of the spectra of older lava emplacements; brighter hues are due to the excavation of fresher iron-bearing materials due to impacts subsequent to the emplacement of the mare infilling (Figure 3.27).

The updated color-based spectral map is shown in Figure 3.28 on top of the Clementine UVVIS Warped Color Ratio basemap.

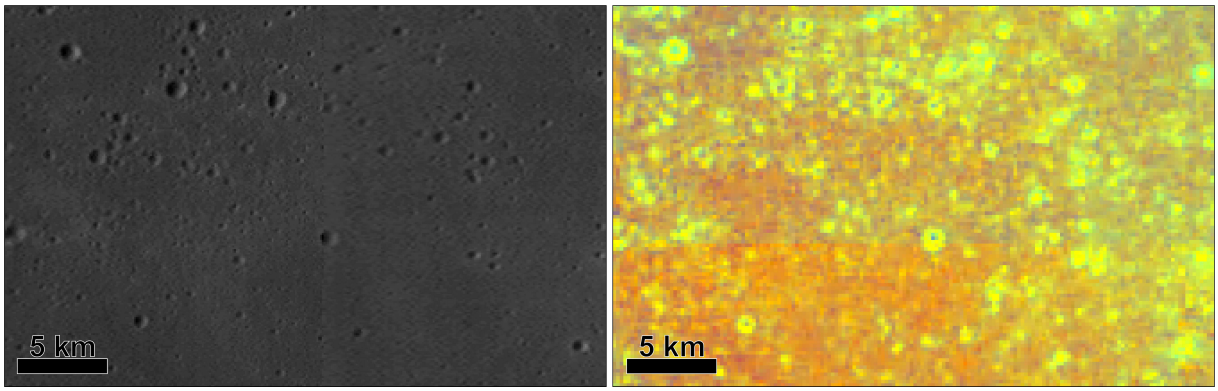

Figure 3.27: Detailed view on LROC-WAC and Clementine color basemaps of Tsiolkovskiy's crater floor highlighting the presence of brighter yellow hues due to the excavation of fresher underlying materials.

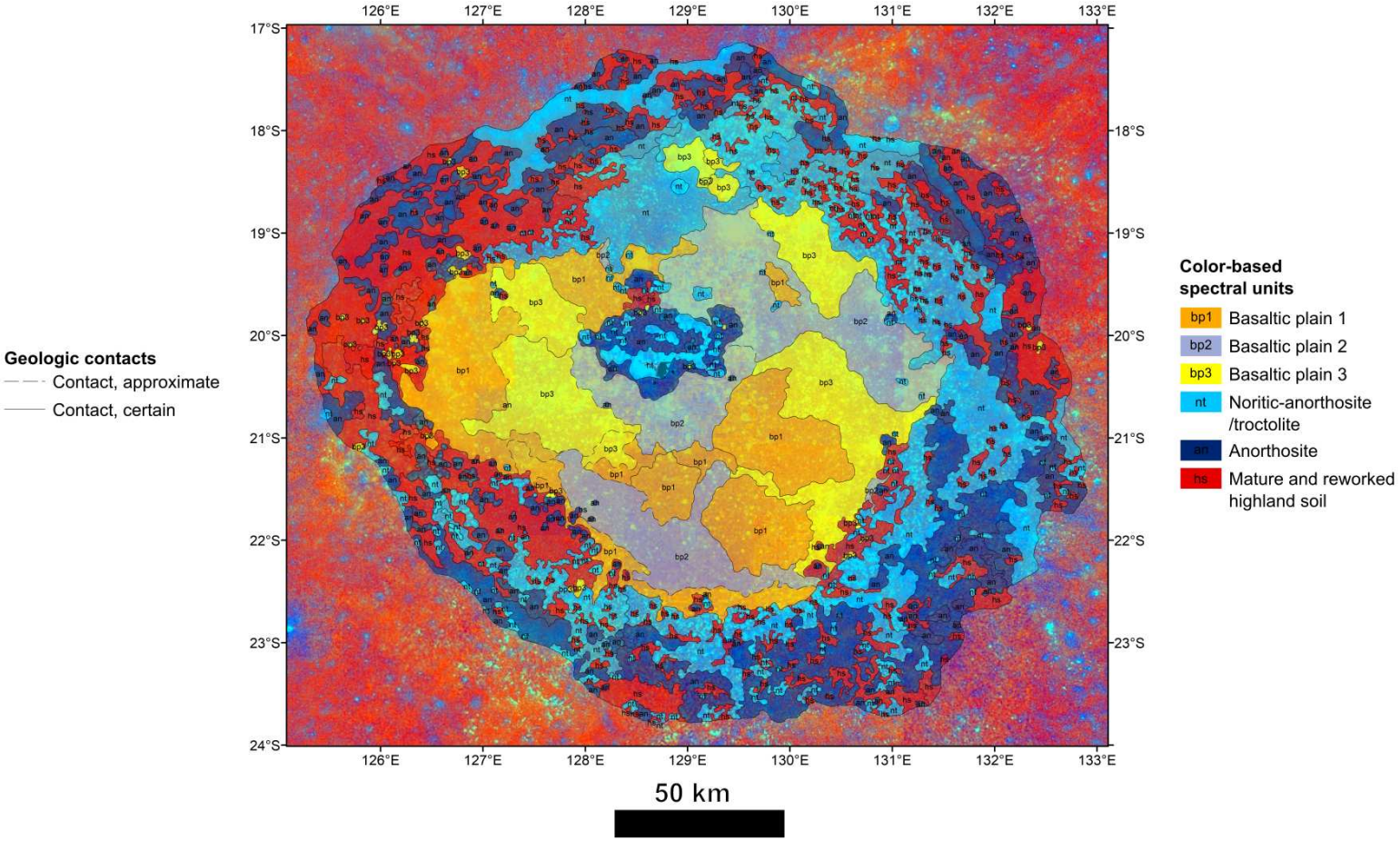

Figure 3.28: Updated color-based spectral map of Tsiolkovskiy crater visualized on top of the Clementine UVVIS Warped Color Ratio mosaic with a 50% of transparency. Refer to the text for unit descriptions.

3.4.4 Spectro-stratigraphic map

The spectro-stratigraphic mapping, similarly to the one presented in chapter 3.4.2, was performed on the basis of the color variations as from the Spectral Units map, derived from M3 data.

Here follows the SUs that have been distinguished enlisted in ascending order.

1. *SU1* – red: characterized by low reflectance values, intermediate to intermediate-high spectral slope values, high band depth values at 1000 nm and intermediate-high band depth values at 2000 nm; it is localized on the crater floor and mainly associated with the *sm* and *bp2* units.

2. *SU2* – green: characterized by low reflectance values, intermediate to high spectral slope values, high band depths values; it is localized on the crater floor and mainly associated with the *sm* and *bp1* units.

3. *SU3* – blue: characterized by low reflectance values, intermediate-low to intermediate-high spectral slope values, very high band depth values at 1000 nm and high band depth values at 2000 nm; it is localized on the crater floor and mainly associated with the *sm* and *bp1* units.

4. *SU4* – yellow: characterized by intermediate-low reflectance values, intermediate to intermediate-high spectral slope values, intermediate-low band depths values; it is mainly associated with the *hm* and *is* units.

5. *SU5* – cyan: characterized by intermediate reflectance values, intermediate to intermediate-high spectral slope values, intermediate-low band depth values at 1000 nm and low band depth values at 2000 nm; it is predominantly located on the northern side of the crater walls and mainly associated with the *is*, and *an*, *hs* units.

6. *SU6* – magenta: characterized by intermediate reflectance values, intermediate-low to intermediate-high spectral slope values, intermediate-low band depths values; it is located both on the crater floor and walls and mainly associated with the *hm* and *nt* units.

7. *SU7* – maroon: characterized by intermediate reflectance values, intermediate spectral slope values, intermediate band depths values at 1000 nm and intermediate-low band depth values at 2000 nm; it is predominantly located on the E-SE side of the crater walls and mainly associated with the *is*, *ss* and *nt*, *an* units.

8. *SU8* – sea green: characterized by intermediate reflectance values, intermediate-low to intermediate spectral slope values, intermediate band depths values; it represents one of the most widespread units with the only evident correlation being with the *sp* unit.

9. *SU9* – purple: characterized by intermediate reflectance values, intermediate-low to intermediate spectral slope values, intermediate band depths values; it represents one of the most widespread units with no unique correlation.

10. *SU10* – coral: characterized by high reflectance values, intermediate-low spectral slope values, intermediate-low band depth values at 1000 nm and low band depth values at 2000 nm; it is predominantly located on the central peak and SE side of the crater walls and mainly associated with the *cp*, *ss* and *nt* units.

11. *UP* (Undefined Pixels) – black: regions mainly associated with noisy data (calibration residuals and instrumental artifacts) not represented by a set of spectral parameters and thus not considered as SUs.

The spectro-stratigraphic map is shown in Figure 3.29 on top of the Spectral Units map.

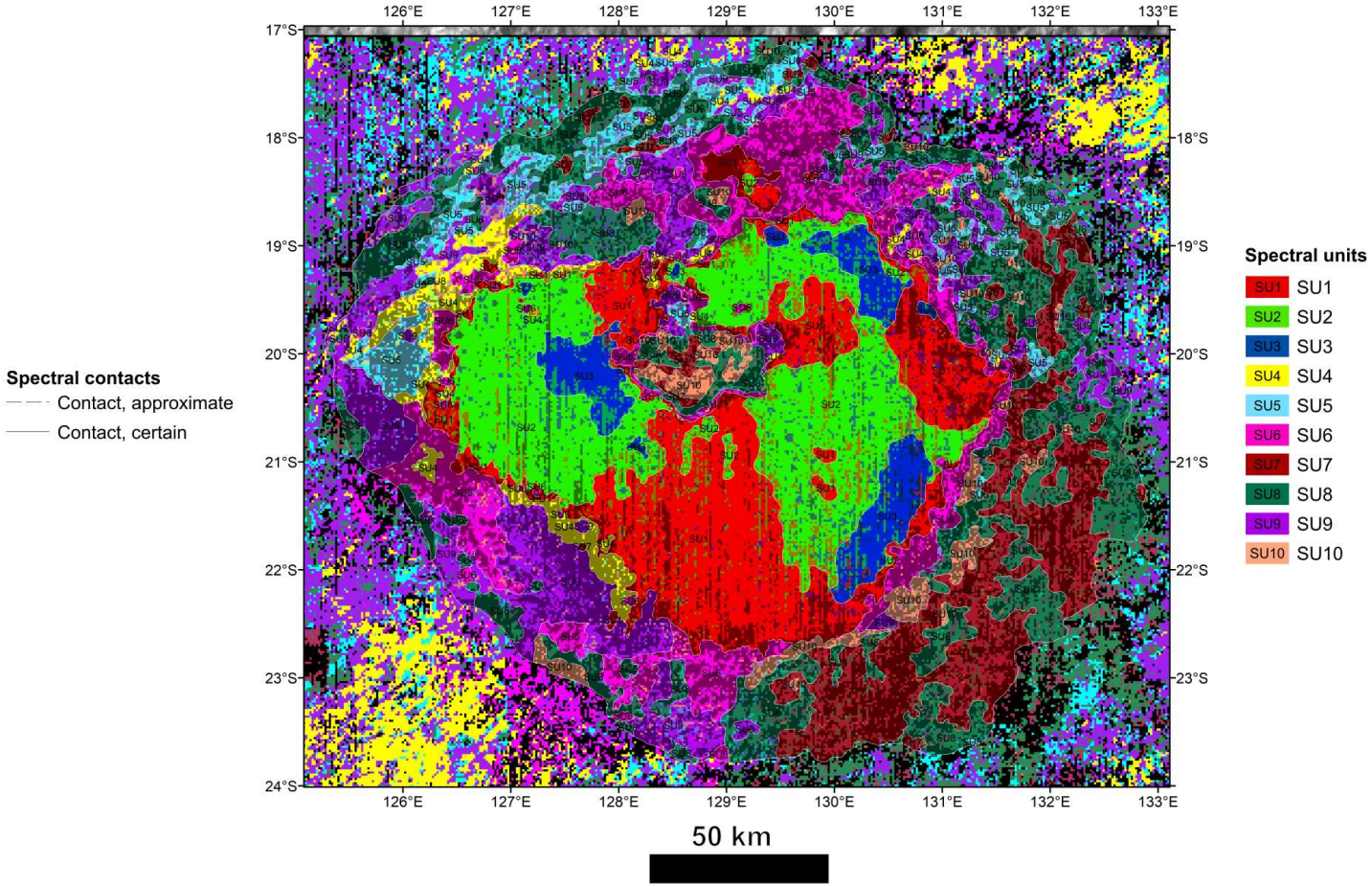

Figure 3.29: Spectro-stratigraphic map of Tsiolkovskiy crater visualized on top of the Spectral Units map with a 50% of transparency. Refer to the text for unit descriptions.

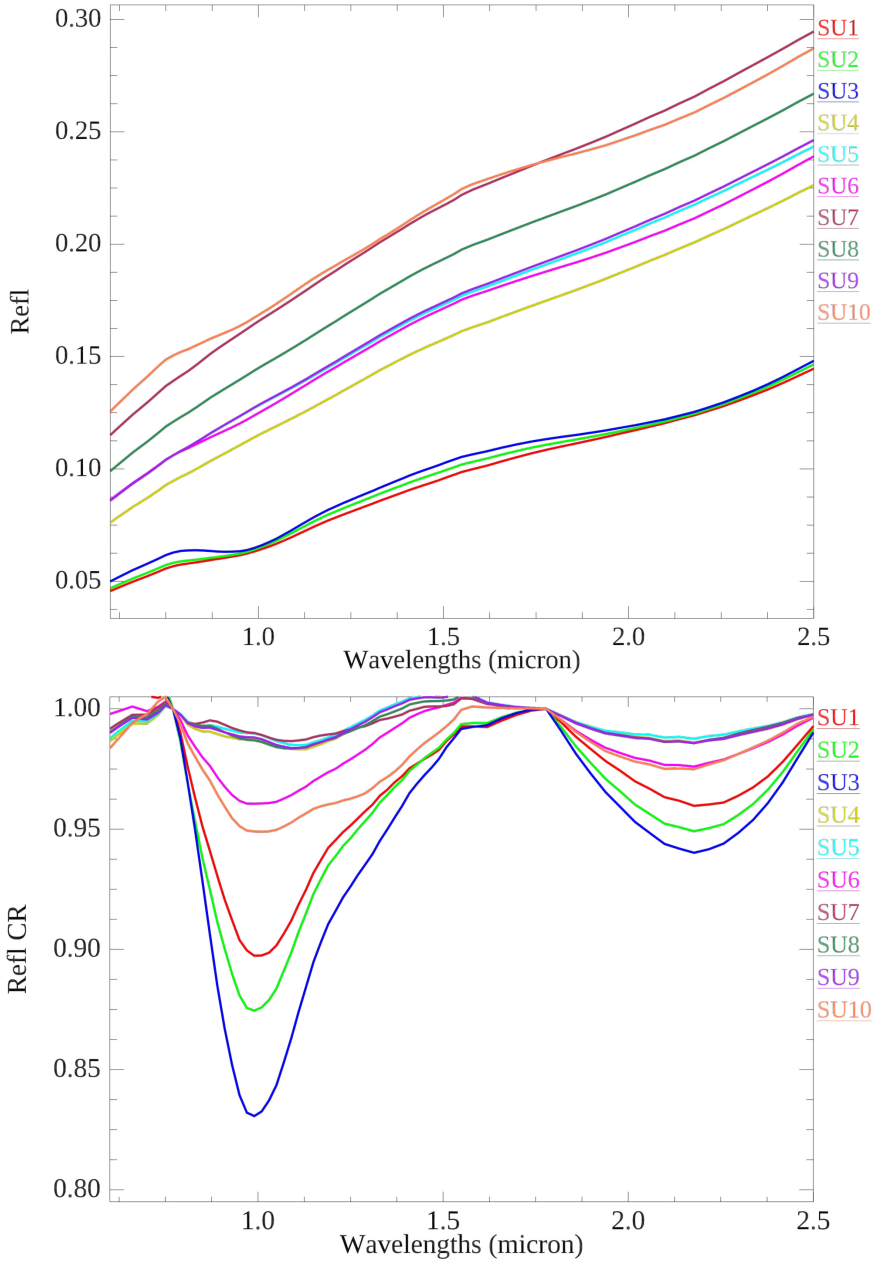

Figure 3.30: *Top panel*: plot of the average reflectance spectra of the SUs. *Bottom panel*: same as the top panel with continuum removal.

The average reflectance spectra of all the SUs have been plotted with the continuum removal (see D4.3 from PLANMAP for more details, Appendix A.1) for emphasizing the different absorptions bands (Figure 3.30). In particular, the spectra of the *SU1*, *SU2* and *SU3*, presenting a relatively lower (i.e. bluer) spectral slope and stronger absorptions around 1000 nm and 2100-2200 nm, are easily distinguishable from the ones of the other SUs highlighting a different spectral behavior for the units localized on the smooth crater floor. Furthermore, excluding the *SU6* and *SU10*, all the remaining units localized on the hummocky crater floor and crater walls present fainter absorptions both at 1000 and 2100-2200 nm.

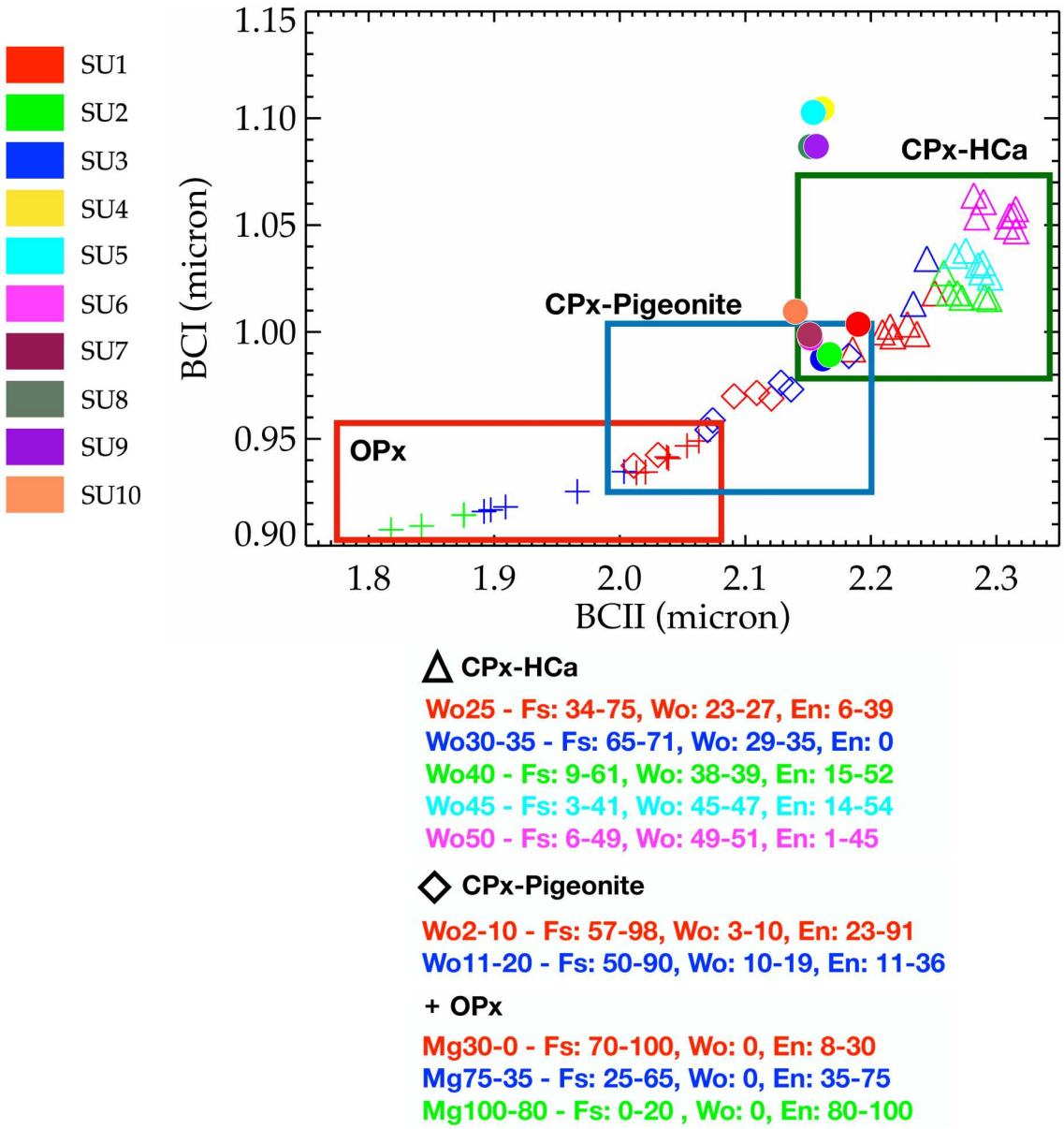

Figure 3.31: *Top panel*: average derived band centers for Ca-free (plus), low-Ca (diamonds) and high-Ca (triangles) synthetic pyroxenes (Klima et al., 2011a,b) and for the SUs (full circles, refer to the legend for color interpretation) plotted within the range of 1000 nm (BCI) and 2000 nm (BCII). *Bottom panel*: abundances of wollastonite (Wo), enstatite (En) and ferrosilite (Fs) for Ca-free, low-Ca and high-Ca synthetic pyroxenes; the different colors reflect the ones used in the *top panel*.

Compositional information were then obtained by comparing the units' reflectance spectra with laboratory spectra of lunar rock forming materials, and in particular those of synthetic pyroxenes, e.g. (Klima et al., 2011a,b), which are among the most common minerals on the Moon (e.g. Lucey (2004)).

Figure 3.31 shows a plot displaying the spectral variability within the range of 1000 nm (BCI) and

2000 nm (BCII) band centers of orthopyroxenes (Ca-free pyroxenes) and clinopyroxenes, namely pigeonites (low-Ca pyroxenes) and augites (high-Ca pyroxenes), characterized by a different abundance of wollastonite (Wo), enstatite (En) and ferrosilite (Fs). In the same plot have been displayed the BCI and BCII of the SUs. The plot highlights that the *SU1*, *SU2*, *SU3*, *SU6*, *SU7* and the *SU10* cluster in between the low-Ca pigeonite (Wo 11-20 – Fs 50-90, Wo 10-19 – En 11-36) and the high-Ca augite (Wo 25 – Fs 34-75, Wo 23-27 – En 6-39) groups suggesting a Ca content around 20% and highest Fe. The remaining SUs (i.e. *SU4*, *SU5*, *SU8* and *SU9*), instead, do not fall inside the defined ranges for what concerns the BCI but display BCII values similar to the other group of SUs. This displacement of the BCI possibly reflects the influence of a different component that would need further investigation.

3.4.5 Insight on landing site characterization

With the final aim of performing a landing site characterization for Tsiolkovskiy crater, I decided to focus my attention on the southern plains surrounding Tsiolkovskiy's central peak in order to produce a high-resolution geologic map aimed at better characterizing the area and defining its suitability for a future geologic and engineering characterization for a rover exploration.

The mapping covers an area of about 360 km^2 which, excluding the steep morphology of the central peak, consists of ∼160 km^2 of planar surface.

Here follows a brief description of the geologic units associated with unit labels enlisted in stratigraphic order.

1. *sc* – secondary crater: crater material of craters larger than 200 m in diameter.
2. *sm* – smooth material: particularly horizontal (mostly <10°) and dark mare deposit.
3. *cp* – central peak: exclusively well-preserved and bright central peak morphology rising about 6.5 km over the crater floor.

On the southeast side of the peak is a mare rille reaching a length of about 3.75 km protruding southeastward. The illuminated walls of the central peak highlight the presence of many rolling trails reaching up to 5 km in length and indicating the approximate detachment area of boulders collapsed from the central peak itself (Figure 3.32). These boulders gathered at the base of the peak forming, in some cases, rockslide deposits (Figure 3.32).

The high resolution of LROC-NAC images allowed to map the distribution of boulders (Figure 3.32) emphasizing a large amount of detached material. Boulders located inside craters, possibly not accessible to a rover, or gathered along the rim of some craters, likely generated by the impact, instead, were excluded from the mapping.

The high-resolution geologic map is shown in Figure 3.33 on top of LROC-NAC images.

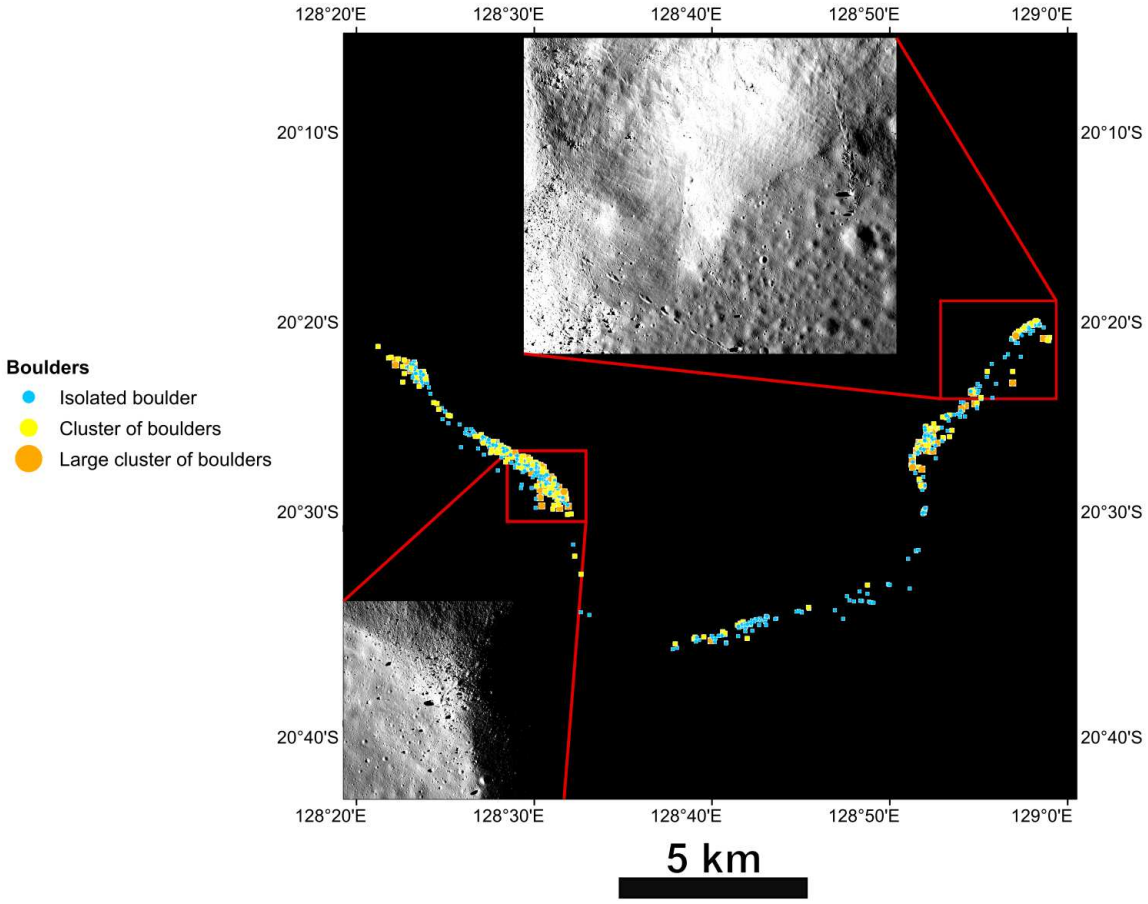

Figure 3.32: Distribution of boulders gathered along the southern portion of Tsiolkovskiy's central peak on top of a black background, for enhancing the visibility of point features. The zoom in show the rolling trails visible on the southeastern wall of the central peak, and partly visible also on the southwestern one, and a rockslide-like deposit at the base of the southwestern wall.

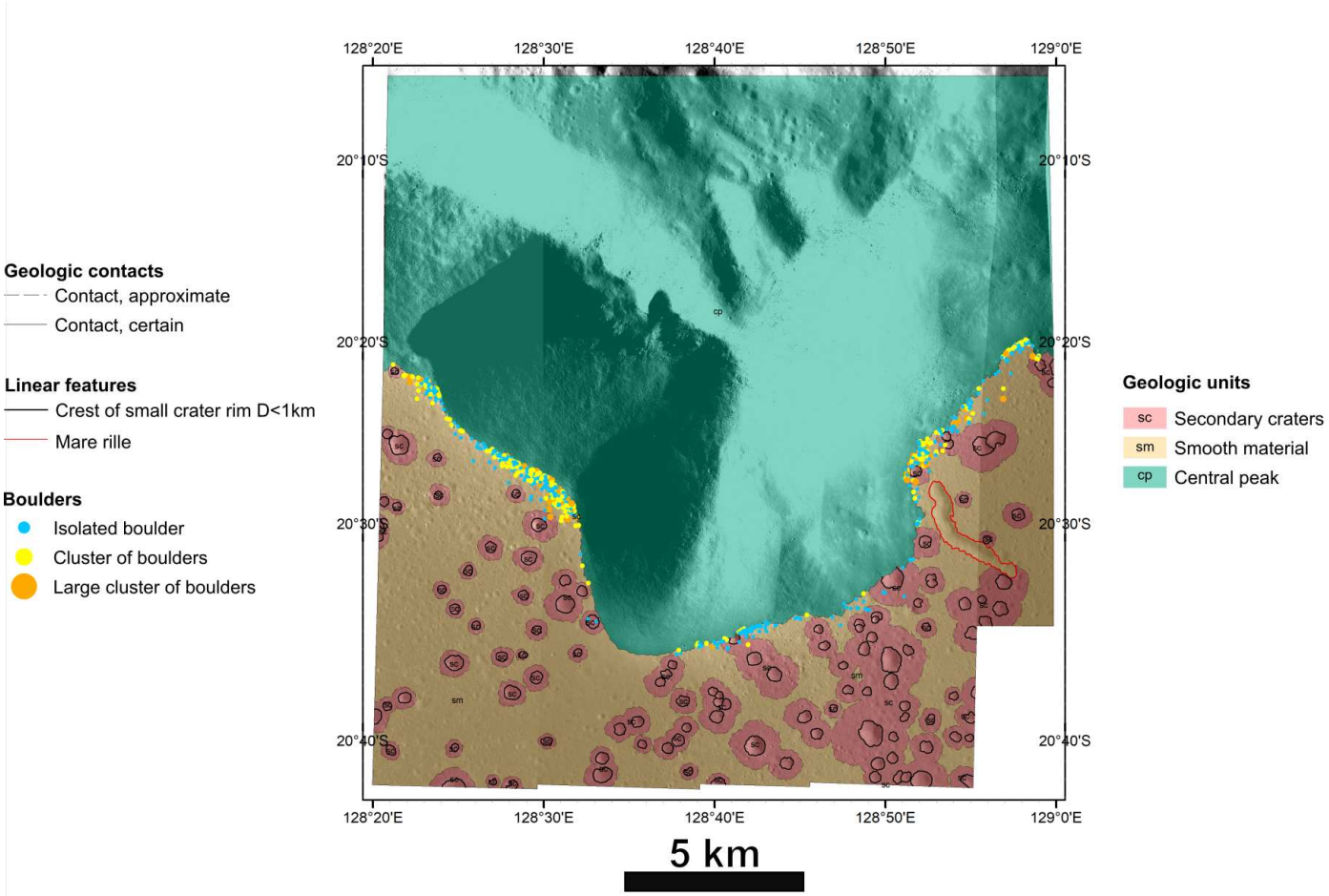

Figure 3.33: High-resolution geologic map of the southern portion of Tsiolkovskiy's central peak visualized on top of LROC-NAC images with a 50% of transparency. Refer to the text for unit descriptions.

As from the current mapping, it is possible to identify at least 6 different areas worthy of attention, namely possible scientific targets to be better defined in a landing site characterization (Figure 3.34).

In particular, 3 target areas (*t1*, *t2* and *t3* on Figure 3.34) focus on rockslide deposits that would represent optimal areas for the sampling of rocks possibly exhumed from the lower crust or mantle. These rocks could be analyzed for determining their textural, chemical and mineralogical composition and age. A couple more areas (*t4* and *t5* on Figure 3.34) focus on maria-like terrains possibly presenting compositional and/or age differences and which could help understanding the origin and variability of basalts, the thermal evolution of the mantle and the magma transportation mechanisms. One more area (*t6* on Figure 3.34), finally, focuses on a mare rille at the borders of which it would be possible to investigate morphological and compositional variations between its interior and the surrounding basalts. Further analyses, moreover, could be performed during a traverse. A rover, indeed, along its path would be able to investigate on the intrusive relationships within highlands and lower crust/mantle materials, the onlap relationship between the central peak and the surrounding mare, the thickness and possible internal layering of the regolith together with its grainsize, texture and mechanical behavior, and to detect the presence of lava tubes, even connected to sinuous rilles.

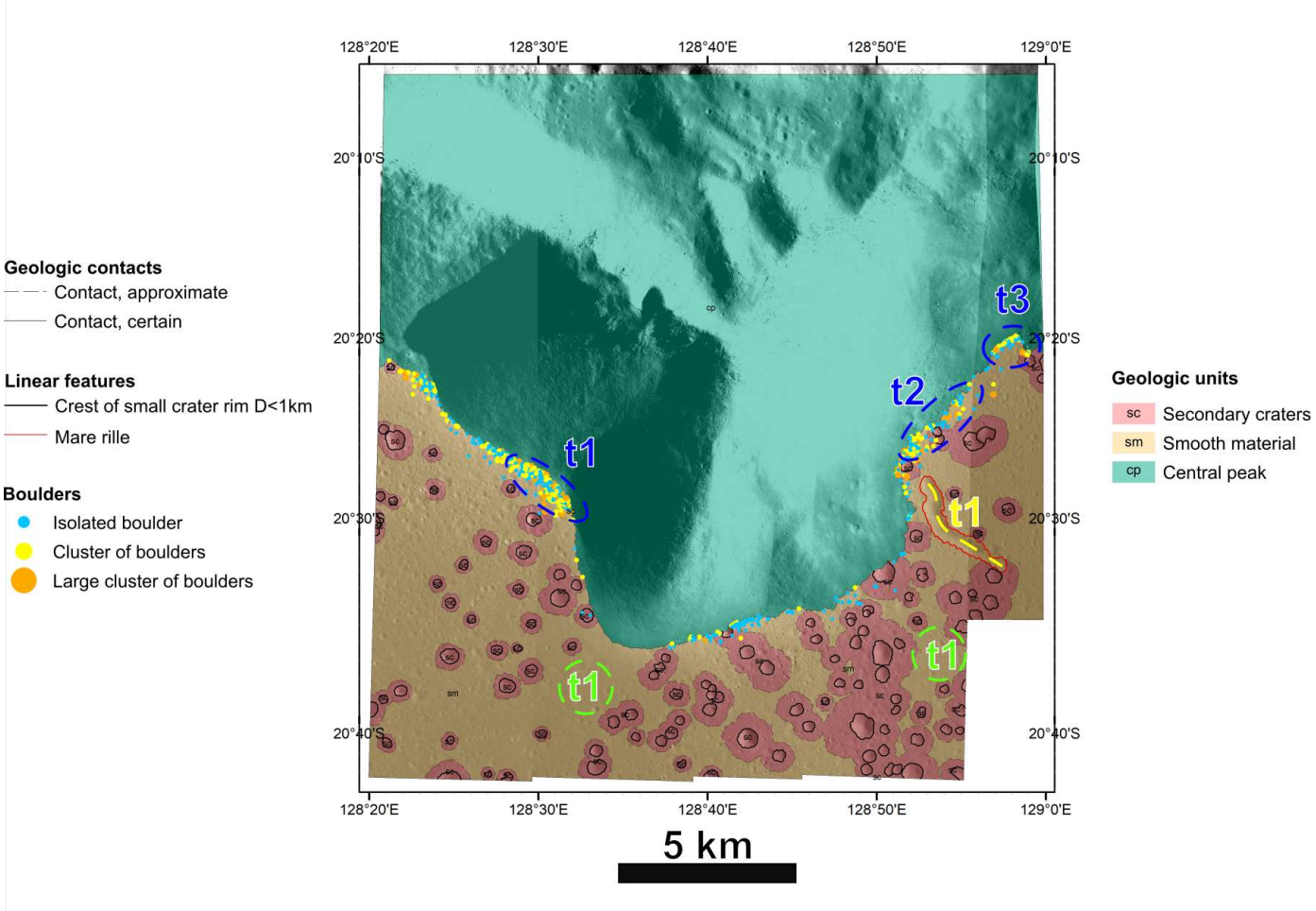

Figure 3.34: Identification of target (tx) areas worthy to be better analyzed in a landing site characterization.

3.5 Discussion

The morpho-stratigraphic map presented here constitutes an advance with respect to previous maps (Gornitz, 1973; Tyrie, 1988; Craddock and Greeley, 1988; Fortezzo et al., 2020; Morse et al., 2021) providing a more thorough geologic insight into the Tsiolkovskiy crater. Combined with the unprecedented color-based spectral map, the new map makes it possible to integrate morphological evidence and compositional information. Moreover, the detailed CSFD measurements permit a better understanding of the geologic evolution of this crater, in particular of its lava emplacements.

Even at first glance, it is possible to observe a correlation between the different units identified by the morpho-stratigraphic (Figure 3.22) and color-based spectral (Figure 3.28) maps. The most striking feature is the correlation between the *sm* geologic unit and the *bp1*, *bp2* and *bp3* spectral units attributable to Tsiolkovskiy's crater floor. Conversely, the hummocky material of the *hm* unit is not as easily ascribable to a spectral color unit. Nonetheless, it can be associated in essence with the same material constituting the *hs* unit, with exposures from the *nt* and *an* units. This is reasonable given the impact origin of the debris in this unit. The *hs* spectral unit, moreover, is predominantly correlated with the *is* unit and it includes also the scattered *sp* units, which in the color-based spectral mapping appear homogenized with the surrounding *hs* unit material. Finally, the fresher deposits exposed by the excavation of the crater ascribed to the *is*, *ss* and *cp* units are clearly associated with the *nt* and *an* spectral units.

Another evident characteristic is that the asymmetric distribution of Tsiolkovskiy's ejecta is not the only asymmetry related to this crater. Indeed, the morpho-stratigraphic map shows that the hummocky material is largely distributed on the western margin of the smooth crater floor relative to the east side. In contrast, the steep scarps and the ponds of smooth material scattered in between the terraces of the rim are more widespread on the SE side of the crater rim than on the NW side.

This is partially reflected also in the irregular distribution of the units identified from the color-based mapping where the NW crater rim is largely made up of the *hs* unit while the SE side of the crater rim is mostly made up of the *nt* and *an* units.

The peculiar distribution of the units presumably reflects the oblique impact origin of the Tsiolkovskiy crater. The SE inner slope proves to have been more affected by the impact than the NW one. It is indeed characterized by widespread rocky slumps and a larger number of steep

scarps that led to the exhumation of greater amounts of *nt* and *an* unit materials. Furthermore, even the reduced presence of hummocky patches on the SE portion of the crater floor could be the result of the covering of these areas by larger volumes of effusion generated in the downrange portion of the crater. In the downrange direction of an oblique impact, the thickness of crust excavated and mostly affected by the impact is greater than in the uprange direction (Pierazzo and Melosh (2000), and references therein). The removal of larger amounts of material and the impact-induced fracturing could have led to an upwelling of lavas in greater quantities with respect to the uprange direction that were nonetheless insufficient to bridge the topographic gap between the NW sector and the SE one.

Finally, the crater counts performed on the *hm* unit (Figure 3.25, white polygons) and interpreted as impact melt material returned a formation age of about 3.6 Ga, which is in accordance with the results derived by (Boyce et al., 2020) on ejecta and landslide deposits.
The apparent discrepancy of our ages with those obtained by (Williams et al., 2013; Pasckert et al., 2015; Greenhagen et al., 2016) lies in the different reference area used for the crater counting. The sum of the ages I derived from the color variegated smooth crater floor (i.e. *bp1*, *bp2* and *bp3* units) returned an average age of 3.28 Ga which is consistent with earlier authors' results of 3.2-3.3 Ga obtained on the same geomorphologic unit.
Nevertheless, the CSFDs I performed on the color units of the mare infilling permit the identification of three different age ranges (i.e. 2.88-2.98 Ga, 3.32-3.47 Ga and 3.57 Ga) clearly associated with each one of the three units (i.e. *bp1*, *bp2* and *bp3* units) being the result of distinct eruptive events. In saying this, I do not presume that only three lava emplacements took place within Tsiolkovskiy, but that at least three events characterized by distinct compositions and ages are discernible.

Furthermore, it is noteworthy that there is strong correlation between the different eruptive events and their color variations from the Clementine UVVIS Color Ratio mosaic and the LROC-WAC-derived TiO_2 abundance estimation basemap by (Sato et al., 2017) (Figure 3.35). In particular, the yellow color and the brighter yellow-green hues of the oldest *bp3* unit in the Clementine UVVIS Color Ratio mosaic indicate a basaltic unit exposed for a longer time to space weathering and thus characterized by a higher degree of maturity. A bluer Clementine color indicative of higher amounts of titanium characterizes instead the intermediate *bp2* unit

which shows a TiO_2 content of up to 4-6 wt%, while the youngest *bp1* unit is characterized by a redder Clementine color, indicative of lower proportions of titanium, with a TiO_2 content <4 wt%.

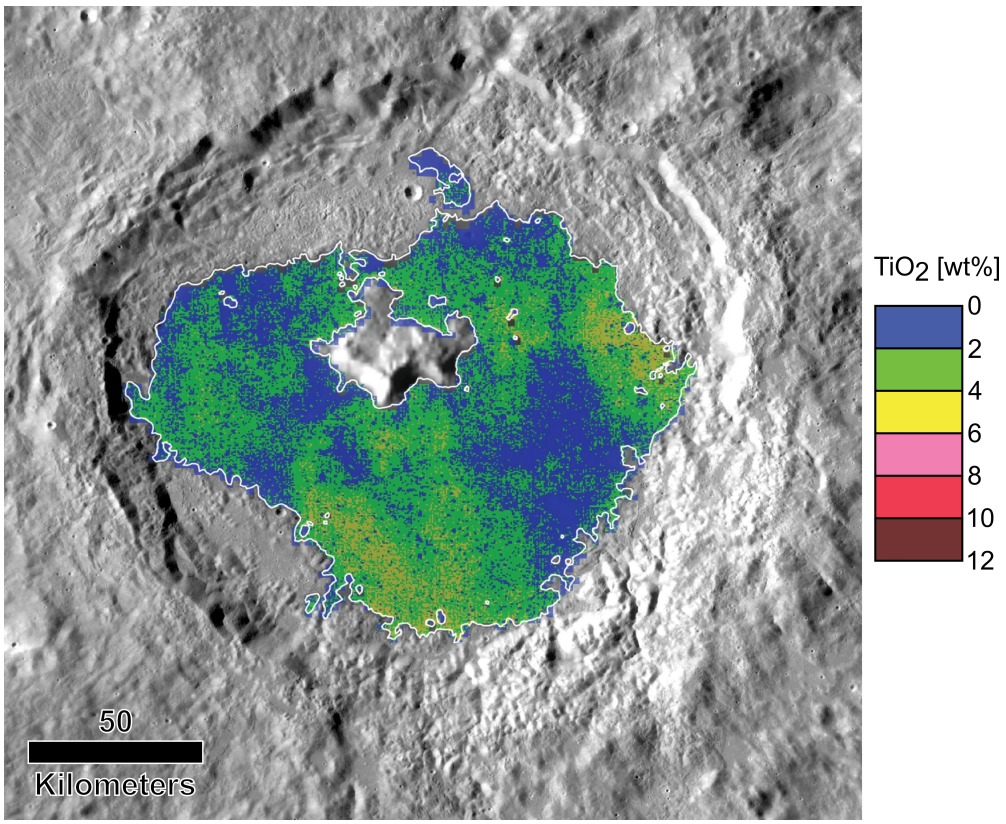

Figure 3.35: LROC-WAC-derived TiO_2 abundance estimation basemap of Tsiolkovskiy's mare infilling, modified from (Sato et al., 2017). The color bar indicates 2 wt% bins in TiO_2 content.

This suggests a compositional difference characterizing the flooding events between 3.6 and 3.4 Ga and around 3.0 Ga, probably indicating a shift in lunar far side volcanism. After the first lava emplacements (∼3.6 Ga), the production of lavas relatively enriched in titanium content (between 3.6 and 3.4 Ga) could have been due to i) the assimilation of TiO_2-enriched rocks, ii) the involvement of a TiO_2-enriched plutonic body located at the crust-mantle boundary or within the lower crust or iii) a distinct magmatic source relatively enriched in titanium content. Subsequently, during the late-stage activity (≤3.0 Ga), the lavas underwent a progressive depletion in the proportion of titanium.

Finally, the presence of younger basalts in particular on the south and west margins of the smooth floor could be the result of the load exerted by older lava emplacements that might have forced the new lavas to flow out into lower-pressure zones such as at the margins of the basaltic

infilling.

Mare volcanism in the Tsiolkovskiy crater, to resume, started in the Late Imbrian and concluded in the Erathostenian period lasting for about 690 Ma.

Another far side mare flooded crater underwent a similar evolution to Tsiolkovskiy's: it is the ∼445 km Moscoviense basin. Despite the different crater diameter, both Tsiolkovskiy and Moscoviense are characterized by an extended effusive activity (∼1.5 Ga for Moscoviense) with the effusions changing in composition, from the oldest and TiO_2-depleted to the youngest and TiO_2-enriched lavas (Morota et al., 2009; Thaisen et al., 2011). The larger volumes of basalts and the longer duration of the flooding event in the Moscoviense basin with respect to the Tsiolkovskiy crater can be attributed to the different crater diameter and the different crustal thickness, being of <5 km and of ∼40 km for the Moscoviense basin and the Tsiolkovskiy crater respectively (Wieczorek et al., 2013).

Even from the spectro-stratigraphic map (Figure 3.29), it is possible to discern a certain correlation between morphology and spectral information. The presence of 3 different flooding events, in particular, is yet again confirmed by 3 SUs (i.e. *SU1*, *SU2* and *SU3*) localized on Tsiolkovskiy's smooth floor and characterized by low reflectance values. The distribution of the *SU1*, *SU2* and *SU3* is fairly well correlated with the distribution of the *bp2*, *bp1* and *bp3* units, respectively.

In the average reflectance spectra, the *SU1*, *SU2* and *SU3*, moreover, stand out for presenting the lowest spectral slopes and the strongest absorptions around 1000 nm and 2100-2200 nm (Figure 3.30). Even further, by comparing the average derived BCI and BCII obtained for Ca-free, low-Ca and high-Ca synthetic pyroxenes with the BCI and BCII of the SUs, the *SU1*, *SU2* and *SU3* are characterized by a similar composition suggesting a low to high Ca content (∼20%) and highest Fe content. This composition is in common also with the *SU6*, *SU7* and *SU10*, of which the *SU6* and *SU10* present also the highest absorption bands at 1000 nm and 2100-2200 nm, after the *SU1*, *SU2* and *SU3*.

As concerns the high-resolution geologic map, the choice of focusing a landing site proposal on a crater's central peak is innovative both in terms of exploration target and location (i.e. near side vs far side). If the China National Space Administration's Chang'e 4 mission was the first robotic mission to land on the far side of the Moon, a mission dedicated to the exploration

of the surroundings of a central peak, indeed, has yet to come.

As stated in chapter 3.1.4, the formation of Tsiolkovskiy's central peak could have exhumed material from the lower crust, or even from the upper mantle. Moreover, the detection of both PAN and olivine make of the material composing the central peak a key scientific target for understanding the lunar interior's origin and evolution.

Considering that over time some boulders could have collapsed from the walls of the peak to its base, as evidenced by rolling trails (Figure 3.32), a robotic mission in this area could be dedicated to the sampling and analysis, in terms of chemistry, mineralogy and texture, of these rocks making it possible to study lower crust materials otherwise out of reach.

Of particular interest, moreover, are the possibility to study the onlap relationships between the basaltic infilling and the central peak morphology and the possible internal layering of regolith and basalts visible on the wall of the mare rille located to the southeast of the peak (Figure 3.34).

The antipodal position of the Tsiolkovskiy crater with respect to the Oceanus Procellarum and the landing safety guaranteed by its particularly smooth floor, finally, allowed to this crater to be proposed as a target area for the possible future deployment of a seismic station. This station would be part of a lunar network of seismometers, to be positioned on the northern plains of Oceanus Procellarum, which would allow to monitor the lunar surface vibrations caused by gravitational waves, to perform electromagnetic observations and to provide a deep view into the internal structure of the Moon (Harms et al., 2021) (see also `https://bit.ly/3ewQGk4`).

Chapter 4

Conclusions

The cartographic products produced during this research project aimed at providing a geologic overview of two different contexts, a broad region on Mercury (half a quadrangle) and a wide crater on the Moon.
As part of the European Horizon 2020 PLANMAP project, these products aim at delivering the highest level of information by coupling different types of datasets. Geologic maps based on photo-interpretation of the surface morphology, indeed, have been integrated with color-based spectral maps performed on color-derived basemaps that allowed inferring more about the geology of these areas also in terms of spectral variations. The final aim of these products is to characterize the geology, geologic and compositional evolution of planetary surfaces for supporting the targeting of instruments onboard the ongoing and future planetary missions by contributing to the selection of regions of interest.

The 1:3M regional small-scale mapping for the eastern portion of the H-9 Eminescu quadrangle (22.5°N-22.5°S, 108°E -144°E) on Mercury was produced to constrain the geo-morphological analysis of a quadrangle that was not yet mapped in detail. The mapping was performed on 85.45% of the working area (3.29% of Mercury's surface). The present geologic framework highlighted as the area in the northeastern side was largely affected by the formation of the Caloris basin, which led to the flattening of the surface, by exterior volcanic plains emplacement, and the formation of deposits (i.e. *CRE*, *OF*, *VEF*) and deformational structures connected to its impact. On the southern side, on the other hand, impact cratering played a major role in shaping the surface morphology. The coupling with the color-based spectral mapping based on color variations, in addition, allowed inferring more information than from monochrome imagery alone

discriminating spectral differences within geologic units, such as smooth crater floors presenting different color hues possibly associated with distinct flooding events.
The in-depth knowledge of the working area, finally, led to the definition of 31 scientific targets of interest to be investigated by the SIMBIO-SYS cameras in coordination with other onboard instruments the BepiColombo dual spacecraft, like BELA, MERTIS, MIXS and MGNS. The proposed targets range from faulted crater allowing to study the kinematic of tectonic structures, to hollows, occasionally associated with LRMs or pyroclastic deposits, for determining their nature and changes over time, up to central peaks exhuming underlying materials with a different composition that would allow investigating the compositional variations of the hermean crust.

The ∼3.60 Ga old lunar far side Tsiolkovskiy crater (20.4°S, 129.1°E) can be summarized as the result of an oblique impact on highland crust. The impact led to the excavation and consequent exhumation of materials less affected by space weathering, such as norites and anorthosites, that combined with mature highland soil constitute the crater rim, the uplifted central peak and the hummocky crater floor. The crater floor was then partially filled by a basaltic deposit generated by at least 3 distinct eruptive events, distinguishable on the basis of their color, spectral properties (i.e. composition) and age. In particular, color-based spectral mapping distinguished 3 different units for the crater floor, characterized by distinctive Clementine color ratio values (i.e. *bp1*, *bp2* and *bp3* units). The CSFD measurements performed on 3 areas respectively for the *bp1* and *bp2* units and on 2 areas for the *bp3* unit made it possible to define an approximate time frame for each unit, with average ages of 2.94, 3.42 and 3.57 Ga. These age determinations allowed the reconstruction of the evolutionary history of the crater floor, with the *bp1* unit being the youngest basaltic unit followed by the intermediate *bp2* unit and the oldest *bp3* unit. The different compositions of the units, with the *bp2* unit presenting the highest proportion of titanium, seem to imply different magma sources and/or suggest melting of TiO_2-enriched material at around 3.40 Ga.
The oblique impact origin of Tsiolkovskiy is reflected also in the distribution of the units. Relative to the NW uprange portion of the crater, the SE downrange portion presents a greater quantity of excavated material (composing the *nt* and *an* units) and rocky slumps and sparse pre-mare material (the *hm* unit), with the latter probably due to the production of larger effusions in the downrange direction.

The further integration with data conveying the spectral information coming from several spectral indexes, moreover, discriminated again the presence of 3 distinct SUs for the smooth crater floor (i.e. *SU1*, *SU2* and *SU3*) characterized by low reflectance values and fairly well correlated with the *bp1*, *bp2* and *bp3* units. These SUs, presenting the lowest spectral slopes and the strongest absorptions (Figure **??**), are characterized by the presence of low to high Ca pyroxenes (pigeonites and/or augites).

Finally, the high-resolution geologic map, produced to laying the groundwork for a landing site characterization, highlighted as Tsiolkovskiy's central peak represents an interesting area for future exploration. Several target areas to perform in-situ analyses were identified (Figure 3.34), but the most striking target is represented by boulders collapsed from the central peak to its base and that would allow the analysis of rocks from the far side lower crust/mantle boundary.

Appendix A

PLANMAP and GMAP deliverables

Table A.1: List of cited deliverables with related links from PLANMAP and GMAP.

Deliverable	Link
PLANMAP D2.1 – Mapping standards definition document	https://wiki.planmap.eu/public/attachments/8193472/8193931.pdf
PLANMAP D4.1 – Spectral index and RGB maps - version 1	https://wiki.planmap.eu/public/attachments/8193472/16777860.pdf
PLANMAP D4.2 – Spectral index and RGB maps - version 2	https://wiki.planmap.eu/public/attachments/8193472/29622289.pdf
PLANMAP D4.3 – Spectral index and RGB maps - version 3	https://wiki.planmap.eu/public/attachments/8193472/30081844.pdf
PLANMAP D4.4 – Retrieved compositional units	https://wiki.planmap.eu/public/attachments/8193472/30083907.pdf
GMAP D8.3 – Mapping training material: basic geological maps	https://www.europlanet-society.org/wp-content/uploads/2021/09/D8.3.pdf
GMAP D9.1 – Standardization definition document	https://www.europlanet-society.org/wp-content/uploads/2020/11/D9.1_Standard-definition-Document-1st-iteration_EPN2024RI_Public-v2.pdf

Appendix B

Mercury data catalog

Table B.1: List of basemaps used for the geologic mapping of the H-9 Eminescu quadrangle with original filenames, spatial resolutions and sources.

Basemap	Original filename	Resolution [m/px]	Source
MDIS BDR	MDIS_BDR_256PPD_H*aabb*2[1]	166	PDS
MDIS HIE	MDIS_HIE_256PPD_H*aabb*2[1]	166	PDS
MDIS HIW	MDIS_HIW_256PPD_H*aabb*2[1]	166	PDS
MDIS LOI	MDIS_LOI_256PPD_H*aabb*2[1]	166	PDS
USGS DEM	Mercury_Messenger_USGS_DEM_Global_665m_v2	665	USGS
MDIS Enhanced Color mosaic	Mercury_MESSENGER_MDIS_Basemap _EnhancedColor_Mosaic_Global_665m	665	USGS
MDIS MD3 Color mosaic	Mercury_MESSENGER_MDIS_Basemap _MD3Color_Mosaic_Global_665m	665	USGS

[1]aa and *bb* refer to the quadrangle and the tile (NE, NW, SE and SW) respectively

Appendix C

Geologic units, legend description

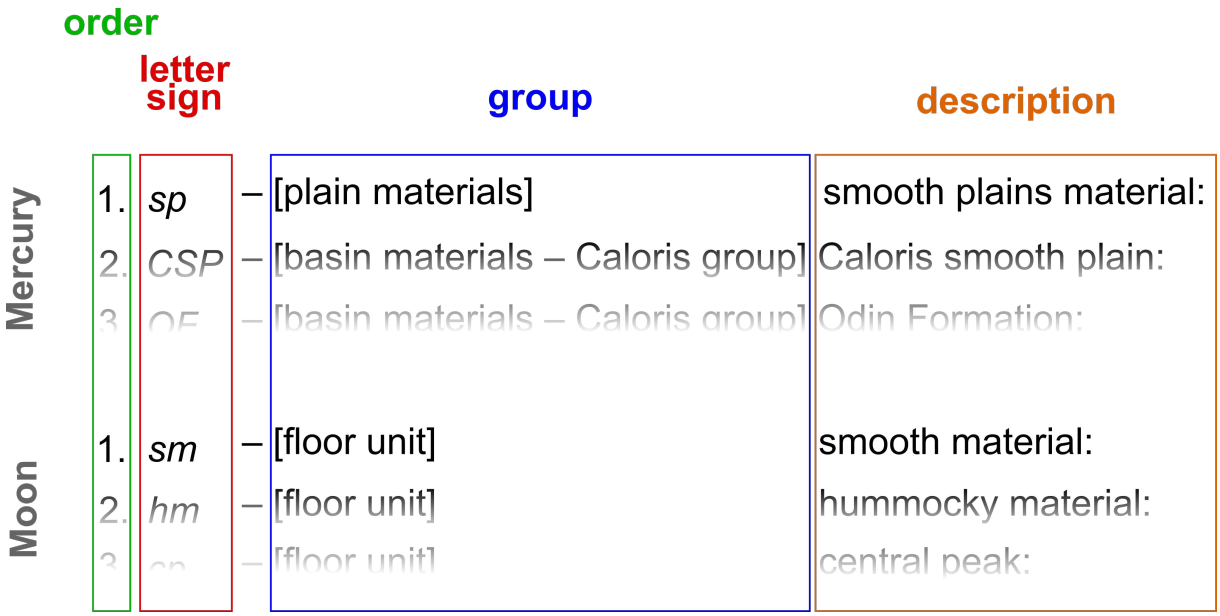

Figure C.1: Geologic units presented in the main chapters are descripted using the following scheme: stratigraphic order, letter sign, group and description, for both Mercury and the Moon.

Appendix D

Moon data catalog

Table D.1: List of basemaps used for the geologic study of the Tsiolkovskiy crater with original filenames, spacial resolutions and sources.

Basemap	Original filename	Resolution [m/px]	Source
LROC-WAC	Lunar_LRO_LROC-WAC_Mosaic_global_100m_June2013	100	USGS
LROC-LOLA & Kaguya TC DEM	Lunar_LRO_LrocKaguya_DEMmerge_60N60S_512ppd	59	USGS
UVVIS Clementine Warped Color Ratio mosaic	Lunar_Clementine_UVVIS_Warp_ClrRatio_Global_200m	200	USGS
Kaguya TC	DTMTCO_03_02900S169E1327SC_img	10^1	KDA[2]
Kaguya TC	DTMTCO_03_02900S183E1327SC_img	10^1	KDA[2]
Kaguya TC	DTMTCO_03_02900S197E1327SC_img	10^1	KDA[2]
Kaguya TC	DTMTCO_03_02900S211E1327SC_img	10^1	KDA[2]
Kaguya TC	DTMTCO_03_02900S225E1327SC_img	10^1	KDA[2]
Kaguya TC	DTMTCO_03_02900S239E1327SC_img	10^1	KDA[2]
Kaguya TC	DTMTCO_03_02901S169E1316SC_img	10^1	KDA[2]
Kaguya TC	DTMTCO_03_02901S183E1316SC_img	10^1	KDA[2]
Kaguya TC	DTMTCO_03_02901S197E1316SC_img	10^1	KDA[2]
Kaguya TC	DTMTCO_03_02901S211E1316SC_img	10^1	KDA[2]
Kaguya TC	DTMTCO_03_02901S225E1316SC_img	10^1	KDA[2]
Kaguya TC	DTMTCO_03_02901S238E1316SC_img	10^1	KDA[2]
Kaguya TC	DTMTCO_03_02902S169E1306SC_img	10^1	KDA[2]
Kaguya TC	DTMTCO_03_02902S183E1306SC_img	10^1	KDA[2]
Kaguya TC	DTMTCO_03_02902S197E1306SC_img	10^1	KDA[2]
Kaguya TC	DTMTCO_03_02902S211E1305SC_img	10^1	KDA[2]

Kaguya TC	DTMTCO_03_02902S225E1305SC_img	10^1	KDA^2
Kaguya TC	DTMTCO_03_02902S239E1305SC_img	10^1	KDA^2
Kaguya TC	DTMTCO_03_02903S169E1295SC_img	10^1	KDA^2
Kaguya TC	DTMTCO_03_02903S183E1295SC_img	10^1	KDA^2
Kaguya TC	DTMTCO_03_02903S197E1295SC_img	10^1	KDA^2
Kaguya TC	DTMTCO_03_02903S211E1295SC_img	10^1	KDA^2
Kaguya TC	DTMTCO_03_02903S224E1295SC_img	10^1	KDA^2
Kaguya TC	DTMTCO_03_02903S238E1295SC_img	10^1	KDA^2
Kaguya TC	DTMTCO_03_02904S169E1284SC_img	10^1	KDA^2
Kaguya TC	DTMTCO_03_02904S169E1284SC_img	10^1	KDA^2
Kaguya TC	DTMTCO_03_02904S197E1284SC_img	10^1	KDA^2
Kaguya TC	DTMTCO_03_02904S211E1284SC_img	10^1	KDA^2
Kaguya TC	DTMTCO_03_02904S224E1284SC_img	10^1	KDA^2
Kaguya TC	DTMTCO_03_02904S238E1284SC_img	10^1	KDA^2
Kaguya TC	DTMTCO_03_02905S169E1273SC_img	10^1	KDA^2
Kaguya TC	DTMTCO_03_02905S183E1273SC_img	10^1	KDA^2
Kaguya TC	DTMTCO_03_02905S196E1273SC_img	10^1	KDA^2
Kaguya TC	DTMTCO_03_02905S210E1273SC_img	10^1	KDA^2
Kaguya TC	DTMTCO_03_02905S224E1273SC_img	10^1	KDA^2
Kaguya TC	DTMTCO_03_02905S238E1273SC_img	10^1	KDA^2
Kaguya TC	DTMTCO_03_02906S169E1263SC_img	10^1	KDA^2
Kaguya TC	DTMTCO_03_02906S183E1263SC_img	10^1	KDA^2
Kaguya TC	DTMTCO_03_02906S210E1263SC_img	10^1	KDA^2
Kaguya TC	DTMTCO_03_02906S224E1263SC_img	10^1	KDA^2
Kaguya TC	DTMTCO_03_02906S238E1263SC_img	10^1	KDA^2
Kaguya TC	DTMTCO_03_02907S169E1252SC_img	10^1	KDA^2
Kaguya TC	DTMTCO_03_02907S183E1252SC_img	10^1	KDA^2
Kaguya TC	DTMTCO_03_02907S196E1252SC_img	10^1	KDA^2
Kaguya TC	DTMTCO_03_02907S210E1252SC_img	10^1	KDA^2
Kaguya TC	DTMTCO_03_02907S224E1252SC_img	10^1	KDA^2
Kaguya TC	DTMTCO_03_02907S238E1252SC_img	10^1	KDA^2
LROC-NAC	M146140171LE	0.61	PILOT
LROC-NAC	M146140171RE	0.61	PILOT
LROC-NAC	M1107453852LE	0.88	PILOT
LROC-NAC	M103682642RE	0.88	PILOT
LROC-NAC	M103682642LE	0.89	PILOT
LROC-NAC	M165015246LE	0.91	PILOT
LROC-NAC	M165015246RE	0.91	PILOT
LROC-NAC	M192116691RE	0.91	PILOT
LROC-NAC	M115469124LE	0.91	PILOT
LROC-NAC	M192109542LE	0.92	PILOT
LROC-NAC	M192116691LE	0.92	PILOT
LROC-NAC	M192109542RE	0.93	PILOT
LROC-NAC	M1183978587RE	0.95	PILOT
LROC-NAC	M1183978587LE	0.96	PILOT

LROC-NAC	M1174571696LE	0.96	PILOT
LROC-NAC	M1174571696RE	0.96	PILOT
LROC-NAC	M1218112965LE	1.12	PILOT
LROC-NAC	M1218112965RE	1.12	PILOT
LROC-NAC	M1187511756RE	1.12	PILOT
LROC-NAC	M1202818973LE	1.17	PILOT
LROC-NAC	M1202818973RE	1.17	PILOT
LROC-NAC	M1202797929LE	1.24	PILOT
LROC-NAC	M1202797929RE	1.24	PILOT
LROC-NAC	M1125111804LE	1.30	PILOT
LROC-NAC	M1125111804RE	1.30	PILOT
LROC-NAC	M1126296816LE	1.30	PILOT
LROC-NAC	M1126296816RE	1.30	PILOT
LROC-NAC	M180336439LE	1.32	PILOT
LROC-NAC	M180336439RE	1.32	PILOT
LROC-NAC	M1126303929LE	1.33	PILOT
LROC-NAC	M1126303929RE	1.34	PILOT
LROC-NAC	M1141585968LE	1.34	PILOT
LROC-NAC	M1141585968RE	1.34	PILOT
LROC-NAC	M1095658447LE	1.35	PILOT
LROC-NAC	M1095665593LE	1.41	PILOT
LROC-NAC	M1095665593LE	1.41	PILOT
LROC-NAC	M1095665593RE	1.42	PILOT
LROC-NAC	M1155723599LE	1.44	PILOT
LROC-NAC	M1233391551RE	1.44	PILOT
LROC-NAC	M1155723599RE	1.45	PILOT
LROC-NAC	M1233391551LE	1.46	PILOT
LROC-NAC	M1155716479RE	1.53	PILOT
M3	M3G20090529T230608_V01_RFL	140	PDS
M3	M3G20090529T183825_V01_RFL	140	PDS
M3	M3G20090529T143509_V01_RFL	140	PDS
M3	M3G20090530T030925_V01_RFL	140	PDS

[1]mean spatial resolution; [2]Kaguya Data Archive

Bibliography

Abbud-Madrid, A. (2018). Planetary geology. In *Planetary geology*, pages 369–394. Springer-Praxis.

Ahrens, T. J. and Rubin, A. M. (1993). Impact-induced tensional failure in rock. *Journal of Geophysical Research*, 98(E1):1185–1203.

Anand, M., Crawford, I. A., Balat-Pichelin, M., Abanades, S., Van Westrenen, W., Péraudeau, G., Jaumann, R., and Seboldt, W. (2012). A brief review of chemical and mineralogical resources on the Moon and likely initial in situ resource utilization (ISRU) applications. *Planetary and Space Science*, 74:42–48.

Baasch, J., Windisch, L., Koch, F., Linke, S., Stoll, E., and Schilde, C. (2021). Regolith as substitute mold material for aluminum casting on the Moon. *Acta Astronautica*, 182:1–12.

Banks, M. E., Watters, T. R., Robinson, M. S., Tornabene, L. L., Tran, T., Ojha, L., and Williams, N. R. (2012). Morphometric analysis of small-scale lobate scarps on the Moon using data from the Lunar Reconnaissance Orbiter. *Journal of Geophysical Research*, 117(3):1–11.

Banks, M. E., Xiao, Z., Braden, S. E., Marchi, S., Chapman, C. R., Barlow, N. G., and Fassett, C. (2016). Revised age constraints for Mercury's Kuiperian and Mansurian systems. *47th Lunar and Planetary Science Conference*, page 2943.

Barker, M. K., Mazarico, E., Neumann, G. A., Zuber, M. T., Haruyama, J., and Smith, D. E. (2016). A new lunar digital elevation model from the Lunar Orbiter Laser Altimeter and SELENE Terrain Camera. *Icarus*, 273:346–355.

Becker, K. J., Robinson, M. S., Becker, T. L., Weller, L. A., Edmundson, K. L., Neumann, G. A., Perry, M. E., and Solomon, S. C. (2016). First global digital elevation model of Mercury. *47th Lunar and Planetary Science Conference*, page 2959.

Benkhoff, J., van Casteren, J., Hayakawa, H., Fujimoto, M., Laakso, H., Novara, M., Ferri, P., Middleton, H. R., and Ziethe, R. (2010). BepiColombo-Comprehensive exploration of Mercury: Mission overview and science goals. *Planetary and Space Science*, 58:2–20.

Benz, W., Slattery, W. L., and Cameron, A. G. W. (1988). Collisional stripping of Mercury's mantle. *Icarus*, 74(3):516–528.

Bhandari, N. and Srivastava, N. (2014). Active moon: evidences from Chandrayaan-1 and the proposed Indian missions. *Geoscience Letters*, 1(11).

Blair, D. M., Freed, A. M., Byrne, P. K., Klimczak, C., Prockter, L. M., Ernst, C. M., Solomon, S. C., Melosh, H. J., and Zuber, M. T. (2013). The origin of graben and ridges in Rachmaninoff, Raditladi, and Mozart basins, Mercury. *Journal of Geophysical Research: Planets*, 118:47–58.

Blewett, D. T., Chabot, N. L., Denevi, B. W., Ernst, C. M., Head, J. W., Izenberg, N. R., Murchie, S. L., Solomon, S. C., Nittler, L. R., McCoy, T. J., Xiao, Z., Baker, D. M. H., Fassett, C. I., Braden, S. E., Oberst, J., Scholten, F., Preusker, F., and Hurwitz, D. M. (2011). Hollows on Mercury: MESSENGER evidence for geologically recent volatile-related activity. *Science*, 333(6051):1856–1859.

Blewett, D. T., Lucey, P. G., Hawke, B. R., Ling, G. G., and Robinson, M. S. (1997). A comparison of mercurian reflectance and spectral quantities with those of the Moon. *Icarus*, 129:217–231.

Blewett, D. T., Vaughan, W. M., Xiao, Z., Chabot, N. L., Denevi, B. W., Ernst, C. M., Helbert, J., D'Amore, M., Maturilli, A., Head, J. W., and Solomon, S. C. (2013). Mercury's hollows: Constraints on formation and composition from analysis of geological setting and spectral reflectance. *Journal of Geophysical Research: Planets*, 118:1013–1032.

Boyce, J. M., Mouginis-Mark, P., and Robinson, M. (2020). The Tsiolkovskiy crater landslide, the moon: An LROC view. *Icarus*, 337:113464.

Bussey, D. B. J., Guest, J. E., and Sorensen, S. A. (1997). On the role of thermal conductivity on thermal erosion by lava. *Journal of Geophysical Research*, 102(E5):10905–10908.

Butler, B. J., Muhleman, D. O., and Slade, M. A. (1993). Mercury: full-disk radar images and the detection and stability of ice at the North Pole. *Journal of Geophysical Research*, 98(E8):15003–15023.

Byrne, P. K., Klimczak, C., Sengör, A. M. C., Solomon, S. C., Watters, T. R., and Hauck, S. A. (2014a). Mercury's global contraction much greater than earlier estimates. *Nature Geoscience*, 7:301–307.

Byrne, P. K., Klimczak, C., Solomon, S. C., Mazarico, E. M., Neumann, G. A., and Zuber, M. T. (2014b). Deep-seated contractional tectonics in Mare Crisium, the Moon. *45th Lunar and Planetary Science Conference*, page 2396.

Byrne, P. K., Klimczak, C., Williams, D. A., Hurwitz, D. M., Solomon, S. C., Head, J. W., Preusker, F., and Oberst, J. (2013). An assemblage of lava flow features on Mercury. *Journal of Geophysical Research: Planets*, 118:1303–1322.

Cameron, A. G. W. (1985). The partial volatilization of Mercury. *Icarus*, 64:285–294.

Canup, R. M. (2004). Simulations of a late lunar-forming impact. *Icarus*, 168:433–456.

Chabot, N. L., Ernst, C. M., Harmon, J. K., Murchie, S. L., Solomon, S. C., Blewett, D. T., and Denevi, B. W. (2013). Craters hosting radar-bright deposits in Mercury's north polar region: Areas of persistent shadow determined from MESSENGER images. *Journal of Geophysical Research: Planets*, 118:26–36.

Colombo, G. (1965). Rotational period of the planet Mercury. *Nature*, 208(5010):575.

Corley, L. M., McGovern, P. J., Kramer, G. Y., Lemelin, M., Trang, D., Gillis-Davis, J. J., Taylor, G. J., Powell, K. E., Kiefer, W. S., Wieczorek, M., and Zuber, M. T. (2018). Olivine-bearing lithologies on the Moon: Constraints on origins and transport mechanisms from M3 spectroscopy, radiative transfer modeling, and GRAIL crustal thickness. *Icarus*, 300:287–304.

Craddock, R. A. and Greeley, R. (1988). Thickness and volume of mare deposits in Tsiolkovsky, lunar farside. In *18th Lunar and Planetary Science Conference*, pages 331–337.

Crane, K. T. and Klimczak, C. (2019). Tectonic patterns of shortening landforms in Mercury's northern smooth plains. *Icarus*, 317:66–80.

Cremonese, G., Capaccioni, F., Capria, M. T., Doressoundiram, A., Palumbo, P., Vincendon, M., Massironi, M., Debei, S., Zusi, M., Altieri, F., Amoroso, M., Aroldi, G., Baroni, M., Barucci, A., Bellucci, G., Benkhoff, J., Besse, S., Bettanini, C., Blecka, M., Borrelli, D., Brucato, J. R., Carli, C., Carlier, V., Cerroni, P., Cicchetti, A., Colangeli, L., Dami, M.,

Da Deppo, V., Della Corte, V., De Sanctis, M. C., Erard, S., Esposito, F., Fantinel, D., Ferranti, L., Ferri, F., Ficai Veltroni, I., Filacchione, G., Flamini, E., Forlani, G., Fornasier, S., Forni, O., Fulchignoni, M., Galluzzi, V., Gwinner, K., Ip, W., Jorda, L., Langevin, Y., Lara, L., Leblanc, F., Leyrat, C., Li, Y., Marchi, S., Marinangeli, L., Marzari, F., Mazzotta Epifani, E., Mendillo, M., Mennella, V., Mugnuolo, R., Muinonen, K., Naletto, G., Noschese, R., Palomba, E., Paolinetti, R., Perna, D., Piccioni, G., Politi, R., Poulet, F., Ragazzoni, R., Re, C., Rossi, M., Rotundi, A., Salemi, G., Sgavetti, M., Simioni, E., Thomas, N., Tommasi, L., Turella, A., Van Hoolst, T., Wilson, L., Zambon, F., Aboudan, A., Barraud, O., Bott, N., Borin, P., Colombatti, G., El Yazidi, M., Ferrari, S., Flahaut, J., Giacomini, L., Guzzetta, L., Lucchetti, A., Martellato, E., Pajola, M., Slemer, A., Tognon, G., and Turrini, D. (2020). SIMBIO-SYS: Scientific Cameras and Spectrometer for the BepiColombo Mission. *Space Science Reviews*, 216.

Danielson, G. E., Klaasen, K. P., and Anderson, J. L. (1975). Acquisition and description of Mariner 10 television science data at Mercury. *Journal of Geophysical Research*, 80(17):2357–2393.

Davies, M. E., Dornik, S. E., Gault, D. E., and Strom, R. G. (1978). *Atlas of Mercury*, volume 423. NASA Special Publication.

DeHon, R. A., Scott, D. H., and Underwood, J. R. (1981). Geologic map of the Kuiper quadrangle of Mercury. *U.S. Geological Survey Report*, pages Map I–1233.

Denevi, B. W., Ernst, C. M., Meyer, H. M., Robinson, M. S., Murchie, S. L., Whitten, J. L., Head, J. W., Watters, T. R., Solomon, S. C., Ostrach, L. R., Chapman, C. R., Byrne, P. K., Klimczak, C., and Peplowski, P. N. (2013). The distribution and origin of smooth plains on Mercury. *Journal of Geophysical Research: Planets*, 118:891–907.

Denevi, B. W., Ernst, C. M., Prockter, L. M., Robinson, M. S., Spudis, P. D., Klima, R. L., Murchie, S. L., Solomon, S. C., Whitten, J. L., Povilaitis, R. Z., and Kinczyk, M. J. (2016). The origin of Mercury's oldest surfaces and the nature of intercrater plains resurfacing. *47th Lunar and Planetary Science Conference*, page 1624.

Denevi, B. W., Robinson, M. S., Solomon, S. C., Murchie, S. L., Blewett, D. T., Domingue, D. L., McCoy, T. J., Ernst, C. M., Head, J. W., Watters, T. R., and Chabot, N. L. (2009). The evolution of Mercury's crust: A global perspective from MESSENGER. *Science*, 324(5927):613–618.

Di Achille, G., Popa, C., Massironi, M., Mazzotta Epifani, E., Zusi, M., Cremonese, G., and Palumbo, P. (2012). Mercury's radius change estimates revisited using MESSENGER data. *Icarus*, 221:456–460.

Ernst, C. M., Murchie, S. L., Barnouin, O. S., Robinson, M. S., Denevi, B. W., Blewett, D. T., Head, J. W., Izenberg, N. R., Solomon, S. C., and Roberts, J. H. (2010). Exposure of spectrally distinct material by impact craters on Mercury: Implications for global stratigraphy. *Icarus*, 209:210–223.

Fassett, C. I., Kadish, S. J., Head, J. W., Solomon, S. C., and Strom, R. G. (2011). The global population of large craters on Mercury and comparison with the Moon. *Geophysical Research Letters*, 38:1–6.

Fortezzo, C. M., Spudis, P. D., and Harrel, S. L. (2020). Release of the digital unified global geologic map of the Moon at 1:5,000,000-scale. In *51st Lunar and Planetary Science Conference*, page 2760.

Galluzzi, V. (2019). Multi-mapper projects: Collaborative mercury mapping. *Lecture Notes in Geoinformation and Cartography*, pages 207–218.

Galluzzi, V., Guzzetta, L., Ferranti, L., Di Achille, G., Rothery, D. A., and Palumbo, P. (2016a). Geology of the Victoria quadrangle (H02), Mercury. *Journal of Maps*, 12:227–238.

Galluzzi, V., Guzzetta, L., Mancinelli, P., Giacomini, L., Ferranti, L., Massironi, M., Palumbo, P., and Rothery, D. A. (2016b). Merging of new 1:3M Mercury geologic maps at northern mid-latitudes: Status report. *47th Lunar and Planetary Science Conference*, page 2119.

Galluzzi, V., Guzzetta, L., Mancinelli, P., Giacomini, L., Malliband, C. C., Mosca, A., Wright, J., Ferranti, L., Massironi, M., Pauselli, C., Rothery, D. A., and Palumbo, P. (2017). The 1:3M geologic map of Mercury: progress and updates. *EGU General Assembly 2017*, 19:13822.

Garrick-Bethell, I., Head, J. W., and Pieters, C. M. (2011). Spectral properties, magnetic fields, and dust transport at lunar swirls. *Icarus*, 212:480–492.

Gault, D. E., Guest, J. E., Murray, J. B., Dzurisin, D., and Malin, M. C. (1975). Some comparisons of impact craters on Mercury and the Moon. *Journal of Geophysical Research*, 80(17):2444–2460.

Giacomini, L., Carli, C., Zambon, F., Galluzzi, V., Ferrari, S., Massironi, M., Altieri, F., Ferranti, L., Palumbo, P., and Capaccioni, F. (2021). Integration between morphological and spectral characteristics for the geological map of Kuiper quadrangle (H06). *EGU General Assembly 2021*, page 15052.

Goins, N. R., Dainty, A. M., and Toksöz, M. N. (1981). Seismic energy release of the Moon. *Journal of Geophysical Research*, 86(B1):378–388.

Gornitz, V. (1973). Igneous vs impact processes for the origin of the mare lavas. *The Moon*, 6:357–379.

Goswami, J. N. and Annadurai, M. (2008). Chandrayaan-1 mission to the Moon. *Acta Astronautica*, 63:1215–1220.

Greeley, R. (1971). Lava tubes and channels in the lunar Marius Hills. *The Moon*, 3:289–314.

Greenhagen, B. T., Neish, C. D., Williams, J.-P., Cahill, J. T. S., Ghent, R. R., Hayne, P. O., Lawrence, S. J., Petro, N. E., and Bandfield, J. L. (2016). Origin of the anomalously rocky appearance of Tsiolkovskiy crater. *Icarus*, 273:237–247.

Grolier, M. J. and Boyce, J. M. (1984). Geologic map of the Borealis region (H-1) of Mercury. *U.S. Geological Survey Report*, pages Map I–1660.

Guest, J. E. and Greeley, R. (1983). Geologic map of the Shakespeare (H-3) quadrangle of Mercury. *U.S. Geological Survey Report*, pages Map I–1408.

Guest, J. E. and Murray, J. B. (1976). Volcanic features of the nearside equatorial lunar maria. *Journal of the Geological Society*, 132:251–258.

Guzzetta, L., Galluzzi, V., Ferranti, L., and Palumbo, P. (2017). Geology of the Shakespeare quadrangle (H03), mercury. *Journal of Maps*, 13(2):227–238.

Harms, J., Ambrosino, F., Angelini, L., Braito, V., Branchesi, M., Brocato, E., Cappellaro, E., Coccia, E., Coughlin, M., Ceca, R. D., Valle, M. D., Dionisio, C., Federico, C., Formisano, M., Frigeri, A., Grado, A., Izzo, L., Marcelli, A., Maselli, A., Olivieri, M., Pernechele, C., Possenti, A., Ronchini, S., Serafinelli, R., Severgnini, P., Agostini, M., Badaracco, F., Bertolini, A., Betti, L., Civitani, M. M., Collette, C., Covino, S., Dall'Osso, S., D'Avanzo, P., DeSalvo, R., Giovanni, M. D., Focardi, M., Giunchi, C., van Heijningen, J., Khetan, N., Melini, D.,

Mitri, G., Mow-Lowry, C., Naponiello, L., Noce, V., Oganesyan, G., Pace, E., Paik, H. J., Pajewski, A., Palazzi, E., Pallavicini, M., Pareschi, G., Pozzobon, R., Sharma, A., Spada, G., Stanga, R., Tagliaferri, G., and Votta, R. (2021). Lunar Gravitational-wave Antenna. *The Astrophysical Journal*, 910(1).

Hartmann, W. K. and Davis, D. R. (1975). Satellite-sized planetesimals and lunar origin. *Icarus*, 24:504–515.

Haruyama, J., Hioki, K., Shirao, M., Morota, T., Hiesinger, H., Van Der Bogert, C. H., Miyamoto, H., Iwasaki, A., Yokota, Y., Ohtake, M., Matsunaga, T., Hara, S., Nakanotani, S., and Pieters, C. M. (2009). Possible lunar lava tube skylight observed by SELENE cameras. *Geophysical Research Letters*, 36.

Haruyama, J., Matsunaga, T., Ohtake, M., Morota, T., Honda, C., Yokota, Y., Torii, M., and Ogawa, Y. (2008). Global lunar-surface mapping experiment using the Lunar Imager/Spectrometer on SELENE. *Earth, Planets and Space*, 60:243–255.

Hawke, B. R., Lawrence, D. J., Blewett, D. T., Lucey, P. G., Smith, G. A., Spudis, P. D., and Taylor, G. J. (2003). Hansteen Alpha: A volcanic construct in the lunar highlands. *Journal of Geophysical Research*, 108(E7).

Hawkins, S. E., Boldt, J. D., Darlington, E. H., Espiritu, R., Gold, R. E., Gotwols, B., Grey, M. P., Hash, C. D., Hayes, J. R., Jaskulek, S. E., Kardian, C. J., Keller, M. R., Malaret, E. R., Murchie, S. L., Murphy, P. K., Peacock, K., Prockter, L. M., Reiter, R. A., Robinson, M. S., Schaefer, E. D., Shelton, R. G., Sterner, R. E., Taylor, H. W., Watters, T. R., and Williams, B. D. (2007). The Mercury Dual Imaging System on the MESSENGER spacecraft. *Space Science Reviews*, 131:247–338.

Heather, D. J. and Dunkin, S. K. (2002). Crustal stratigraphy of the Al-Khwarizmi-King/Tsiolkovsky-Stark region of the lunar farside as seen by Clementine. *Planetary and Space Science*, 50:1311–1321.

Hiesinger, H. and Head, J. W. (2006). New views of lunar geoscience: An introduction and overview. *Reviews in Mineralogy and Geochemistry*, 60:1–81.

Honniball, C. I., Lucey, P. G., Li, S., Shenoy, S., Orlando, T. M., Hibbitts, C. A., Hurley, D. M.,

and Farrell, W. M. (2021). Molecular water detected on the sunlit Moon by SOFIA. *Nature Astronomy*, 5:121–127.

Hood, L. L., Zakharian, A., Halekas, J., Mitchell, D. L., Lin, R. P., Acuña, M. H., and Binder, A. B. (2001). Initial mapping and interpretation of lunar crustal magnetic anomalies using Lunar Prospector magnetometer data. *Journal of Geophysical Research*, 106(E11):27825–27839.

Hunten, D. M. and Morgan, T. H. (1988). The Mercury atmosphere. In *Mercury*, pages 562–612.

Hurwitz, D. M., Head, J. W., Wilson, L., and Hiesinger, H. (2012). Origin of lunar sinuous rilles: Modeling effects of gravity, surface slope, and lava composition on erosion rates during the formation of Rima Prinz. *Journal of Geophysical Research*, 117(3):1–15.

Jolliff, B. L., Gillis, J. J., Haskin, L. A., Korotev, R. L., and Wieczorek, M. A. (2000). Major lunar crustal terranes: Surface expressions and crust-mantle origins. *Journal of Geophysical Research*, 105(E2):4197–4216.

Kato, M., Sasaki, S., Tanaka, K., Iijima, Y., and Takizawa, Y. (2008). The Japanese lunar mission SELENE: Science goals and present status. *Advances in Space Research*, 42:294–300.

Kerber, L., Head, J. W., Solomon, S. C., Murchie, S. L., Blewett, D. T., and Wilson, L. (2009). Explosive volcanic eruptions on Mercury: Eruption conditions, magma volatile content, and implications for interior volatile abundances. *Earth and Planetary Science Letters*, 285:263–271.

Kinczyk, M. J., Prockter, L. M., Byrne, P. K., Denevi, B. W., Buczkowski, D. L., Ostrach, L. R., and Miller, E. B. (2019). The first global geological map of Mercury. *EPSC-DPS Joint Meeting 2019*, 13:1045.

King, J. S. and Scott, D. H. (1990). Geologic Map of the Beethoven Quadrangle of Mercury. *U.S. Geological Survey Report*, pages Map I–2048.

King, S. D. (2008). Pattern of lobate scarps on Mercury's surface reproduced by a model of mantle convection. *Nature Geoscience*, 1(4):229–232.

Kipp, M. E. and Melosh, H. J. (1986). Origin of the Moon: a preliminary numerical study of colliding planets. *17th Lunar and Planetary Science Conference*, pages 420–421.

Klima, R. L., Dyar, M. D., and Pieters, C. M. (2011a). Near-infrared spectra of clinopyroxenes: Effects of calcium content and crystal structure. *Meteoritics and Planetary Science*, 46(3):379–395.

Klima, R. L., Pieters, C. M., Boardman, J. W., Green, R. O., Head, J. W., Isaacson, P. J., Mustard, J. F., Nettles, J. W., Petro, N. E., Staid, M. I., Sunshine, J. M., Taylor, L. A., and Tompkins, S. (2011b). New insights into lunar petrology: Distribution and composition of prominent low-Ca pyroxene exposures as observed by the Moon Mineralogy Mapper (M3). *Journal of Geophysical Research*, 116(4):1–13.

Klimczak, C., Byrne, P. K., and Solomon, S. C. (2015). A rock-mechanical assessment of Mercury's global tectonic fabric. *Earth and Planetary Science Letters*, 416:82–90.

Kneissl, T., van Gasselt, S., and Neukum, G. (2011). Map-projection-independent crater size-frequency determination in GIS environments - New software tool for ArcGIS. *Planetary and Space Science*, 59:1243–1254.

Korteniemi, J., Walsh, L. S., and Hughes, S. S. (2015). *Wrinkle Ridge*, pages 2324–2331. Springer New York.

Leary, J. C., Conde, R. F., Dakermanji, G., Engelbrecht, C. S., Ercol, C. J., Fielhauer, K. B., Grant, D. G., Hartka, T. J., Hill, T. A., Jaskulek, S. E., Mirantes, M. A., Mosher, L. E., Paul, M. V., Persons, D. F., Rodberg, E. H., Srinivasan, D. K., Vaughan, R. M., and Wiley, S. R. (2007). The MESSENGER spacecraft. *Space Science Reviews*, 131:187–217.

Lemelin, M., Lucey, P. G., Song, E., and Taylor, G. J. (2015). Lunar central peak mineralogy and iron content using the Kaguya Multiband Imager: Reassessment of the compositional structure of the lunar crust. *Journal of Geophysical Research: Planets*, 120:869–887.

Li, S., Lucey, P. G., Milliken, R. E., Hayne, P. O., Fisher, E., Williams, J.-P., Hurley, D. M., and Elphic, R. C. (2018). Direct evidence of surface exposed water ice in the lunar polar regions. *Proceedings of the National Academy of Sciences of the United States of America*, 115(36):8907–8912.

Lock, S. J., Stewart, S. T., Petaev, M. I., Leinhardt, Z., Mace, M. T., Jacobsen, S. B., and Cuk, M. (2018). The origin of the Moon within a Terrestrial Synestia. *Journal of Geophysical Research: Planets*, 123(4):910–951.

Lucchetti, A., Pajola, M., Poggiali, G., Semenzato, A., Munaretto, G., Cremonese, G., Brucato, J. R., and Massironi, M. (2021). Volatiles on mercury: The case of hollows and the pyroclastic vent of Tyagaraja crater. *Icarus*, 370:114694.

Lucey, P. G. (2004). Mineral maps of the Moon. *Geophysical Research Letters*, 31(8):3–6.

Lucey, P. G., Blewett, D. T., Taylor, G. J., and Hawke, B. R. (2000). Imaging of lunar surface maturity. *Journal of Geophysical Research*, 105(E8):20377–20386.

Mancinelli, P., Minelli, F., Pauselli, C., and Federico, C. (2016). Geology of the Raditladi quadrangle, Mercury (H04). *Journal of Maps*, 12:190–202.

Margot, J. L., Peale, S. J., Jurgens, R. F., Slade, M. A., and Holin, I. V. (2007). Large longitude libration of Mercury reveals a molten core. *Science*, 316:710–714.

Martellato, E., Foing, B. H., and Benkhoff, J. (2013). Numerical modelling of impact crater formation associated with isolated lunar skylight candidates on lava tubes. *Planetary and Space Science*, 86:33–44.

Massironi, M. and Byrne, P. K. (2015). High-Relief Ridge. In *Encyclopedia of Planetary Landforms*, pages 932–934. Springer New York.

Massironi, M., Byrne, P. K., and van der Bogert, C. H. (2015a). Lobate Scarp. In *Encyclopedia of Planetary Landforms*, pages 1255–1262. Springer New York.

Massironi, M., Di Achille, G., Rothery, D. A., Galluzzi, V., Giacomini, L., Ferrari, S., Zusi, M., Cremonese, G., and Palumbo, P. (2015b). Lateral ramps and strike-slip kinematics on Mercury. *Geological Society Special Publication*, 401:269–290.

Mccauley, J. F., Guest, J. E., Schaber, G. G., Trask, N. J., and Greeley, R. (1981). Stratigraphy of the Caloris basin, Mercury. *Icarus*, 47:184–202.

McClintock, W. E., Izenberg, N. R., Holsclaw, G. M., Blewett, D. T., Domingue, D. L., Head, J. W., Helbert, J., McCoy, T. J., Murchie, S. L., Robinson, M. S., Solomon, S. C., Sprague, A., and Vilas, F. (2008). Spectroscopic Observations of Mercury's surface reflectance during MESSENGER's first flyby. *Science*, 321:62–65.

McEwen, A. S. and Robinson, M. S. (1997). Mapping of the Moon by Clementine. *Advances in Space Research*, 19(10):1523–1533.

McGill, G. E. and King, E. A. (1983). Geologic map of the Victoria Quadrangle of Mercury. *U.S. Geological Survey Report*, pages Map I–1409.

Melosh, H. J. (1975). Large impact craters and the moon's orientation. *Earth and Planetary Science Letters*, 26(3):353–360.

Melosh, H. J. and Dzurisin, D. (1978). Mercurian global tectonics: A consequence of tidal despinning? *Icarus*, 35(2):227–236.

Michael, G. G., Kneissl, T., and Neesemann, A. (2016). Planetary surface dating from crater size-frequency distribution measurements: Poisson timing analysis. *Icarus*, 277:279–285.

Michael, G. G. and Neukum, G. (2010). Planetary surface dating from crater size-frequency distribution measurements: Partial resurfacing events and statistical age uncertainty. *Earth and Planetary Science Letters*, 294:223–229.

Michael, G. G., Platz, T., Kneissl, T., and Schmedemann, N. (2012). Planetary surface dating from crater size-frequency distribution measurements: Spatial randomness and clustering. *Icarus*, 218:169–177.

Mighani, S., Wang, H., Shuster, D. L., Caue S, B., Nichols, C. I. O., and Weiss, B. P. (2020). The end of the lunar dynamo. *Science Advances*, 6:1–8.

Milillo, A., Fujimoto, M., Kallio, E., Kameda, S., Leblanc, F., Narita, Y., Cremonese, G., Laakso, H., Laurenza, M., Massetti, S., McKenna-Lawlor, S., Mura, A., Nakamura, R., Omura, Y., Rothery, D. A., Seki, K., Storini, M., Wurz, P., Baumjohann, W., Bunce, E. J., Kasaba, Y., Helbert, J., and Sprague, A. (2010). The BepiColombo mission: An outstanding tool for investigating the Hermean environment. *Planetary and Space Science*, 58:40–60.

Morota, T., Haruyama, J., Honda, C., Ohtake, M., Yokota, Y., Kimura, J., Matsunaga, T., Ogawa, Y., Hirata, N., Demura, H., Iwasaki, A., Miyamoto, H., Nakamura, R., Takeda, H., Ishihara, Y., and Sasaki, S. (2009). Mare volcanism in the lunar farside moscoviense region: Implication for lateral variation in magma production of the moon. *Geophysical Research Letters*, 36(21).

Morse, Z. R., Osinski, G. R., Tornabene, L. L., and Neish, C. D. (2021). Morphologic mapping and interpretation of ejecta deposits from Tsiolkovskiy crater. *Meteoritics and Planetary Science*, 56(4):767–793.

Mouginis-Mark, P. J. and Boyce, J. M. (2017). Mare infilling of Tsiolkovsky crater, the Moon. *48th Lunar and Planetary Science*, page 1206.

Murchie, S. L., Watters, T. R., Robinson, M. S., Head, J. W., Strom, R. G., Chapman, C. R., Solomon, S. C., McClintock, W. E., Prockter, L. M., Domingue, D. L., and Blewett, D. T. (2008). Geology of the Caloris basin, Mercury: A view from MESSENGER. *Science*, 321:73–76.

Murray, B. C., Strom, R. G., Trask, N. J., and Gault, D. E. (1975). Surface history of Mercury: Implications for terrestrial planets. *Journal of Geophysical Research*, 80(17):2508–2514.

Nakamura, Y. (2003). New identification of deep moonquakes in the Apollo lunar seismic data. *Physics of the Earth and Planetary Interiors*, 139:197–205.

Nakamura, Y. (2005). Farside deep moonquakes and deep interior of the Moon. *Journal of Geophysical Research E: Planets*, 110(1):1–12.

Ness, N. F., Behannon, K. W., Lepping, R. P., Whang, Y. C., and Schatten, K. H. (1974). Magnetic field observations near Mercury: Preliminary results from Mariner 10. *Science*, 185(4146):151–160.

Neukum, G. and Ivanov, B. A. (1994). Crater size distributions and impact probabilities on Earth from lunar, terrestrial-planet, and asteroid cratering data. In *Hazards Due to Comets and Asteroids*, pages 359–416. University of Arizona Press.

Neukum, G., Ivanov, B. A., and Hartmann, W. K. (2001). Cratering records in the inner solar system in relation to the lunar reference system. *Space Science Reviews*, 96:55–86.

Nozette, S., Rustan, P., Pleasance, L. P., Horan, D. M., Regeon, P., Shoemaker, E. M., Spudis, P. D., Acton, C. H., Baker, D. N., Blamont, J. E., Buratti, B. J., Corson, M. P., Davies, M. E., Duxbury, T. C., Eliason, E. M., Jakosky, B. M., Kordas, J. F., Lewis, I. T., Lichtenberg, C. L., Lucey, P. G., Malaret, E., Massie, M. A., Resnick, J. H., Rollins, C. J., Park, H. S., McEwen, A. S., Priest, R. E., Pieters, C. M., Reisse, R. A., Robinson, M. S., Simpson, R. A., Smith, D. E., Sorenson, T. C., Vorder Breugge, R. W., and Zuber, M. T. (1994). The Clementine mission to the Moon: Scientific overview. *Science*, 266(5192):1835–1839.

Ohtake, M., Matsunaga, T., Haruyama, J., Yokota, Y., Morota, T., Honda, C., Ogawa, Y., Torii, M., Miyamoto, H., Arai, T., Hirata, N., Iwasaki, A., Nakamura, R., Hiroi, T., Sugihara,

T., Takeda, H., Otake, H., Pieters, C., Saiki, K., Kitazato, K., Abe, M., Asada, N., Demura, H., Yamaguchi, Y., Sasaki, S., Kodama, S., Terazono, J., Shirao, M., Yamaji, A., Minami, S., Akiyama, H., and Josset, J.-L. (2009). The global distribution of pure anorthosite on the Moon. *Nature*, 461:236–240.

Osio-Norgaard, J., Hayes, A. C., and Whiting, G. L. (2021). Sintering of 3D printable simulated lunar regolith magnesium oxychloride cements. *Acta Astronautica*, 183:227–232.

Paige, D. A., Siegler, M. A., Zhang, J. A., Hayne, P. O., Foote, E. J., Bennett, K. A., Vasavada, A. R., Greenhagen, B. T., Schofield, J. T., McCleese, D. J., Foote, M. C., DeJong, E., Bills, B. G., Hartford, W., Murray, B. C., Allen, C. C., Snook, K., Soderblom, L. A., Calcutt, S., Taylor, F. W., Bowles, N. E., Bandfield, J. L., Elphic, R., Ghent, R., Glotch, T. D., Wyatt, M. B., and Lucey, P. G. (2010). Diviner Lunar Radiometer observations of cold traps in the Moon's south polar region. *Science*, 330:479–483.

Pasckert, J. H., Hiesinger, H., and van der Bogert, C. H. (2015). Small-scale lunar farside volcanism. *Icarus*, 257:336–354.

Peale, S. J. and Gold, T. (1965). Rotation of the planet Mercury [2]. *Nature*, 206:1240–1241.

Pegg, D. L., Rothery, D. A., Balme, M. R., Conway, S. J., Malliband, C. C., and Man, B. (2021). Geology of the Debussy quadrangle (H14), Mercury. *Journal of Maps*, 17(2):859–870.

Pierazzo, E. and Melosh, H. J. (2000). Understanding oblique impacts from experiments, observations, and modeling. *Annual Review of Earth and Planetary Sciences*, 28:141–167.

Pieters, C. M., Boardman, J., Buratti, B., Chatterjee, A., Clark, R., Glavich, T., Green, R., Head, J., Isaacson, P., Malaret, E., McCord, T., Mustard, J., Petro, N., Runyon, C., Staid, M., Sunshine, J., Taylor, L., Tompkins, S., Varanasi, P., and White, M. (2009a). The Moon mineralogy mapper (M3) on Chandrayaan-1. *Current Science*, 96(4):500–505.

Pieters, C. M., Goswami, J. N., Clark, R. N., Annadurai, M., Boardman, J., Buratti, B., Combe, J.-P., Dyar, M. D., Green, R., Head, J. W., Hibbitts, C., Hicks, M., Isaacson, P., Klima, R., Kramer, G., Kumar, S., Livo, E., Lundeen, S., Malaret, E., McCord, T., Mustard, J., Nettles, J., Petro, N., Runyon, C., Staid, M., Sunshine, J., Taylor, L. A., Tompkins, S., and Varanasi, P. (2009b). Character and spatial distribution of OH/H2O on the surface of the Moon seen by M3 on Chandrayaan-1. *Science*, 326:568–573.

Pieters, C. M., He, G., and Tompkins, S. (1996). Anorthosite and olivine layers of the farside upper crust at Tsiolkovsky. In *27th Lunar and Planetary Science Conference*, pages 1035–1036.

Pieters, C. M., He, G., Tompkins, S., Staid, M. I., and Fischer, E. M. (1995). The low-Ti basalts of Tsiolkovsky as seen by Clementine. In *26th Lunar and Planetary Science Conference*, pages 1121–1122.

Pieters, C. M. and Tompkins, S. (1999). Tsiolkovsky crater: A window into crustal processes on the lunar farside. *Journal of Geophysical Research*, 104(E9):21935–21949.

Pinet, P. C., Shevchenko, V. V., Chevrel, S. D., Daydou, Y., and Rosemberg, C. (2000). Local and regional lunar regolith characteristics at Reiner Gamma Formation: Optical and spectroscopic properties from Clementine and Earth-based data. *Journal of Geophysical Research*, 105(E4):9457–9475.

Platz, T., Byrne, P. K., Massironi, M., and Hiesinger, H. (2014). Volcanism and tectonism across the inner solar system: An overview. *Geological Society Special Publication*, 401:1–56.

Pouwels, C., Wamelink, W., Musilova, M., and Foing, B. (2020). Food for extra-terrestrial astronaut missions on native soil. *EGU General Assembly 2020*, page 20507.

Prockter, L. M. (2015). Mercury Global Geological Map. Technical report.

Robinson, M. S., Brylow, S. M., Tschimmel, M., Humm, D., Lawrence, S. J., Thomas, P. C., Denevi, B. W., Bowman-Cisneros, E., Zerr, J., Ravine, M. A., Caplinger, M. A., Ghaemi, F. T., Schaffner, J. A., Malin, M. C., Mahanti, P., Bartels, A., Anderson, J., Tran, T. N., Eliason, E. M., McEwen, A. S., Turtle, E., Jolliff, B. L., and Hiesinger, H. (2010). Lunar Reconnaissance Orbiter Camera (LROC) instrument overview. *Space Science Reviews*, 150:81–124.

Rothery, D. and Fegan, E. (2015). Mysterious origins of some catenae on Mercury. *EGU General Assembly 2015*, 17:12771.

Rothery, D. A. (2015). *Planet Mercury. From pale pink dot to dynamic world*. Springer-Praxis.

Rothery, D. A., Massironi, M., Alemanno, G., Barraud, O., Besse, S., Bott, N., Brunetto, R., Bunce, E., Byrne, P., Capaccioni, F., Capria, M. T., Carli, C., Charlier, B., Cornet, T.,

Cremonese, G., D'Amore, M., De Sanctis, M. C., Doressoundiram, A., Ferranti, L., Filacchione, G., Galluzzi, V., Giacomini, L., Grande, M., Guzzetta, L. G., Helbert, J., Heyner, D., Hiesinger, H., Hussmann, H., Hyodo, R., Kohout, T., Kozyrev, A., Litvak, M., Lucchetti, A., Malakhov, A., Malliband, C., Mancinelli, P., Martikainen, J., Martindale, A., Maturilli, A., Milillo, A., Mitrofanov, I., Mokrousov, M., Morlok, A., Muinonen, K., Namur, O., Owens, A., Nittler, L. R., Oliveira, J. S., Palumbo, P., Pajola, M., Pegg, D. L., Penttilä, A., Politi, R., Quarati, F., Re, C., Sanin, A., Schulz, R., Stangarone, C., Stojic, A., Tretiyakov, V., Väisänen, T., Varatharajan, I., Weber, I., Wright, J., Wurz, P., and Zambon, F. (2020). Rationale for BepiColombo studies of Mercury's surface and composition. *Space Science Reviews*, 216(4).

Sato, H., Robinson, M. S., Lawrence, S. J., Denevi, B. W., Hapke, B., Jolliff, B. L., and Hiesinger, H. (2017). Lunar mare TiO2 abundances estimated from UV/Vis reflectance. *Icarus*, 296:216–238.

Schaber, G. G. and McCauley, J. F. (1980). Geologic map of the Tolstoj quadrangle of Mercury (H-8). Map I-1199. *U.S. Geological Survey Report*, pages Map I–1199.

Schon, S. C., Head, J. W., Baker, D. M. H., Ernst, C. M., Prockter, L. M., Murchie, S. L., and Solomon, S. C. (2011). Eminescu impact structure: Insight into the transition from complex crater to peak-ring basin on Mercury. *Planetary and Space Science*, 59:1949–1959.

Schubert, G., Lingenfelter, R. E., and Peale, S. J. (1970). The morphology, distribution , and origin of the lunar sinuous rilles. *Reviews of Geophysics and Space Physics*, 8(1):199–224.

Schultz, P. H. (1992). Atmospheric effects on ejecta emplacement and crater formation on Venus from Magellan. *Journal of Geophysical Research*, 97(E10):16183–16248.

Schultz, R. A. (2000). Localization of bedding plane slip and backthrust faults above blind thrust faults: Keys to wrinkle ridge structure. *Journal of Geophysical Research*, 105(E5):12035–12052.

Schultz, R. A. and Zuber, M. T. (1994). Observations, models, and mechanisms of failure of surface rocks surrounding planetary surface loads. *Journal of Geophysical Research*, 99(E7):14691–14702.

Semenzato, A., Massironi, M., Ferrari, S., Galluzzi, V., Rothery, D. A., Pegg, D. L., Pozzobon, R., and Marchi, S. (2020). An integrated geologic map of the Rembrandt Basin, on Mercury, as a starting point for stratigraphic analysis. *Remote Sensing*, 12(19).

Slade, M. A., Butler, B. J., and Muhleman, D. O. (1992). Mercury radar imaging: Evidence for polar ice. *Science*, 258(5082):635–640.

Smith, D. E., Zuber, M. T., Jackson, G. B., Cavanaugh, J. F., Neumann, G. A., Riris, H., Sun, X., Zellar, R. S., Coltharp, C., Connelly, J., Katz, R. B., Kleyner, I., Liiva, P., Matuszeski, A., Mazarico, E. M., McGarry, J. F., Novo-Gradac, A.-M., Ott, M. N., Peters, C., Ramos-Izquierdo, L. A., Ramsey, L., Rowlands, D. D., Schmidt, S., Scott, V. S., Shaw, G. B., Smith, J. C., Swinski, J.-P., Torrence, M. H., Unger, G., Yu, A. W., and Zagwodzki, T. W. (2010). The Lunar Orbiter Laser Altimeter investigation on the Lunar Reconnaissance Orbiter mission. *Space Science Reviews*, 150:209–241.

Smith, D. E., Zuber, M. T., Phillips, R. J., Solomon, S. C., Hauck, S. A., Lemoine, F. G., Mazarico, E., Neumann, G. A., Peale, S. J., Margot, J. L., Johnson, C. L., Torrence, M. H., Perry, M. E., Rowlands, D. D., Goossens, S., Head, J. W., and Taylor, A. H. (2012). Gravity field and internal structure of mercury from MESSENGER. *Science*, 336:214–217.

Solomon, S. C. and Chaiken, J. (1976). Thermal expansion and thermal stress in the Moon and terrestrial planets: clues to early thermal history. In *Proceedings of the Lunar Science Conference 7th*, pages 3229–3243.

Spudis, P. D. and Guest, J. E. (1988). Stratigraphy and geologic history of Mercury. In *Mercury*, pages 118–164.

Spudis, P. D. and Prosser, J. G. (1984). Geologic map of the Michelangelo Quadrangle of Mercury. *U.S. Geological Survey Report*, pages Map I–1659.

Stevenson, D. J. (2012). Mercury's mysteries start to unfold. *Nature*, 485:52–53.

Stoffler, D. and Ryder, G. (2001). Stratigraphy and isotope ages of lunar geologic units: chronological standard for the inner solar system. *Space Science Reviews*, 96:9–54.

Strom, R. G., Chapman, C. R., Merline, W. J., Solomon, S. C., and Head, J. W. (2008). Mercury cratering record viewed from MESSENGER's first flyby. *Science*, 321:79–82.

Strom, R. G., Malin, M. C., and Leake, M. A. (1990). Geologic map of the Bach region of Mercury. *U.S. Geological Survey Report*, pages Map I–2015.

Strom, R. G. and Neukum, G. (1988). The cratering record on Mercury and the origin of impacting objects. In *Mercury*, pages 336–373.

Strom, R. G., Trask, N. J., and Guest, J. E. (1975). Tectonism and volcanism on Mercury. *Journal of Geophysical Research*, 80(17):2478–2507.

Tanaka, K. L., Skinner, J. A., and Hare, T. M. (2011). *Planetary Geologic Mapping Handbook*.

Thaisen, K., Head, J., Taylor, L., Kramer, G., Isaacson, P., Nettles, J., Petro, N., and Pieters, C. (2011). Geology of the moscoviense basin. *Journal of Geophysical Research: Planets*, 116(E6).

Thomas, R. J., Rothery, D. A., Conway, S. J., and Anand, M. (2014a). Hollows on Mercury: Materials and mechanisms involved in their formation. *Icarus*, 229:221–235.

Thomas, R. J., Rothery, D. A., Conway, S. J., and Anand, M. (2014b). Mechanisms of explosive volcanism on Mercury: implications from its global distribution and morphology. *Journal of Geophysical Research*, 119:2239–2254.

Tobler, W. (1987). Measuring spatial resolution. In *Proceedings, Land Resources Information Systems Conference*, pages 12–16.

Tognon, G., Pozzobon, R., Massironi, M., and Ferrari, S. (2021). Geologic mapping and age determinations of tsiolkovskiy crater. *Remote Sensing*, 13(18).

Tooley, C. R., Houghton, M. B., Saylor, R. S., Peddie, C., Everett, D. F., Baker, C. L., and Safdie, K. N. (2010). Lunar Reconnaissance Orbiter mission and spacecraft design. *Space Science Reviews*, 150:23–62.

Trask, N. J. and Dzurisin, D. (1984). Geologic map of the Discovery (H-11) quadrangle of Mercury. *U.S. Geological Survey Report*, pages Map I–1658.

Trask, N. J. and Guest, J. E. (1975). Preliminary geologic terrain map of Mercury. *Journal of Geophysical Research*, 80(17):2461–2477.

Tyrie, A. (1988). A description of the crater Tsiolkovsky on the lunar far side. *Earth, Moon and Planets*, 42:265–275.

Vaughan, W. M., Helbert, J., Blewett, D. T., Head, J. W., Murchie, S. L., Gwinner, K., McCoy, T. J., and Solomon, S. C. (2012). Hollow-forming layers in impact craters on Mercury: massive sulfide or chloride deposits formed by impact melt differentiation? *43rd Lunar and Planetary Science Conference*, page 1187.

Vilas, F. (1988). Surface Composition of Mercury from reflectance spectrophotometry. In *Mercury*, pages 59–76.

Wagner, R. V. and Robinson, M. S. (2021). Occurence and origin of lunar pits: observations from a new catalog. *52nd Lunar and Planetary Science Conference*, page 2530.

Walsh, L. S., Watters, T. R., Banks, M. E., and Solomon, S. C. (2013). Wrinkle ridges on Mercury and the Moon: a morphometric comparison of length–relief relations with implications for tectonic evolution. *44th Lunar and Planetary Science Conference*, page 2937.

Watters, T. R. (1988). Wrinkle ridge assemblages on the terrestrial planets. *Journal of Geophysical Research*, 93(B9):10236–10254.

Watters, T. R. and Johnson, C. L. (2010). Lunar tectonics. In *Planetary Tectonics*, pages 121–182.

Watters, T. R. and Nimmo, F. (2010). The tectonics of Mercury. In *Planetary Tectonics*, Cambridge Planetary Science, pages 15–80. Cambridge University Press.

Watters, T. R., Robinson, M. S., Bina, C. R., and Spudis, P. D. (2004). Thrust faults and the global contraction of Mercury. *Geophysical Research Letters*, 31(4).

Watters, T. R., Solomon, S. C., Robinson, M. S., Head, J. W., André, S. L., Hauck, S. A., and Murchie, S. L. (2009). The tectonics of Mercury: The view after MESSENGER's first flyby. *Earth and Planetary Science Letters*, 285:283–296.

Weber, R. C., Lin, P. Y., Garnero, E. J., Williams, Q., and Lognonné, P. (2011). Seismic detection of the lunar core. *Science*, 331:309–312.

Weidenschilling, S. J. (1978). Iron/silicate fractionation and the origin of Mercury. *Icarus*, 35:99–111.

Whitford-Stark, J. L. (1982). Geologic studies of the lunar far side crater Tsiolkovsky. In *13th Lunar and Planetary Science Conference*, pages 861–862.

Whitten, J. L., Head, J. W., Denevi, B. W., and Solomon, S. C. (2014). Intercrater plains on Mercury: Insights into unit definition, characterization, and origin from MESSENGER datasets. *Icarus*, 241:97–113.

Wieczorek, M., Neumann, G., Nimmo, F., Kiefer, W., Taylor, G., Melosh, H., Phillips, R., Solomon, S., Andrews-Hanna, J., Asmar, S., Konopliv, A., Lemoine, F., Smith, D., Watkins, M., Williams, J., and Zuber, M. (2013). The crust of the Moon as seen by GRAIL. *Science*, 339:671–675.

Wieczorek, M., Zuber, M., and Phillips, R. (2001). The role of magma buoyancy on the eruption of lunar basalts. *Earth and Planetary Science Letters*, 185(1):71–83.

Wieczorek, M. A., Jolliff, B. L., Khan, A., Pritchard, M. E., Weiss, B. P., Williams, J. G., Hood, L. L., Righter, K., Neal, C. R., Shearer, C. K., McCallum, I. S., Tompkins, S., Hawke, B. R., Peterson, C., Gillis, J. J., and Bussey, B. (2006). The constitution and structure of the Lunar interior. *Reviews in Mineralogy and Geochemistry*, 60:221–364.

Wilbur, C. L. (1978). Volcano-tectonic history of Tsiolkovskij. In *9th Lunar and Planetary Science Conference*, pages 1253–1254.

Wilhelms, D. E. (1987). *The geologic history of the Moon.*

Wilhelms, D. E. and El-Baz, F. (1977). Geologic map of the east side of the Moon. *U.S. Geological Survey Report*, pages Map I–948.

Williams, J.-P., Petro, N. E., Greenhagen, B. T., and Neish, C. (2013). Inferred age of mare fill in Tsiolkovskiy crater: constraints on the preservation of exterior impact melt deposits. In *44th Lunar and Planetary Science Conference*, page 2756.

Wilson, L. and Head, J. W. (1981). Ascent and eruption of basaltic magma on the Earth and Moon. *Journal of Geophysical Research*, 86(B4):2971–3001.

Wilson, L. and Head, J. W. (2017). Generation, ascent and eruption of magma on the Moon: New insights into source depths, magma supply, intrusions and effusive/explosive eruptions (Part 1: Theory). *Icarus*, 283:146–175.

Wright, J., Rothery, D. A., Balme, M. R., and Conway, S. J. (2019). Geology of the hokusai quadrangle (H05), Mercury. *Journal of Maps*, 15(2):509–520.

Zambon, F., Carli, C., Wright, J., Rothery, D. A., Altieri, F., Massironi, M., Capaccioni, F., and Cremonese, G. (2022). Spectral units analysis of quadrangle H05-Hokusai on1Mercury. *Journal of Geophysical Research: Planets*, 127.

Zuber, M. T., Montési, L. G. J., Farmer, G. T., Hauck, S. A., Ritzer, J. A., Phillips, R. J., Solomon, S. C., Smith, D. E., Talpe, M. J., Head, J. W., Neumann, G. A., Watters, T. R., and Johnson, C. L. (2010). Accommodation of lithospheric shortening on Mercury from altimetric profiles of ridges and lobate scarps measured during MESSENGER flybys 1 and 2. *Icarus*, 209:247–255.

Acknowledgements

I would like to express my deepest appreciation to my supervisor, Matteo Massironi, for his valuable comments and support during these years. Meeting with him and his contagious enthusiasm for geology even before starting university confirmed once more that the field of geosciences was my way. In particular, I will always thank him for introducing me to planetary geology. I thank profusely Giampiero Naletto, Lorenza Giacomini and Riccardo Pozzobon for their, unfortunately mostly online, kind support and collaboration and for teaching me how to be a good researcher, able to afford everyday problems with perspicacity and savoir-faire. I wish to thank also the extra help provided by my "Science family", and in particular by Valentina Galluzzi, Francesca Zambon, Cristian Carli and Sabrina Ferrari.

I am also very grateful to all my PhD colleagues for their positive confrontation and moral boosts and to all my friends for always supporting me during my academic career.

In closing, my most loving acknowledgement to my family for always believing in me and watching my back.

Last but not least, my best wishes of a speedy recovery to Mr Covid19 that destroyed my beloved everyday life and exacerbated my craziness.

This research was supported by the European Union's Horizon 2020 research and innovation programs under grant agreements No 776276-PLANMAP and No 871149-GMAP and by the Italian Space Agency within the SIMBIO-SYS project (ASI-INAF agreement No I/022/10/0).